This is to certify that the

dissertation entitled

RADAR TARGET DISCRIMINATION USING EARLY-TIME RESPONSES

presented by

QING LI

has been accepted towards fulfillment of the requirements for

DOCTOR degree in **DEPT. OF EE**

Edward J Rothwell

Major professor

Date 06/25/95

RADAR TARGET DISCRIMINATION USING EARLY-TIME RESPONSES

by

Qing Li

A DISSERTATION

Submitted to
Michigan State University
in partial fulfillment of the requirements
for the degree of

DOCTOR OF PHILOSOPHY

Department of Electrical Engineering

1995

As a test of the Altes's model and an investigation into the scattering properties of some particular targets, the theoretical and experimental scattering center analysis of simple canonical targets such as a flat plate, 90^0 corner reflector, and cylinder is undertaken. Physical optics (PO) and geometrical theory of diffraction (GTD) or physical theory of diffraction (PTD) are used to determine the scattering center transfer functions. The results obtained using the above high frequency theory and the Altes's model from measurements are presented and compared. The match is quite good in both magnitude and phase. Altes's model can describe scattering center properties accurately.

Accurate measurement is essential for implementing an automated discrimination scheme for radar targets. The measurement calibration procedure and improved methods in measurements of aircraft models are briefly reviewed. Measurement results using two different frequency bands for two antennas systems are also demonstrated. Successful discrimination among scale aircraft models is illustrated by utilizing their measured scattered field responses.

ABSTRACT

RADAR TARGET DISCRIMINATION USING EARLY-TIME RESPONSES

By

Qing Li

This dissertation addresses several topics associated with automated radar target discrimination. Automated discrimination schemes based on combined E-pulse and early-time correlation are presented. The performance of these schemes is evaluated for the case of scale model aircrafts in the presence of various levels of random noise. Since the early-time E-pulse and correlation techniques use the early-time information of the target, they are both aspect dependent.

Development of successful radar target discrimination schemes using ultra-wideband signatures hinges on an accurate understanding of the scattering behavior of complex radar targets. As we know it is very difficult to calculate the scattered field of complex targets theoretically. Thus, we give a mathematical model (Altes's model) to represent the scattering center impulse response. The extraction of target scattering center temporal positions, pulse responses and transfer functions from a measured response is considered. Some techniques including the fitting scheme and the genetic algorithm method are introduced. The genetic algorithm produces better results when the temporal overlapping of scattering center responses is severe, but it has no guarantee of convergence and requires far more computer effort.

ACKNOWLEDGMENTS

I would like to express my sincerest appreciation to Dr. K. M. Chen. His encouragement to finish my graduate studies at Michigan State University and his teaching and guidance during my research will not be forgotten. Thank him very much for his generous support throughout my work. To D. P. Nyquist, thank for his outstanding teaching, deep concern and guidance. To Dr. Byron Drachman, thank him for his participating as a member of my committee. I am especially grateful to Dr. E. J. Rothwell, the finest thesis advisor I have ever met. His sincere interest, encouragement and expert technical advice will long be remembered.

I also want to thank my fellows at EM lab. It has been a great pleasure to work and learn with them.

To my sisters, I want to express appreciation for their constant encouragement and financial support.

Finally, to my wonderful husband, Dai, thanks for his constant love, support, and understanding.

TABLE OF CONTENTS

LIST OF TABLES

LIST OF FIGURES

F

F

F

F

Fi

Fig

Fig.

Fig.

F

F

F

Fi

Fi

Fig

Fig

Fig

Figu

CHAPTER 1

INTRODUCTION

Radar target discrimination and identification have been important topics during the past ten years. It is necessary to have an effectively automated scheme to discriminate friendly targets from enemy targets in such special situations as war. Since the scattering problems of complex targets (aircraft, missiles, etc.) are extremely difficult to solve, the commonly used discrimination techniques always extract target features from the measurement of scattered fields. This dissertation is concerned with the scattering center temporal position extraction and pulse responses, transfer function determination of scale aircraft models using the fitting scheme and genetic algorithm (G.A.). This dissertation also presents discrimination schemes called the combined E-pulse and early-time correlation techniques, which utilize the early-time scattered response of a target.

It is well known that the late-time portion of the time domain scattered field response of conducting radar targets is composed entirely of damped sinusoids, oscillating at frequencies which are functions only of target geometry. Many techniques such as the K-pulse [1], [2], and the late-time E-pulse technique [3], [4], [5], [6] developed at Michigan State University by K. M. Chen and his associates are based on natural frequencies present in the late-time response. These techniques are aspect independent. Although they have successfully shown that discrimination is possible for radar targets, these approaches ignore the early-time behavior which is dominated by localized specular reflections from target scattering centers. For targets with low Q or targets whose natural resonances are not excited by the interrogating waveform, the late-time signal energy is quite small, and the above techniques are impractical. To overcome this problem, the early-time extinction pulse (E-pulse) is defined such that when it is convolved with an early-time response, it produces zero signal in the "late frequency" range. There is a duality between the temporal late-time response and the spectral early-time response. This duality allows the direct application of late-time E-pulse cancellation to spectral early-time data. We also discuss a correlation-based discrimination scheme.

This thesis covers a wide variety of topics pertinent to radar target identification and discrimination. Development of successful radar target discrimination schemes using ultra-wideband signatures hinges on an accurate understanding of the scattering behavior of complex radar targets. Chapter 2 describes a model (Altes's model) representing the scattering center impulse response of a target. The fitting scheme is exploited to determine scattering center temporal positions and amplitudes. Two scale aircraft models, a B-58 and a B-52, are utilized to demonstrate the fitting scheme performance. This model provides not only a better understanding of scattering behavior but also a method for reducing data storage. The effects of various noise levels and different measurement bands on the fitting scheme are also discussed.

There are many approaches to determine the peaks of a function. Perhaps most straightforward is the gradient search method. Difficulty arises with this technique, however, since it needs initial guesses and tends to get "stuck" at local minima. Chapter 3 introduces a genetic algorithm, which provides a more natural minimization procedure based on a survival rule, to simultaneously extract several scattering center temporal positions. Numerical results will be shown and compared to those obtained in the previous chapter. Genetic algorithms can also be used to extract the natural frequencies of a target [7].

Chapter 4 presents a theoretical verification of the Altes's model introduced in Chapter 2. Three simple canonical targets, a flat plate, 90^0 corner reflector, and circular cylinder, are selected. Since physical optics (PO) and geometrical theory of diffraction (GTD) or physical theory of diffraction (PTD) are only accurate when the scatterers are much larger than a wavelength, the canonical targets are chosen to be physically large. Scattering center transfer functions (magnitude and phase) of targets determined from the measured data using the Altes's model are compared to those determined using the high frequency theory.

Chapter 5 shows a duality between the temporal behavior of the late-time component of a transient response and the spectral behavior of the early-time component. Because of this duality, it is possible to devise an early-time E-pulse technique identical to the late-time E-pulse technique with the exception that discrimination is aspect dependent. Early-time and late-time information can be incorporated to provide a single discrimination decision. Possibilities include using late-time information to estimate possible targets and aspect angles, then using early-time information to finalize the identification decision.

Chapter 6 gives two techniques, the "time-domain" method, and the "frequency-domain" method, for reducing data storage. Correlation-based target discrimination could be performed on data which are stored in terms of scattering center temporal positions and amplitudes or "complex times" associated with scattering centers. A "discrimination range" obtained using two correlation techniques will be demonstrated as a function of various noise levels.

Lastly, Chapter 7 reviews the calibration procedures and improved methods in measurements of aircraft models developed at the EM lab at MSU. The measurements are performed in the frequency domain with a frequency sweeping vector network analyzer. Experimental results using two different frequency bands for two measurement systems are presented and utilized throughout the dissertation.

CHAPTER 2

DETERMINATION OF RADAR TARGET SCATTERING CENTER TRANSFER FUNCTIONS

2.1 Introduction

Development of successful radar target discrimination schemes using ultra-wideband signatures hinges on an accurate understanding of the scattering behavior of complex radar targets. In the time domain, a target response consists of an early-time component which is localized and specular in nature. The temporal shape of specular responses depends on the localized geometry of the target. Many radar targets can be well approximated as consisting of a set of discrete scattering centers.

One common approach to estimate a time-domain scattering profile, and to locate and characterize the discrete scattering centers, is a parametric scattering model, such as the Prony's model. The prony's model was considered in [8], where it was shown that the model could determine scattering center temporal positions of point scatters, and in [9], where the model dealt with temporal positions of complex targets. Although Prony's method is simple to use, it is extremely sensitive to random noise and selection of the number of scattering centers present in the measured response waveform. The most important drawback is the scattering center temporal positions determined by the above scheme do not correspond to the actual ones for a band-limited measurement system. These papers never presented pulse responses and transfer functions of individual scattering centers. Other approaches include the early-time E-pulse extraction technique [10], which will be discussed in Chapter 5.

This chapter introduces a model suggested by Altes [11], which presents a more fundamental study of scattering properties of radar targets. The pulse responses and transfer functions of individual scattering centers have been identified using early-time time domain data with temporally separated "hotspots". By understanding how these centers process the transmitted waveform, it is hoped that a better model can be created and a correlation-based radar target discrimination scheme using the reconstructed response stored in terms of temporal positions and amplitudes can be developed. This scheme will be demonstrated in Chapter 6.

The outline of this chapter is as follows: In section 2.2, we describe a scattering model (Altes's model) and present an approach to determine scattering center temporal positions and amplitudes. To verify our scheme, Three types of artificial pulse responses, each of which has three scattering centers located at different time positions, are chosen. The reconstructed waveforms, pulse responses, and transfer functions of three scattering centers are demonstrated. Two scale aircraft models, a B-58 and a B-52, are utilized in section 2.3 and section 2.4 to demonstrate scheme performance for complex targets. The effects of various level of random noise and different measurement bands on the scheme are also discussed.

2.2 Scattering Model and Its Simple Test

Altes [11] suggests that the early-time scattered field response, $s_0(t)$, consists of distinct specular reflections arising from scattering centers on the target. The response is assumed to be sampled at time t_i, $i=1,2,\ldots,I$. If $h_m(t)$ represents impulse response of the m^{th} scattering center at some aspect angle, then the early-time scattered field pulse response is modeled as

$$s_0(t) \approx p(t) * \sum_m h_m(t) = \sum_m f_m(t) \tag{2.1}$$

where $p(t)$ is the transmitted pulse waveform, and $f_m(t)$ is pulse response of the m^{th} scattering center given by

$$f_m(t) = p(t) * h_m(t) \tag{2.2}$$

If (2.2) is taken to be an accurate physical description of early-time scattering, only the impulse response $h_m(t)$ needs to be determined to specify the scattered field response. If the scattering centers are purely specular, each impulse response will take the form of a delta function. We hypothesize that the impulse response might be dominated by a delta function, its integrals, and derivatives. Obviously, this assumption is a purely mathematical representation. We now wish to characterize each of the scattering center impulse responses more accurately.

Without loss of generality, the impulse response of m^{th} scattering center located at temporal position T_m can be expanded as [11]

$$h_m(t) = \sum_n a_{mn} \delta^{(n)}(t - T_m) \tag{2.3}$$

here a negative value of n refers to the n^{th} integral of the delta function while a position value of n refers to the n^{th} derivative of the delta function. This is equivalent to representing the transfer function of m^{th} scattering center as a polynomial function. Using the time shifting and differentiation theorem for Fourier transform gives

$$H_m(\omega) = \mathscr{F}\{h_m(t)\} = \sum_n a_{mn} e^{-j\omega T_m} (j\omega)^n \tag{2.4}$$

Unfortunately, it is not possible to measure $H_m(\omega)$ since only a finite portion of the spectrum can be covered in any measurement. Thus it is necessary to deal with the band-limited pulse responses of the scattering centers. Let $F_m(\omega)$ represent the band-limited frequency domain response of the m^{th} scattering center

$$F_m(\omega) = \mathscr{F}\{f_m(t)\} = \sum_n a_{mn} G_{mn}(\omega) \tag{2.5}$$

where

$$G_{mn}(\omega) = P(\omega) e^{-jT_m \omega} (j\omega)^n \tag{2.6}$$

Thus the pulse response of the m^{th} scattering center can be written as

$$f_m(t) = \sum_m a_{mn} g_{mn}(t) \tag{2.7}$$

where

$$g_{mn}(t) = \mathscr{F}^{-1}\{G_{mn}(\omega)\} \tag{2.8}$$

When the response of a target is measured in the frequency domain, the scattering center transfer functions are all overlapped and cannot be separated. However, if the frequency band is wide enough, the pulse responses found by windowing and inverse transforming the frequency domain target response will be temporally separated. Thus, computation of the scattering center transfer functions must be done in the time domain, by calculating the unknown amplitudes a_{mn}. These then give the transfer functions through (2.4).

The procedure for computing the amplitudes a_{mn} is as follows. The measured frequency domain scattered field response of a particular target is windowed with the incident pulse spectrum $P(\omega)$ (to reduce unwanted truncation-induced oscillations) and inverse transformed into time domain using the FFT. The early-time portion of the time domain pulse response will consist of events representing the pulse responses of the scattering centers. If the equivalent pulse $p(t)$ is wide, some of the pulse responses will overlap. It is extremely difficult to separate scattering centers. However, if the pulse is narrow, the events will be temporally separated and can be easily analyzed using the least squares method. First, the first scattering center pulse response $f_1(t)$ calculated from (2.7) is fit to the measured pulse response $s_0(t)$ with the amplitudes, a_{1n}, determined to provide a minimum error best fit. This best fit will match the scattering center with the largest energy. After the scattering center pulse response has been determined, a signal, $r_2(t)$, is formed by subtracting off $f_1(t)$ from $s_0(t)$ (providing a signal with one less scattering center). Then a waveform $f_2(t)$, is fit to $r_2(t)$, determining the pulse response of the scattering center with the second highest energy. This response is then subtracted off to form a signal $r_3(t)$ and the process is repeated until all of the dominant scattering center pulse responses have been determined.

In the process of determining the scattering center pulse responses, it is necessary to find T_m, the m^{th} temporal position of the scattering center. This is done by the least squares method during the minimization process which determines the amplitudes a_{mn}. Define the error function to be minimized as

$$\begin{aligned}\epsilon(T_m) &= \sum_i \left[s_0(t_i) - \sum_{k=1}^{m} \sum_n a_{kn} g_{kn}(t_i) \right]^2 \\ &= \sum_i \left[r_m(t_i) - \sum_n a_{mn} g_{mn}(t_i) \right]^2\end{aligned} \tag{2.9}$$

where

$$\begin{aligned} r_m(t) &= s_0(t) - \sum_{k=1}^{m-1} \sum_n a_{kn} g_{kn}(t) \qquad && m>1 \\ r_m(t) &= s_0(t) && m=1 \end{aligned} \tag{2.10}$$

In

an

de

sq

va

$\frac{\partial}{\partial x}$

wh

equ

whe

resul

T_a an

fini

functi

functi

is vers

The G

In essence, the scattering center pulse response is "placed" over the pulse response at T_m and a_{mn} are determined to minimize the error for that choice of T_m. The proper T_m which describes the temporal position of the scattering center is that which produces the least square error in (2.9). To determine the minimum, the entire early-time range of possible values of T_m is searched.

Note that the error is minimized when

$$\frac{\partial \epsilon}{\partial a_{mk}} = -2\sum_i \left[r_m(t_i) - \sum_n a_{mn} g_{mn}(t_i) \right] g_{mk}(t_i) = 0 \qquad k = 1,2,..,N \qquad (2.11)$$

where N is the total number of n in (2.4). The above equation can be written in linear equation form as

$$\sum_n a_{mn} A_{nk} = b_k \qquad k=1,2,\ldots,N \qquad (2.12)$$

where

$$\begin{aligned} A_{mk} &= \sum_i g_{mn}(t_i) g_{mk}(t_i) \\ b_k &= \sum_i r_m(t_i) g_{mk}(t_i) \end{aligned} \qquad (2.13)$$

To ensure reasonable accuracy it is important to calculate $g_{mn}(t)$ carefully. For the results described in this section, the quantity $G_{mn}(\omega)$ is computed for a certain value of T_m and $g_{mn}(t)$ is found using the inverse FFT from (2.6). The above method is called the "fitting scheme".

The weighting functions must be addressed before moving on. Weighting functions are used to eliminate the effect an edge discontinuity has on a spectrum. The function used below is the Gaussian modulated cosine (GMC). This weighting function is versatile since the center frequency and spectral width can be adjusted independently. The GMC waveform is given by

$$w_{gc}(t) = \cos(\pi f_c)\exp(-\pi(t/\tau)^2) \tag{2.14}$$

and its corresponding spectrum is

$$W_{gc}(f) = \tau\exp(-\pi(f-f_c)\tau^2) + \exp(-\pi(f+f_c)\tau^2) \tag{2.15}$$

where f_c is the frequency of the cosine and τ is the shape factor.

In order to test this algorithm, we have created four artificial responses. Each response has three scattering centers located at different time positions. Each scattering center impulse response is represented by an integral of a delta function, a delta function, and a derivative of a delta function. They have a relative amplitude of 0.25, 1, and 0.5, respectively. The first three pulse responses are obtained by creating 601 points in the frequency band 1 to 7 GHz, windowed using a Gaussian modulated cosine function (GMC) centered at 4 GHz (giving an equivalent pulse width of about 0.4 ns) and inverse transformed with a 4096 point FFT. As a demonstration of the fitting scheme performance, Figure 2.1 shows the artificial response created with the scattering centers separated about 2.0 ns, and the reconstructed response using three scattering centers, and $n=-2,-1,\ldots,2$ for better fit. The agreement is very good. The heights and positions of the stars (*) shown in Figure 2.1 represent the relative energy in each scattering center response and the temporal positions of three scattering centers. The pulse responses of three scattering centers calculated using (2.2) are shown in Figure 2.2. Once all the scattering center pulse responses have been determined, the overall early-time pulse response of the target can be reconstructed by summing all the pulse responses. The scattering center transfer functions for three scattering centers, calculated using (2.4) are shown in Figure 2.3. As expected, the first, second, and third scattering center are domin

functi

the se

at low

transi

somew

will no

of the s

ns apar

dotted

scatter

and th

trans

freq

th

po

er

ov

resp

that t

three p

the timing

dominated by a constant, ω, and $1/\omega$, respectively. Note that to get the true transfer function, the spectrum of the pulse $P(\omega)$ has been divided out of (2.5). We notice that the second transfer function is not exactly a straight line since the spectrum is very small at low frequencies. The scheme is ill-conditioned when it determines scattering center transfer functions at these lower or upper frequency limits.

If the bandwidth is narrow, the scattering center pulse responses overlap somewhat, and it is anticipated that the accuracy of the resulting center transfer functions will not be optimum. To show the effects of response overlapping on the performance of the scheme, three scattering center pulse responses are put a smaller distance of 0.6 ns apart. This results in the slightly overlapped responses shown in Figure 2.4. The dotted line represents the reconstructed response, which shows an excellent match. The scattering center pulse responses of three scattering centers are illustrated in Figure 2.5, and the corresponding transfer functions are shown in Figure 2.6. We observe that the transfer functions of the first and second scattering centers are good except at the lower frequency where some error is introduced in dividing out the pulse spectrum.

Even when the pulse response overlapping is considerable as shown in Figure 2.7, the reconstructed response fits well, but the first and second scattering center temporal positions are shifted from their peak positions about 0.1 ns due to this overlapping. The error caused by this shifting is tolerable here. This demonstrates that pulse response overlapping does not affect determination of temporal positions greatly. The pulse responses and transfer functions are illustrated in Figure 2.8 and Figure 2.9. We note that three waveforms change somewhat especially for the pulse response sidelobes. The three scattering center transfer functions are distorted greatly due to ill-conditioning of the fitting scheme. We will discuss the genetic algorithm (G.A.) in the next chapter. The

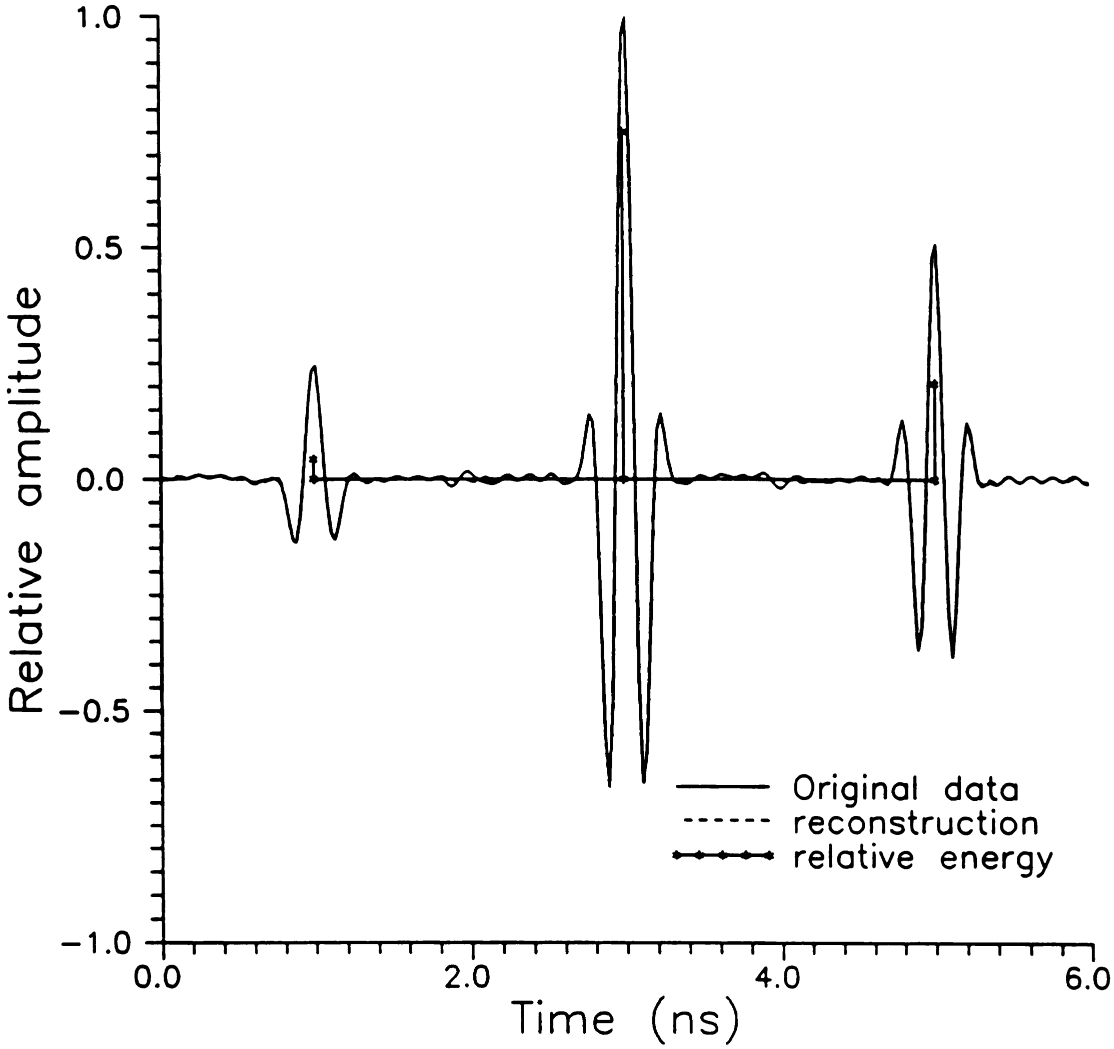

Figure 2.1 Artificial response created in the frequency band 1-7 GHz, and reconstructed response using 3 scattering centers, 4096 pt FFT, n=-2,-1,...,2, and GMC window with τ=0.3 ns, f_c=4 GHz.

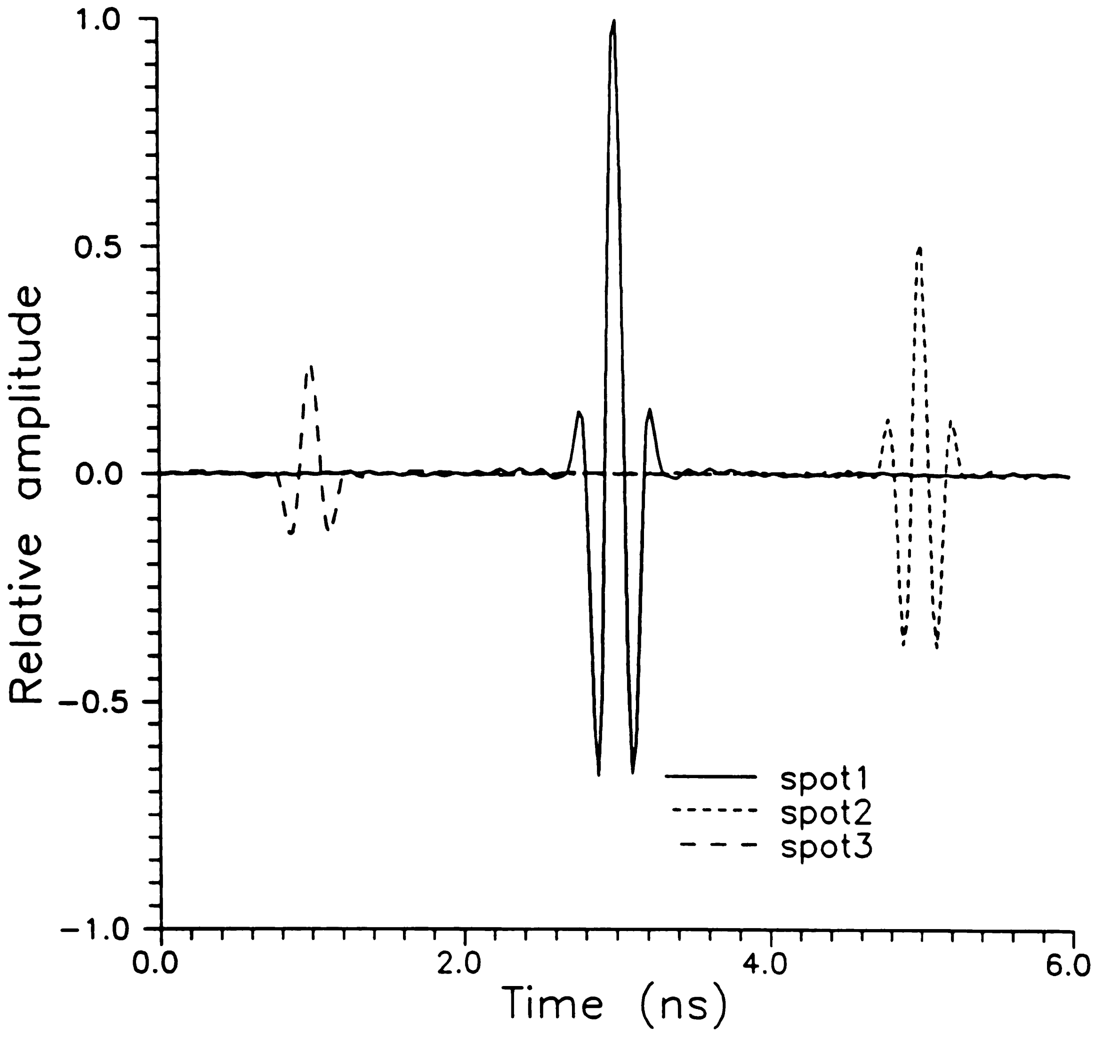

Figure 2.2 Pulse responses of three specular points.

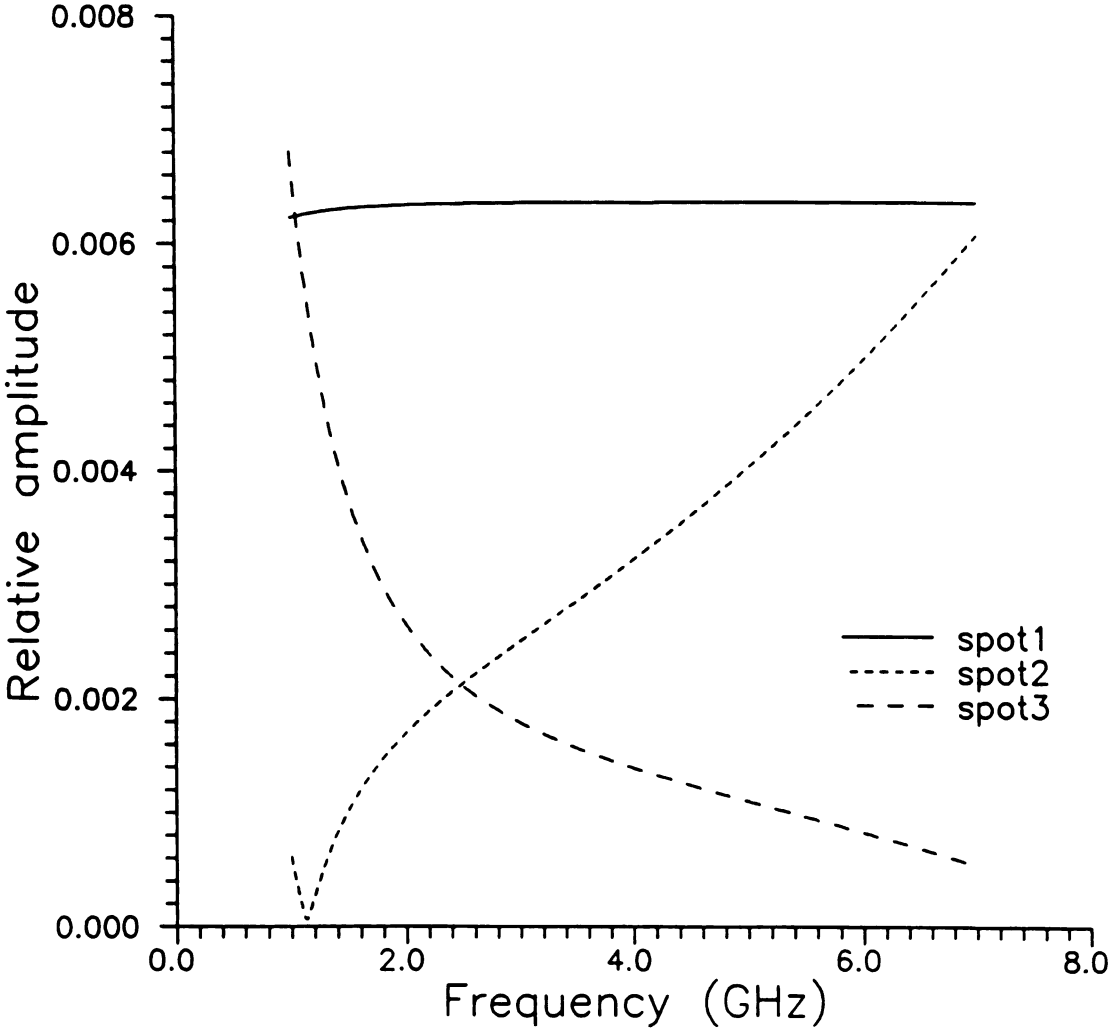

Figure 2.3 Transfer functions of three specular points.

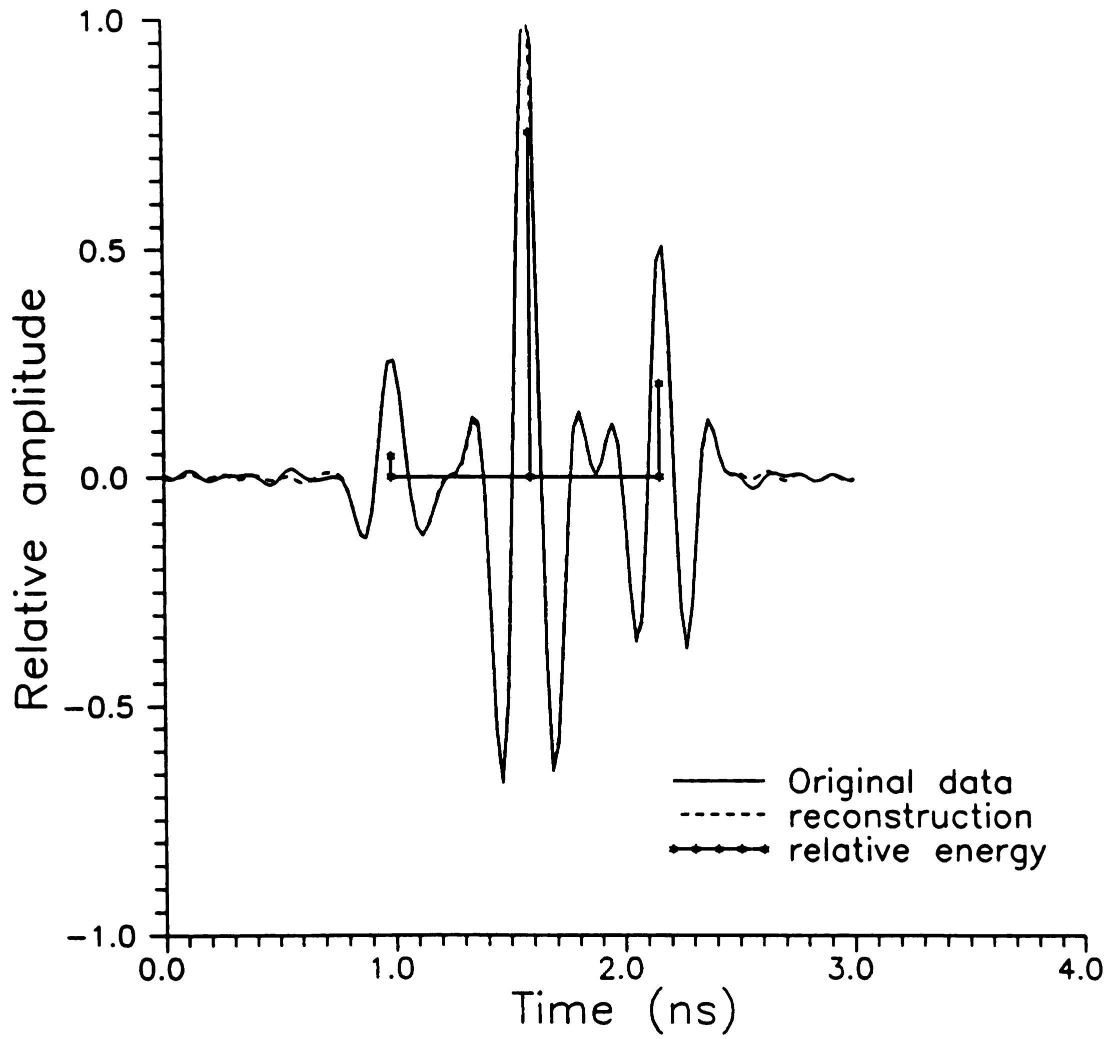

Figure 2.4 Artificial response created in the frequency band 1-7 GHz, and reconstructed response using 3 scattering centers, 4096 pt FFT, n=-2,-1,...,2, and GMC window with τ=0.3 ns, f_c=4 GHz.

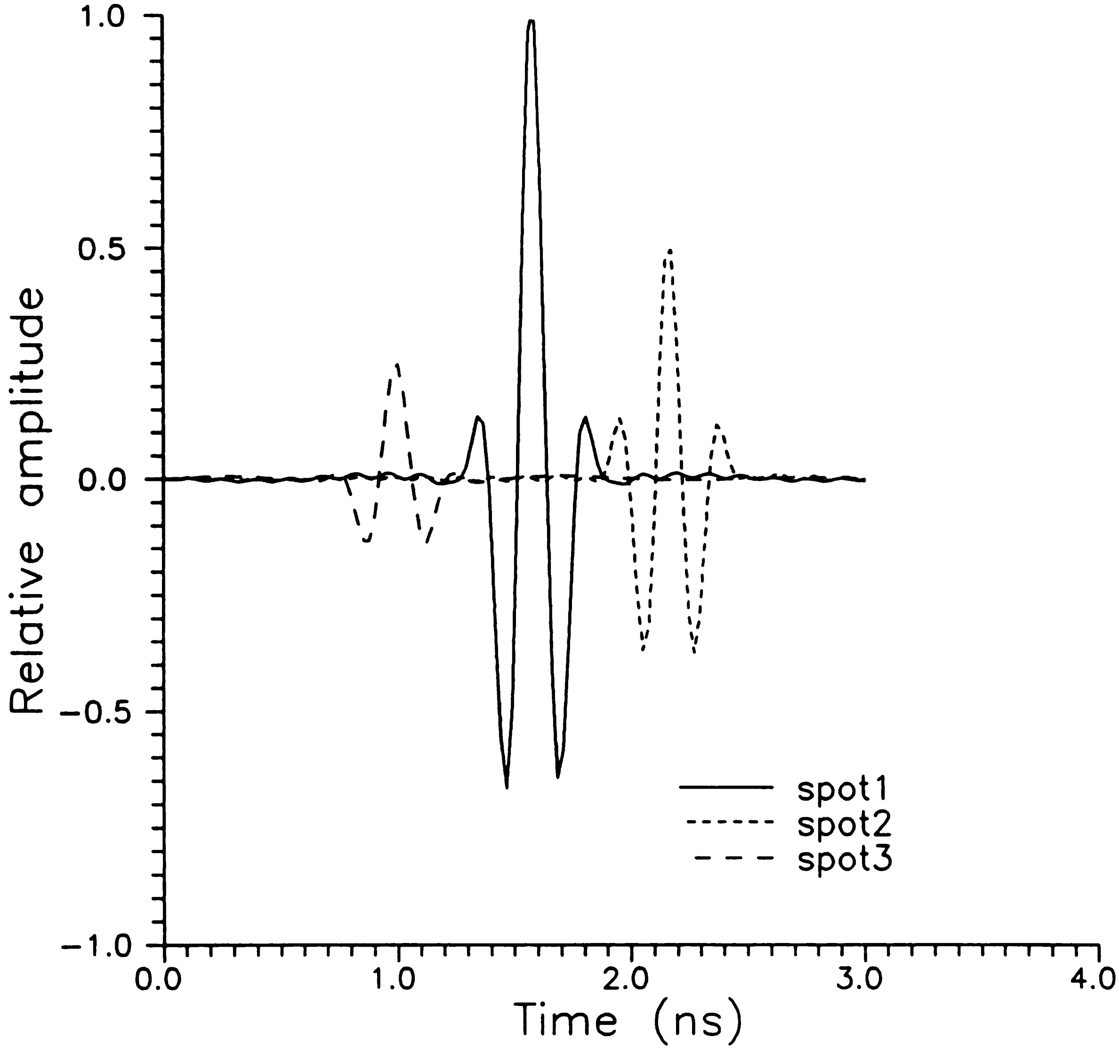

Figure 2.5 Pulse responses of three specular points.

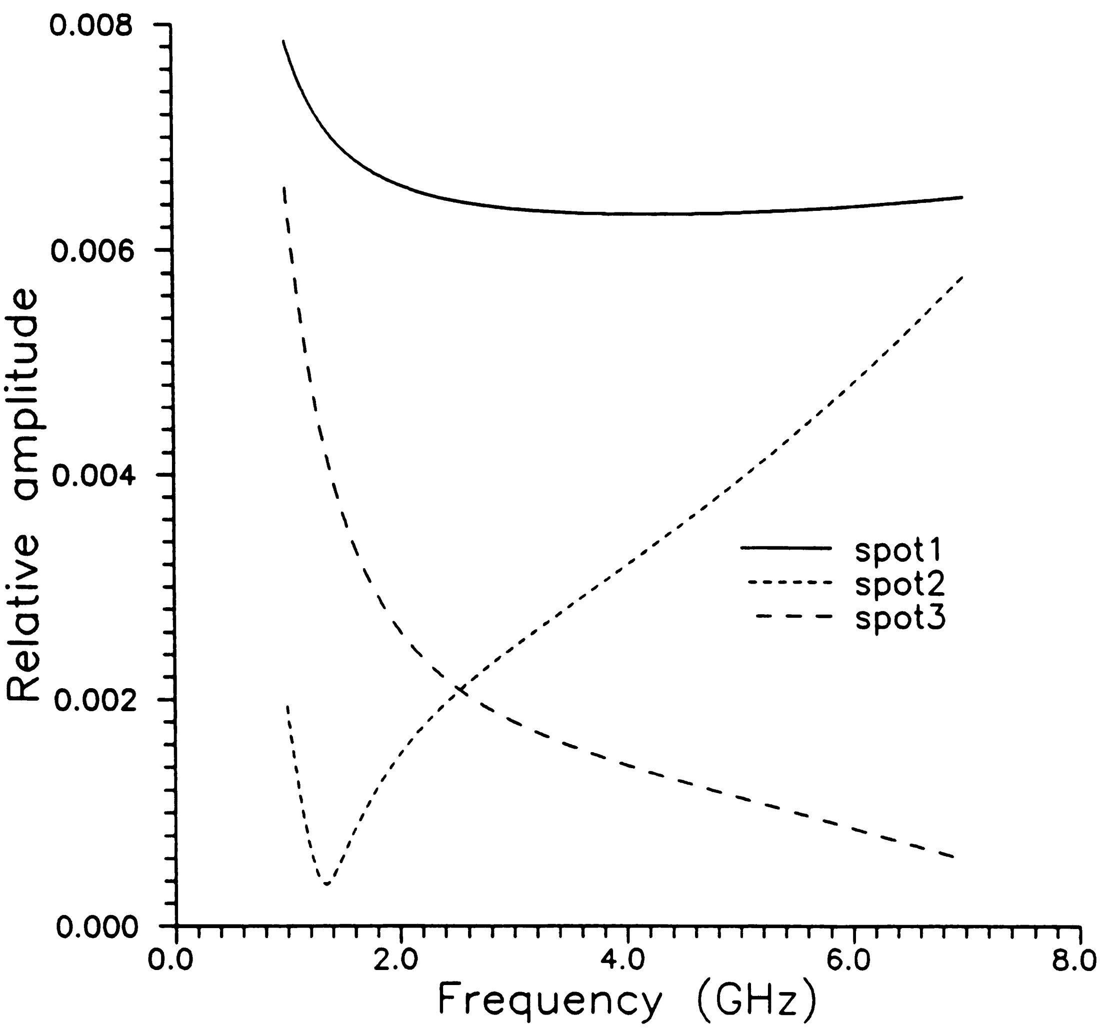

Figure 2.6 Transfer functions of three specular points.

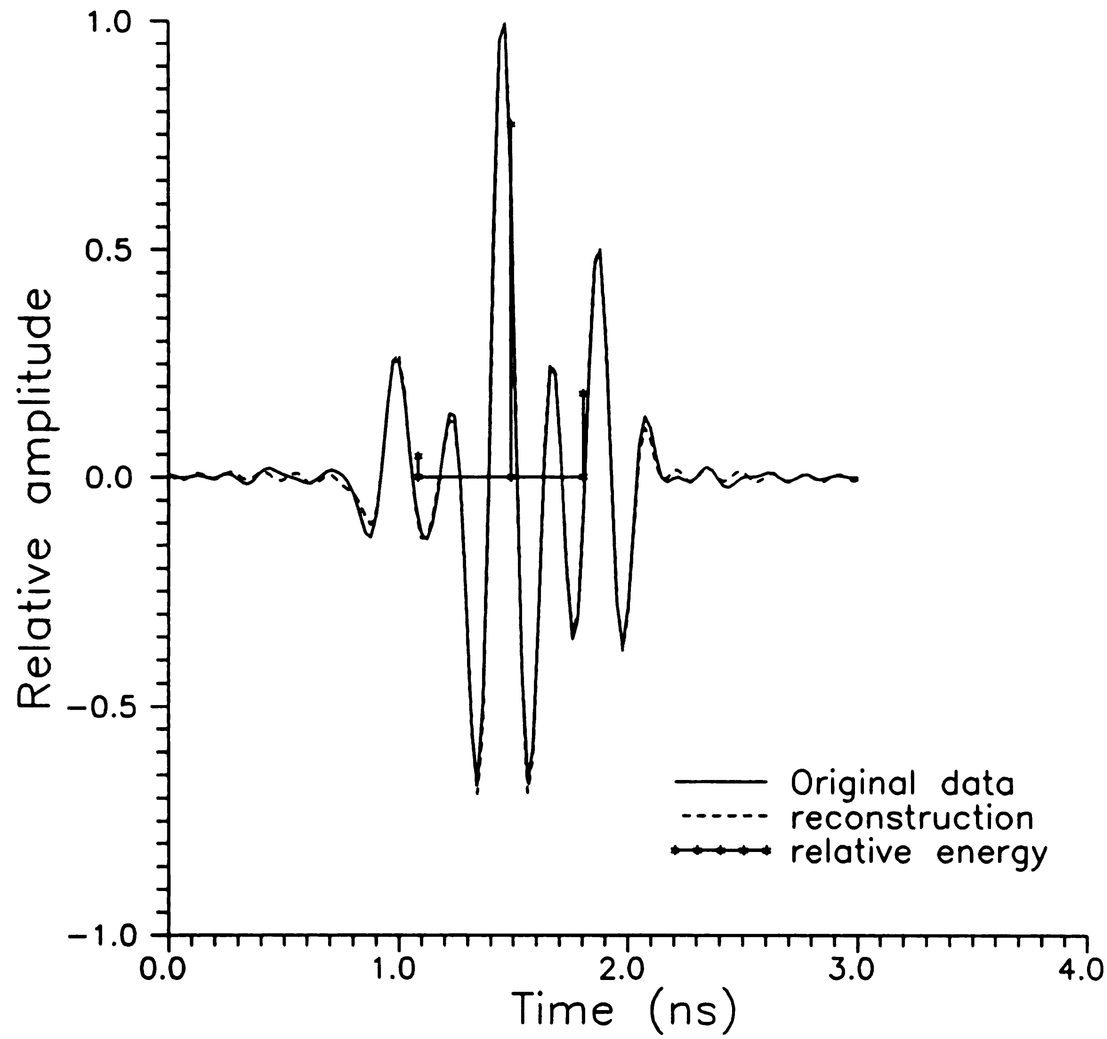

Figure 2.7 Artificial response created in the frequency band 1-7 GHz, and reconstructed response using 3 scattering centers, 4096 pt FFT, n=-2,-1,...,2, and GMC window with τ=0.3 ns, f_c=4 GHz.

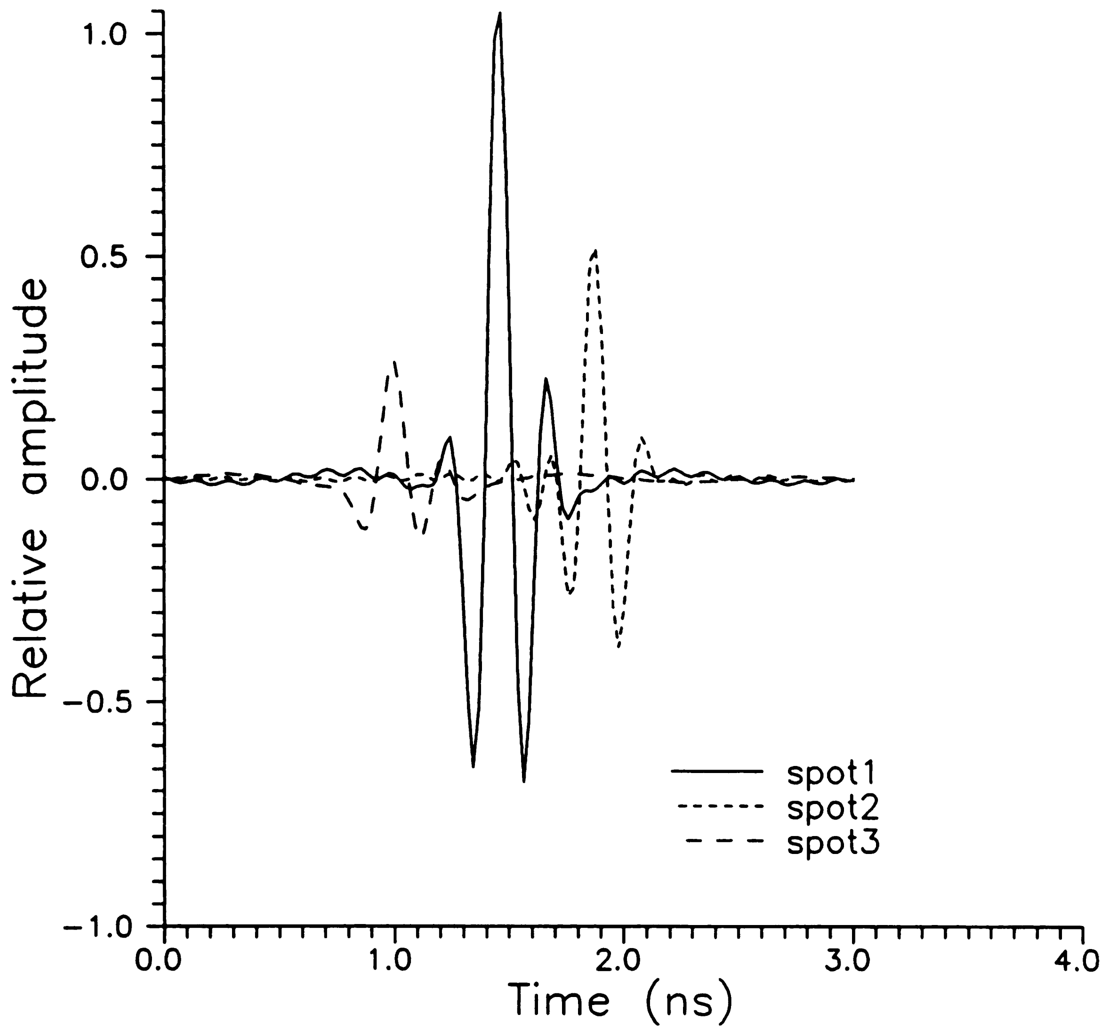

Figure 2.8 Pulse responses of three specular points.

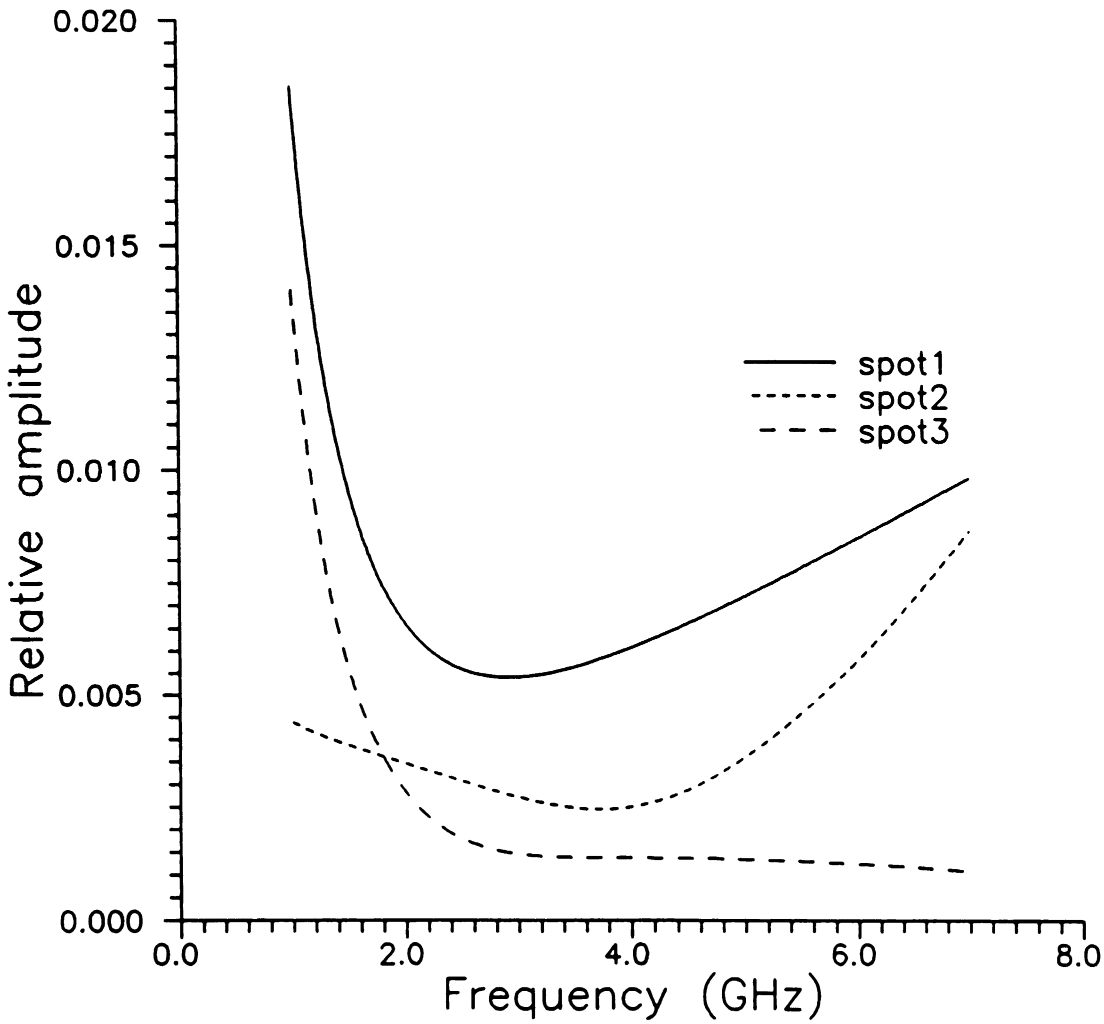

Figure 2.9 Transfer functions of three specular points.

results will be much more accurate since G.A. extracts all the scattering center temporal positions simultaneously. In order to obtain accurate results, it is necessary that each of the scattering center pulse responses match quite well. This requires that the pulse response of a target is smooth enough, which can be satisfied by using the GMC function instead of the cosine taper function, and that the scattering center pulse responses are less overlapped, which can be improved by either using a larger target or a larger bandwidth.

If severe overlapping of pulse responses occurs, an accurate estimation of the number of scattering centers is not possible. To test the effect of overguessing the number of scattering centers, Figure 2.10 shows the reconstructed response with 4 scattering centers assumed present. The energy in the "fourth" scattering center is very small. This reveals that the scattering center is an artifact. Similar conclusions can be based on the pulse responses, shown in Figure 2.11, and the transfer functions, shown in Figure 2.12. Note that the pulse responses and transfer functions of 1st, 2nd, and 3rd scattering centers are nearly same as those shown in Figure 2.5 and Figure 2.6 because of scattering center extraction procedure used.

At this point, we may want to know the effect of underestimating the number of scattering centers on the scheme as shown in Figure 2.13, Figure 2.14, and Figure 2.15. Since less information is included, the reconstructed data does not match well. The above conclusions suggest a method of estimating the number of scattering centers: first, use a lesser number and observe the pulse responses and transfer functions. Second, if the reconstructed data does not match well, increase the estimation number until a better fit and reasonable larger responses are obtained.

As we mentioned before, accuracy could be improved by a larger bandwidth. We have acquired wideband TEM horn antennas (2-18 GHz operational band) with extremely

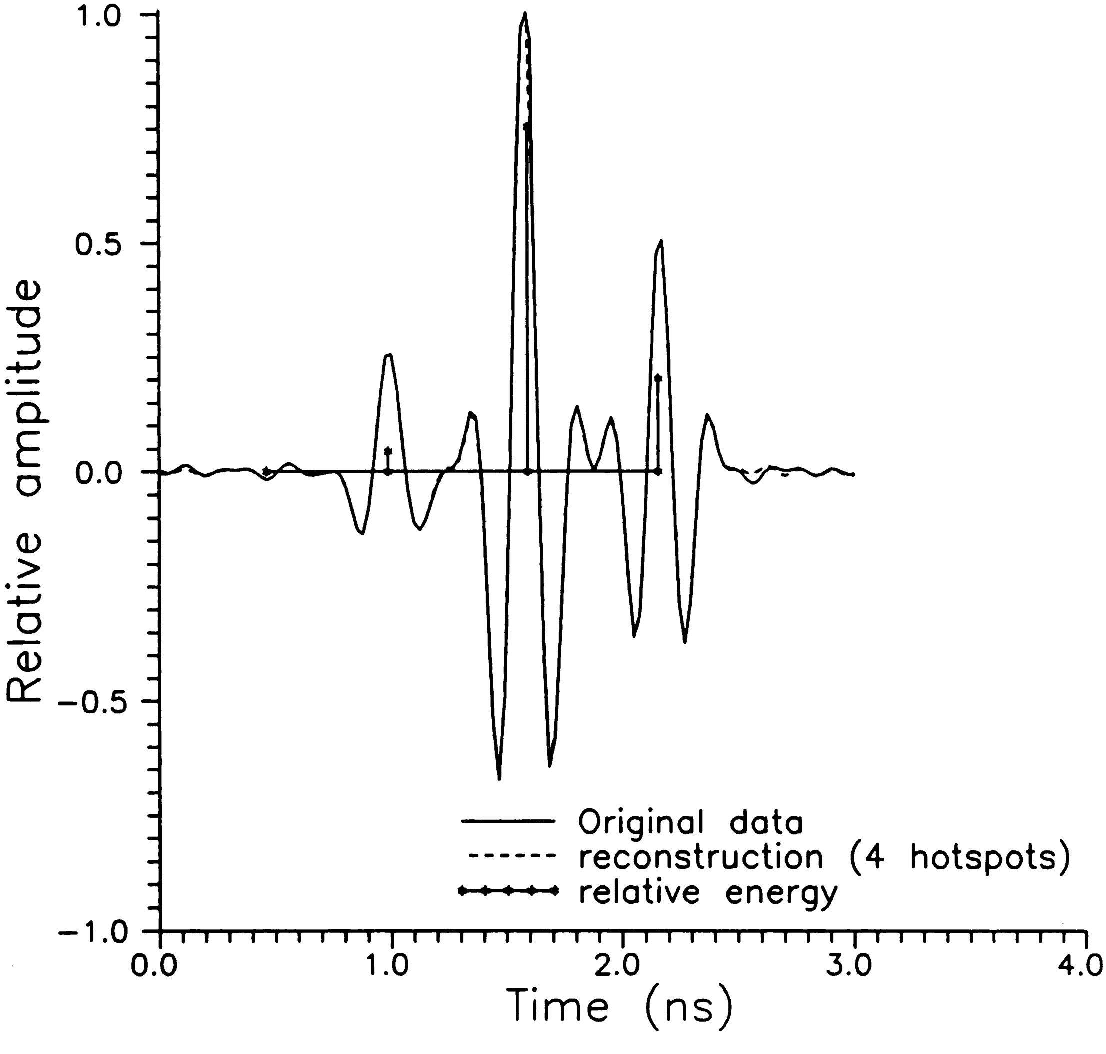

Figure 2.10 Artificial response created in the frequency band 1-7 GHz, and reconstructed response using 4 scattering centers, 4096 pt FFT, n=-2,-1,...,2, and GMC window with τ=0.3 ns, f_c=4 GHz.

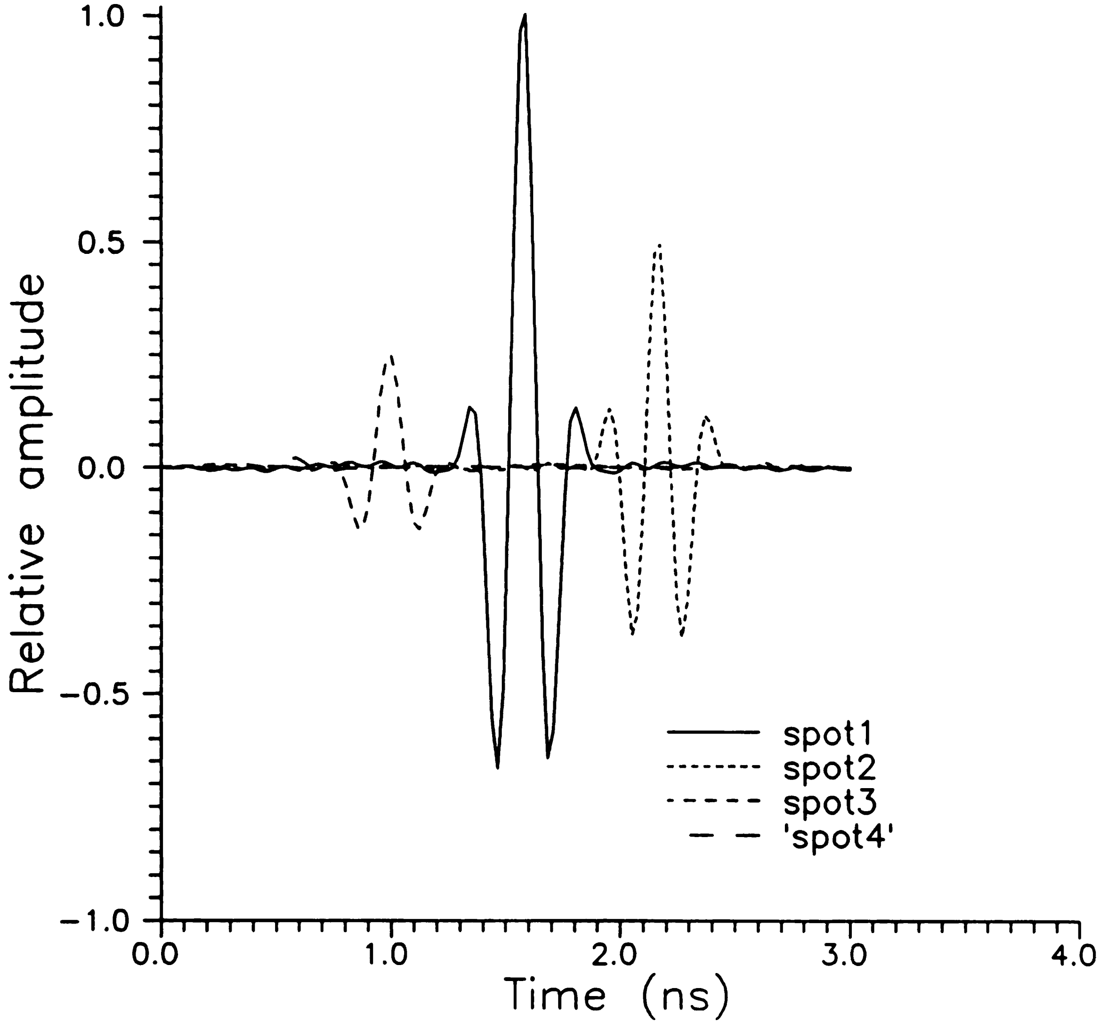

Figure 2.11 Pulse responses of three specular points.

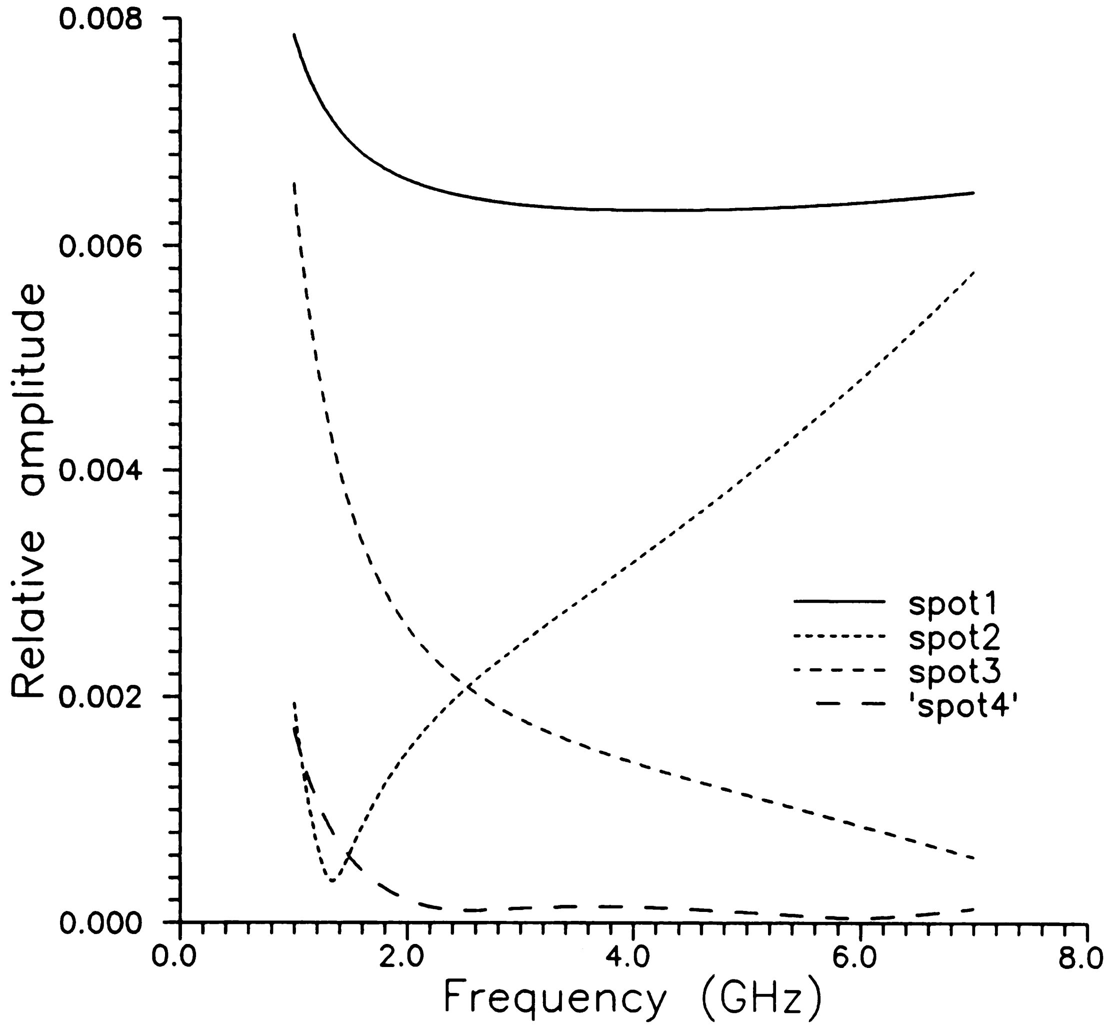

Figure 2.12 Transfer functions of three specular points.

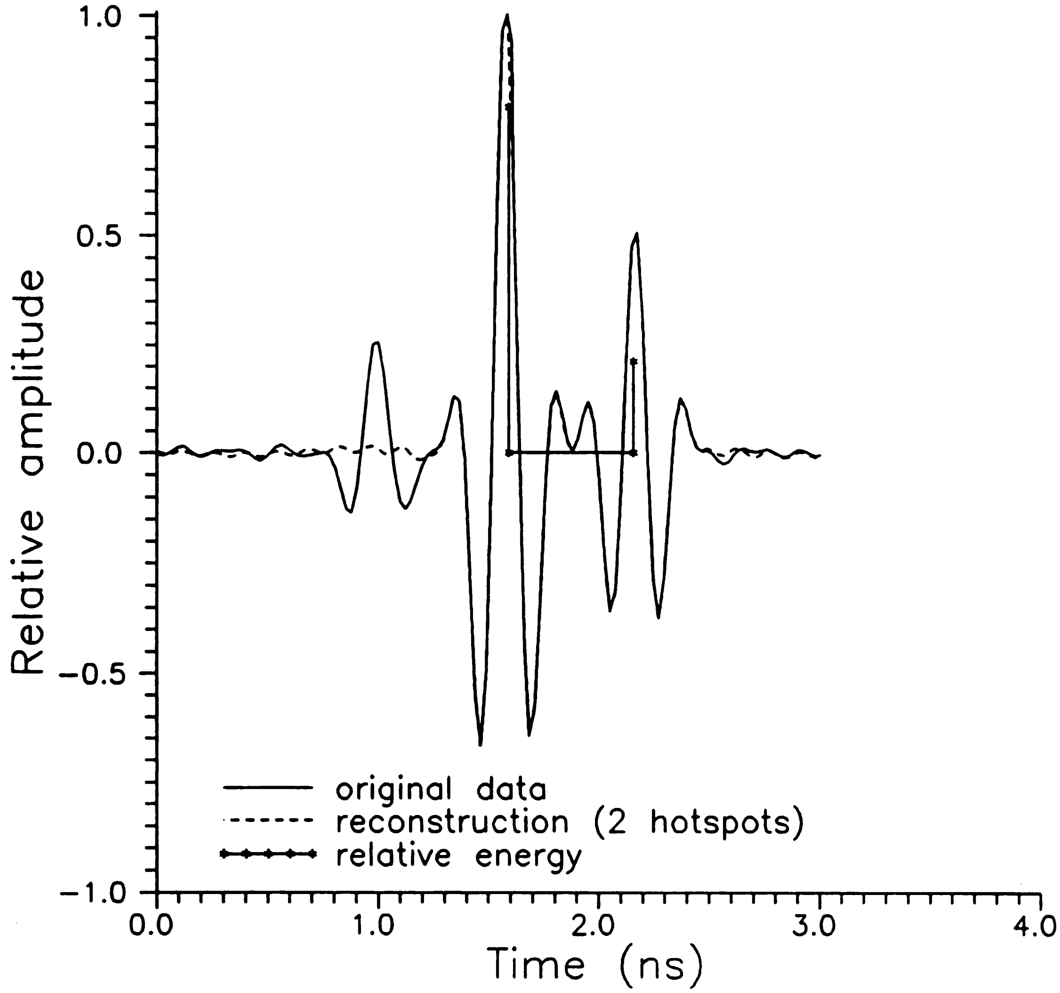

Figure 2.13 Artificial response created in the frequency band 1-7 GHz, and reconstructed response using 2 scattering centers, 4096 pt FFT, n=-2,-1,...,2, and GMC window with τ=0.3 ns, f_c=4 GHz.

Figure

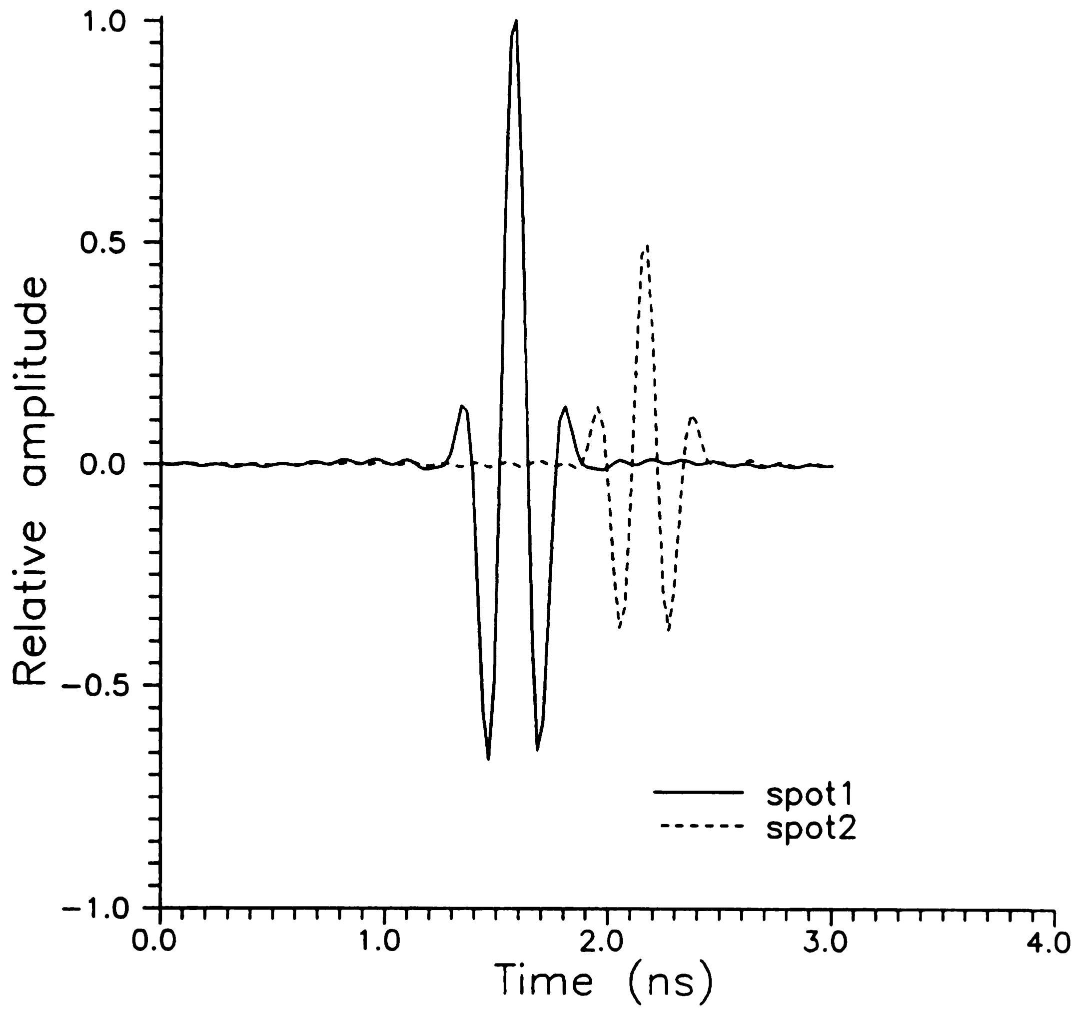

Figure 2.14 Pulse responses of two specular points.

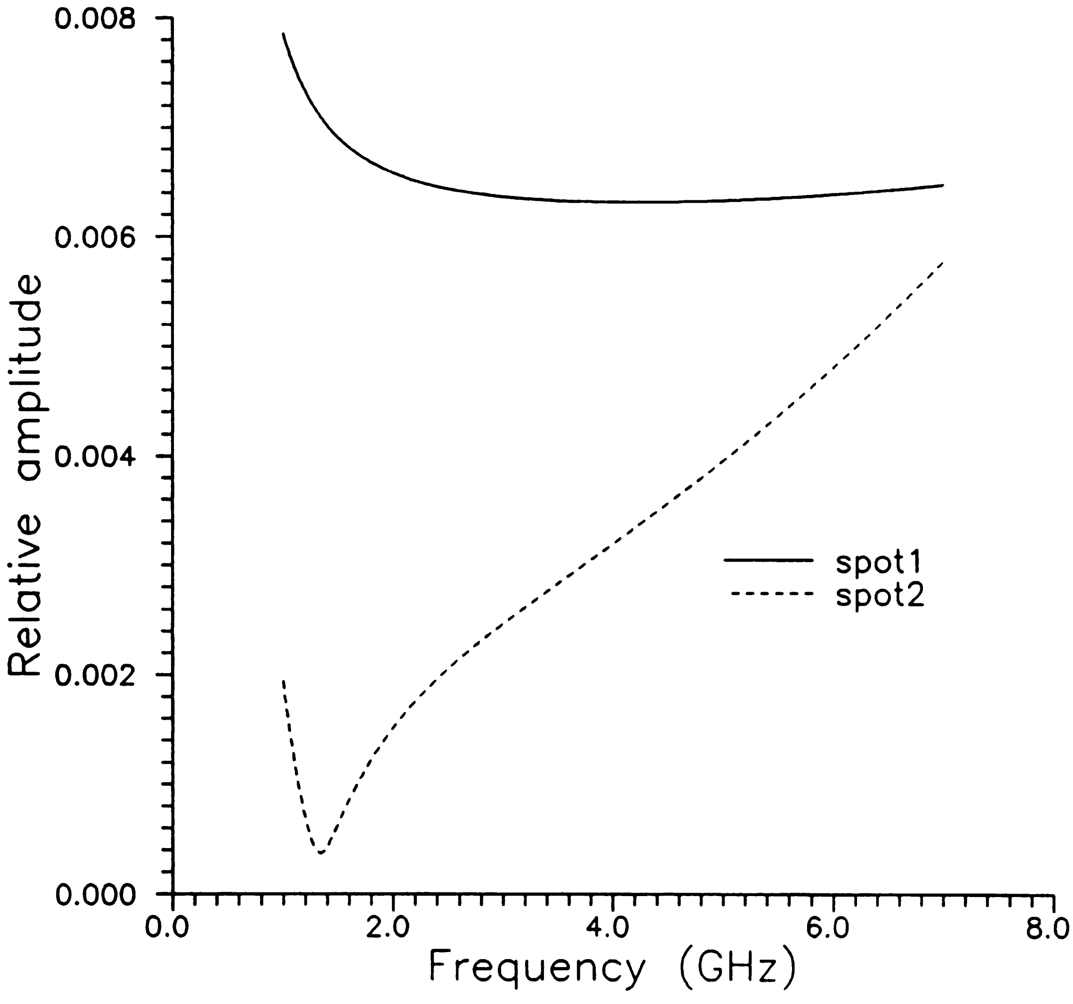

Figure 2.15 Transfer functions of two specular points.

lov

of

Fi

fre

eq

an

di

be

th

to

a

fu

sc

us

low-loss cables (see Chapter 7). This results in a spatial resolution increase by a factor of 16/6=2.67. To demonstrate the effect of larger bandwidth on the performance, Figure 2.16 shows the artificial pulse response obtained by creating 1601 points in the frequency band 2 to 18 GHz, windowed using a GMC centered at 10 GHz (giving an equivalent pulse width of about 0.2 ns) and inverse transformed with a 8192 point FFT, and the reconstructed waveform. Three scattering center pulse responses are put a distance of 0.23 ns apart, which introduces some overlapping. Even though separation between scattering centers is decreased twicefold compared to that shown in Figure 2.7, the corresponding scattering center pulse responses illustrated in Figure 2.17 are shown to be dominated by a delta function, a derivative of a delta function, and an integral of a delta function as expected. This can be seen in Figure 2.18, which shows transfer functions dominated by a constant, ω, and $1/\omega$. Note that the transfer function of the first scattering center is good except at the lower frequency due to ill-conditioning.

In the next two sections, we will demonstrate the performance of fitting scheme using scale aircraft B-58 and B-52 models.

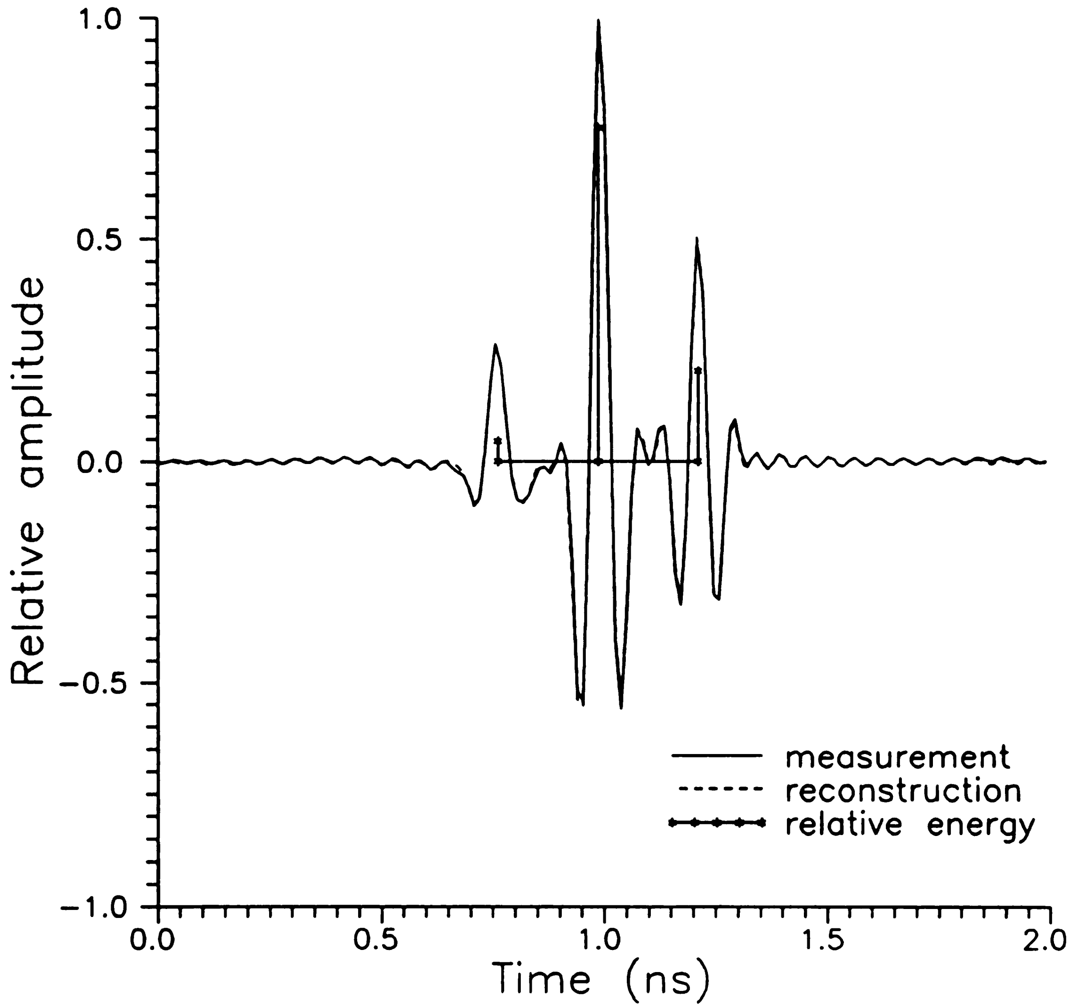

Figure 2.16 Artificial response created in the frequency band 2-18 GHz, and reconstructed response using 3 scattering centers, 8192 pt FFT, n=-2,-1,...,2, and GMC window with τ=0.1 ns, f_c=10 GHz.

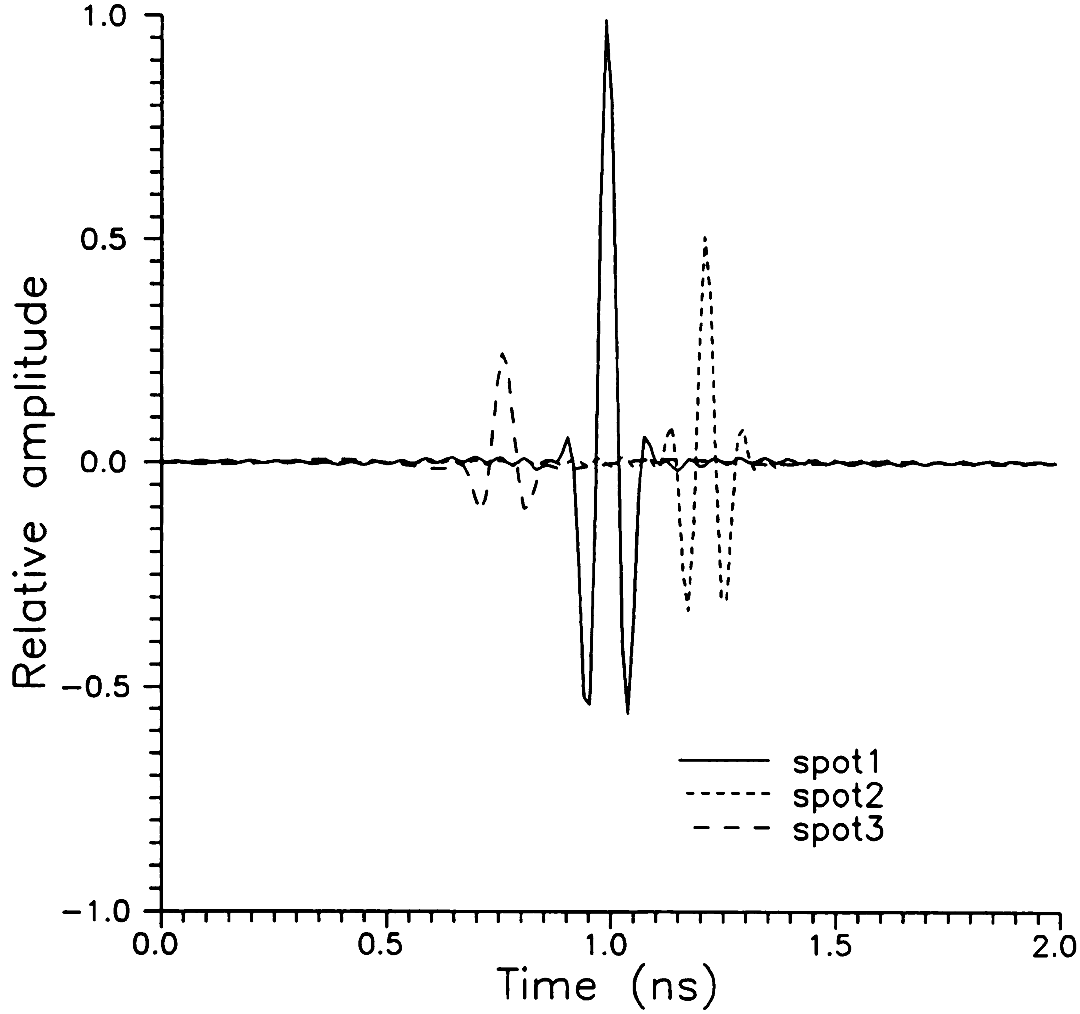

Figure 2.17 Pulse responses of three specular points.

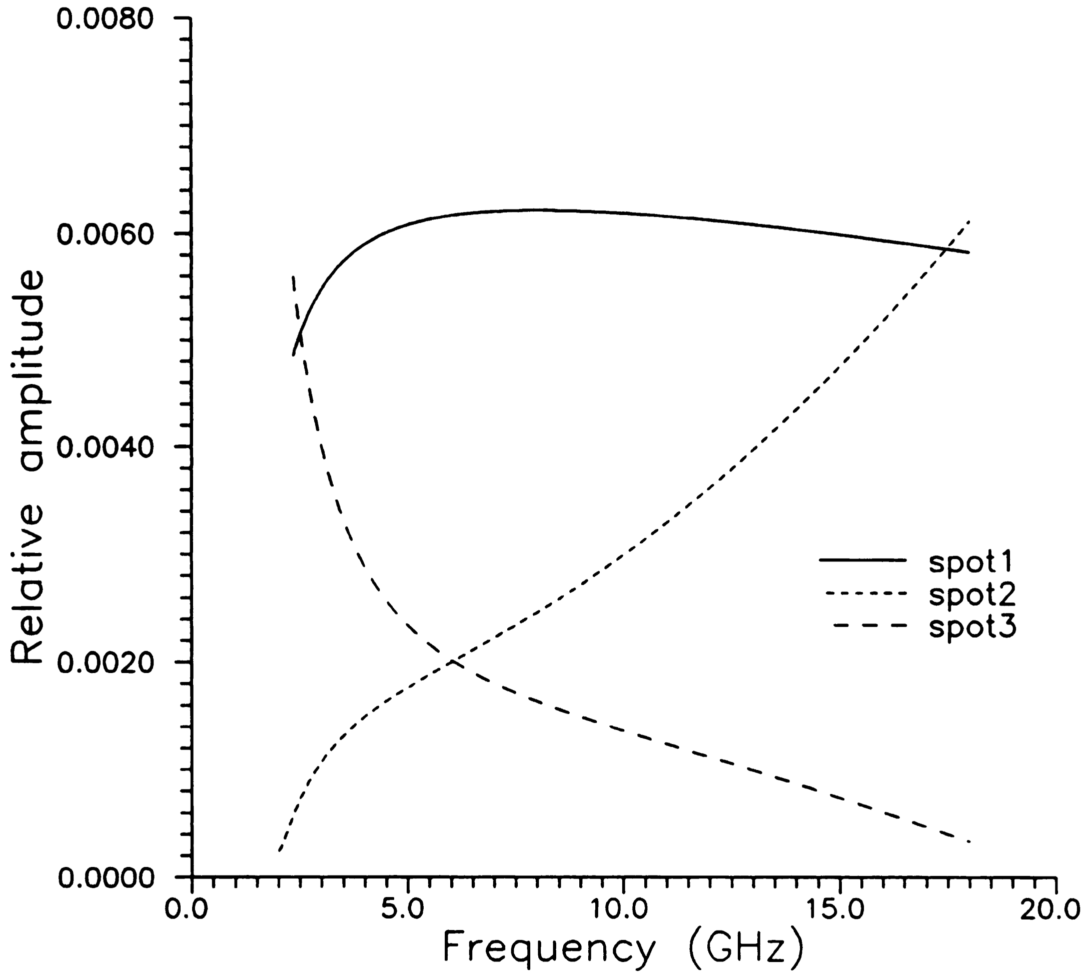

Figure 2.18 Transfer functions of three specular points.

2.3 Transfer Function Determination of A B-58 Aircraft

The last section describes an algorithm for extracting scattering center temporal positions and determining transfer functions and its application to several simple artificially created pulse responses. We will study scattering center behaviors of complex scale aircraft B-58 model using the same procedure.

How many polynomial terms in (2.3) we should use depends on the actual situation. In order to reach reasonable accuracy, more polynomial terms should be used in the computation when the scattering centers are widely separated and less terms used when there is some overlapping of scattering center pulse responses. According to our experience, n is always taken as -2,-1,...,2 or -3,-2,...,3.

Figure 2.19 shows the nose-on pulse response of a B-58 measured at 601 points in the frequency band 1 to 7 GHz, windowed using a GMC function centered at 4 GHz and inverse transformed with a 4096 point FFT. Since the bandwidth is limited, there existed some scattering center pulse response overlapping. Also shown in Figure 2.19 are the temporal positions of six scattering centers found using the fitting scheme outlined before. The transfer functions of these scattering centers have been found using $n=-2,-1,\ldots,2$. As before the heights of stars shown in Figure 2.19 represent the relative energy in each scattering center pulse response. The dominant specular reflection comes from the first engine mount and the next largest reflection comes from the second engine mount. Note that each specular reflection matches quite well with a physical feature on the target, including the front stabilizer and the inlet of the first engine. It is noticed that the reflection from the nose of the aircraft can not be detected in terms of relative energy.

Once the scattering center pulse responses have been determined, the overall early-time pulse response of the target can be reconstructed using (2.1). This is shown in Figure 2.19 as the dotted line. The reconstructed response matches extremely well.

The scattering center pulse responses for the first three dominant scattering centers, calculated using (2.7), are shown in Figure 2.20. Each response has different shape, with some overlapping between them. Figure 2.21 shows the scattering center transfer function found using (2.4). The first and second scattering centers are dominated by a relatively flat shape, indicating a primarily impulsive response. The third scattering center is dominated by the first integral of equivalent pulse. Similar results are seen in Figure 2.22 and Figure 2.23, which show the pulse responses and transfer functions of 4th, 5th, and 6th scattering centers.

To test the effects of random noise on the scheme, zero-mean white Gaussian noise is added. SNR for a sampled transient waveform is defined by [12]

$$SNR = 10.0 \log_{10} \left\{ \frac{\int_W v^2(t)\, dt}{W \psi_0} \right\} \tag{2.16}$$

where $v(t)$ is the noise-free signal, ψ_0 is the mean-square value of the noise voltage, and W is chosen as the minimum duration window that contains ninety-nine percent of the total energy in the noise-free data.

As a example, Figure 2.24 shows the pulse response of 0^0 B-58 scale aircraft model with zero-mean white Gaussian noise added, here SNR=10 dB. We notice that the response is slightly distorted due to this random noise. Figure 2.25 shows the noise-free response of 0^0 B-58, and its reconstructed response at this noise level as dotted line. The reconstructed response matches quite well except for small portions caused by noise distortion. The temporal positions of the two largest scattering centers remain the same,

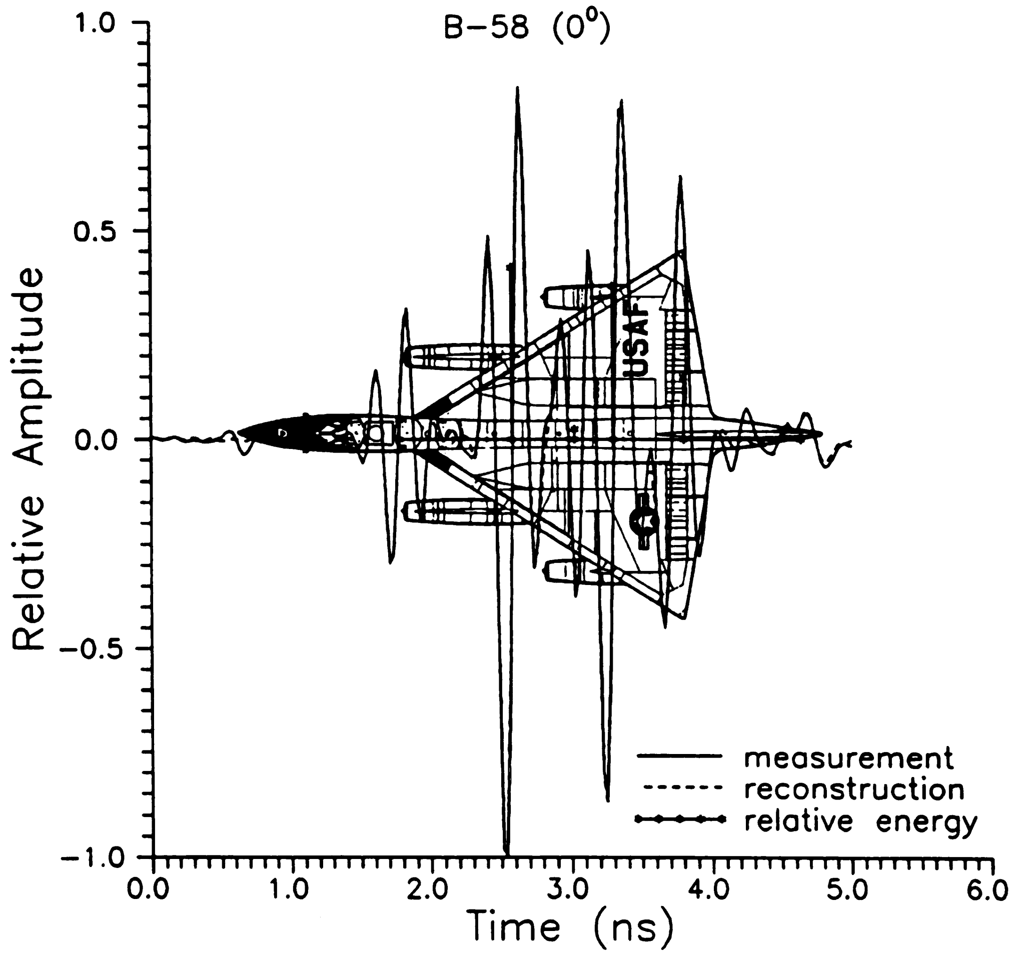

Figure 2.19 Response of B-58 at 0^0 aspect measured in band 1-7 GHz, and reconstructed response using 6 scattering centers, 4096 pt FFT, n=-2,-1,...,2, and GMC window with τ=0.3 ns, f_c=4 GHz.

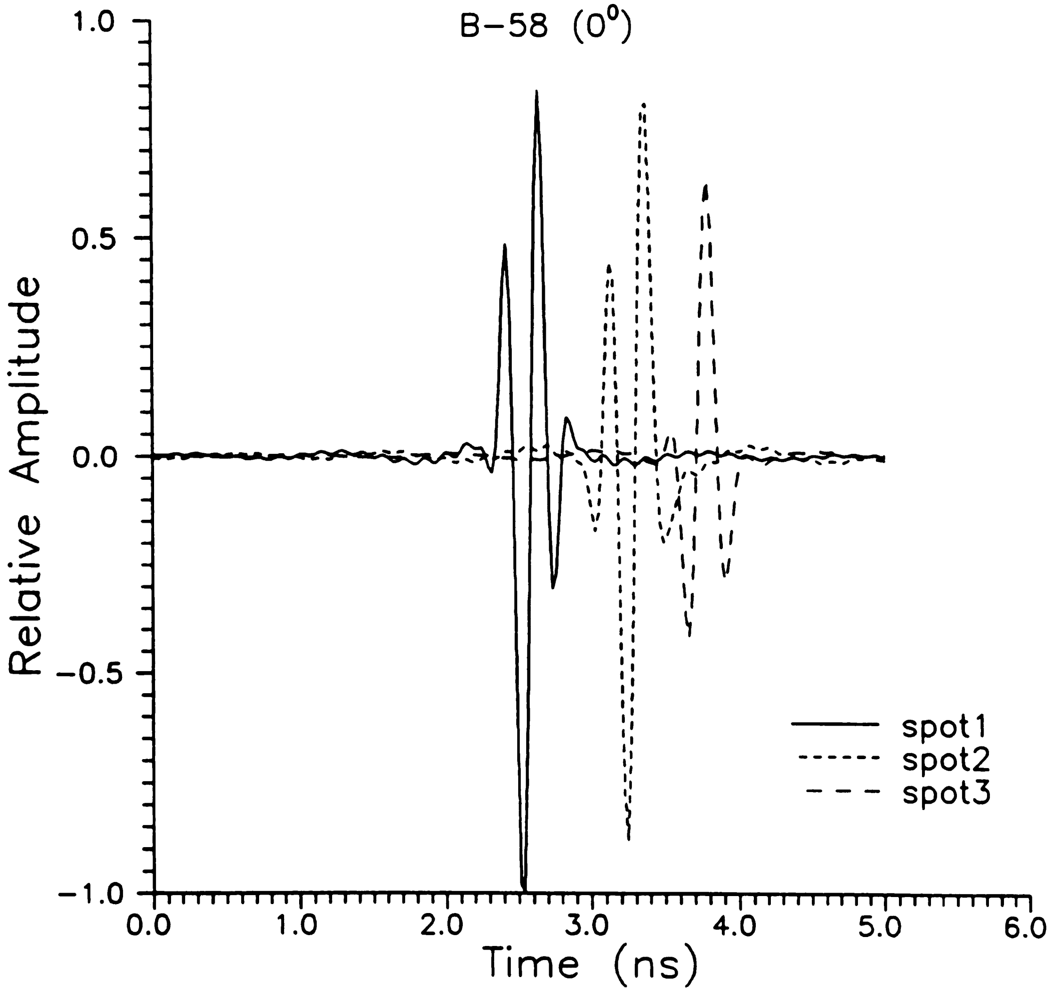

Figure 2.20 Pulse responses of 1st, 2nd, and 3rd specular points.

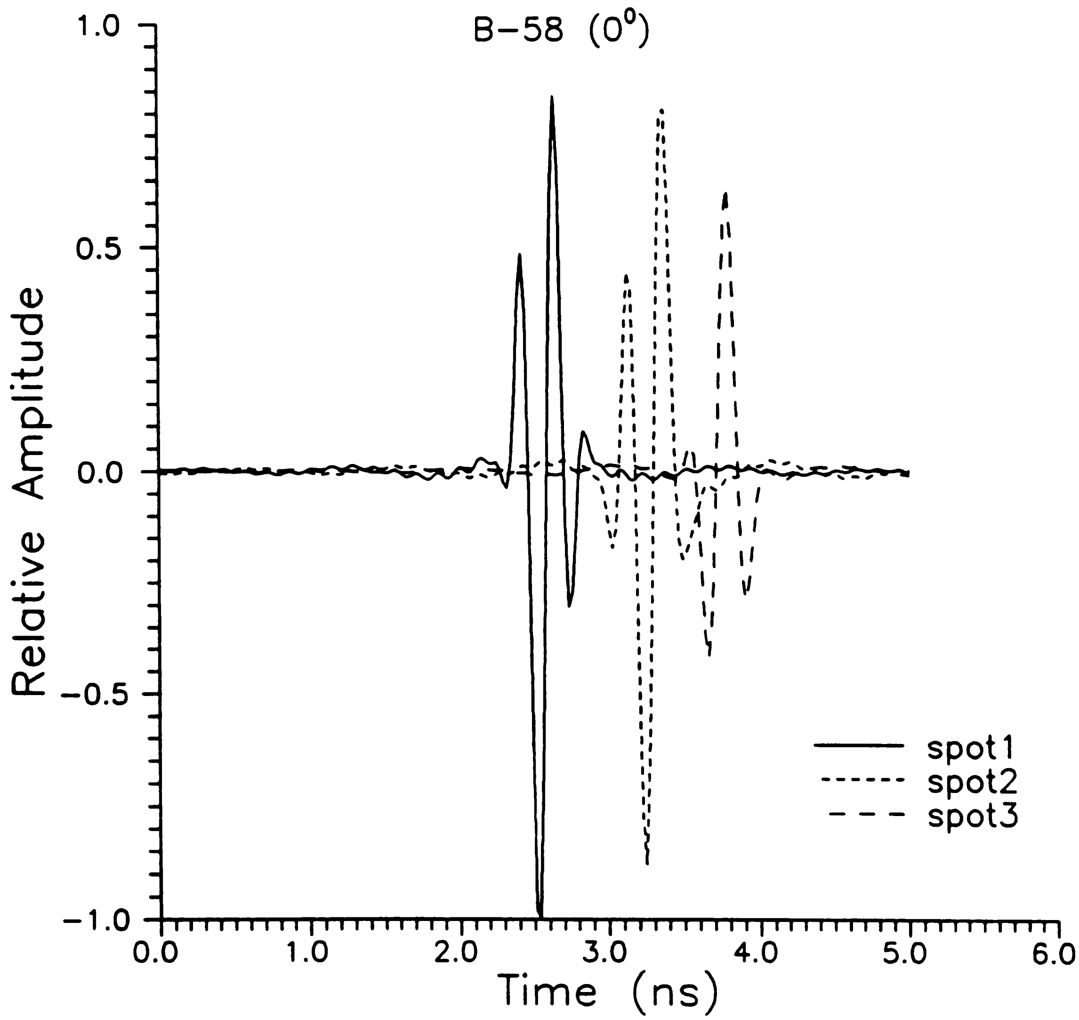

Figure 2.20 Pulse responses of 1st, 2nd, and 3rd specular points.

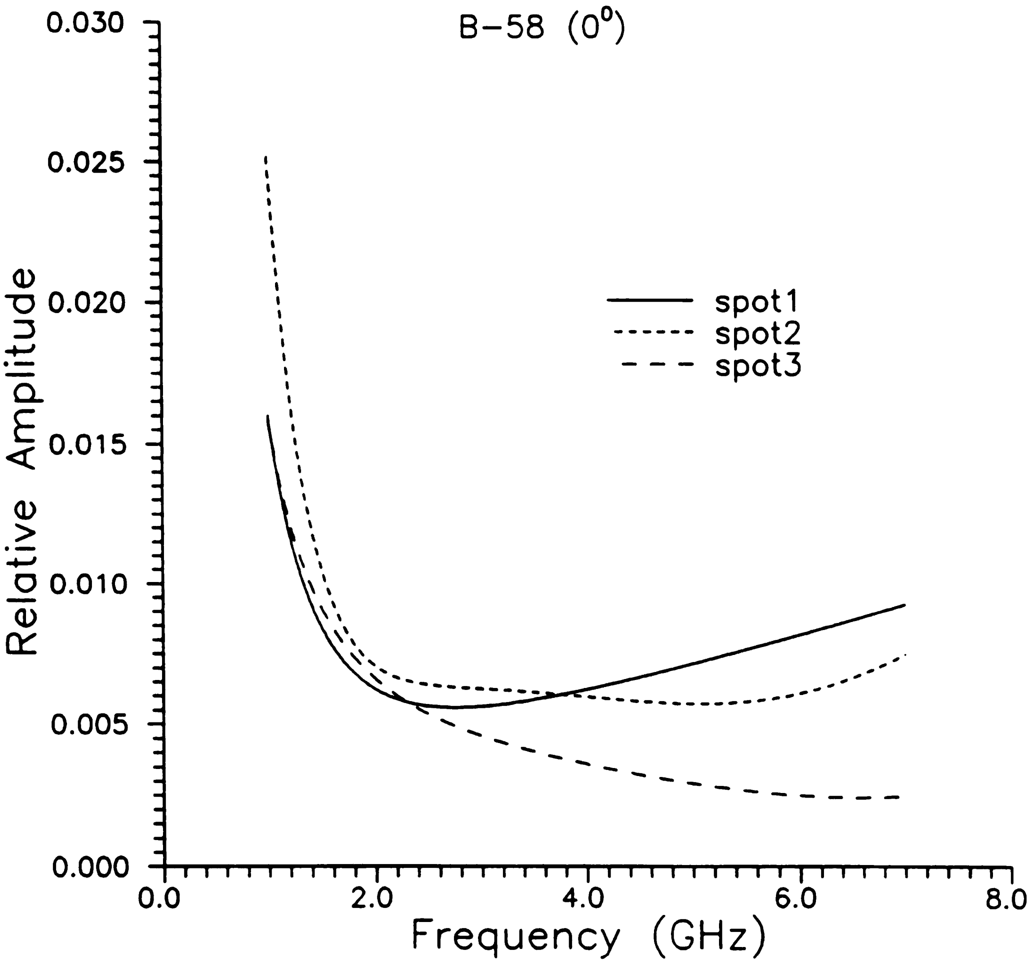

Figure 2.21 Transfer functions of 1st, 2nd, and 3rd specular points.

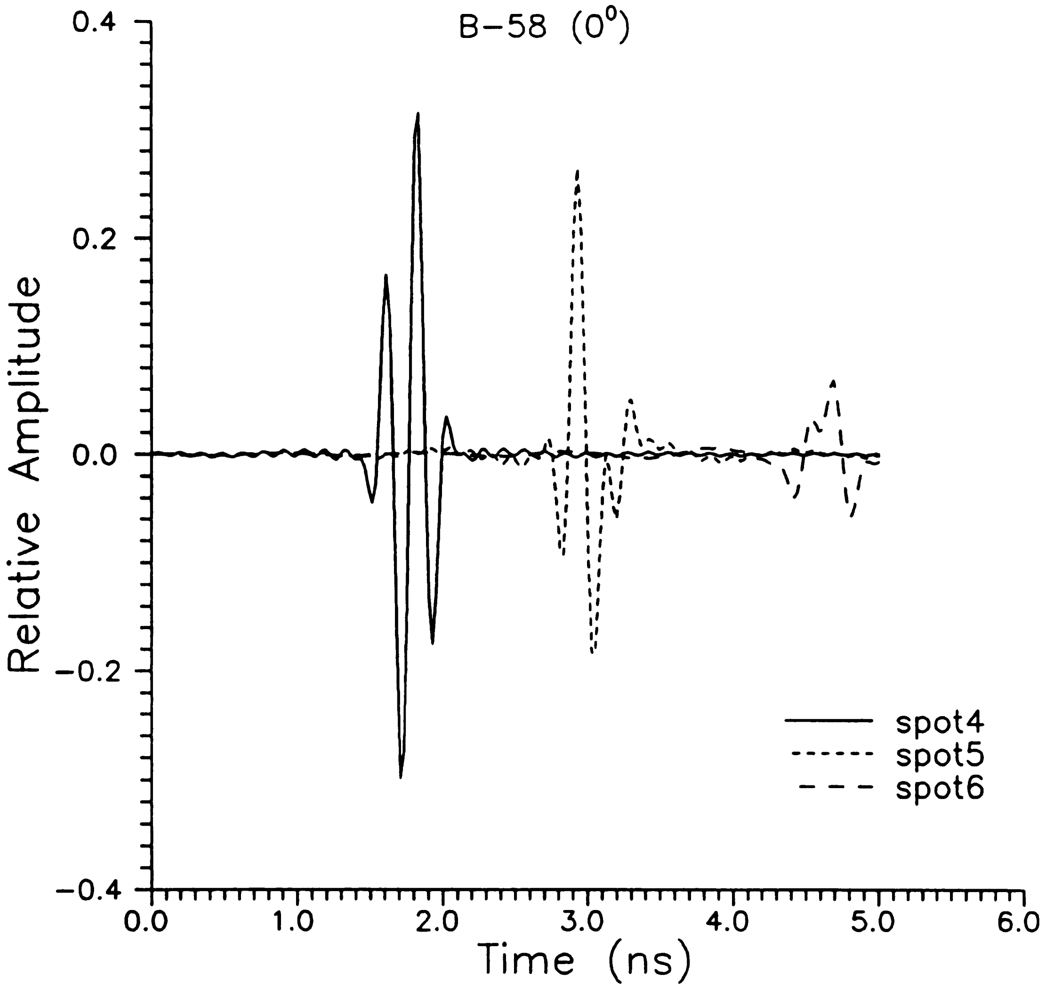

Figure 2.22 Pulse responses of 4th, 5th, and 6th specular points.

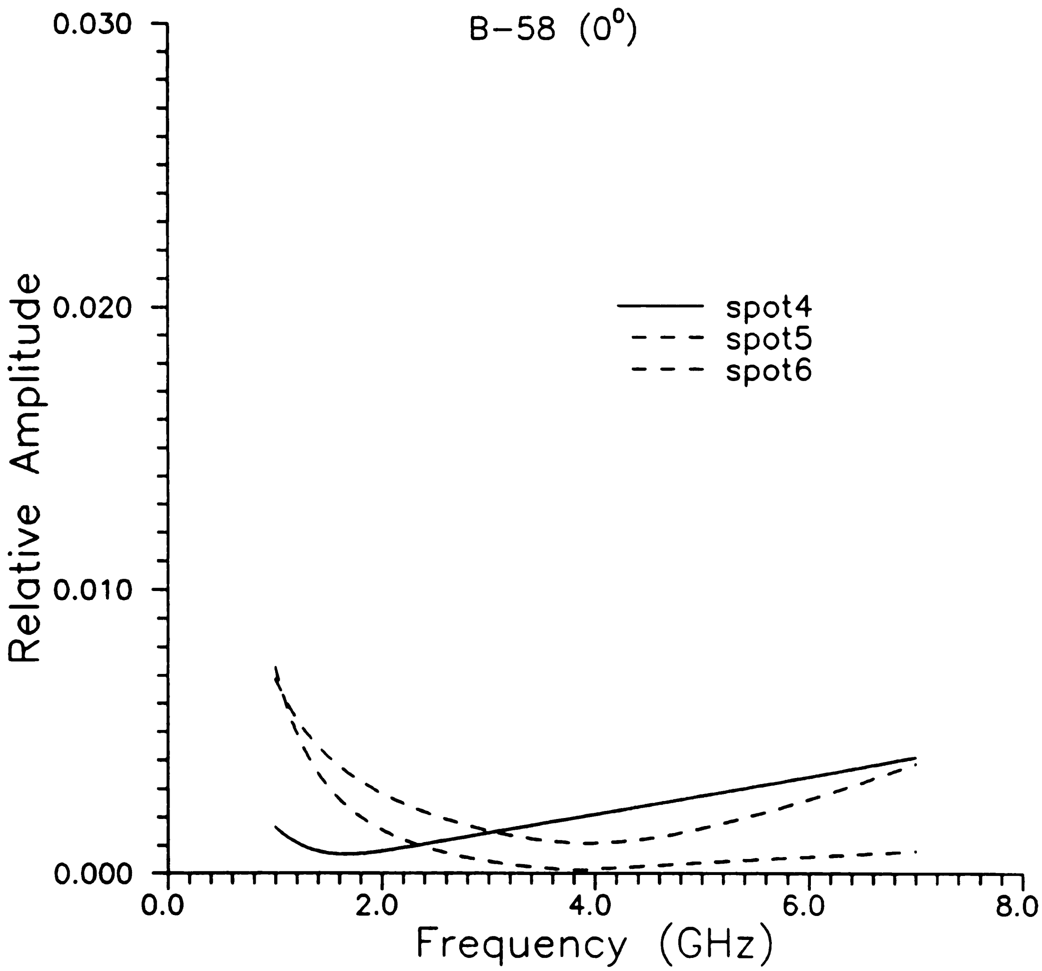

Figure 2.23 Transfer functions of 4th, 5th, and 6th specular points.

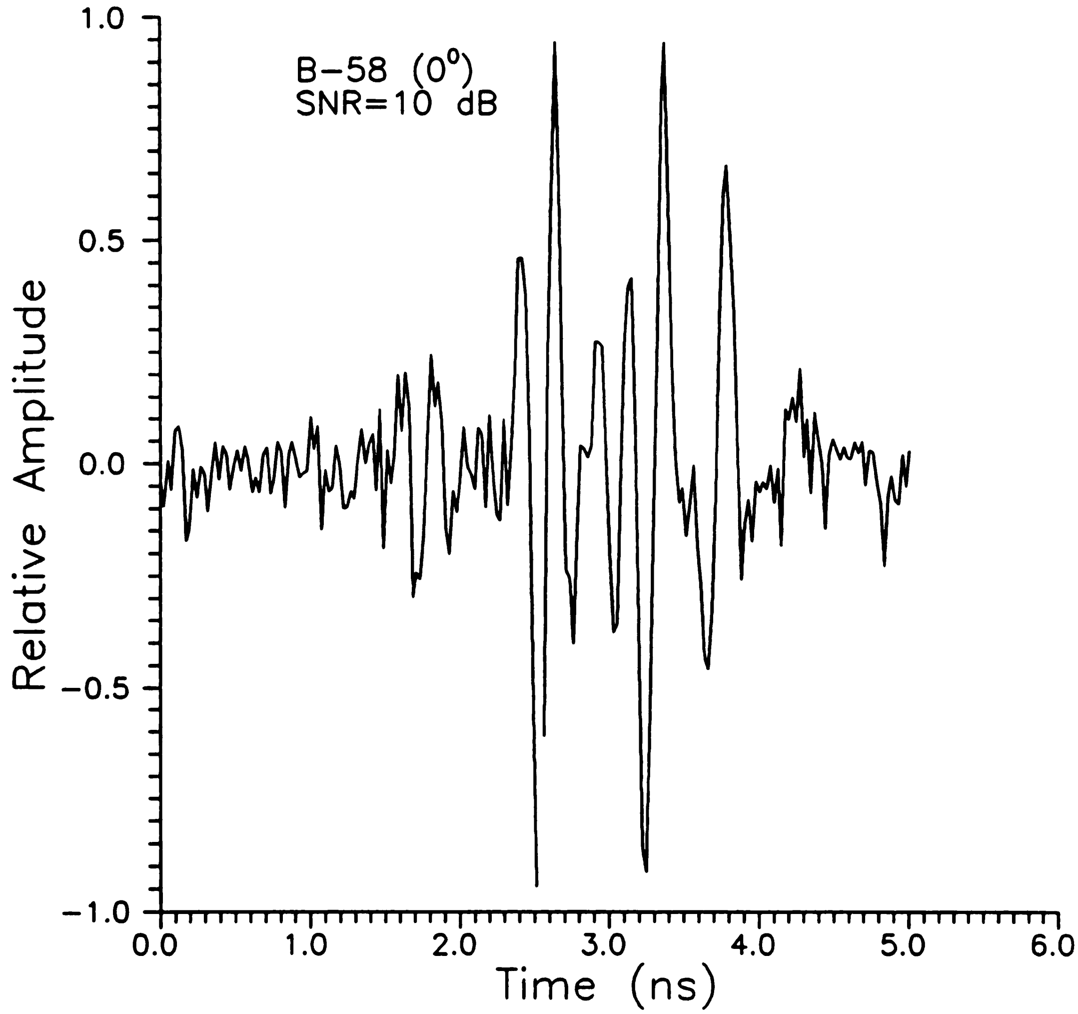

Figure 2.24 Response of B-58 aircraft model at nose-on incidence with zero-mean white Gaussian noise added. SNR = 10 dB.

the 3rd, 4th, and 5th scattering centers shift slightly, and the remaining scattering center does not represent any physical feature on the target but noise. Compared to scattering center pulse responses shown in Figure 2.20, Figure 2.26 shows very similar results. As a result, the three largest scattering center transfer functions have quite similar slopes as those in Figure 2.27. Other results are illustrated in Figure 2.28 and Figure 2.29, which show pulse responses and transfer functions of the remaining three scattering centers. Note that the smaller scattering centers can not be reproduced properly even when SNR is higher. The results will be worse with even lower SNR. This reveals that determination of scattering center transfer functions is noise sensitive.

It is interesting to see the effect of enhanced frequency bandwidth on the extraction process. Figure 2.30 shows measured early-time response at 90^0 of the B-58 measured in the band 2-18 GHz, and the reconstructed response using $n=-2,-1,\ldots,2$. Because of higher spatial resolution the scattering centers are largely separated. We also observe that a large response occurs after 1.5 ns. This may be caused by incomplete shadowing after the incident waveform passes over the fuselage, or reflection from some smaller scattering centers or multiple reflection between scattering centers. Therefore, 5 scattering centers are assumed here. Note that the three largest scattering centers correspond to the fuselage, first engine mount, and second engine mount. They match the target geometry quite well. Note that the scattered field of the wing tip is too small to be observed. Figure 2.31 and Figure 2.32 show pulse responses and transfer functions of these five scattering centers. Unfortunately, It is difficult to compare these transfer functions with those measured in the frequency band 1-7 GHz due to ill-conditioning of our algorithm or aspect angle difference between the two measurement systems. We hope this situation can be improved in the future.

To test the effect of aspect angle on the performance, the pulse response of the B-58 model at 10^0 measured at 601 points in the frequency band 1-7 GHz, with 6 scattering centers and $n=-2,-1,\ldots,2$, is shown in Figure 2.33. At this aspect angle the second inner engine inlet and first outer engine mount, the second inner engine mount and second outer engine inlet are at almost the same down range point. In the figure we see that the dominant specular reflection comes from the first inner engine mount and the next largest reflection comes from the second inner engine mount. The front stabilizer and first inner engine inlet are also located at the expected place. The scattering center pulse responses are shown in Figure 2.34 and Figure 2.36. Because of aspect angle variation, the transfer functions of associated scattering centers show some difference as illustrated in Figure 2.35 an Figure 2.37.

2.4 Transfer Function Determination of A B-52 Aircraft

In this section we will demonstrate the performance of fitting scheme on a different radar target, a B-52 aircraft model.

Figure 2.38 shows the nose-on pulse response of a B-52 measured at 601 points in the frequency band 1 to 7 GHz. Note that due to the relatively narrow bandwidth, the scattering center pulse responses overlap somewhat just like before. Also shown in Figure 2.38 are temporal positions of nine scattering centers found using $n=-2,-1,\ldots,2$. According to the knowledge of relative energy shown in stars (*), the dominant specular reflection comes from the first engine mount (which coincides with the second engine inlet) and the next largest reflection comes from the second engine mount. Note that each specular reflection matches quite well with a physical feature on the target, including the wing joint, trailing edges of the wing and rear stabilizer (rear wing). It is interesting to

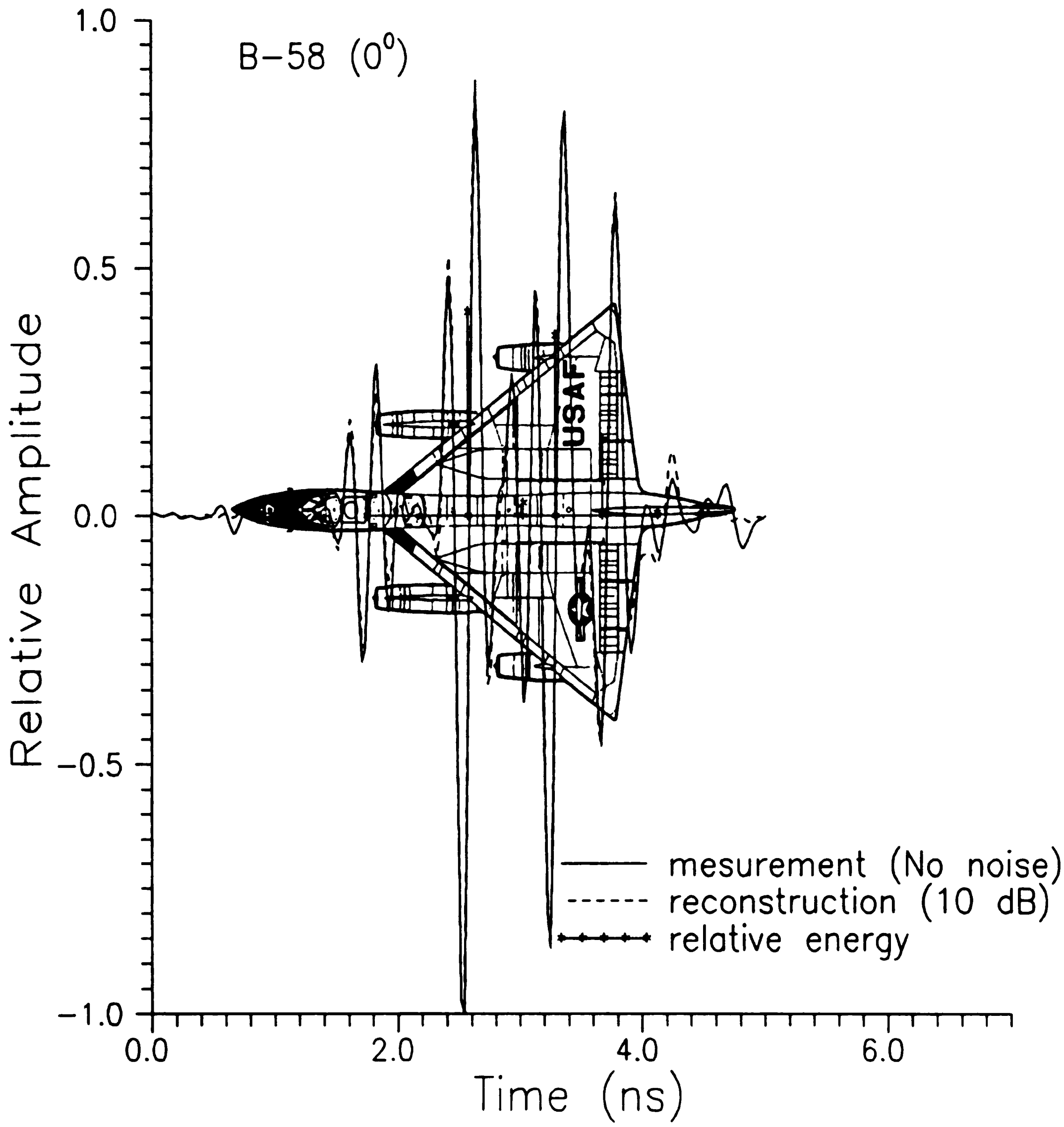

Figure 2.25 Response of B-58 at 0^0 aspect measured in band 1-7 GHz, and reconstructed response using 6 scattering centers with SNR=10 dB, n=-2,-1,...,2, and GMC window with τ=0.3 ns, f_c=4 GHz.

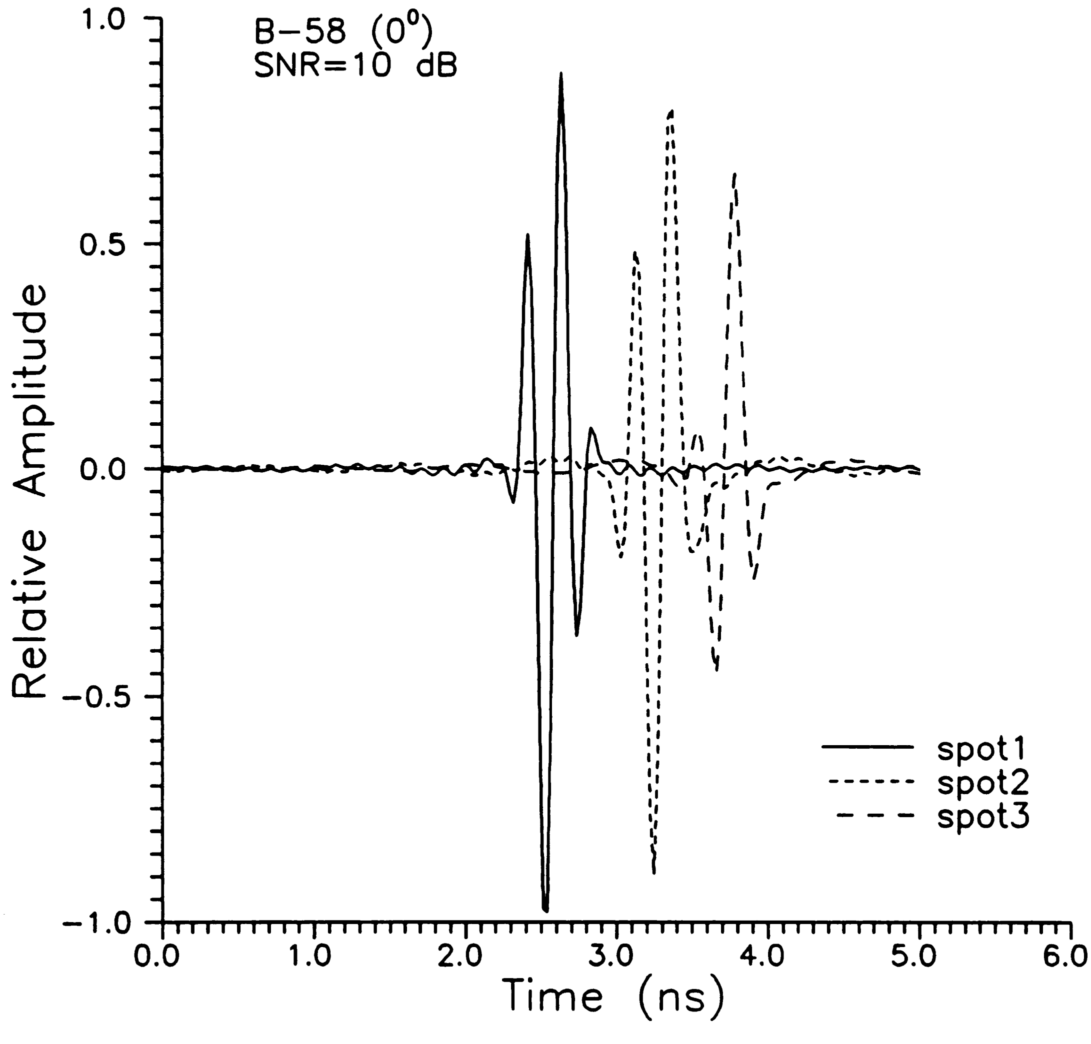

Figure 2.26 Pulse responses of 1st, 2nd, and 3rd specular points. SNR=10 dB.

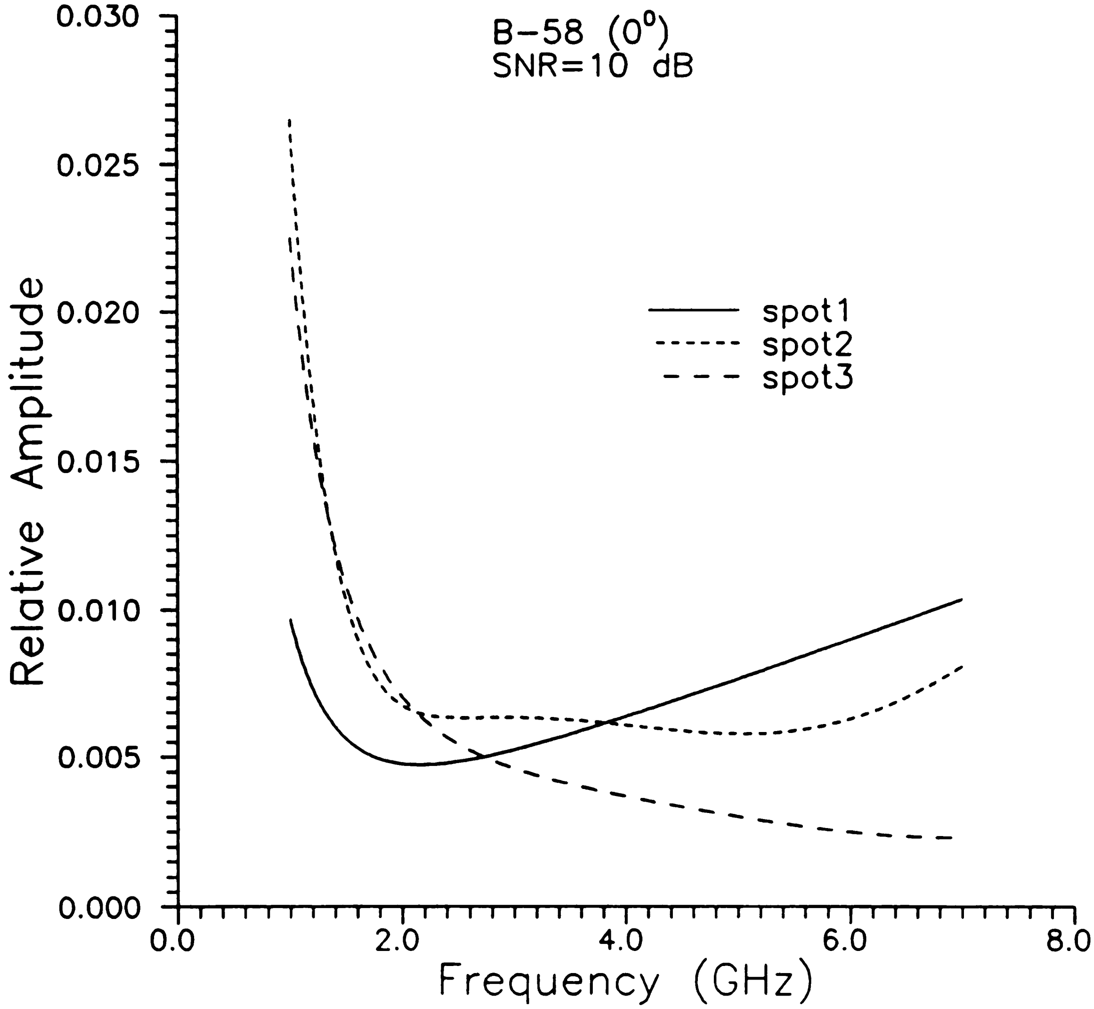

Figure 2.27 Transfer functions of 1st, 2nd, and 3rd specular points. SNR=10 dB.

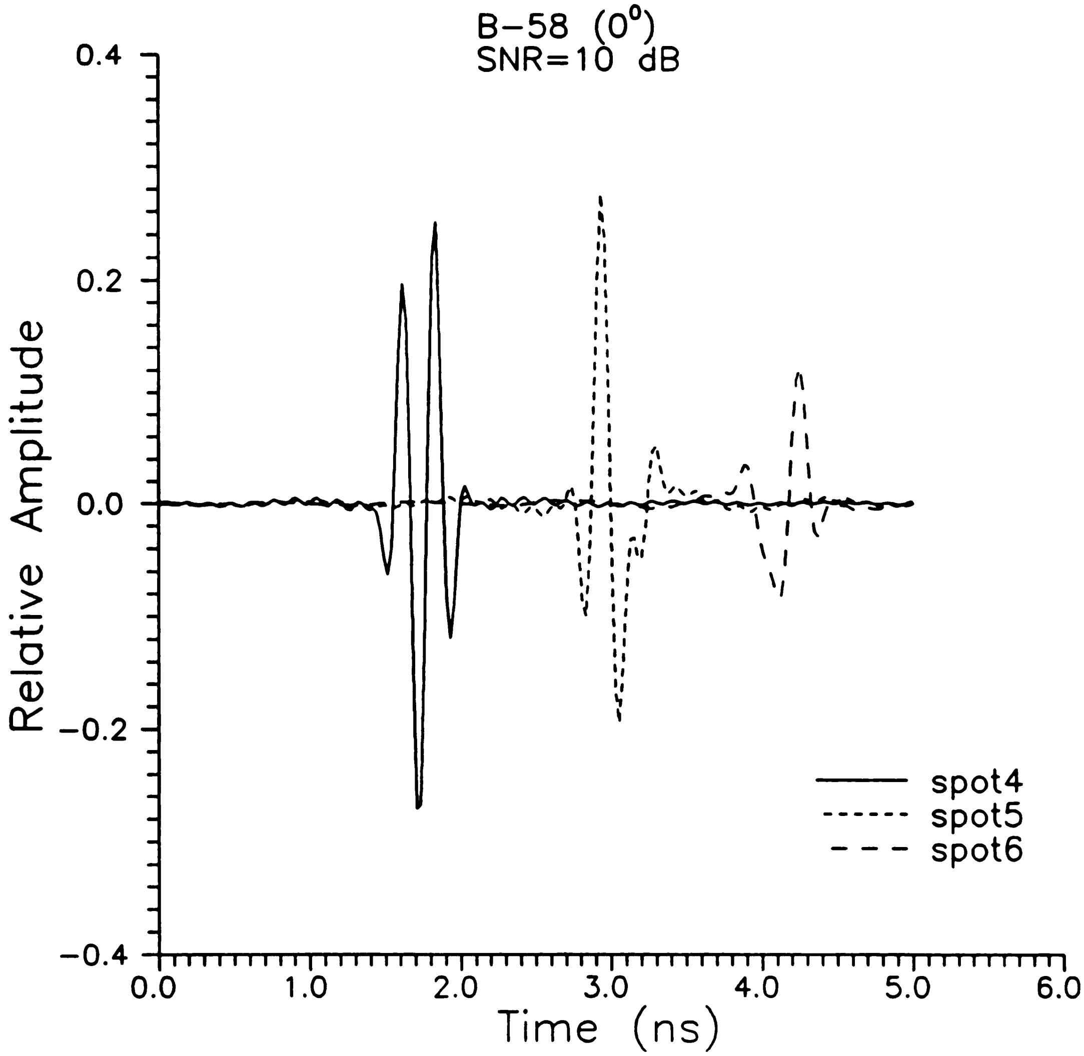

Figure 2.28 Pulse responses of 4th, 5th, and 6th specular points. SNR=10 dB.

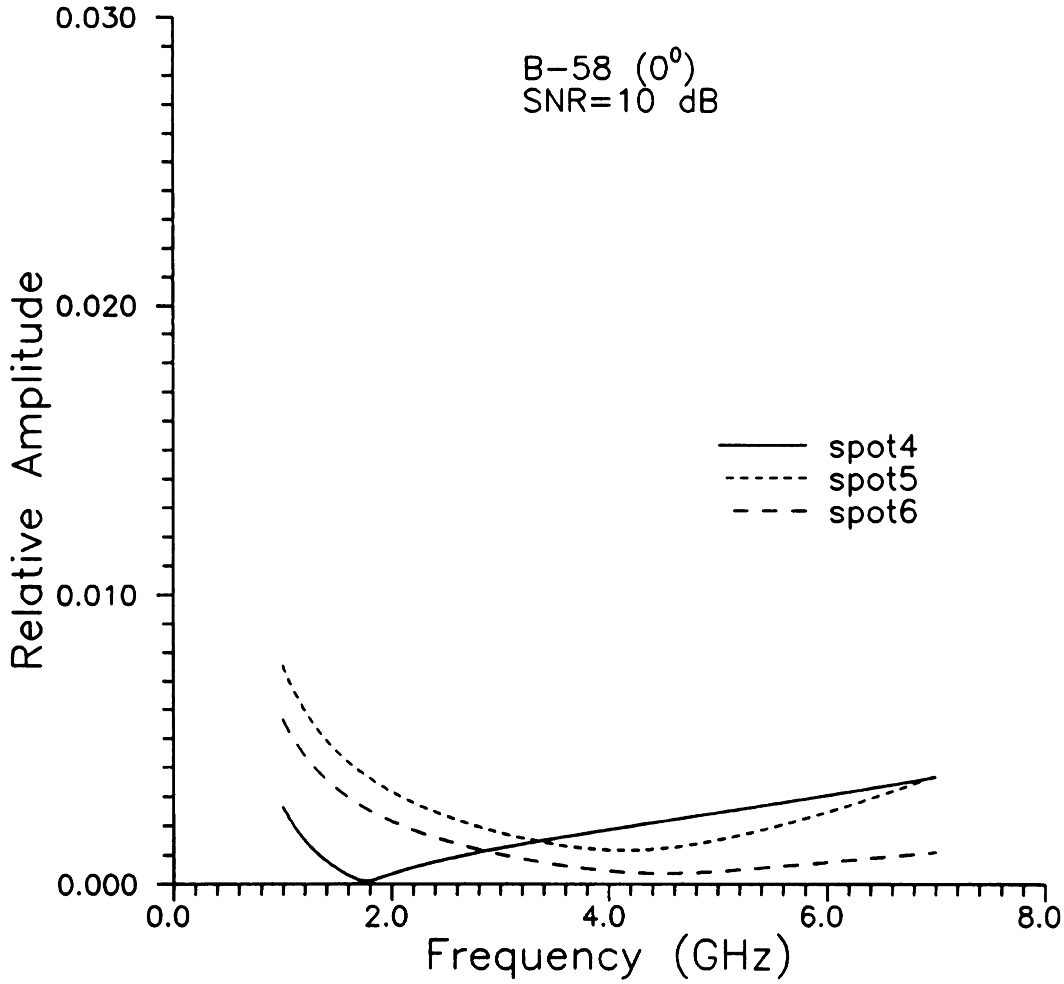

Figure 2.29 Transfer functions of 4th, 5th, and 6th specular points. SNR=10 dB.

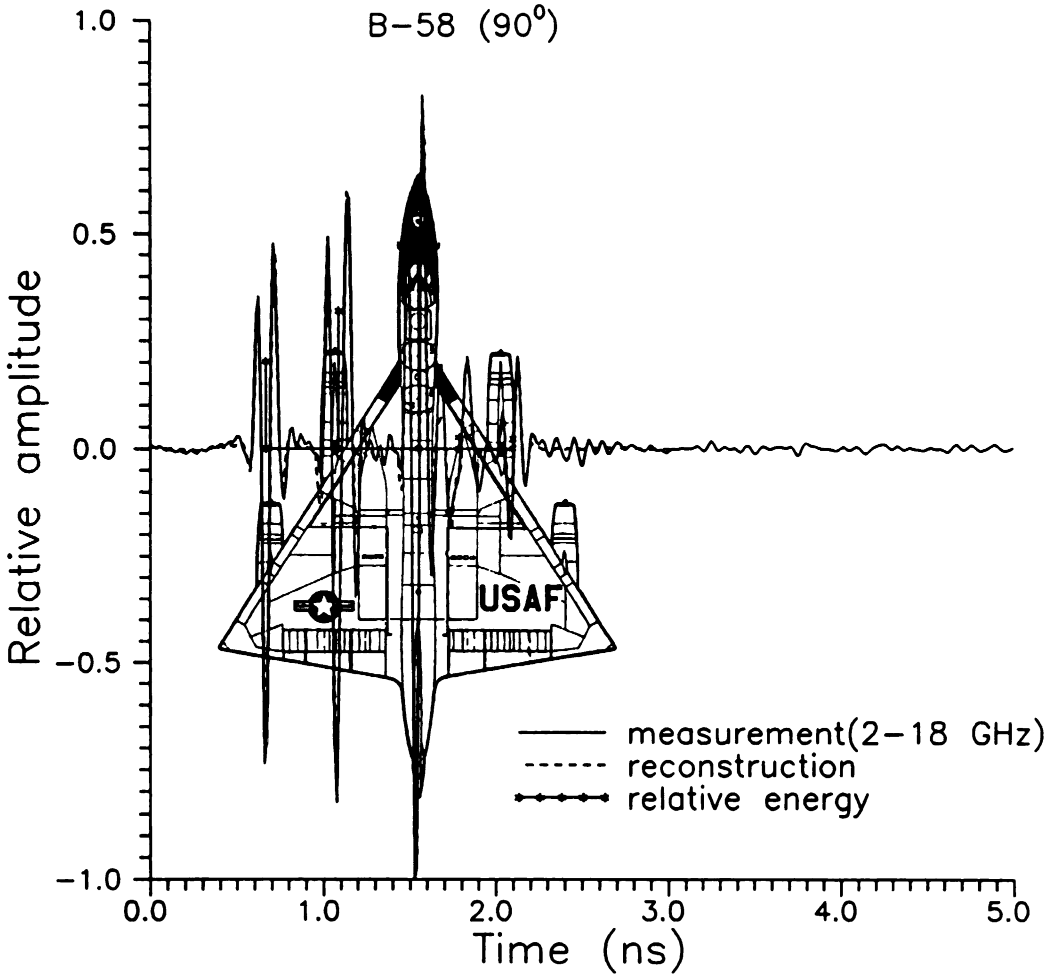

Figure 2.30 Response of B-58 at 90^0 aspect measured in band 2-18 GHz, and reconstructed response using 5 scattering centers, 8192 pt FFT, n=-2,-1,...,2, and GMC window with τ=0.1 ns, f_c=10 GHz.

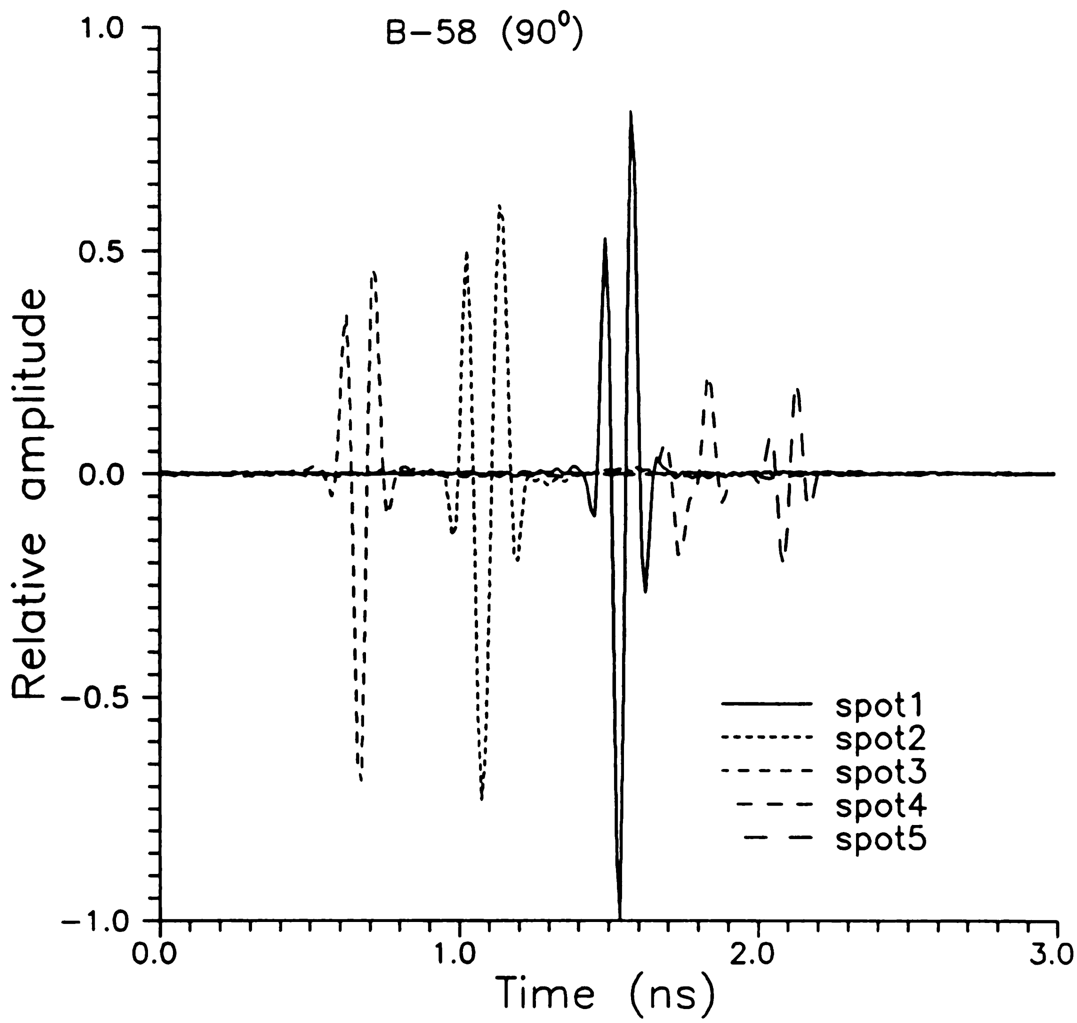

Figure 2.31 Pulse responses of 1st, 2nd, 3rd, 4th, and 5th specular points.

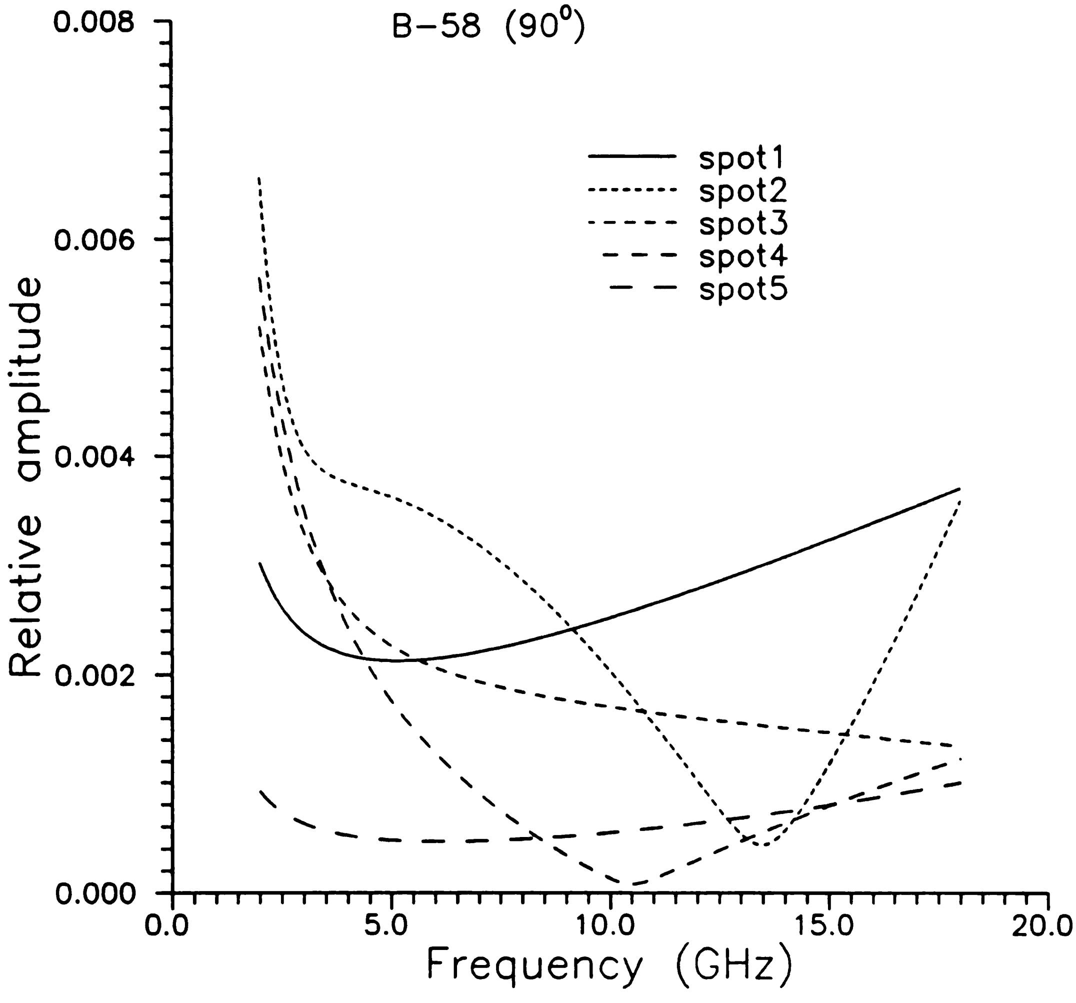

Figure 2.32 Transfer functions of 1st, 2nd, 3rd, 4th, and 5th specular points.

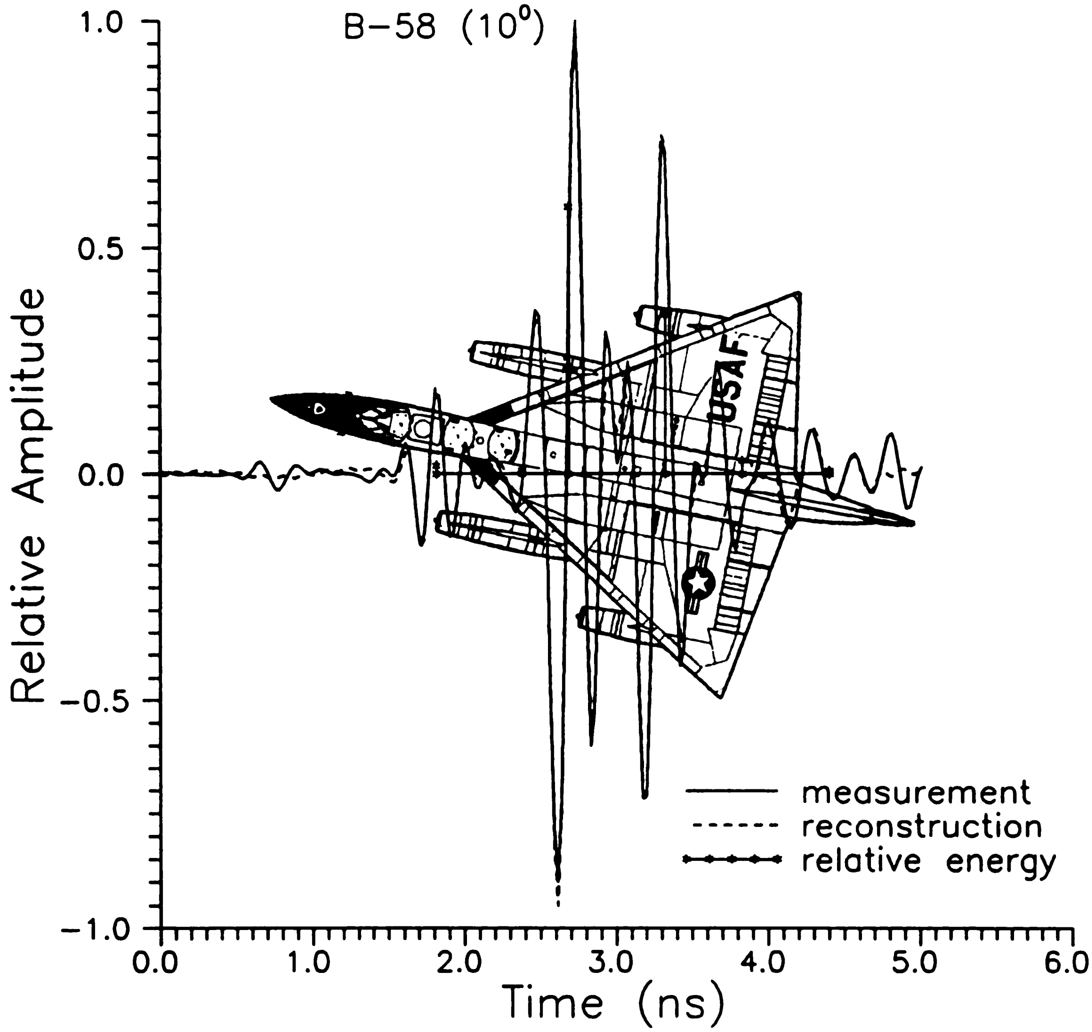

Figure 2.33 Response of B-58 at 10^0 aspect measured in band 1-7 GHz, and reconstructed response using 6 scattering centers, 4096 pt FFT, n=-2,-1,...,2, and GMC window with τ=0.3 ns, f_c=4 GHz.

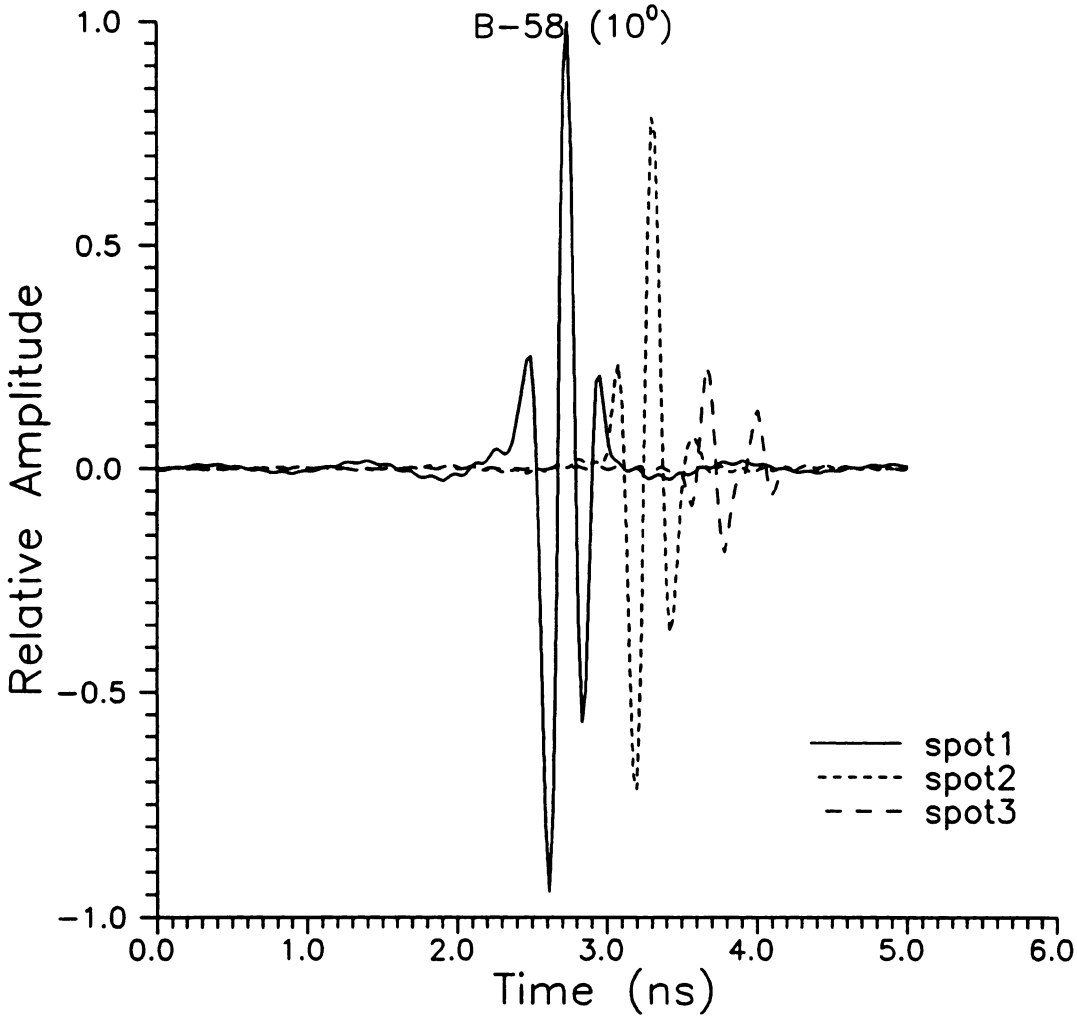

Figure 2.34 Pulse responses of 1st, 2nd, and 3rd specular points.

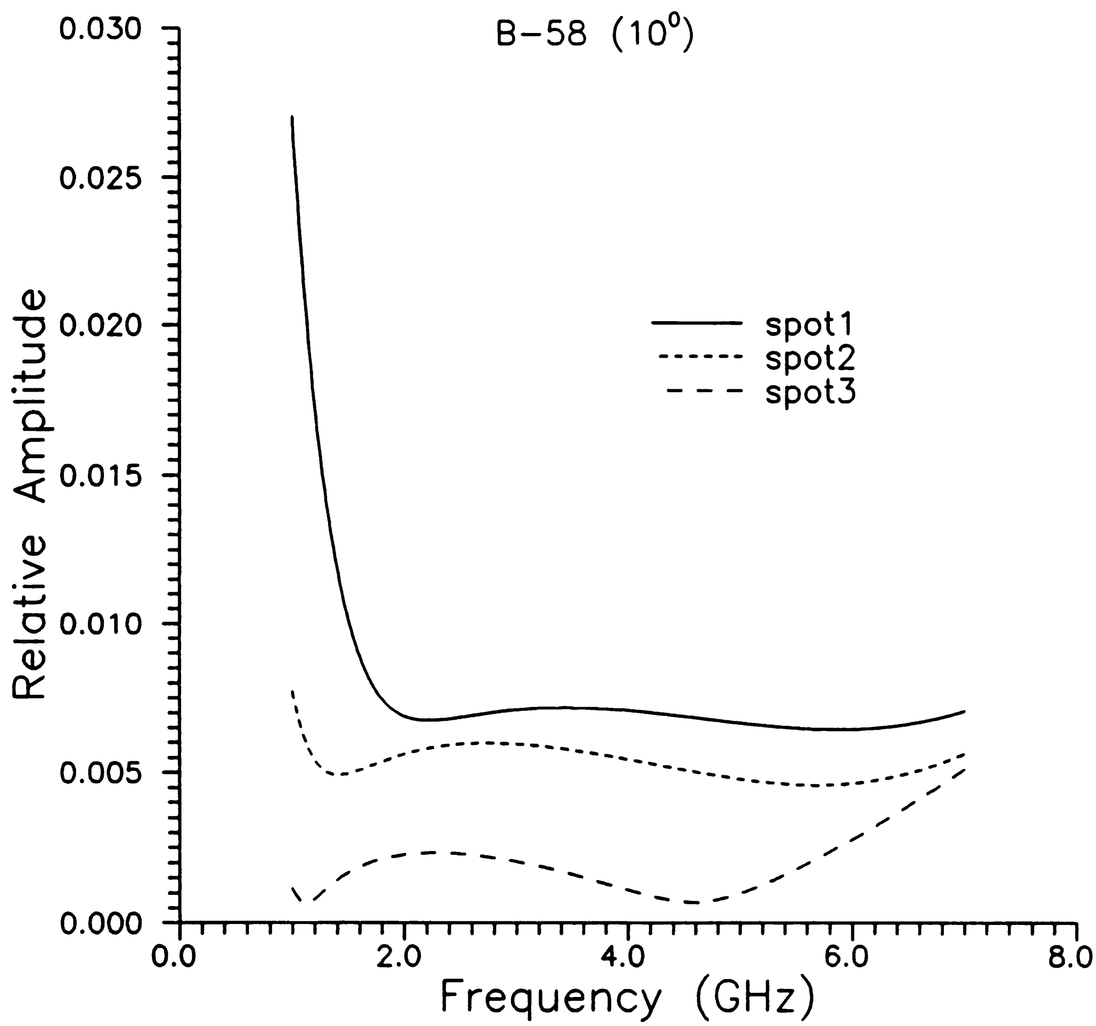

Figure 2.35 Transfer functions of 1st, 2nd, and 3rd specular points.

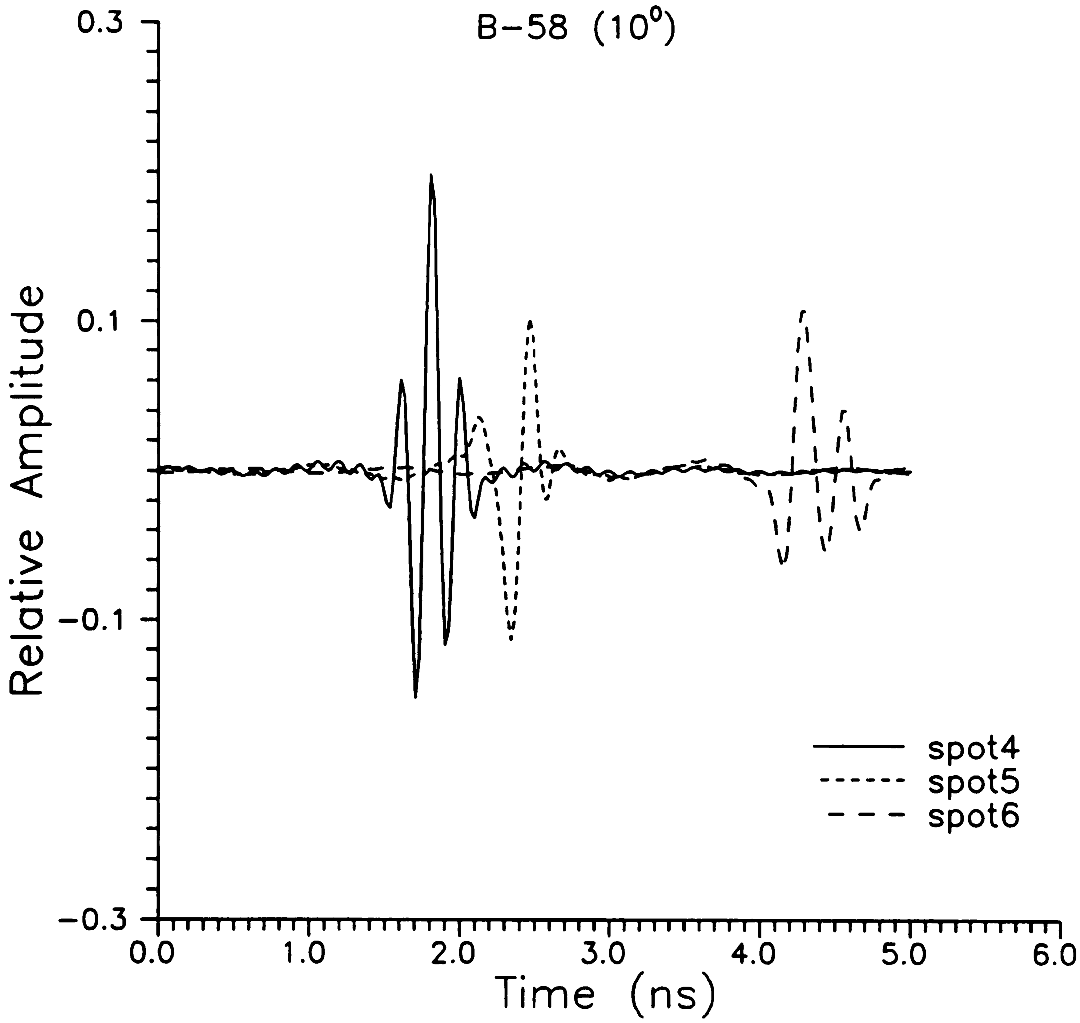

Figure 2.36 Pulse responses of 4th, 5th, and 6th specular points.

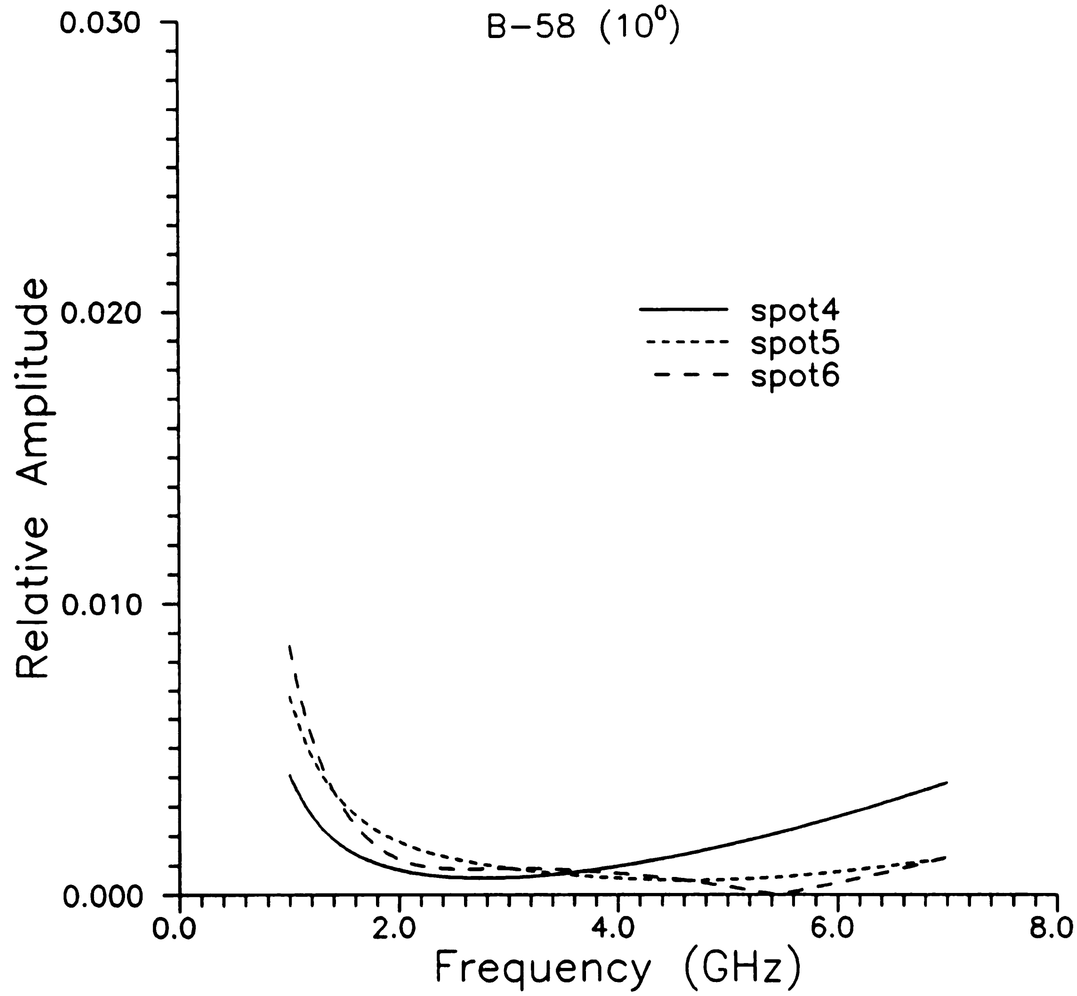

Figure 2.37 Transfer functions of 4th, 5th, and 6th specular points.

see that in terms of relative energy, the reflection from the nose of the aircraft is quite small.

The scattering center pulse responses for the three largest dominant scattering centers are shown in Figure 2.39. The first scattering center transfer function is dominated by a downward slope, indicating a $1/\omega$ or integral impulse response. The next two responses are relatively flat, indicating a primarily impulsive response as shown in Figure 2.40. Similar results are seen in Figure 2.41, Figure 2.42, Figure 2.43, and Figure 2.44, which shows the pulse responses and transfer functions of the remaining scattering centers. Note that the nose response is quite close to a delta function over the measurement band.

Figure 2.45-2.52 show the results of the B-52 with white Gaussian noise added at signal-to-noise ratios (SNR) from 15 dB to 0 dB. All of the reconstructed waveforms are found using nine scattering centers and $n=-2,-1,\ldots,2$. The five largest dominated scattering center temporal positions can be extracted well with SNR as high as 10 dB, and their three largest scattering center pulse responses and transfer functions match quite well (see Figure 2.39 and Figure 2.40). The smallest scattering centers do not represent physical features on the target, but noise realizations.

The scattering center pulse responses and transfer functions cannot be reconstructed well at lower noise level (less than 10 dB) due to waveform distortion as mentioned in section 2.3. Even so, we observe that the locations of four largest scattering centers, which represent the first engine mount, the second engine mount, the wing joint and trailing edge of wing, are estimated accurately in the presence of larger noise.

Figure 3.53 shows the reconstructed response of the noisy 0^0 B-52 measured in

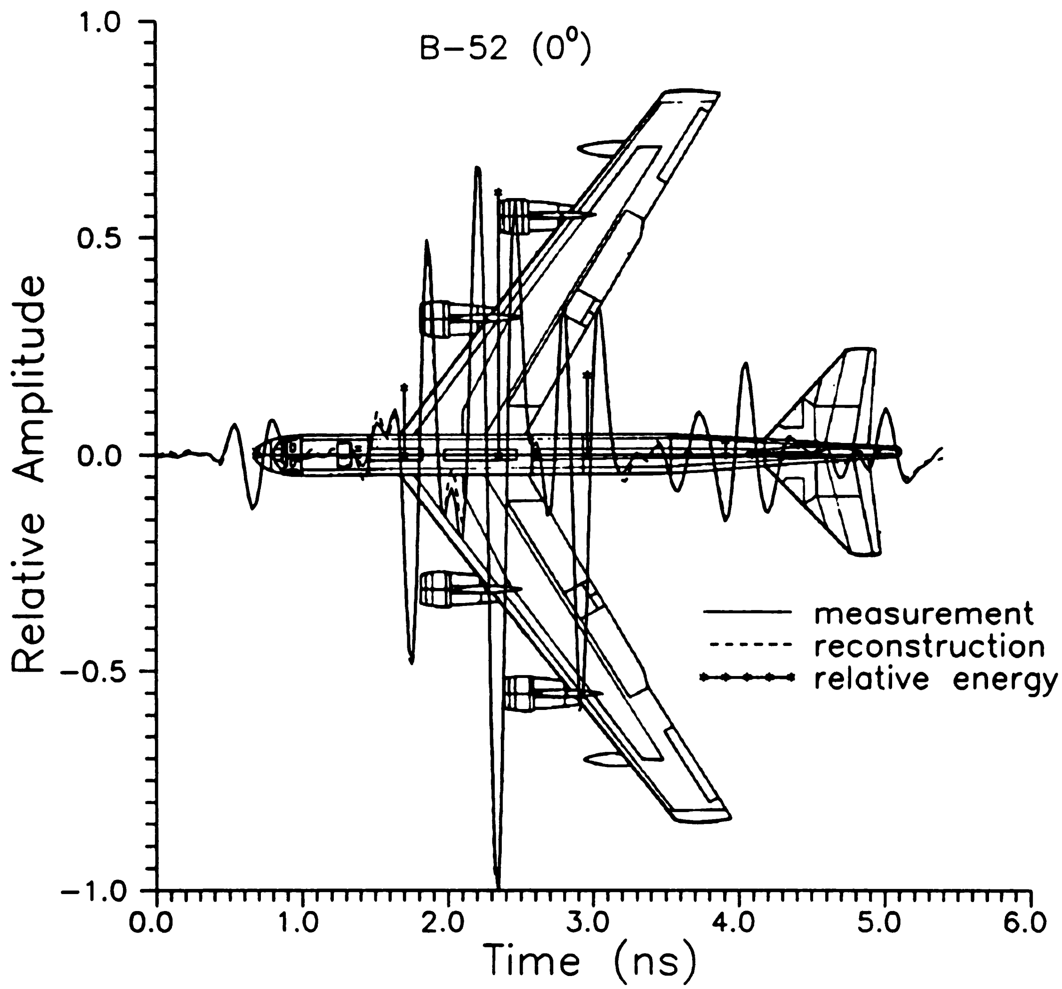

Figure 2.38 Response of B-52 at 0^0 aspect measured in band 1-7 GHz, and reconstructed response using 9 scattering centers, 4096 pt FFT, n=-2,-1,...,2, and GMC window with τ=0.3 ns, f_c=4 GHz.

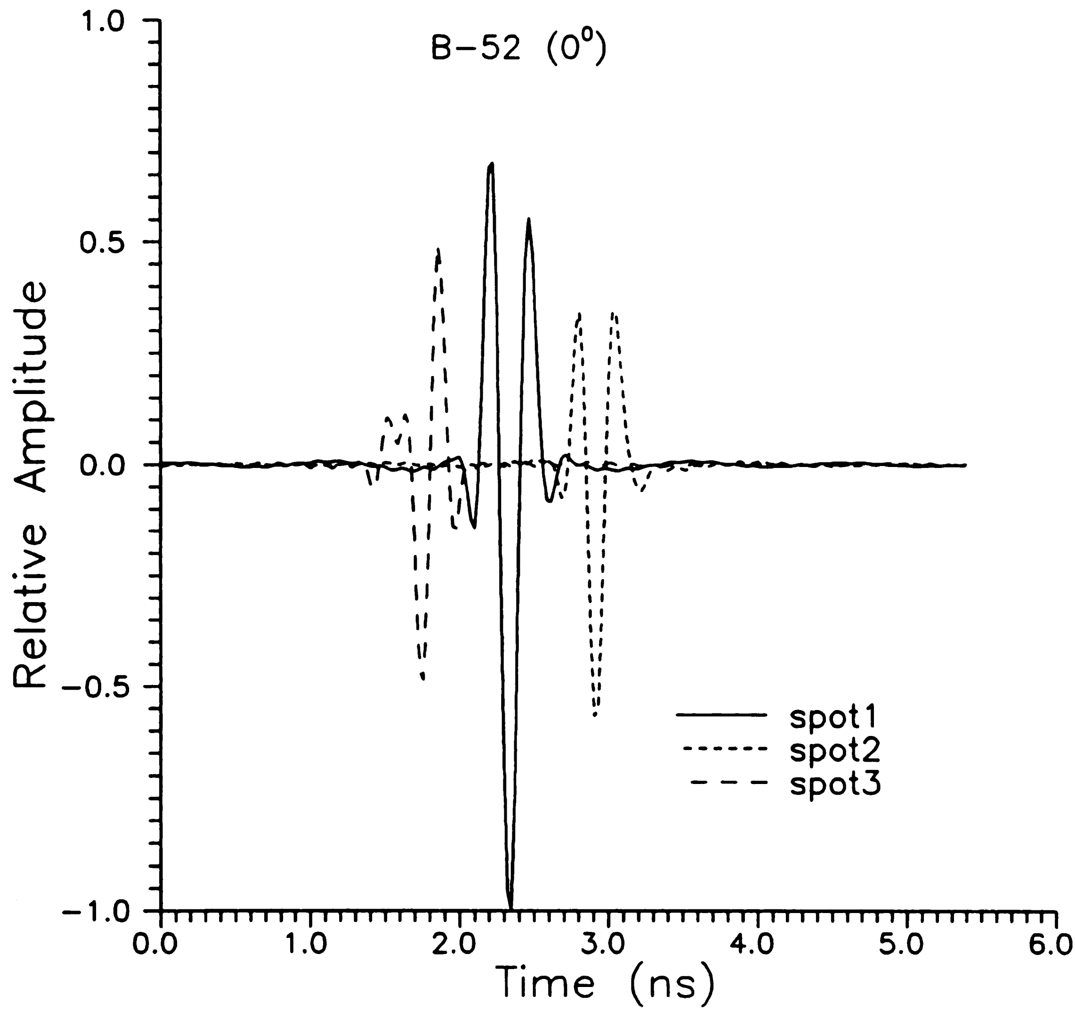

Figure 2.39 Pulse responses of 1st, 2nd, and 3rd specular points.

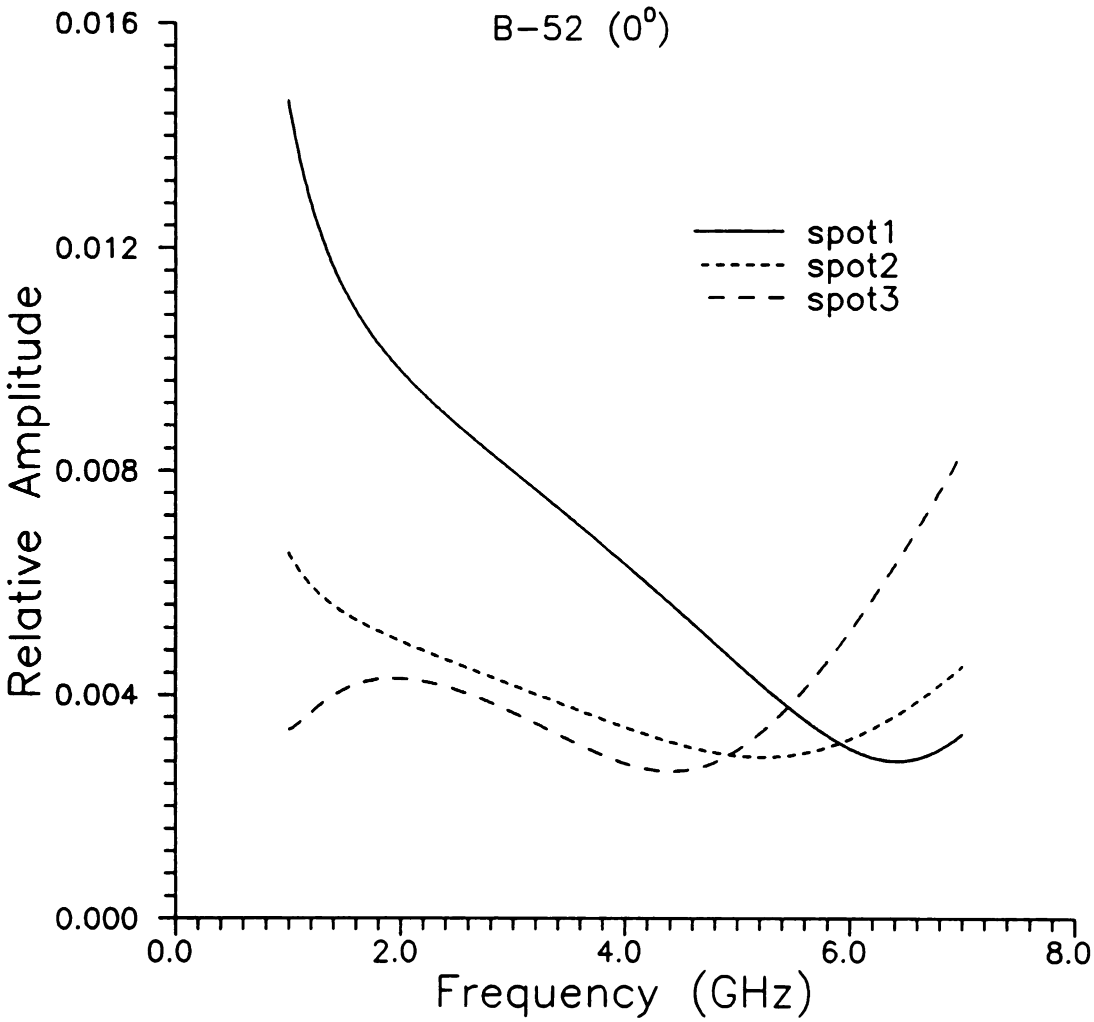

Figure 2.40 Transfer functions of 1st, 2nd, and 3rd specular points.

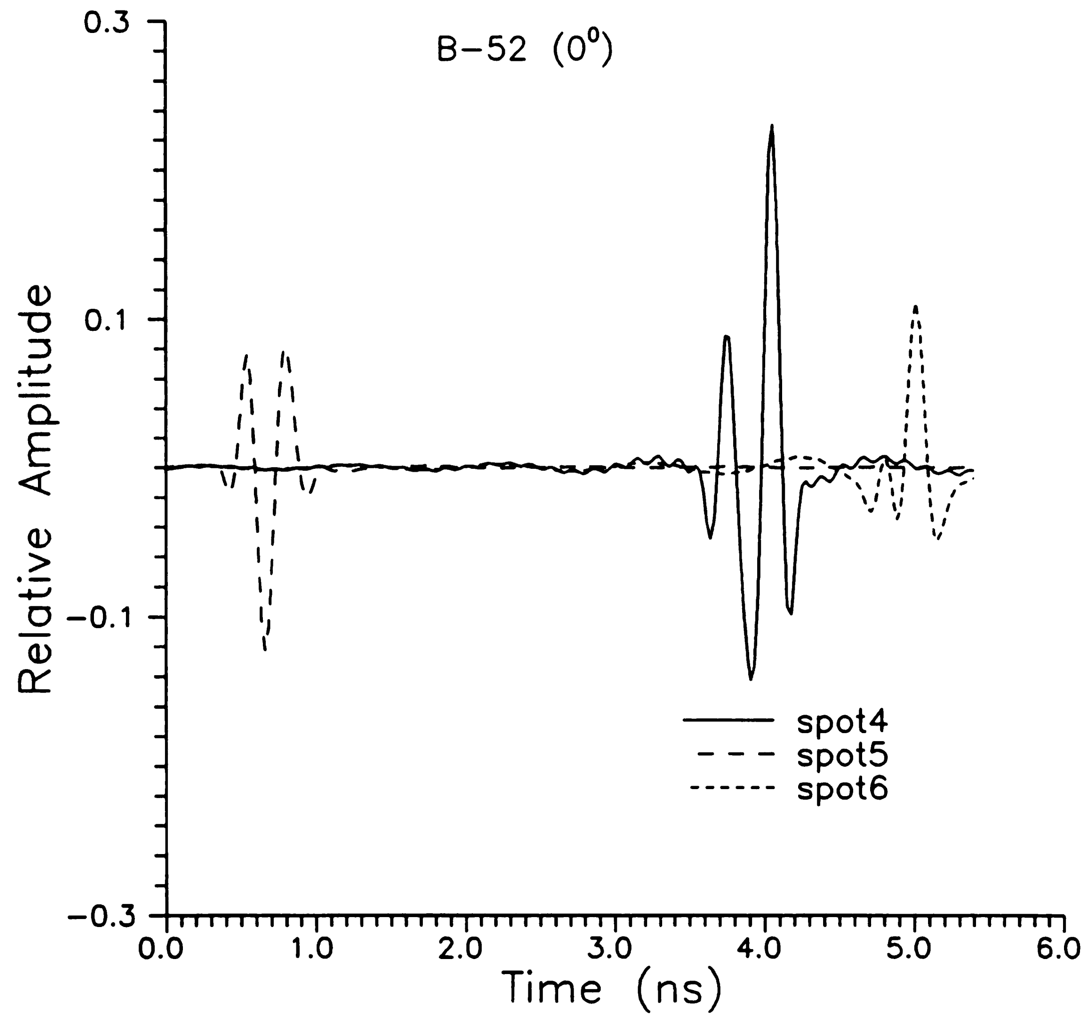

Figure 2.41 Pulse responses of 4th, 5th, and 6th specular points.

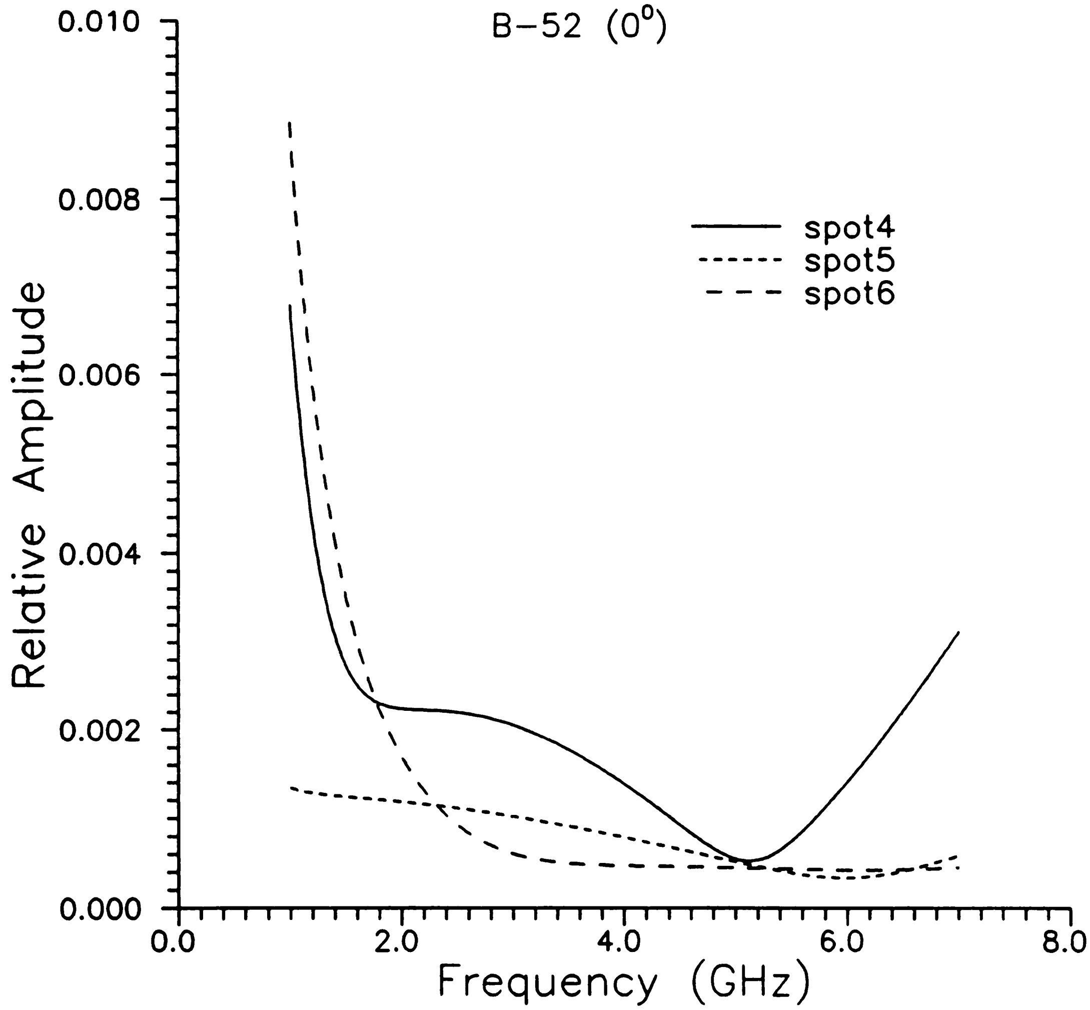

Figure 2.42 Transfer functions of 4th, 5th, and 6th specular points.

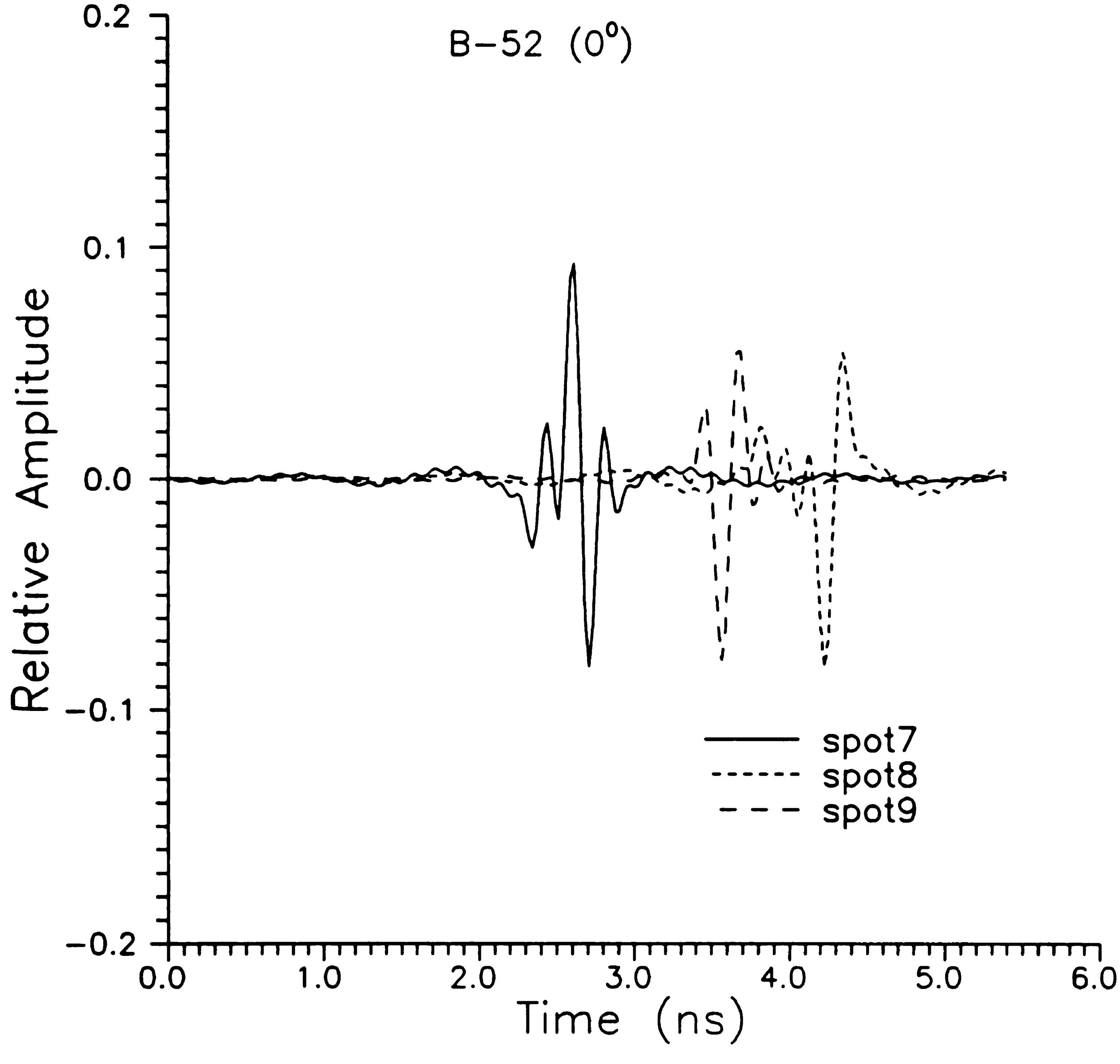

Figure 2.43 Pulse responses of 7th, 8th, and 9th specular points.

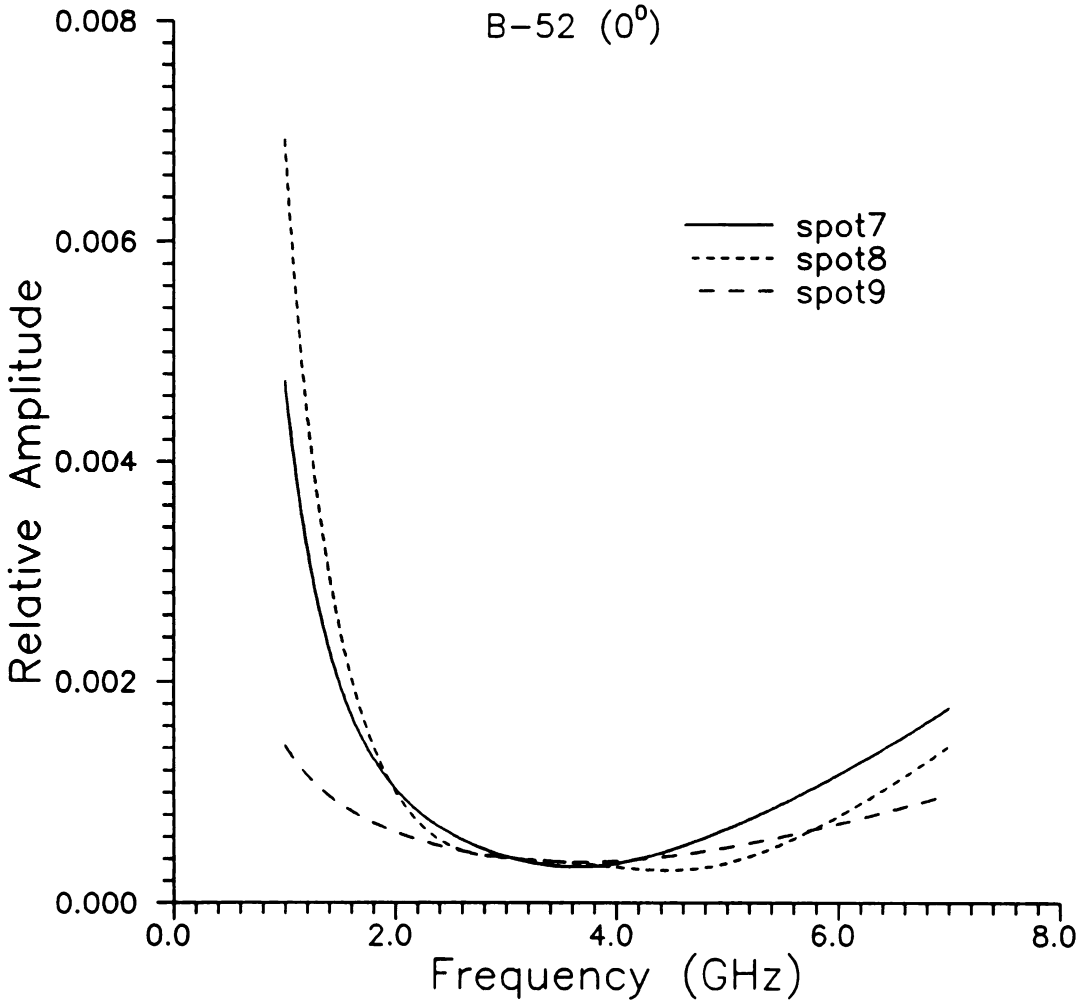

Figure 2.44 Transfer functions of 7th, 8th, and 9th specular points.

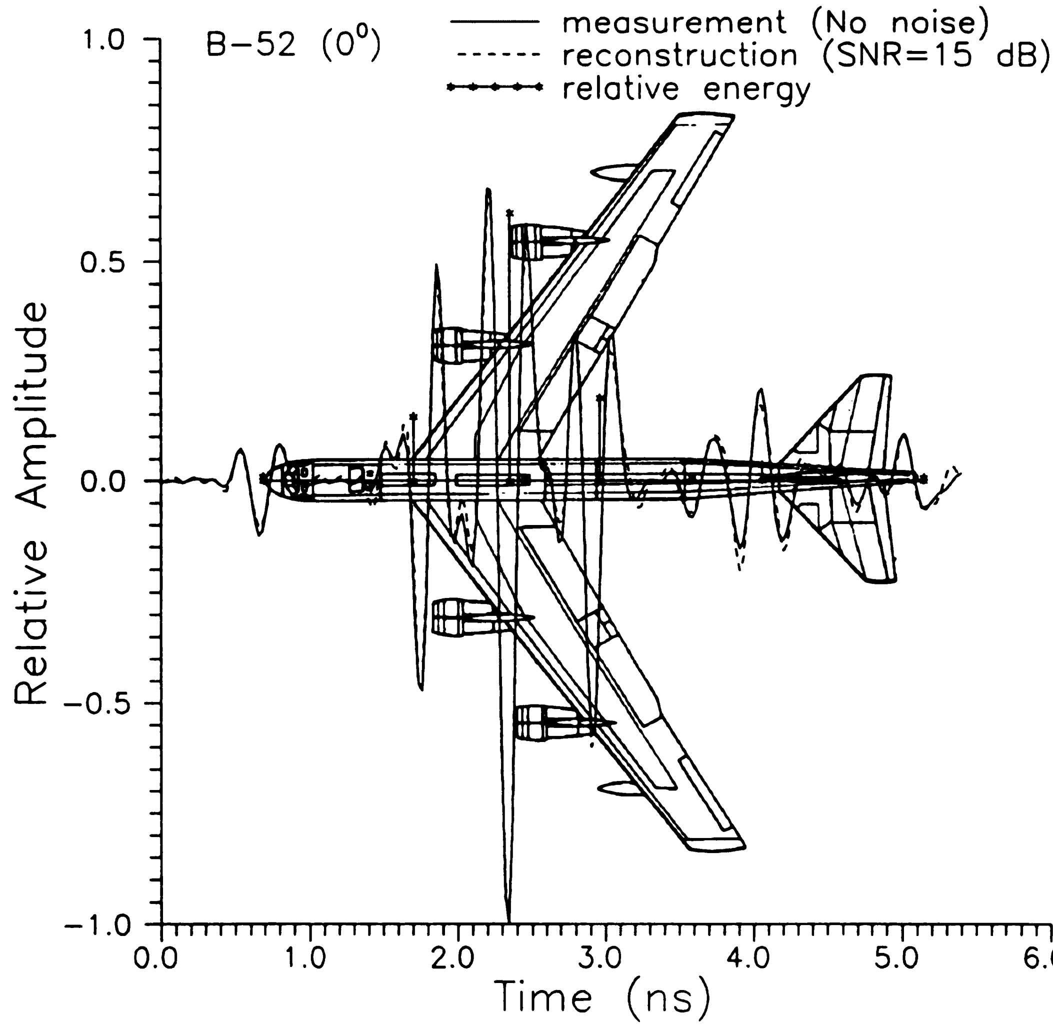

Figure 2.45 Response of B-52 at 0^0 aspect measured in band 1-7 GHz, and reconstructed response using 9 scattering centers with SNR=15 dB, n=-2,-1,...,2, and GMC window with τ=0.3 ns, f_c=4 GHz.

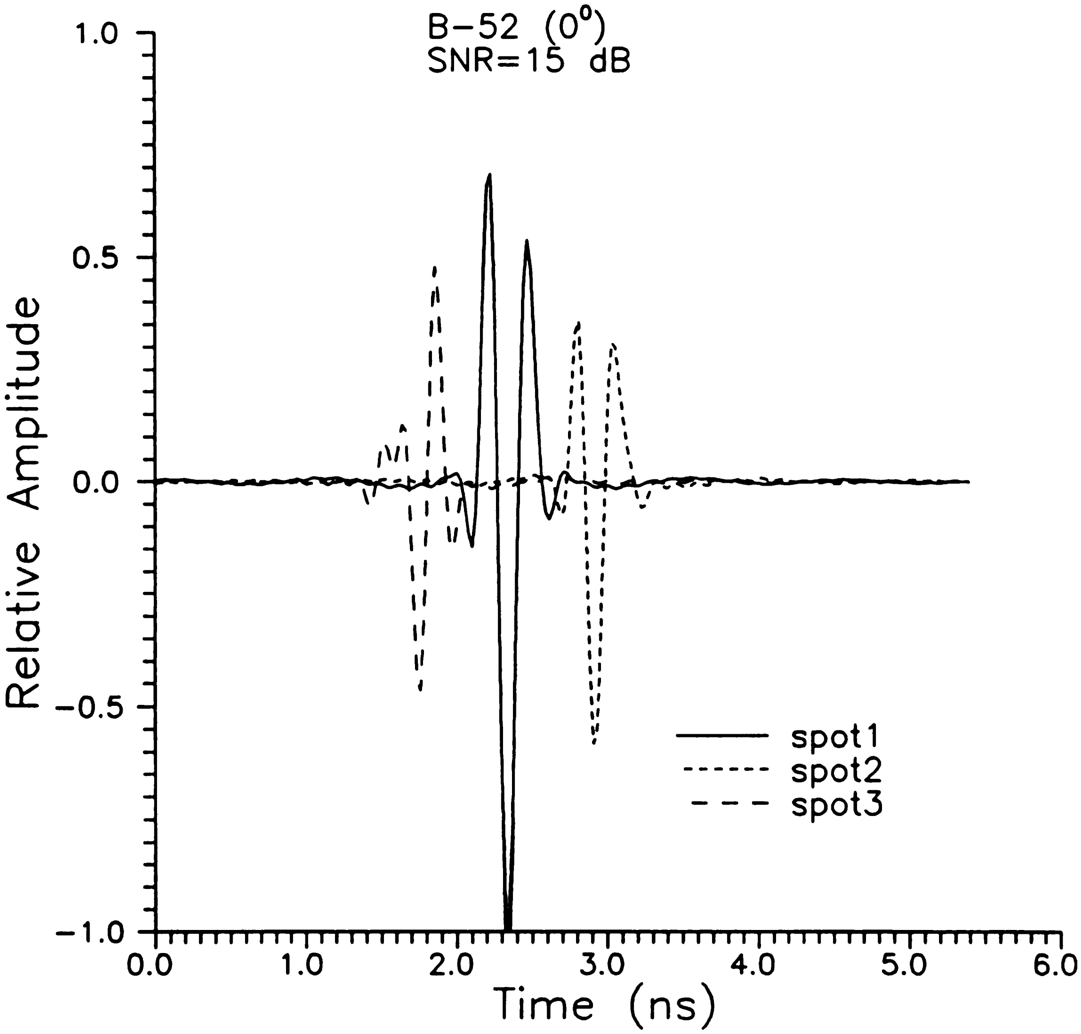

Figure 2.46 Pulse responses of 1st, 2nd, and 3rd specular points. SNR=15 dB.

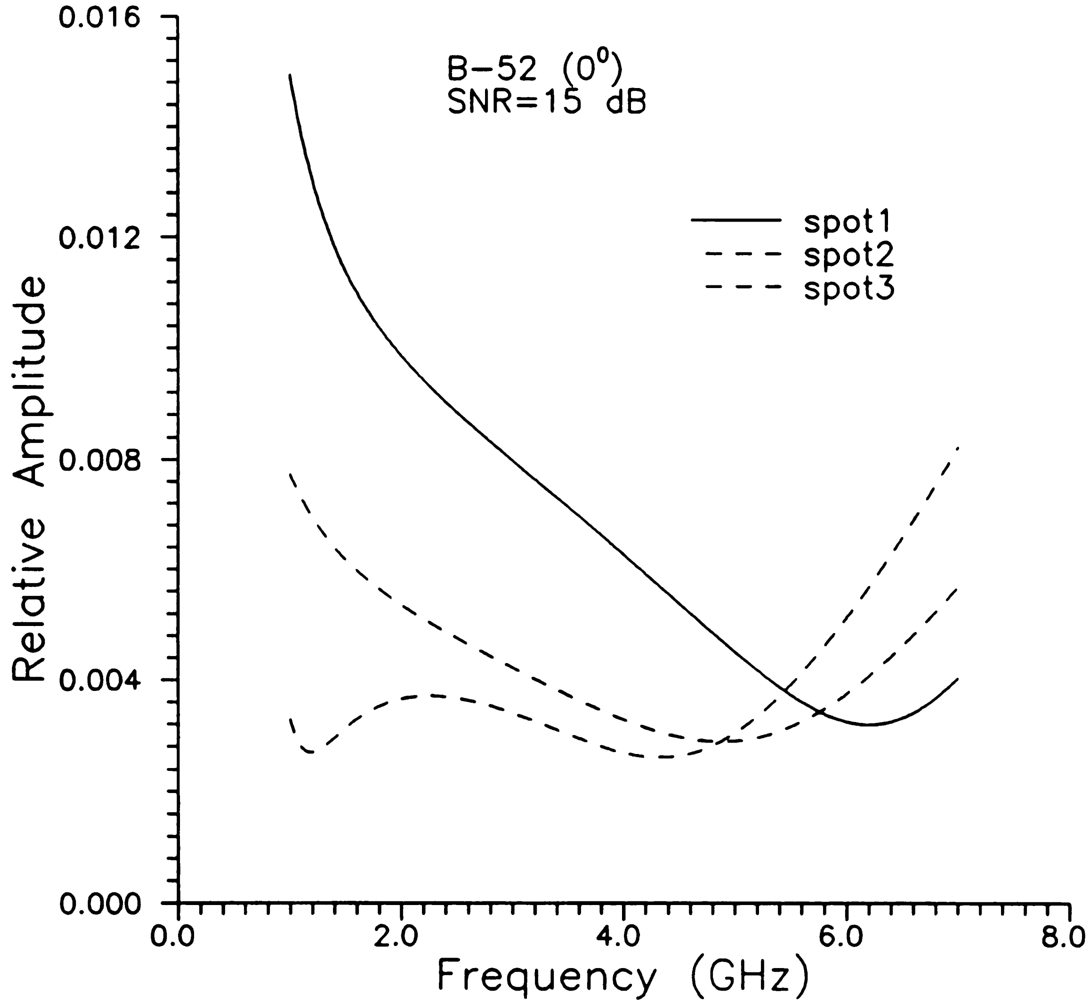

Figure 2.47 Transfer functions of 1st, 2nd, and 3rd specular points. SNR=15 dB.

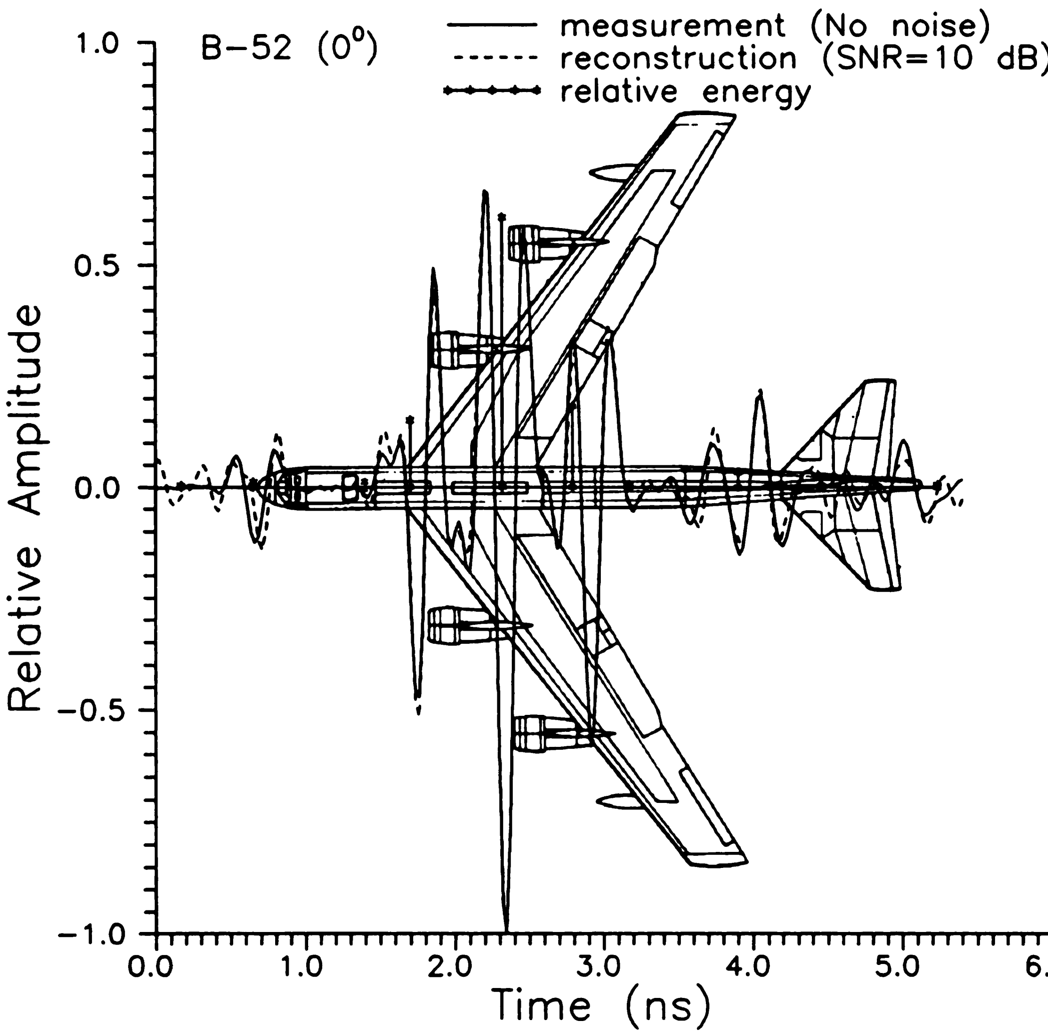

Figure 2.48 Response of B-52 at 0^0 aspect measured in band 1-7 GHz, and reconstructed response using 9 scattering centers with SNR=10 dB, n=-2,-1,...,2, and GMC window with τ=0.3 ns, f_c=4 GHz.

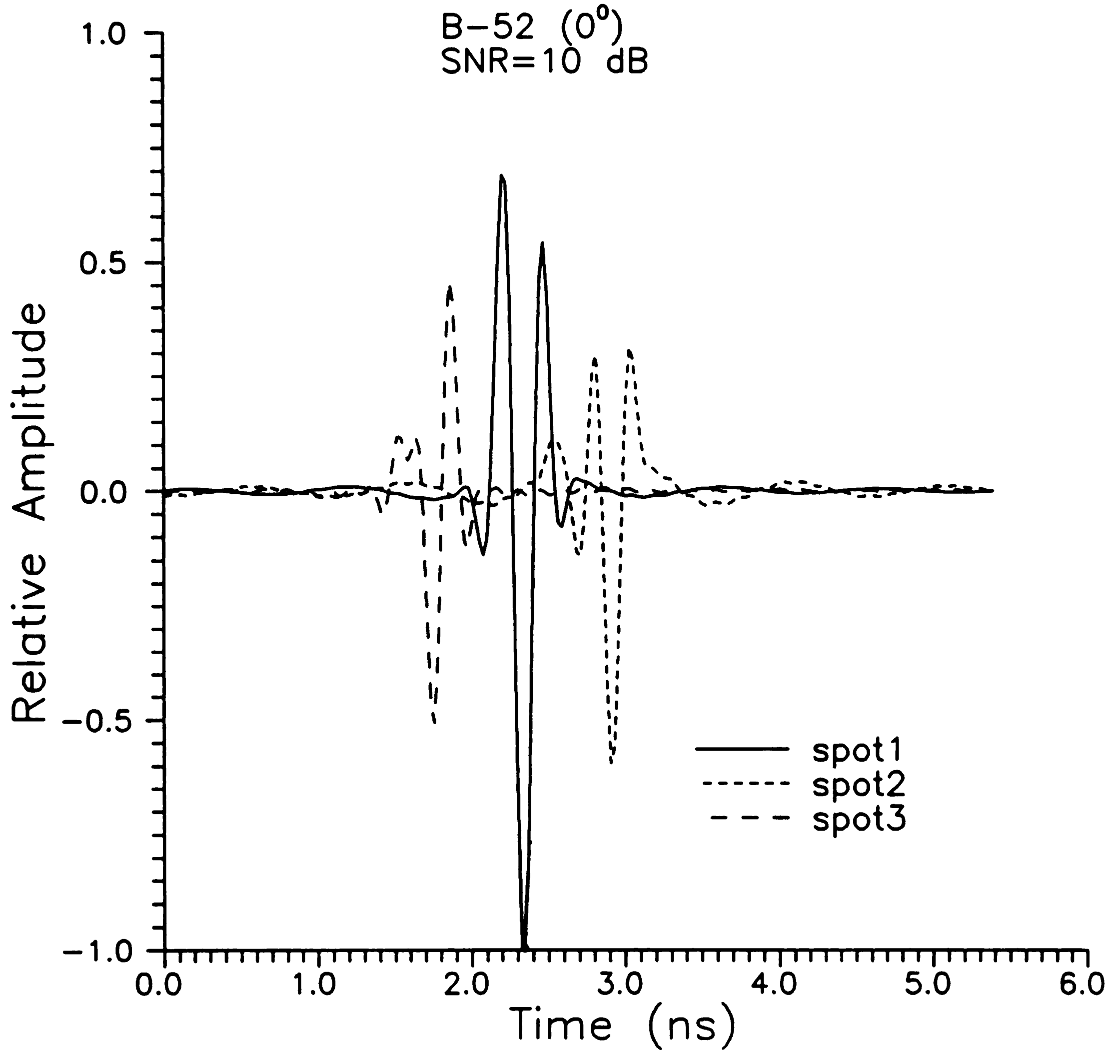

Figure 2.49 Pulse responses of 1st, 2nd, and 3rd specular points. SNR=10 dB.

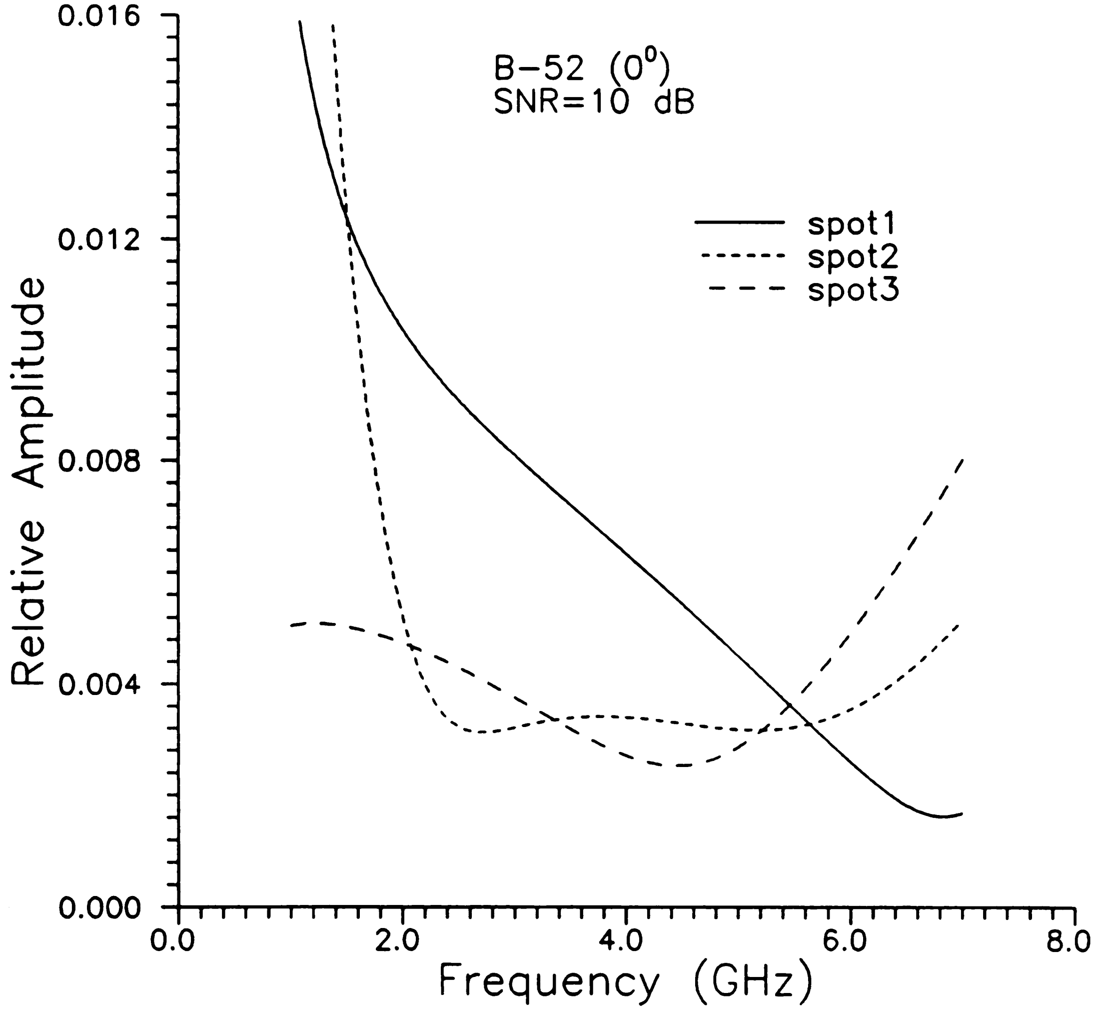

Figure 2.50 Transfer functions of 1st, 2nd, and 3rd specular points. SNR=10 dB.

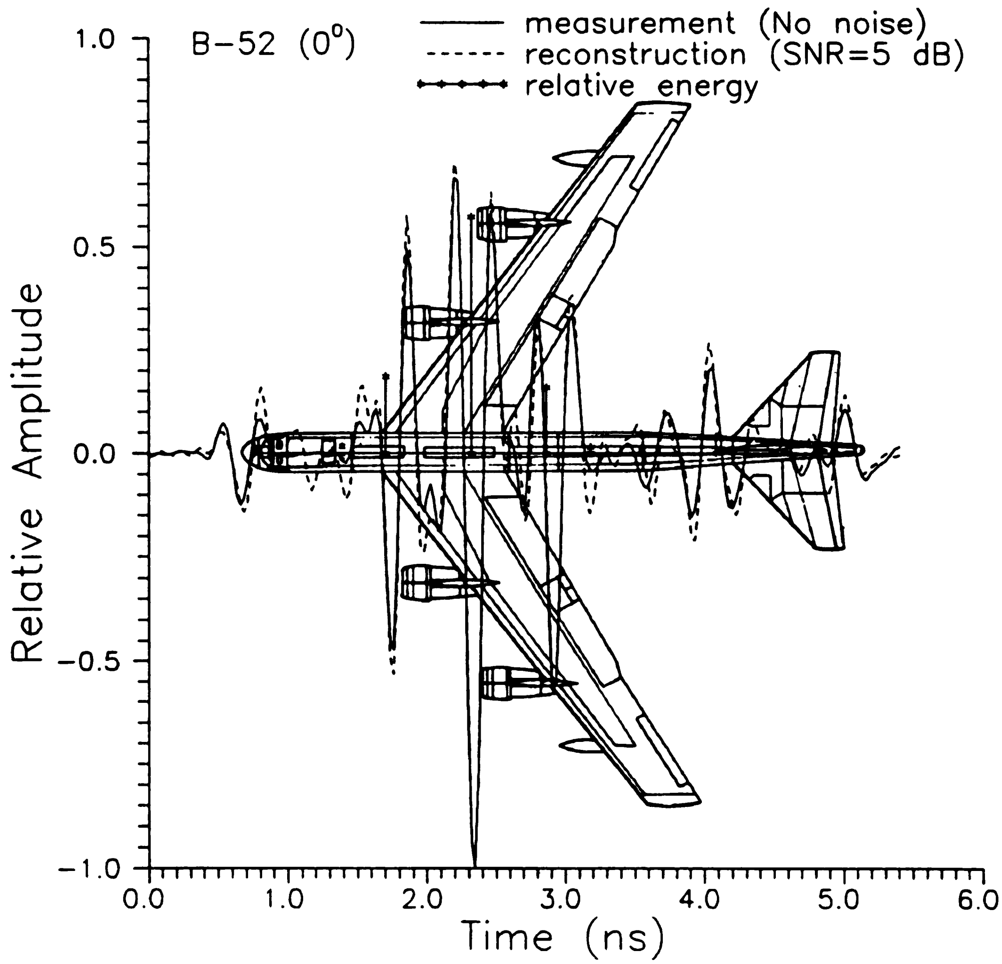

Figure 2.51 Response of B-52 at 0^0 aspect measured in band 1-7 GHz, and reconstructed response using 9 scattering centers with SNR=5 dB, n=-2,-1,...,2, and GMC window with τ=0.3 ns, f_c=4 GHz.

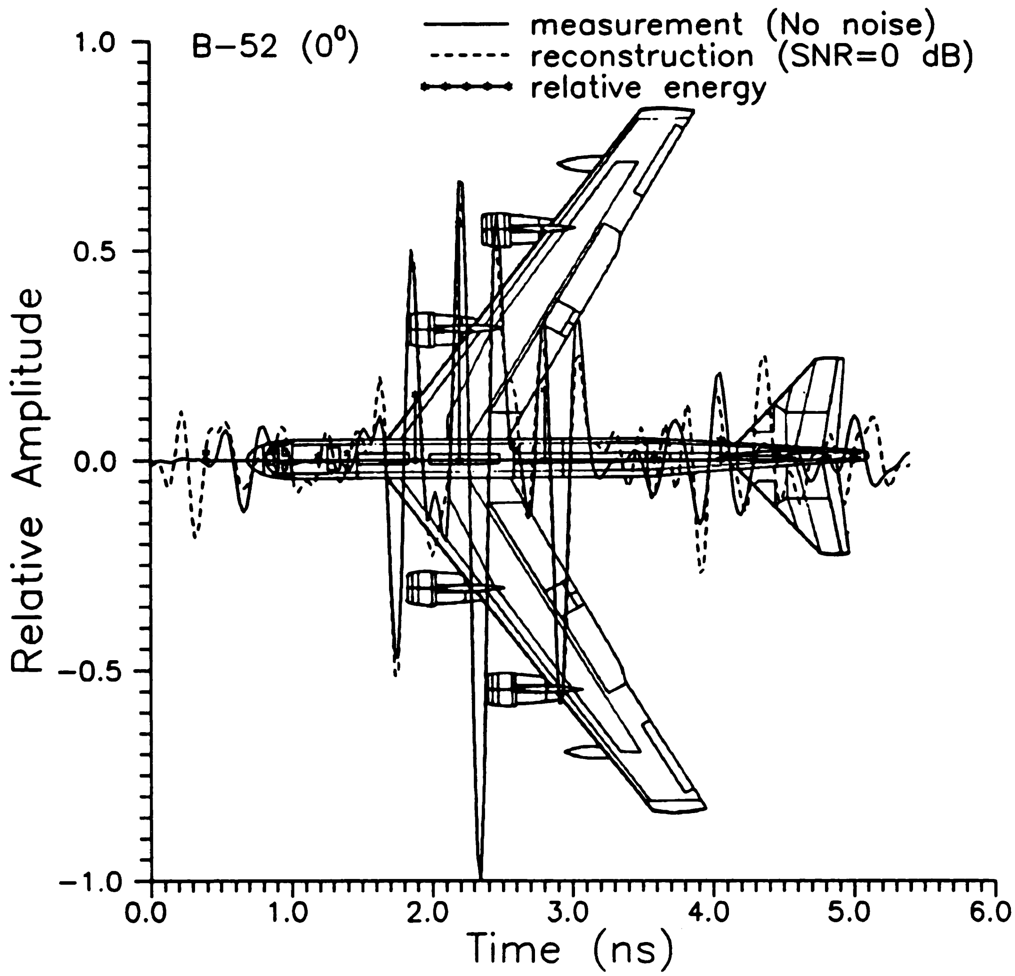

Figure 2.52 Response of B-52 at 0^0 aspect measured in band 1-7 GHz, and reconstructed response using 9 scattering centers with SNR=0 dB, n=-2,-1,...,2, and GMC window with τ=0.3 ns, f_c=4 GHz.

the frequency band 1-7 GHz with SNR=-5 dB, using six scattering centers, and n=-*1,0,1*. It is interesting to note that the locations of first engine mount, the second engine mount, the wing joint and trailing edge of wings scattering centers match quite well. The reconstructed response is a much better representation than the original noisy waveform and representation using more polynomial terms. We conclude that the determination of scattering center temporal positions is much less sensitive to noise than that of transfer functions.

Finally, Figure 2.54 shows response of the 90^0 B-52 measured in the band 2-18 GHz, and the reconstructed response using 5 scattering centers. we notice that the four largest scattering centers match the fuselage, second engine mount, first engine mount, and wing tip. The fuselage pulse response is dominated by a delta function as shown in Figure 2.55, which shows scattering center pulse responses and Figure 2.56, which shows scattering center transfer functions.

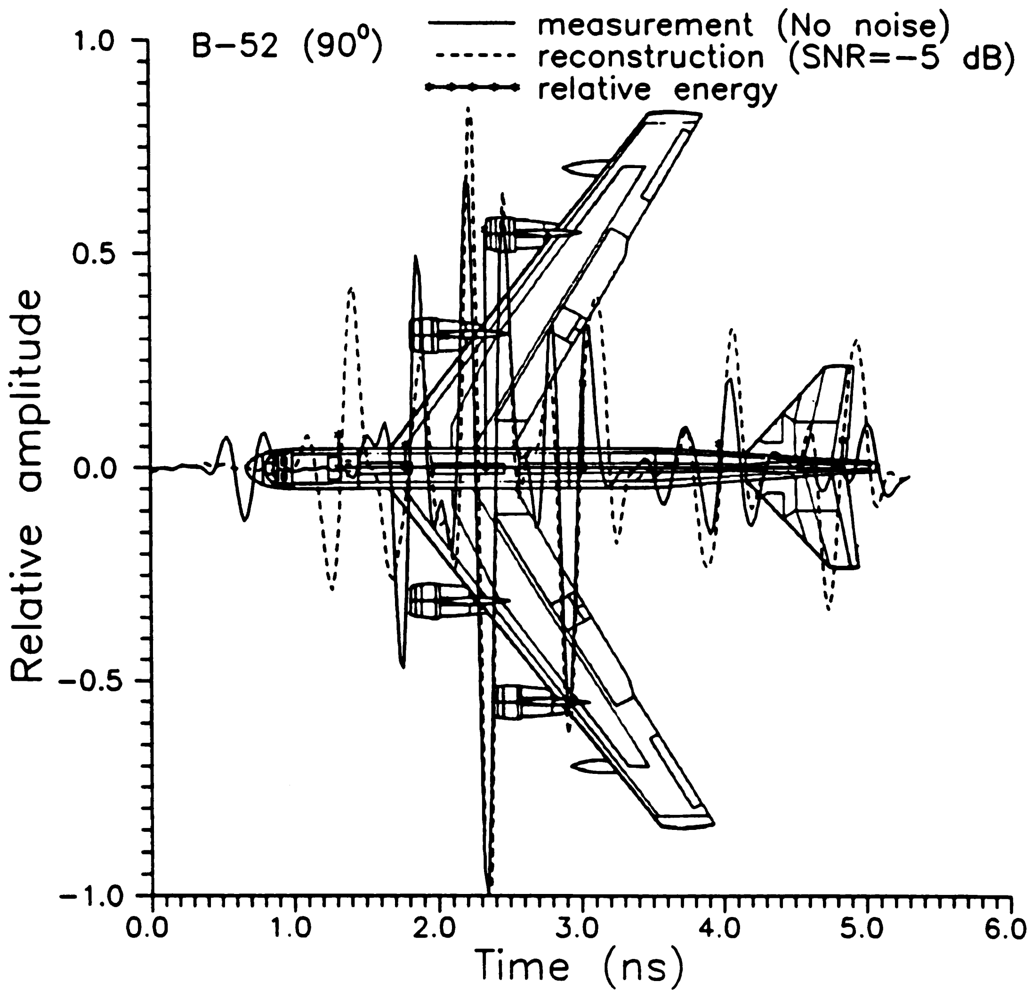

Figure 2.53 Response of B-52 at 0^0 aspect angle measured in band 1-7 GHz, and reconstructed response using 6 scattering centers with SNR=-5 dB, n=-1,0,1, and GMC window with τ=0.3 ns, f_c=4 GHz.

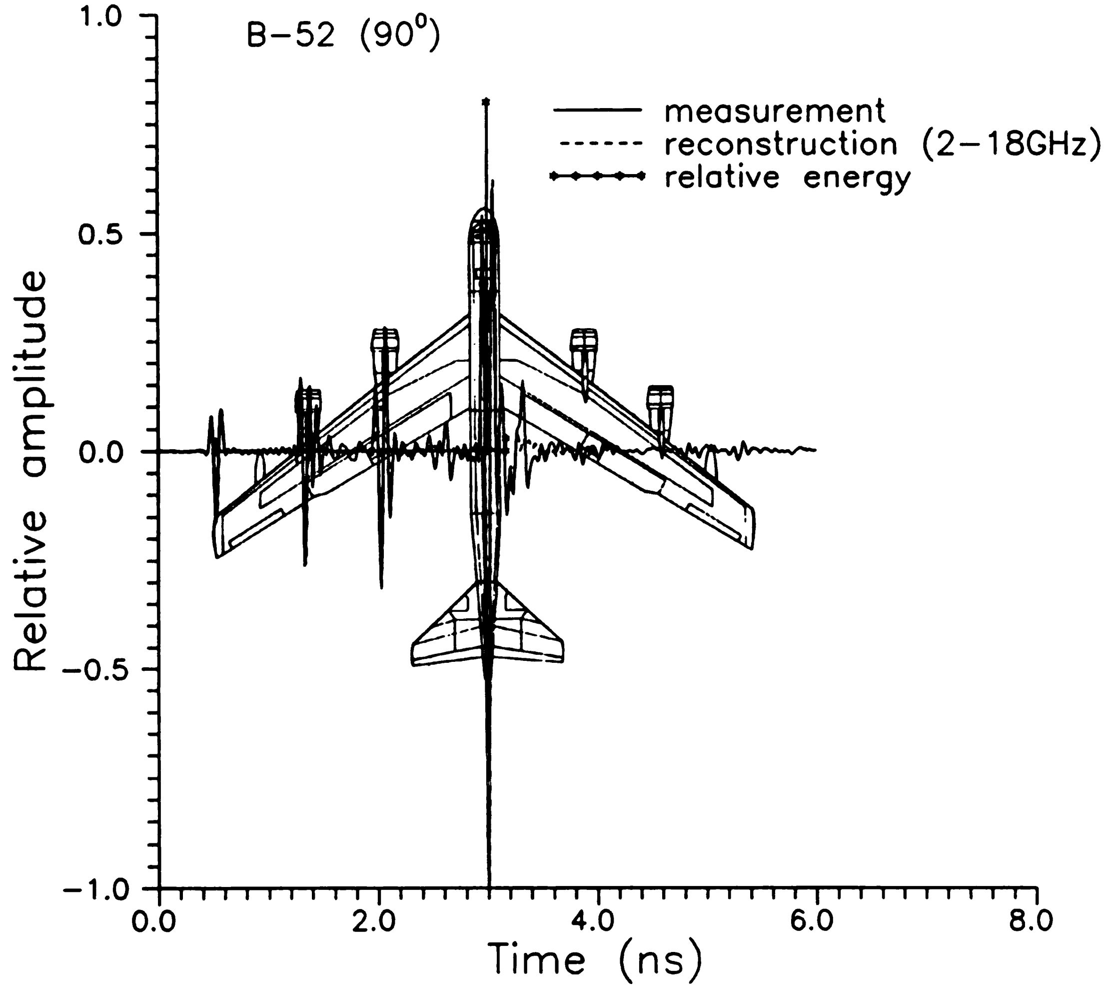

Figure 2.54 Response of B-52 at 90^0 aspect measured in band 2-18 GHz, and reconstructed response using 5 scattering centers, 8192 pt FFT, n=-2,-1,...,2, and GMC window with τ=0.1 ns, f_c=10 GHz.

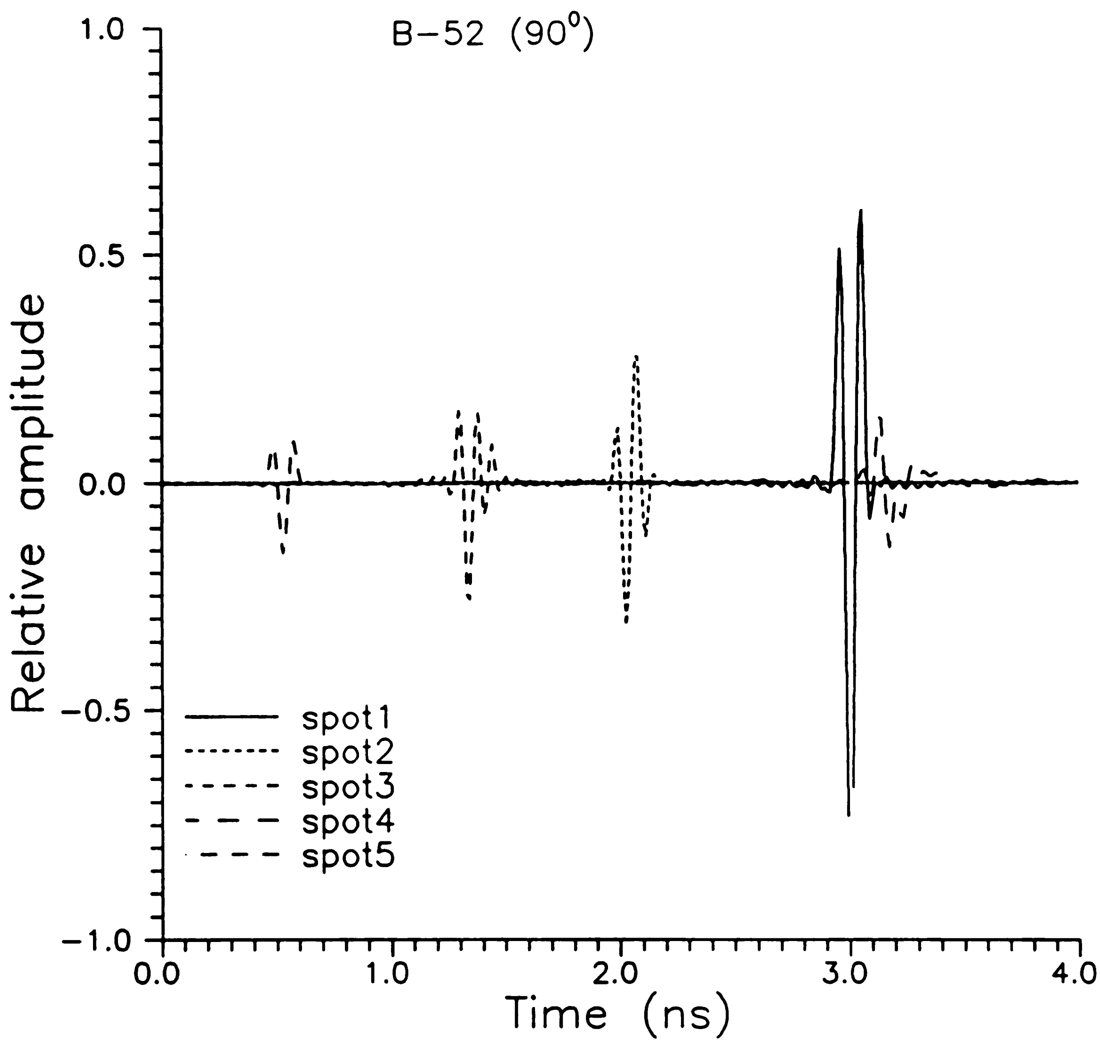

Figure 2.55 Pulse responses of 1st, 2nd, 3rd, 4th, and 5th specular points.

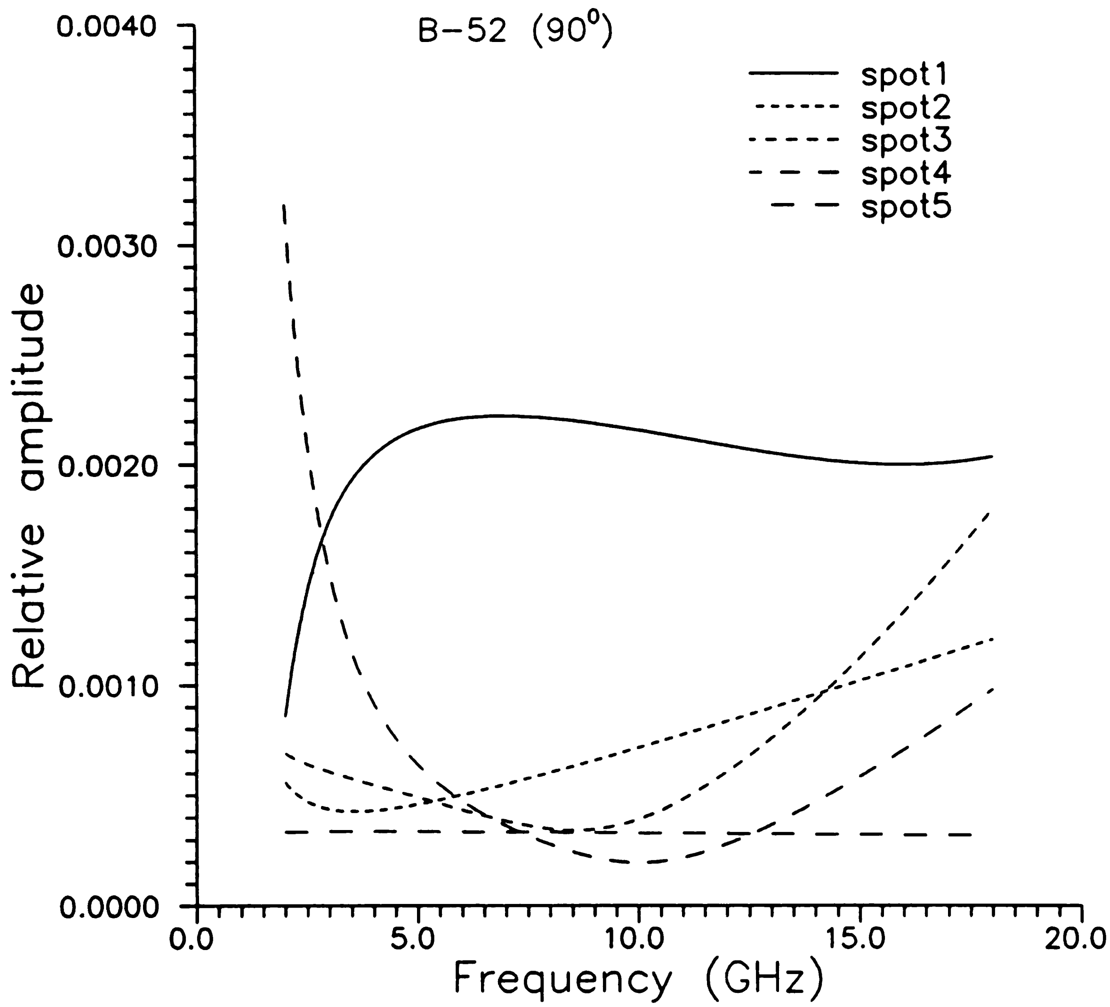

Figure 2.56 Transfer functions of 1st, 2nd, 3rd, 4th, and 5th specular points.

CHAPTER 3

SCATTERING CENTER ANALYSIS USING A GENETIC ALGORITHM

3.1 Introduction

The scattering center temporal positions and amplitudes are extracted one at a time in the previous chapter. The results for the scattering center transfer functions are quite good when the scattering centers are widely separated. Satisfactory results can not be obtained, though, when the overlapping of the scattering center pulse responses is severe. To solve this problem, an interesting algorithm called a genetic algorithm (G.A.), which is based on the mechanics of natural selection and natural genetics, is introduced. It combines survival of the fittest among string structures with a structural yet randomized information exchange to form a search algorithm with some of the innovative flair of human search. In every generation, a new set of artificial creatures (strings) is created using bits and pieces of the fittest of the old; an occasional new part is tried for good measure. While randomized, genetic algorithms are not a simple random walk. They efficiently exploit historical information to speculate on new search points with expected improved performance.

Genetic algorithms were developed originally by John Holland and his students at the University of Michigan [13]. Many papers and dissertations have also contributed to genetic algorithms development [14], [15], [16], [17]. Genetic algorithms are now finding widespread applications in industry, business, science, and engineering. These algorithms are computationally simple yet powerful in their search. Genetic algorithms are different from other methods in four ways [18]:

(1) Genetic algorithms work with a coding of the parameter set, not the parameters themselves.

(2) Genetic algorithms search from a population of points, not a single point.

(3) Genetic algorithms use objective function information, not derivatives or other auxiliary knowledge.

(4) Genetic algorithms use probalistic rules, not deterministic rules.

A simple G.A. is composed of three operations: selection, crossover, and mutation.

The second portion of this chapter introduces some genetic algorithm notations and procedures. Section 3.3 presents application of the G.A. to scattering center analysis through extraction of scattering center temporal positions, and determination of scattering center pulse responses and transfer functions. Both artificial data and measured data are evaluated using the G.A.. The performance of the G.A. is studied in the presence of noise. The effects of the number of scattering centers on G.A. are discussed. Comparisons between results obtained using the fitting scheme and the G.A. are also described.

3.2 Genetic Algorithm Theory

The most straightforward approaches to extracting target scattering center temporal positions may be those based on nonlinear least squares algorithms. Difficulty arises with least squares techniques because of their dependence on initial guesses and their tendency to get "stuck" at local minima. Since a genetic algorithm has no such limitations, it provides a more natural minimization procedure.

Consider the sampled early-time response $r(t_i)$ created or measured at time t_i. The scattering center pulse response amplitudes $\{a_{mn}\}$ can be found by minimizing the residual

$$R(T_m) = \sum_i \frac{1}{\epsilon}[r(t_i) - g(t_i)]^2 \tag{3.1}$$

where $g(t)$ is fitting function given by

$$g(t) = \sum_{m=1}^{M} f_m(t) = \sum_{m=1}^{M}\sum_n a_{mn}[p(t) * \delta^{(n)}(t - T_m)] \tag{3.2}$$

Here $p(t)$ is the pulse waveform, ϵ is the energy in the response, M is the number of scattering centers assumed, T_m is m^{th} scattering center temporal position, and n is typically truncated to -2,-1,...,2 as before.

Once the time positions T_m are found by minimizing (3.1), the scattering center amplitudes, a_{mn} are determined for given $\{T_m\}$ using the linear least squares method. Then, the m^{th} scattering center transfer function can be reconstructed as

$$H_m(\omega) = \sum_n a_{mn} e^{-j\omega T_m} (j\omega)^n \tag{3.3}$$

In the standard implementation of genetic algorithms, only a function maximization is defined. Thus, to minimize (3.1) we must maximize a fitness function defined as

$$F(T_m) = C - R(T_m) \tag{3.4}$$

where $F(T_m)$ must be greater than zero. The constant C is given by the user and can be updated to reduce $\max[F(T_m)]$ toward zero.

$F(T_m)$ is maximized by repeating a three step process: selection, crossover, and mutation. Thus genetic algorithm mimics biological natural selection by encoding the parameters as binary strings, and then cross-breeding and mutating the strings using a survival rule. Let T_m be defined on $[T_m^{min}, T_m^{max}]$ and be coded by

$$T_m = T_m^{\min} + \frac{T_m^{\max} - T_m^{\min}}{2^L - 1} \sum_{l=1}^{L} b_{m,l} 2^{l-1} \tag{3.5}$$

where L is length of a bit string, and $b_{m,l}$ is the bit pattern. The bit strings are then concatenated to form a single string B of length ML which represents all the variables. There are many ways to choose offsprings with appropriate bias toward the best [18]. One way is that breeding begins by using "stochastic reminder sampling without replacement" to create a "pool" (population) of K (K is even) bit strings. Letting

$$F_k = F(T_m(B_k)) \tag{3.6}$$

$$P_k = \frac{F_k}{\sum_k F_k} \tag{3.7}$$

$$e_k = K P_k \tag{3.8}$$

where T includes $T_1, T_2, \ldots, T_M$, P_k is probability of k^{th} bit string, B_k is a bit string consisting of the concatenation of all the variable bit strings, and e_k is the "expected" allocation of members to the pool. By applying a rule of survival, we place the integer part of e_k copies of B_k into the pool, and fill the remainder of pool by selecting at random from $\{B_k\}$ with probability

$$p_k = e_k - (e_k) \tag{3.9}$$

where (e_k) is integer part of e_k.

After the pool is filled, $K/2$ pairs of bit strings from pool are selected at random. Pairs are bred with probability P_c (selected by the user, typically P_c=0.5 to 0.6), a crossover point is chosen at random and bit string information is "swapped". After the population has been completely bred, one bit in B_k is chosen at random and is replaced with probability P_m by Not(bit) to mimic mutation. The probability P_m is selected by the user, but is generally chosen as

$$P_m \approx \frac{1}{K} \tag{3.10}$$

In order to improve results, the three steps are repeated many times by creating a new population from the old one. Thus the more "fit" bit strings pass on their information with the greatest probability, and on average produces a larger value of the objective function. The process is terminated when the population becomes stable.

We should regulate the level of competition among members of the population to achieve the performance we desire. Regulation of the number of copies is especially important in a G.A.. At the start of the G.A. runs, it is common to have a few extraordinary individuals in the population, and using the normal selection rule, these individuals would take over a significant proportion of the finite population in a single generation. This is undesirable. So we must use "fitness scaling". The scaling method used here is the linear scaling

$$F^* = aF + b \tag{3.11}$$

where F is the raw fitness function, and F^* is a scaled fitness function.

We choose the average scaled fitness F^*_{avg} to be equal to the average raw fitness F_{avg}, because subsequent use of the selection procedure will then insure that each average population number contributes one expected offspring to the next generation. To control the number of offspring given to the population member with maximum raw fitness, the maximum scaled fitness, F^*_{max}, is taken as

$$F^*_{\max} = c_{mult} F_{avg} \tag{3.12}$$

where c_{mult} is the scaling factor desired for the best population member, and is typically taken between 1.2 and 2. From the above two conditions, a and b are given by

$$\begin{aligned} a &= (c_{mult} - 1)\frac{F_{avg}}{F_{\max} - F_{avg}} \\ b &= (1 - a) F_{avg} \end{aligned} \tag{3.13}$$

so a few extraordinary individuals get scaled down and lower members of the population get scaled up. When some bad strings are far below the population average and maximum, using the above linear scaling may lead lower fitness values to go to negative. In this case, we still let the raw and scaled fitness average be the same, but map the minimum raw fitness F_{min} to scaled fitness $F^*_{min} = 0$. Then a and b are expressed as

$$\begin{aligned} a &= \frac{F_{avg}}{F_{avg} - F_{\min}} \\ b &= -aF_{\min} \end{aligned} \tag{3.14}$$

Generally the genetic algorithm is not likely to get stuck at a local minima, since the random nature forces it to investigate a dense range of parameters simuteneously. However, there is no guarantee that the global maximum will be reached due to this random nature. Two methods to solve this problem are to increase the numbers L and K, and improve the fitness scaling. The genetic algorithm is quite slow, The global nature of the algorithm and the lack of derivative information causes it to converge very slowly compared to other nonglobal methods. However, these other methods might not converge at all.

3.3 Performance of Genetic Algorithm

The parameter extraction, described in Chapter 2, consists of a repeated process of obtaining one scattering center at a time. This technique is most accurate when the scattering centers are widely separated. If there is considerable overlapping of the scattering center pulse responses, a scheme which extracts all the scattering centers simultaneously should produce more accurate results. Simultaneous extraction leads to a problem which is nonlinear in the temporal locations of the scattering centers, and thus a complicated minimization routine is required. One group of routines which have been gaining popularity due to their simple implementation and their ability to find global minima, are genetic algorithms.

Ilavarasan, et al. demonstrated how to use a genetic algorithm to extract natural frequencies from a measured data set [7]. It is found that a G.A. provides results equivalent to the constrained E-pulse technique [27]. A G.A. describes a more natural minimization procedure for implementing constraints and avoiding initial guesses since parameter constraints are built into the coding form. For instance, if the measurements were made within a particular frequency band, the variation of radian frequency can be restricted to that band thorough (3.5). Similarly, since a damping coefficient must be negative its maximum coded value is set to be zero.

In this section we extend G.A. to early-time data, and determine scattering center modes (temporal positions and amplitudes). This data is then used to reconstruct the pulse responses and obtain the transfer functions of individual scattering centers.

3.3.1 Artificial Data

In order to test the genetic algorithm and compare it with the fitting scheme, we will use the three artificial responses shown in section 2.2, Chapter 2. We remember that each response has three scattering centers located at different time positions, each scattering center impulse response is represented by an integral of a delta function, a delta function, and a derivative of a delta function, which have peaks of 0.25, 1, and 0.5, respectively. Figure 3.1 shows the artificial response created with the scattering centers widely separated about 2.0 ns, and the reconstructed response found by the G.A. using three scattering centers, and n=-2,-1,...,2, a population size of K=100, a bit string length of L=30, and a total of 20 generations (repeations of the selection/crossover/mutation process). The agreement is very good. The heights and positions of the stars * shown in Figure 3.1 represent the relative energy in each response and the temporal positions of the three scattering centers. As expected, the dominant reflection comes from the one which has a maximum peak of unity. The scattering center transfer functions of three scattering centers, calculated using (3.3) are shown in Figure 3.2. As expected, The 1st, 2nd, and 3rd scattering center transfer functions are dominated by a constant, ω and $1/\omega$. Note that the second transfer function is not exactly a straight line since the spectrum of the pulse $P(\omega)$ has been divided out, and that spectrum is very small at low frequencies. If we increase the population size and bit string length, the result is improved and a better minimum is found in (3.1), as shown latter. In this case, quite similar results are observed when compared to Figure 2.1 and Figure 2.3. This demonstrates that both the G.A. and the fitting scheme do their job quite well when scattering centers are widely separated. We prefer to utilize the latter method since the genetic algorithm consumes far more computer time.

To show the effects of response overlapping on the performance of the genetic algorithm, three scattering center pulse responses are put closer at a distance of 0.6 ns apart. This results in the slightly overlapped responses shown in Figure 3.3. The genetic algorithm is used within the time window [0.0,3.0 ns], and the resulting reconstructed response is also shown in Figure 3.3. Here $K=200$, $L=40$, and 25 generations were used. The results match very well. The scattering center pulse responses of three scattering centers, are illustrated in Figure 3.4, and the corresponding transfer functions are demonstrated in Figure 3.5. We observe that the transfer function of the second scattering center is good except at the lower frequency. The G.A. shows better results than those shown in Figure 2.6. In order to obtain good agreement with transfer functions, scattering center pulse responses must match very well.

Even when the pulse response overlapping is considerable, as shown in Figure 3.6, the reconstructed response obtained by G.A. fits well. Here the same parameters were used as the previous example, and the pulse responses and transfer functions of the three scattering centers are shown in Figure 3.7, and Figure 3.8. The agreement is still good since G.A. considers all specular responses simultaneously. As a comparison, when the original method described in Chapter 2 is used, the pulse responses and transfer functions, shown in Figure 2.8 and Figure 2.9, do not match nearly well as with the genetic algorithm results. Thus, G.A. shows better performance.

Genetic algorithm has many variables to control and trade-offs to consider. In order to show the effects of parameters K and L on the performance of the G.A., Figure 3.9 shows the reconstructed waveform using G.A. with K=100, L=40. The temporal positions are shifted some. The pulse responses of three scattering centers, shown in Figure 3.10, and the transfer functions, shown in Figure 3.11, are significantly poorer than the results obtained with K=200 and L=40. Thus, the accuracy of the results is highly dependent on both the initial population size and the bit string length. More bits L give greater accuracy but slow convergence. A larger population provides a better sampling of the solution space, but demonstrates slow convergence too. Note that mutation guards against the algorithm getting stuck at a local minima, but results in slow convergence. It is difficult to determine a stopping point for the algorithm. Eventually the selection, crossover and mating process will cause all the bit strings to be the same. All these considerations make genetic algorithms an interesting numerical method to explore.

If the severe overlapping of scattering center pulse responses occurs, an accurate estimation of the number of scattering centers is not possible. To test the effect of over-guessing the number of scattering centers on the G.A., Figure 3.12 shows the reconstructed response with 4 scattering centers assumed present. The energy in the "fourth" scattering center is very small. This suggests that this scattering center is not real, but is a purely mathematical representation. Similar conclusions are observed in the pulse responses, shown in Figure 3.13, and the transfer functions, shown in Figure 3.14. Just like the fitting scheme, the G.A. reveals the same conclusions about the effect of over-guessing or underestimating scattering center number shown below.

The effect of underestimating the number of scattering centers is shown in

Figure 3.15, Figure 3.16, and Figure 3.17. Since less information is included, the reconstructed data does not match well. But two brightest scattering centers are reproduced with reasonable accuracy as before.

3.3.2 Measured Data

The early-time responses of B-58 and B-52 aircrafts are used to test the genetic algorithm on actual measured data. Figure 3.18 shows the measured early-time response, and the reconstructed responses of 0^0 B-58 found using the genetic algorithm. Here, 6 scattering centers were assumed present as before, n=-2,...,2, K=600, L=80 and 30 generations were followed. Since there is some overlapping of pulse responses, the third, fifth, and sixth scattering center temporal positions are shifted under the different methods (see Figure 2.19). But they match the physical features on the target better. For example, the fifth scattering center seems to match the inlet of second engine. This is not obvious using fitting scheme. Figure 3.19 and Figure 3.20 show the scattering center pulse responses and transfer functions for the three dominant scattering centers. Each response has a different shape, but the second and third response are dominated by the delta function and the first integral of the equivalent pulse. The results illustrated are quite good compared to those obtained using fitting scheme as expected. The 4th, 5th, and 6th scattering center responses are shown in Figure 3.21 and Figure 3.22.

Similar conclusions are observed from 90^0 B-58 and 90^0 B-52 responses as shown in Figure 3.23, Figure 3.24, Figure 3.25, Figure 3.26, Figure 3.27, and Figure 3.28. These results are quite similar to those shown in chapter 2 since both methods can reproduce scattering centers well when scattering centers are largely separated.

Finally, the noisy 0^0 early-time response of a B-58 with SNR=10 dB is used to test the noise sensitivity of the genetic algorithm. Again, the temporal positions of smaller scattering centers are shifted due to noise as shown in Figure 3.29. The sixth scattering center may not be an actual one, but a noise representation. The pulse responses and transfer functions of the three largest scattering centers are shown in Figure 3.30 and Figure 3.31. The transfer functions cannot be determined accurately using a genetic algorithm below SNR=10 dB even though the results may be improved compared to the fitting scheme.

From the above, we note that the genetic algorithm performs better than the fitting scheme, especially when overlapping is severe. The drawback is that the genetic algorithm consumes far more computer time. If overlapping is too serious, both methods cannot describe the behavior of scattering centers accurately and a better scattering model should be chosen.

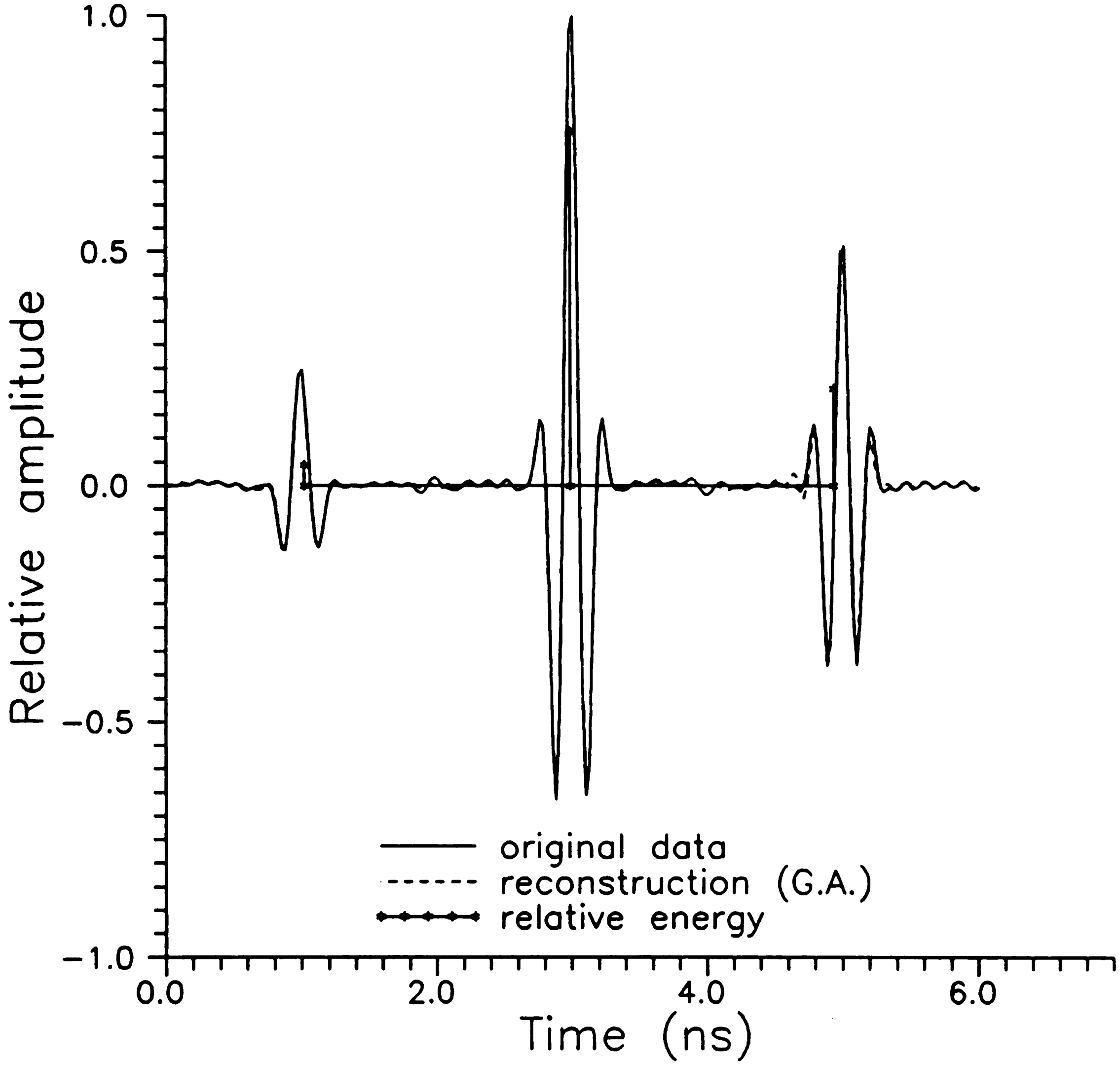

Figure 3.1 Artificial response and reconstructed response using 3 scattering centers, n=-2,...,2, and K=100, L=30, P_c=0.6, P_m=0.03 and 20 generations.

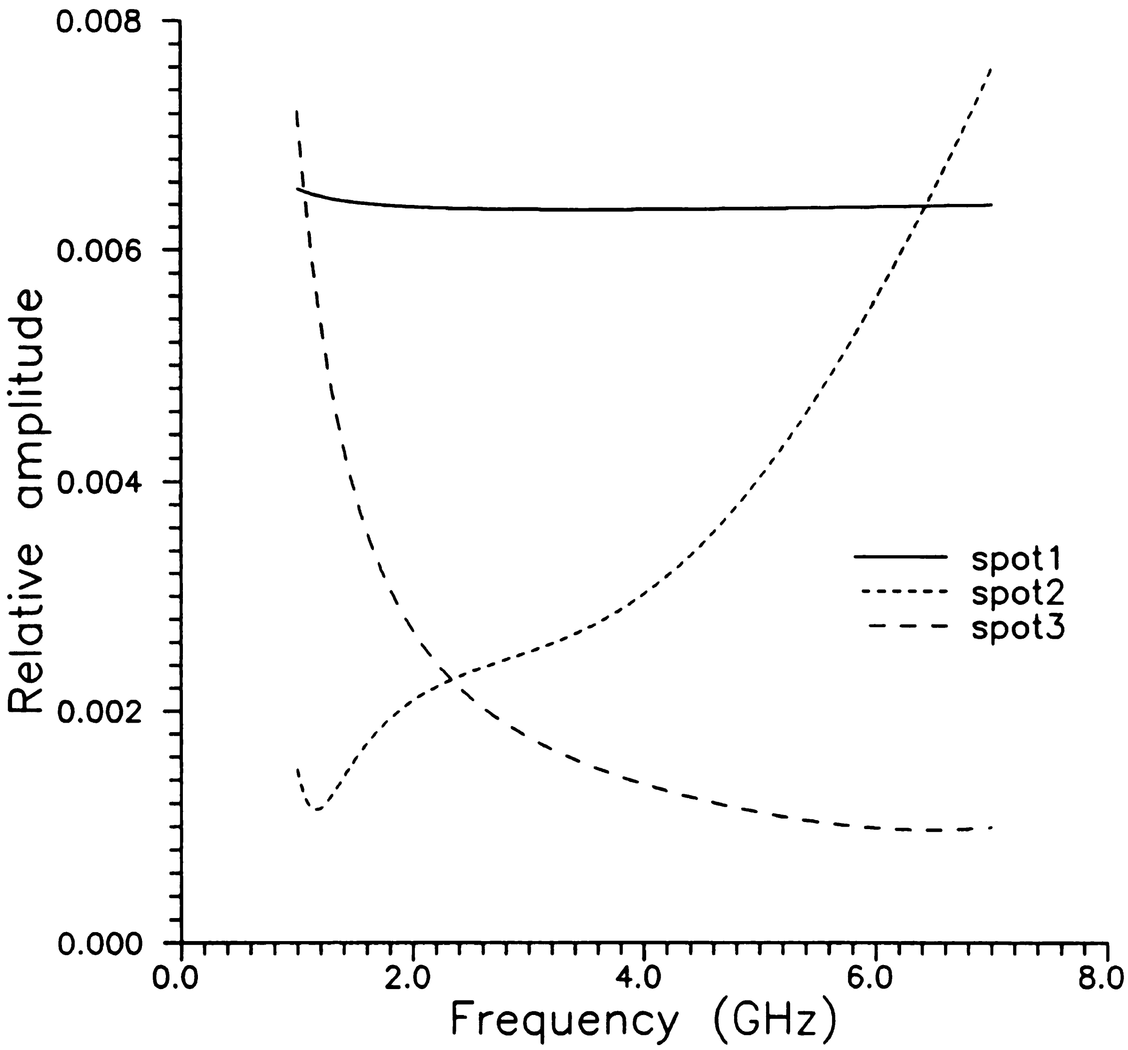

Figure 3.2 Transfer functions of three specular points.

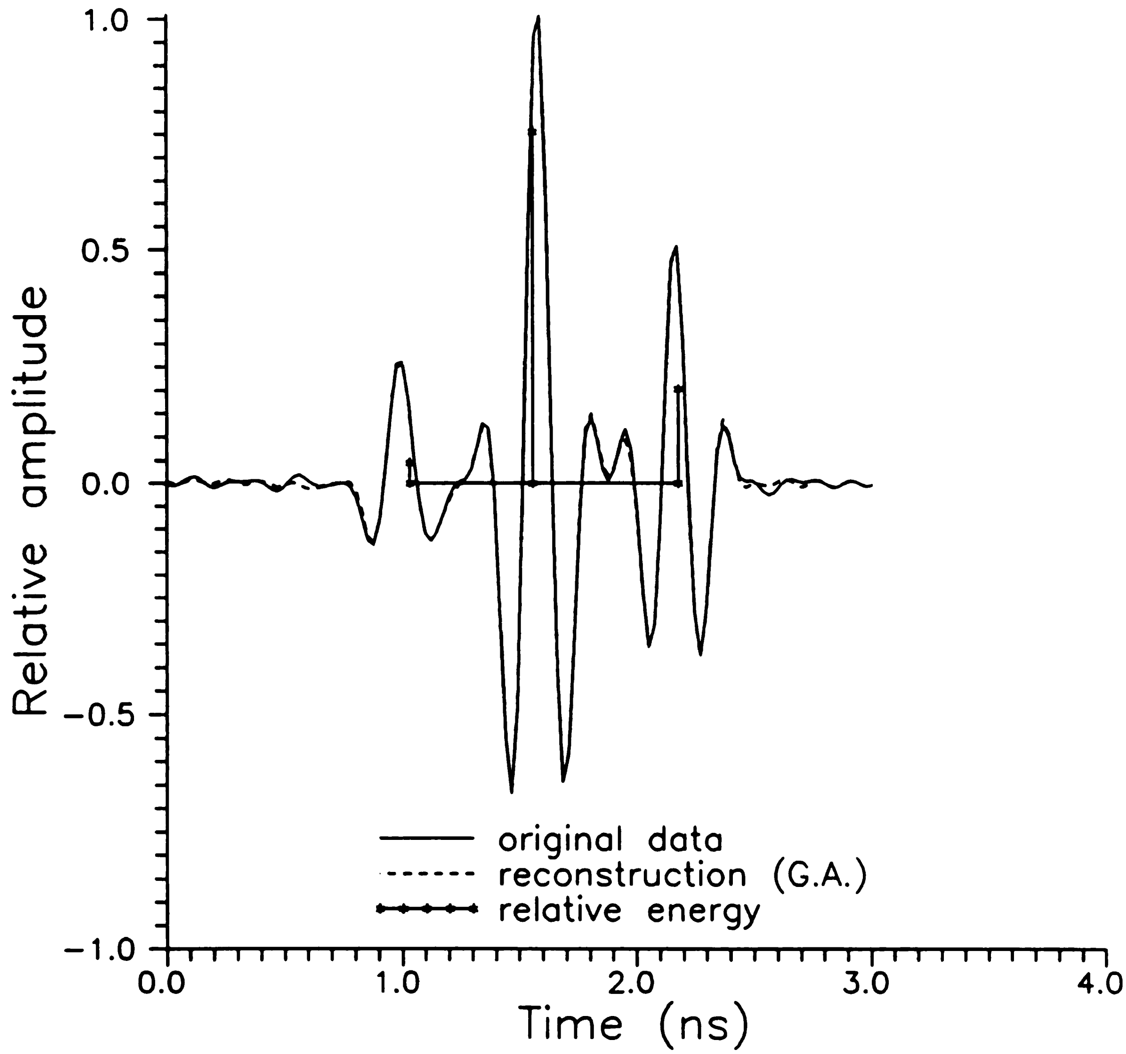

Figure 3.3 Artificial response and reconstructed response using 3 scattering centers, n=-2,...,2, and K=200, L=40, P_c=0.6, P_m=0.03 and 25 generations.

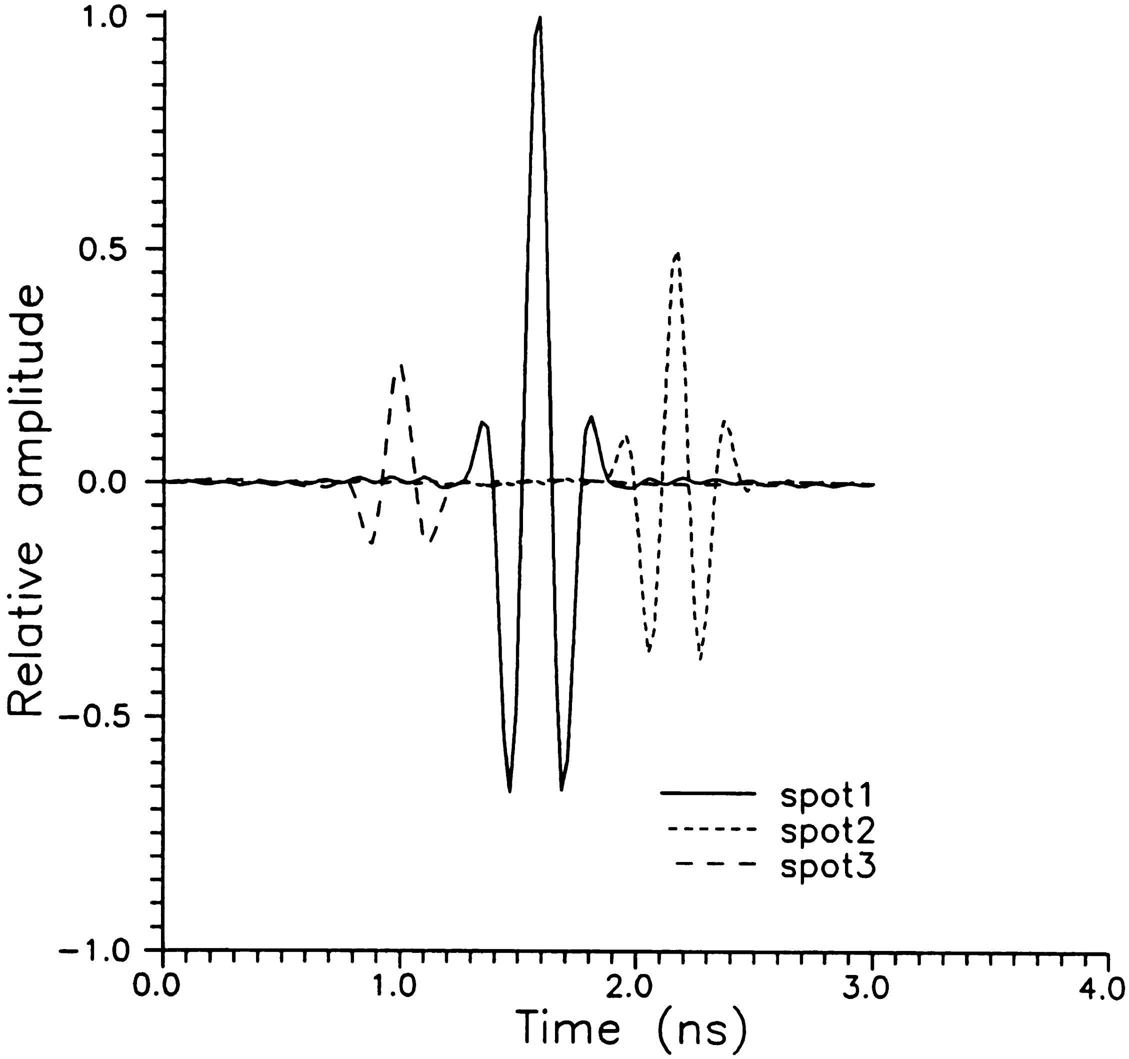

Figure 3.4 Pulse responses of three specular points.

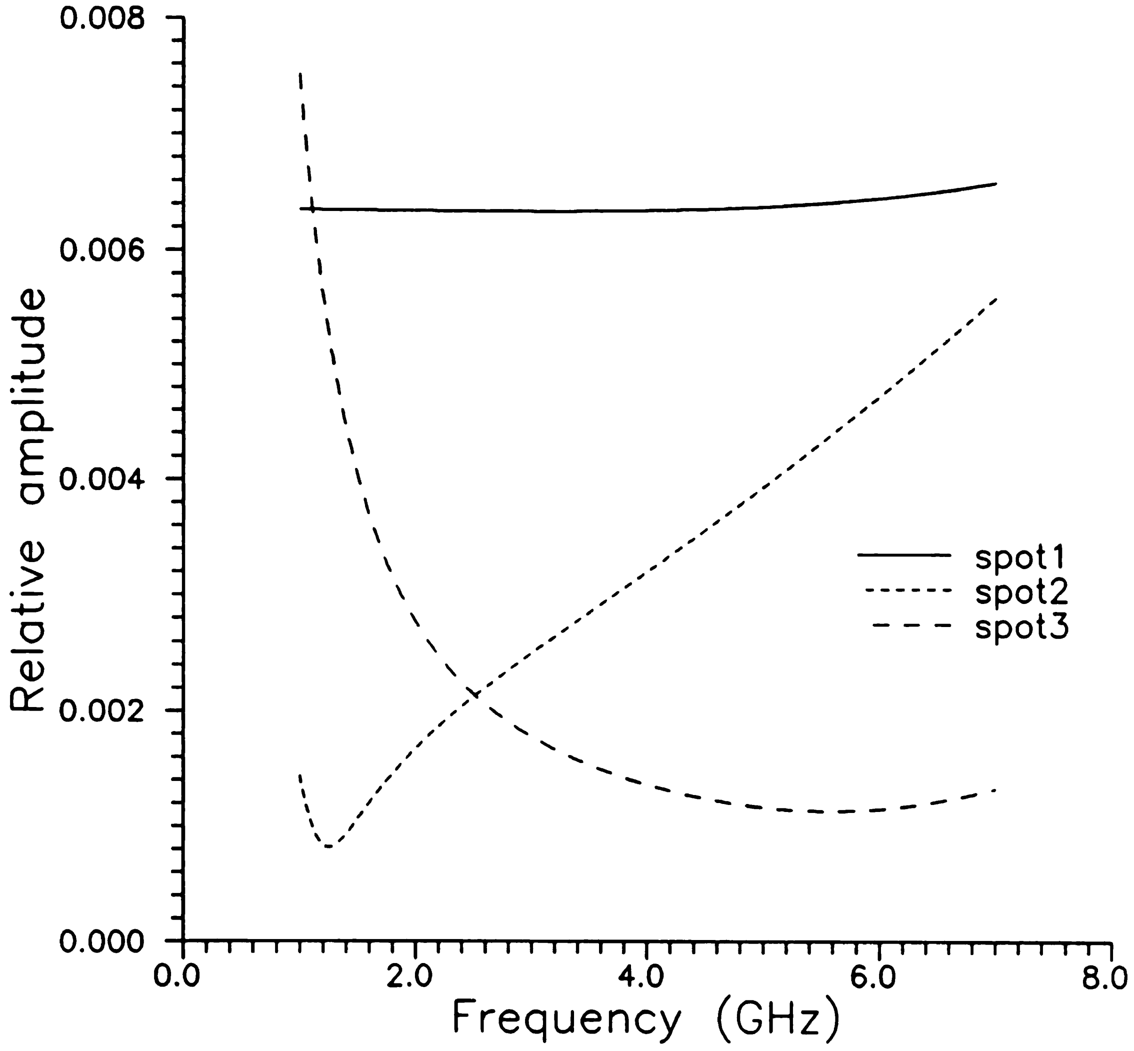

Figure 3.5 Transfer functions of three specular points.

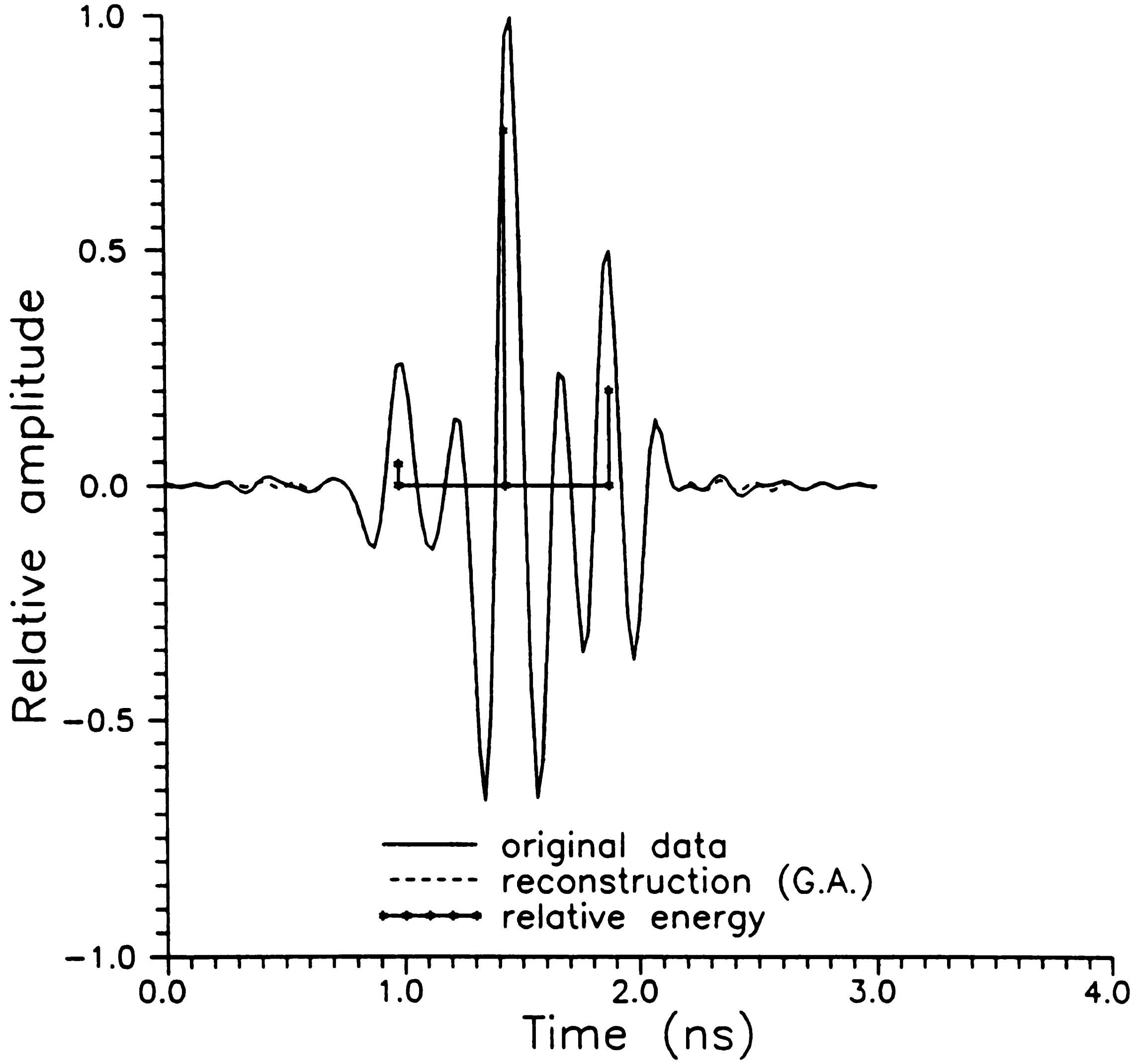

Figure 3.6 Artificial response and reconstructed response using 3 scattering centers, n=-2,...,2, and K=200, L=40, P_c=0.6, P_m=0.03 and 25 generations.

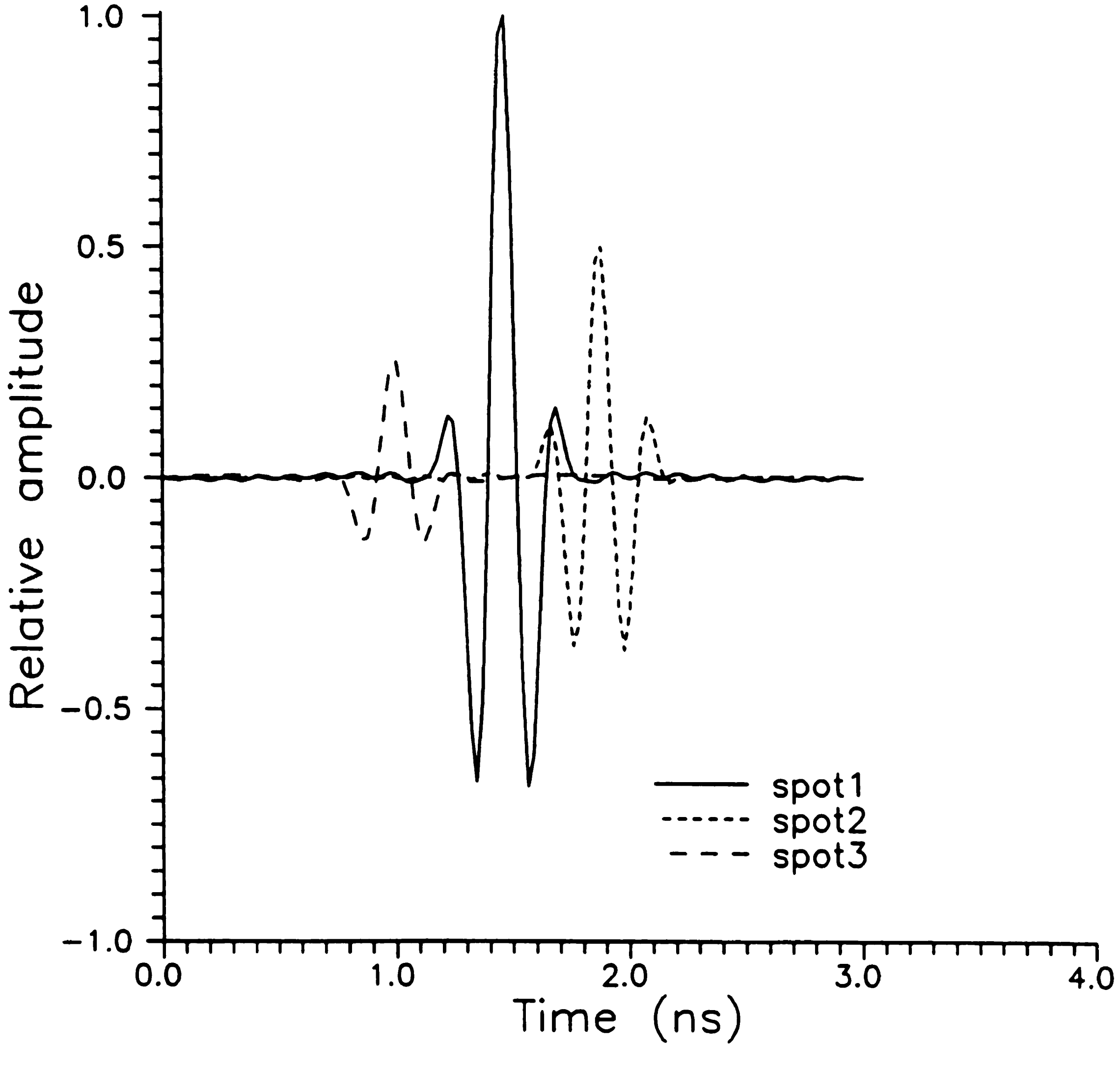

Figure 3.7 Pulse responses of three specular points.

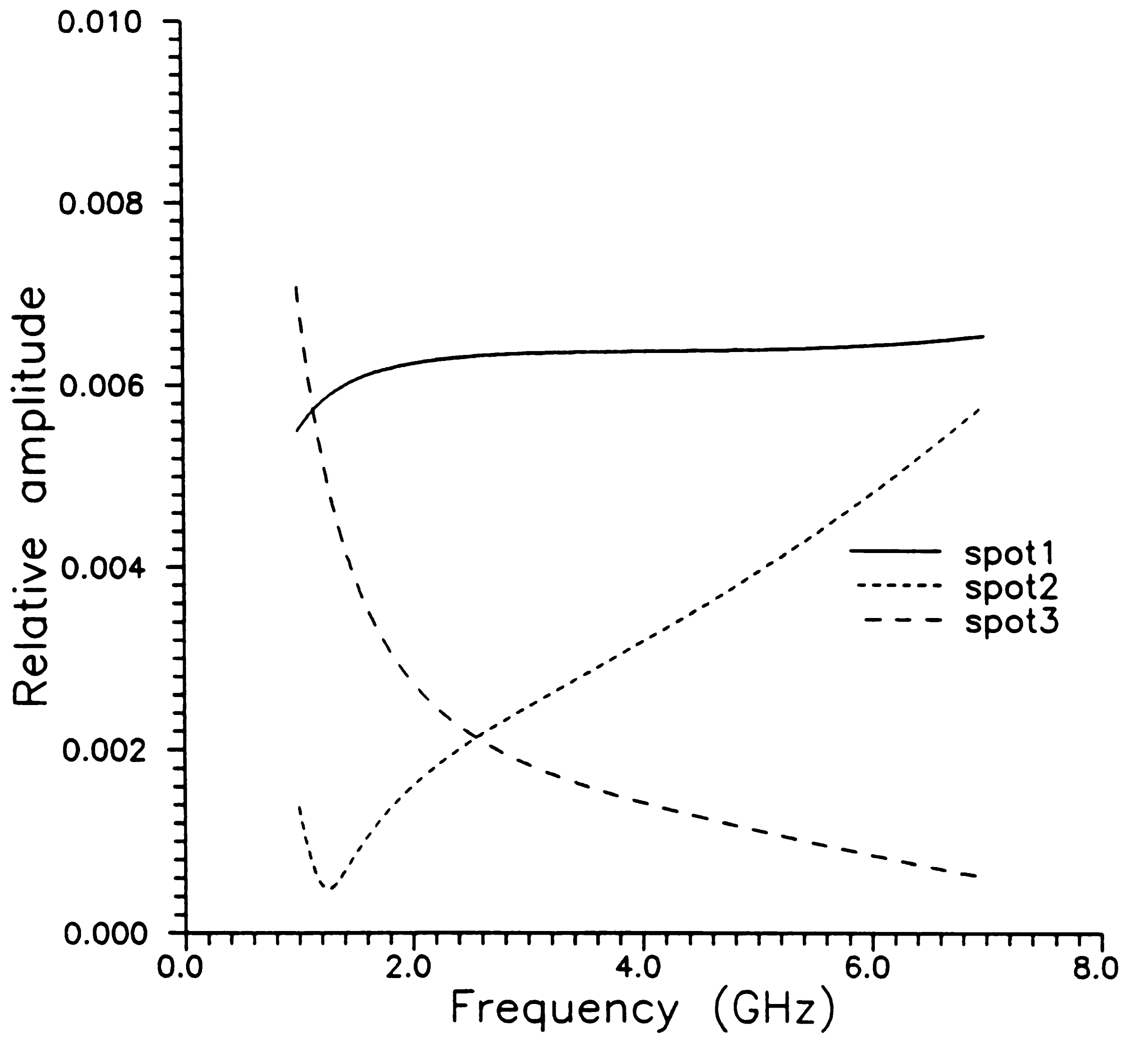

Figure 3.8 Transfer functions of three specular points.

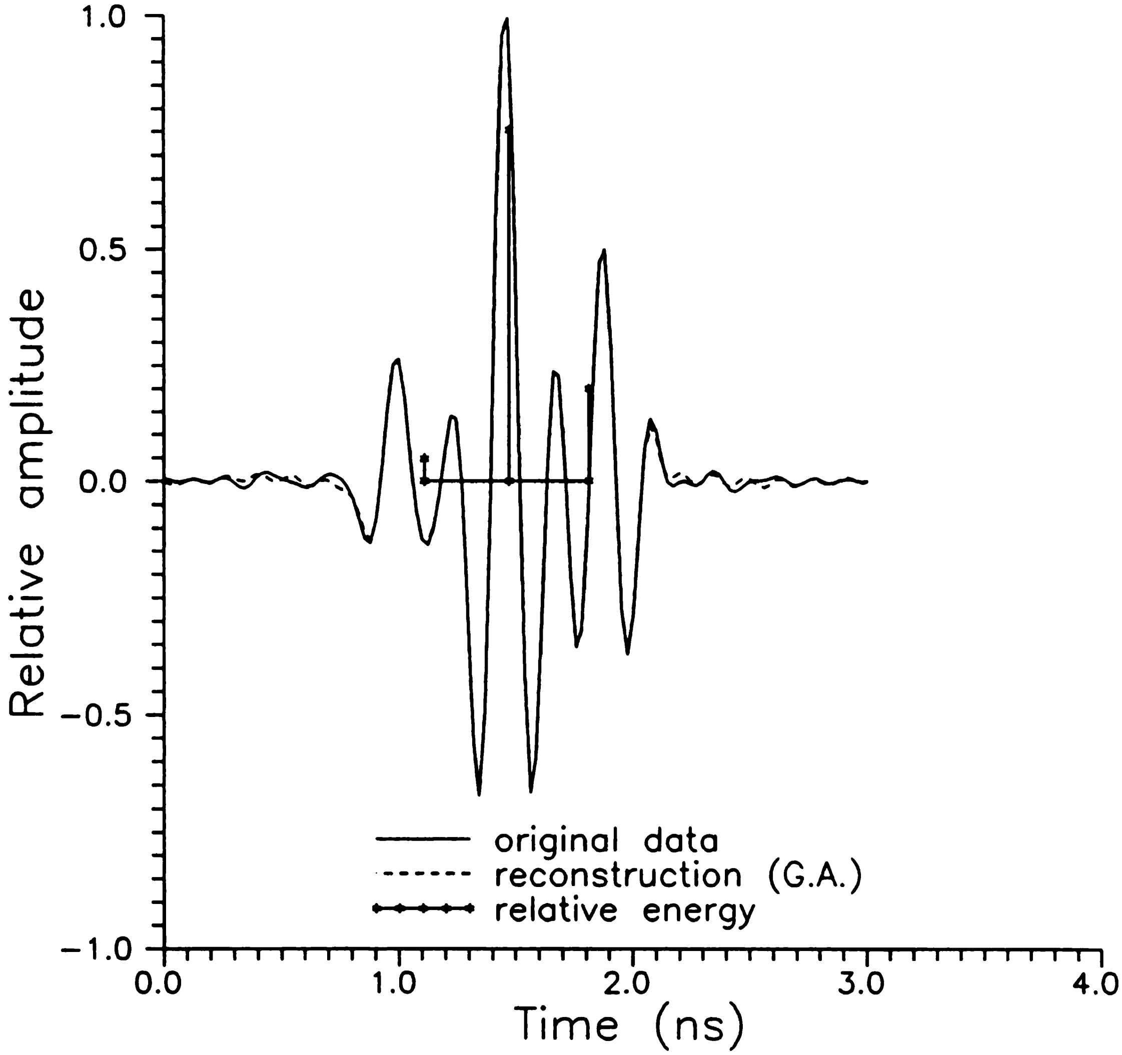

Figure 3.9 Artificial response and reconstructed response using 3 scattering centers, n=-2,...,2, and K=100, L=30, P_c=0.6, P_m=0.03 and 20 generations.

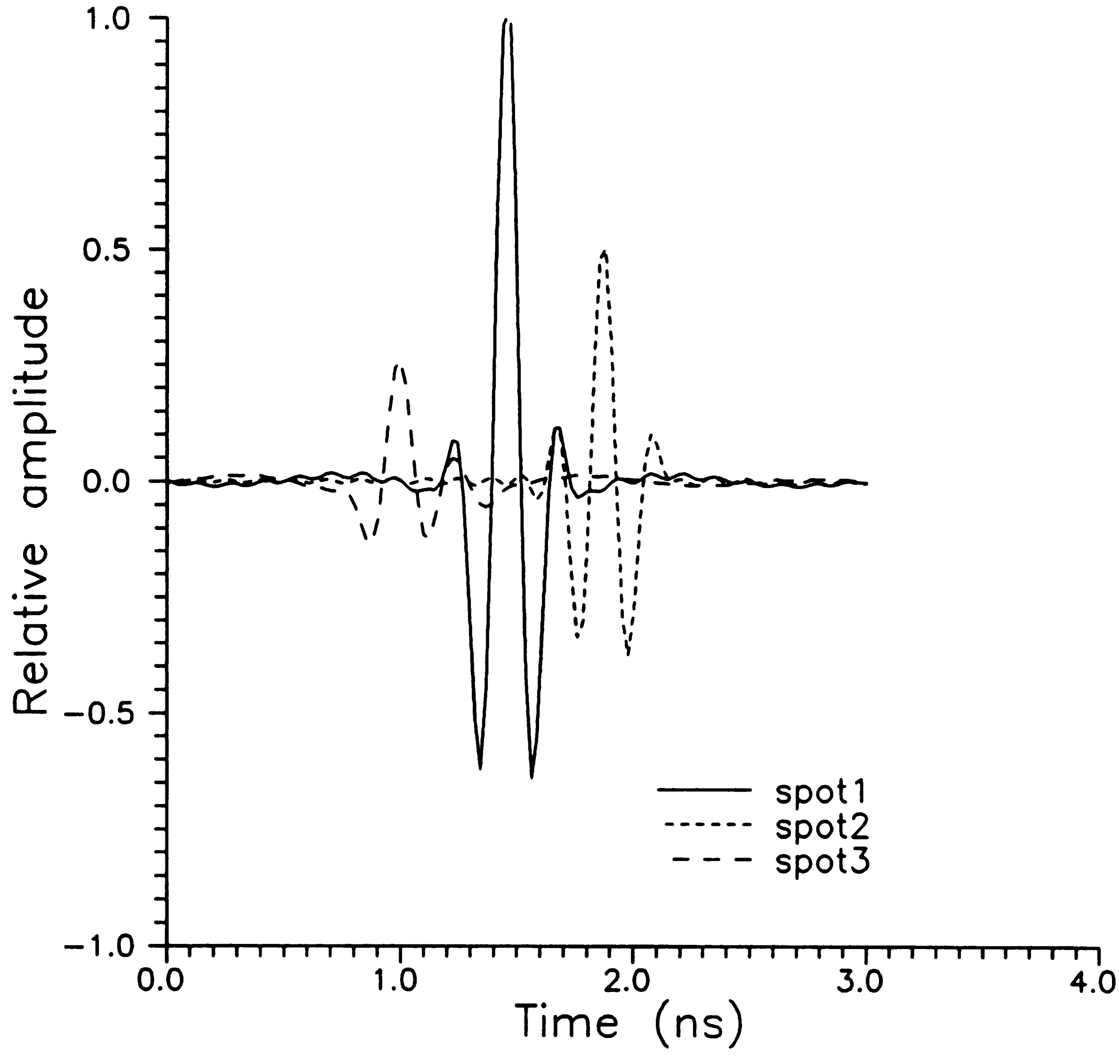

Figure 3.10 Pulse responses of three specular points.

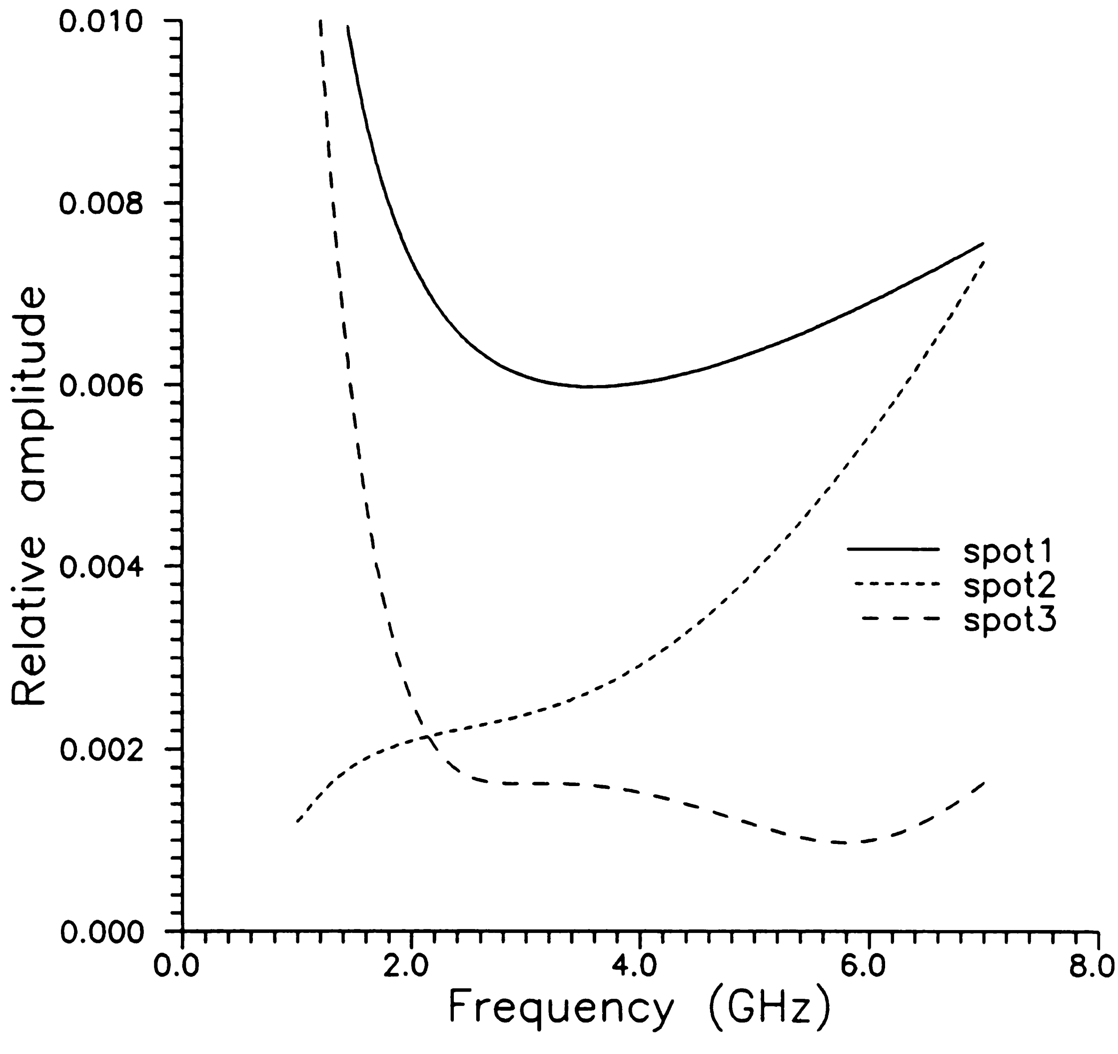

Figure 3.11 Transfer functions of three specular points.

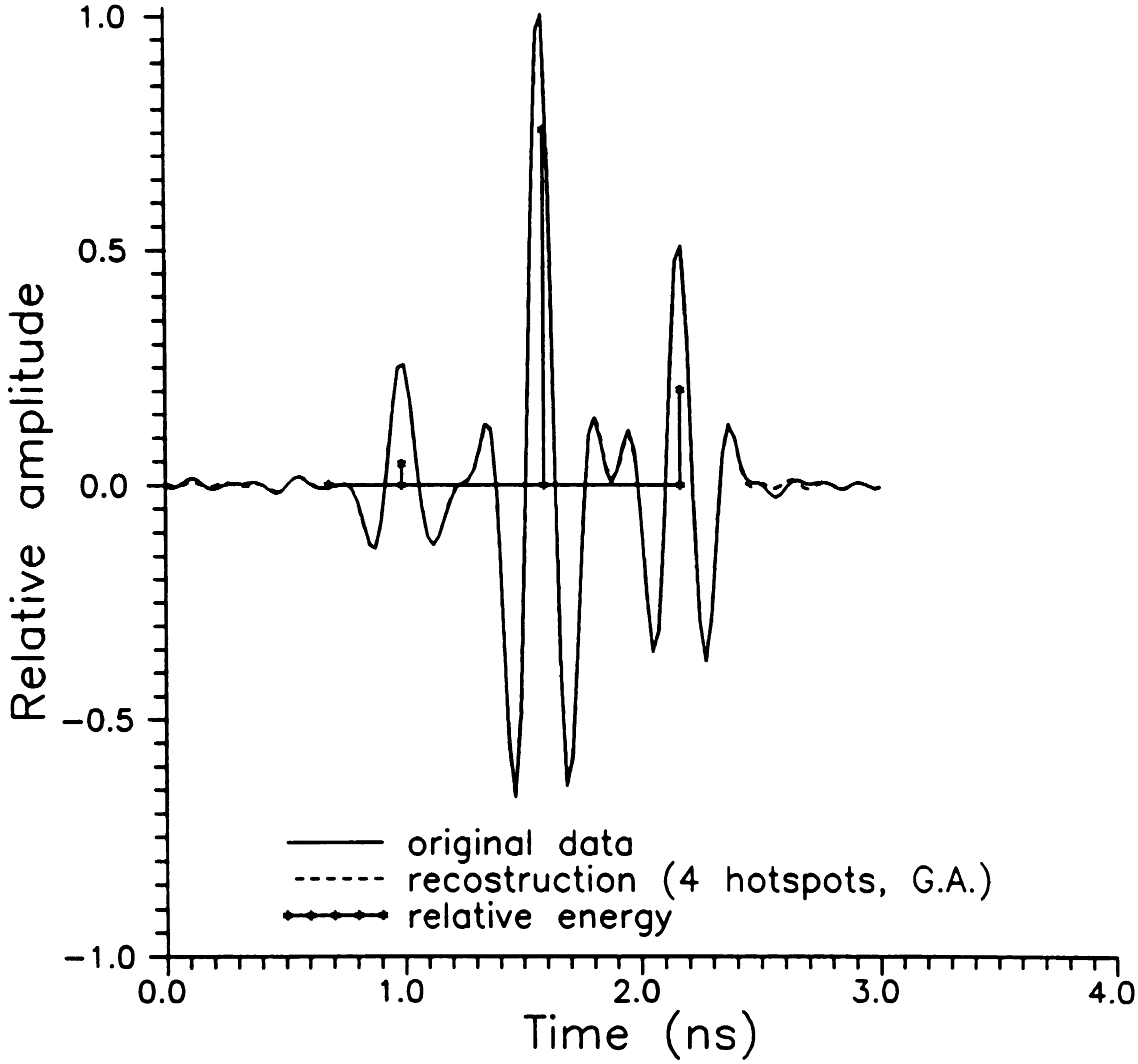

Figure 3.12 Artificial response and reconstructed response using 4 scattering centers, n=-2,...,2, and K=200, L=40, P_c=0.6, P_m=0.03 and 25 generations.

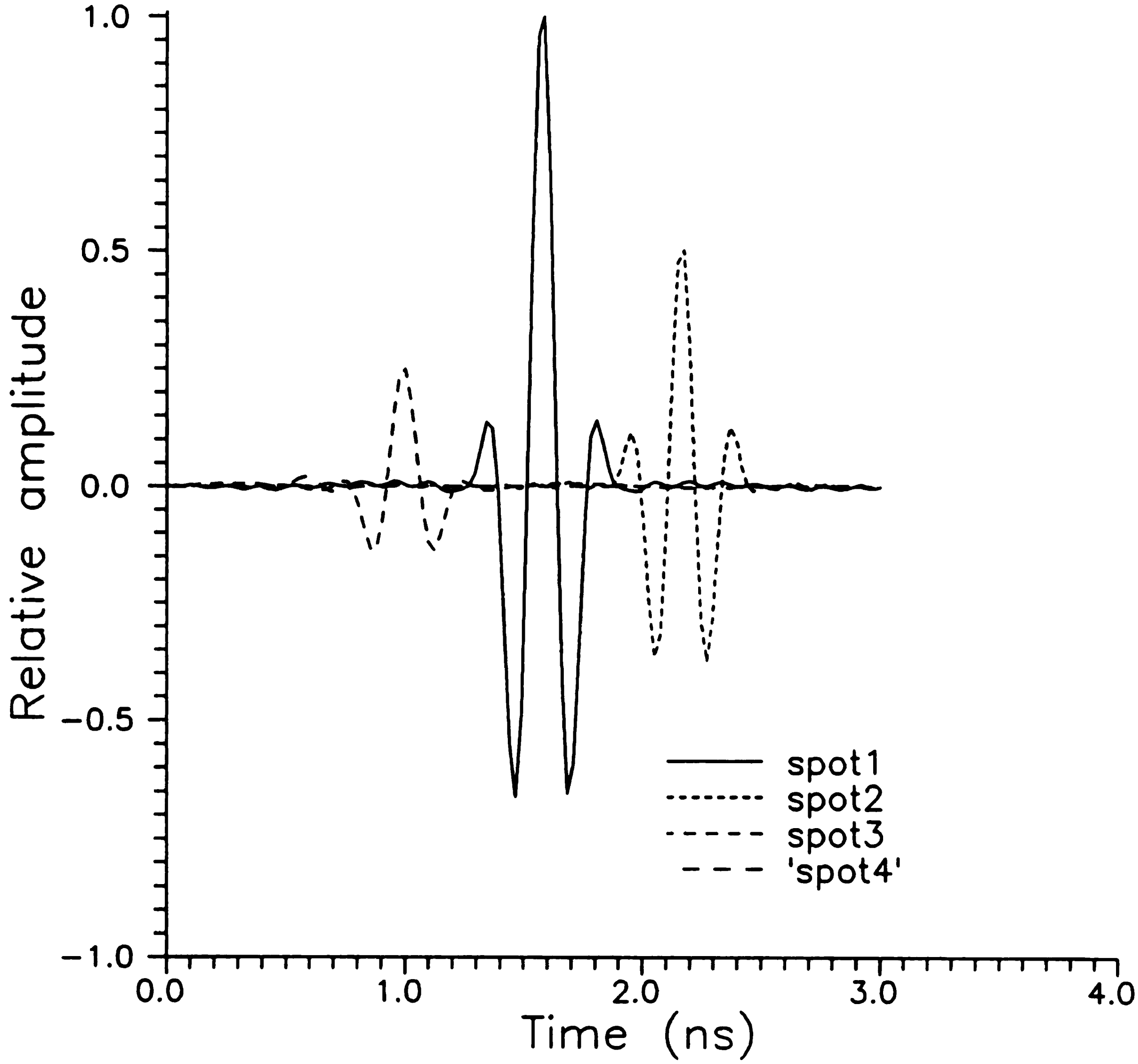

Figure 3.13 Pulse responses of four specular points.

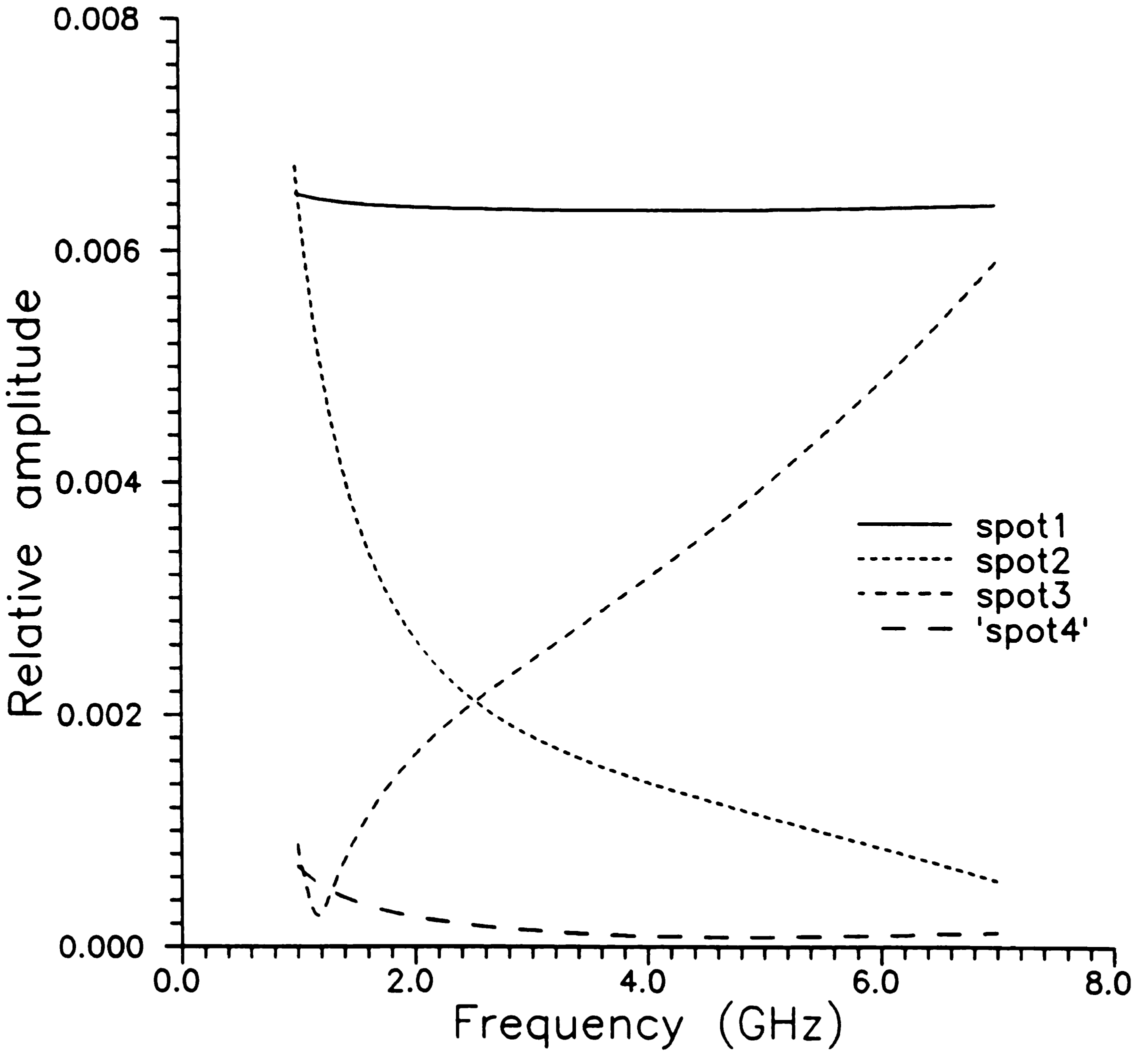

Figure 3.14 Transfer functions of four specular points.

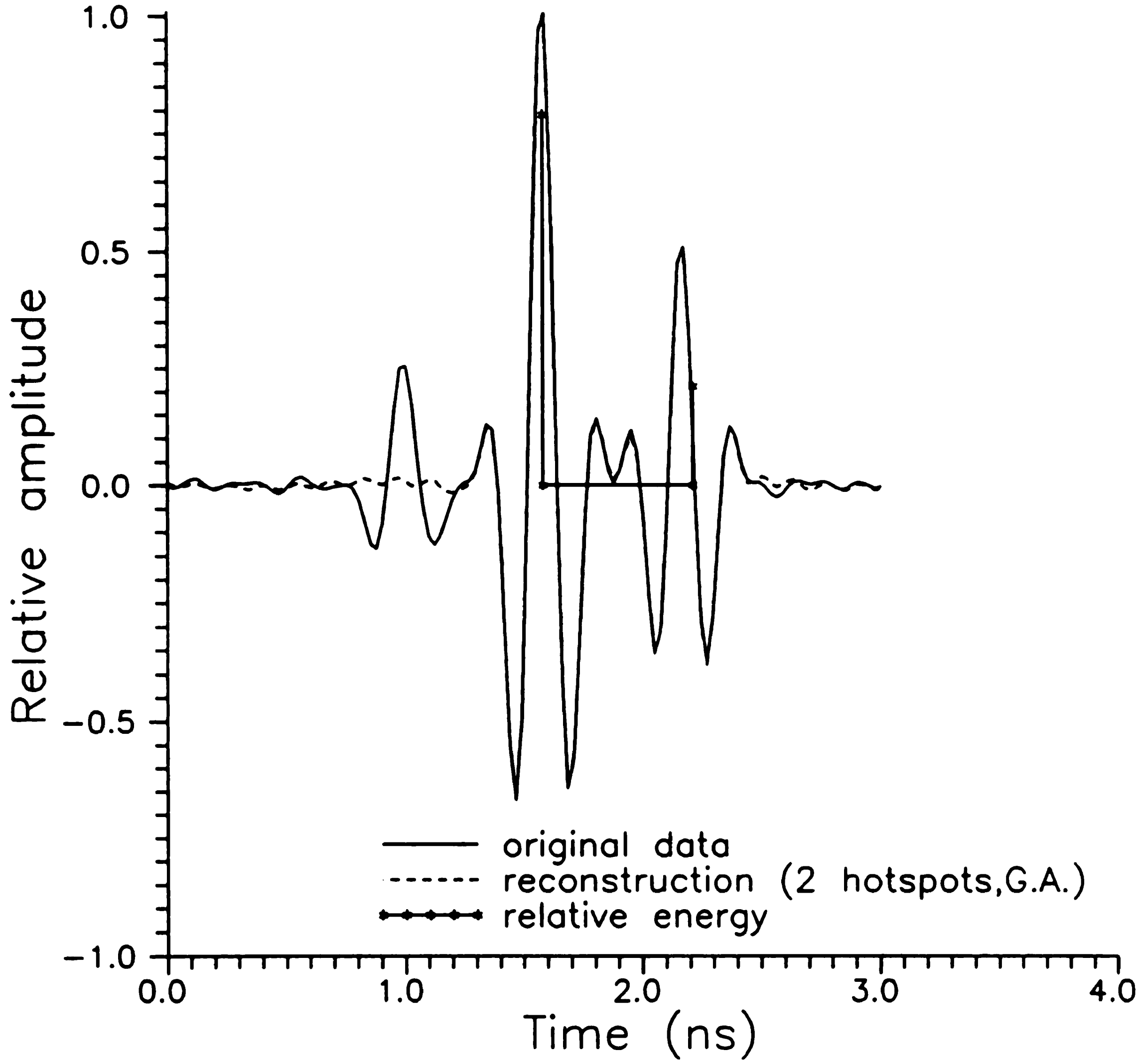

Figure 3.15 Artificial response and reconstructed response using 2 scattering centers, n=-2,...,2, and K=200, L=40, P_c=0.6, P_m=0.03 and 25 generations.

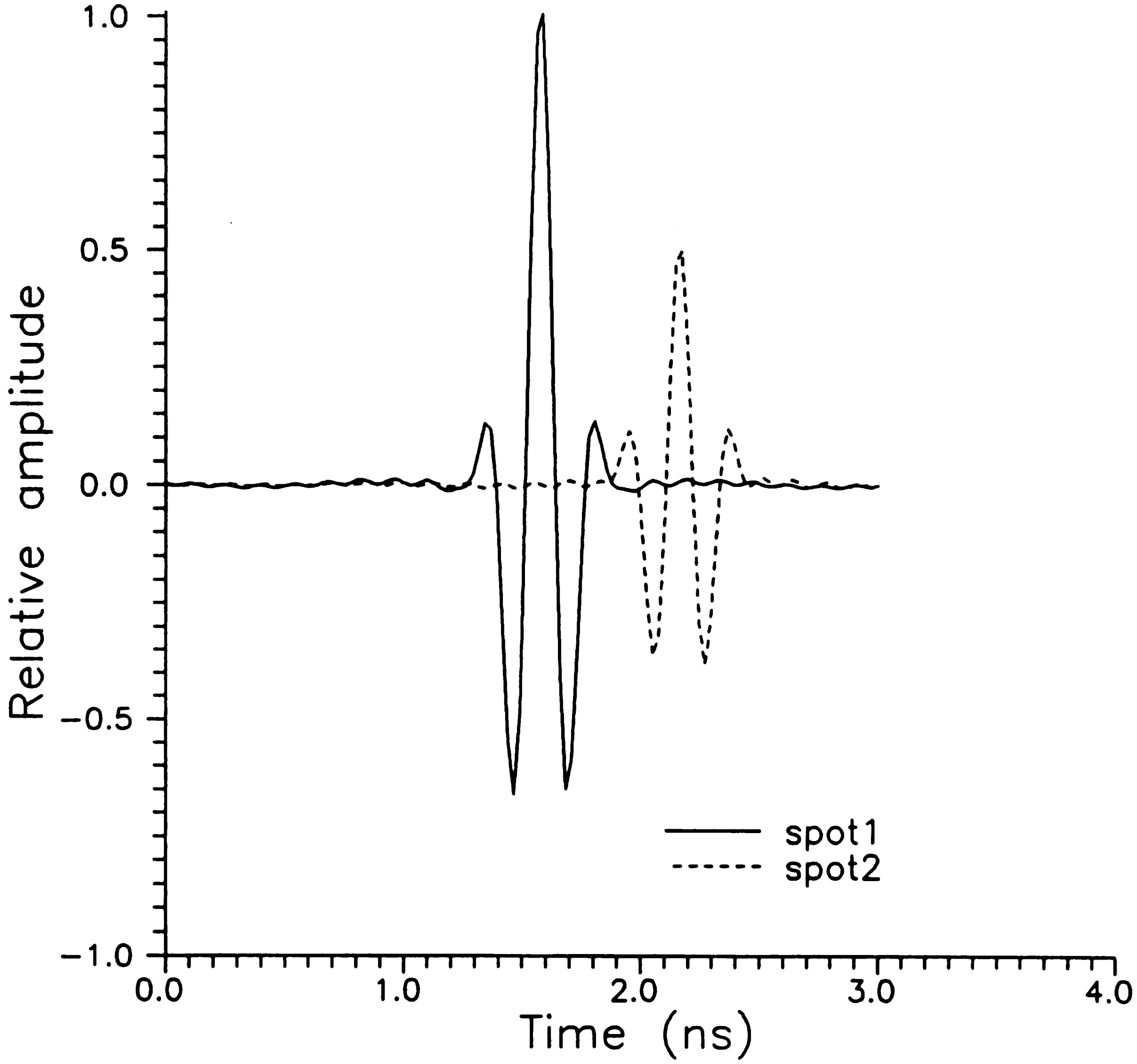

Figure 3.16 Pulse responses of two specular points.

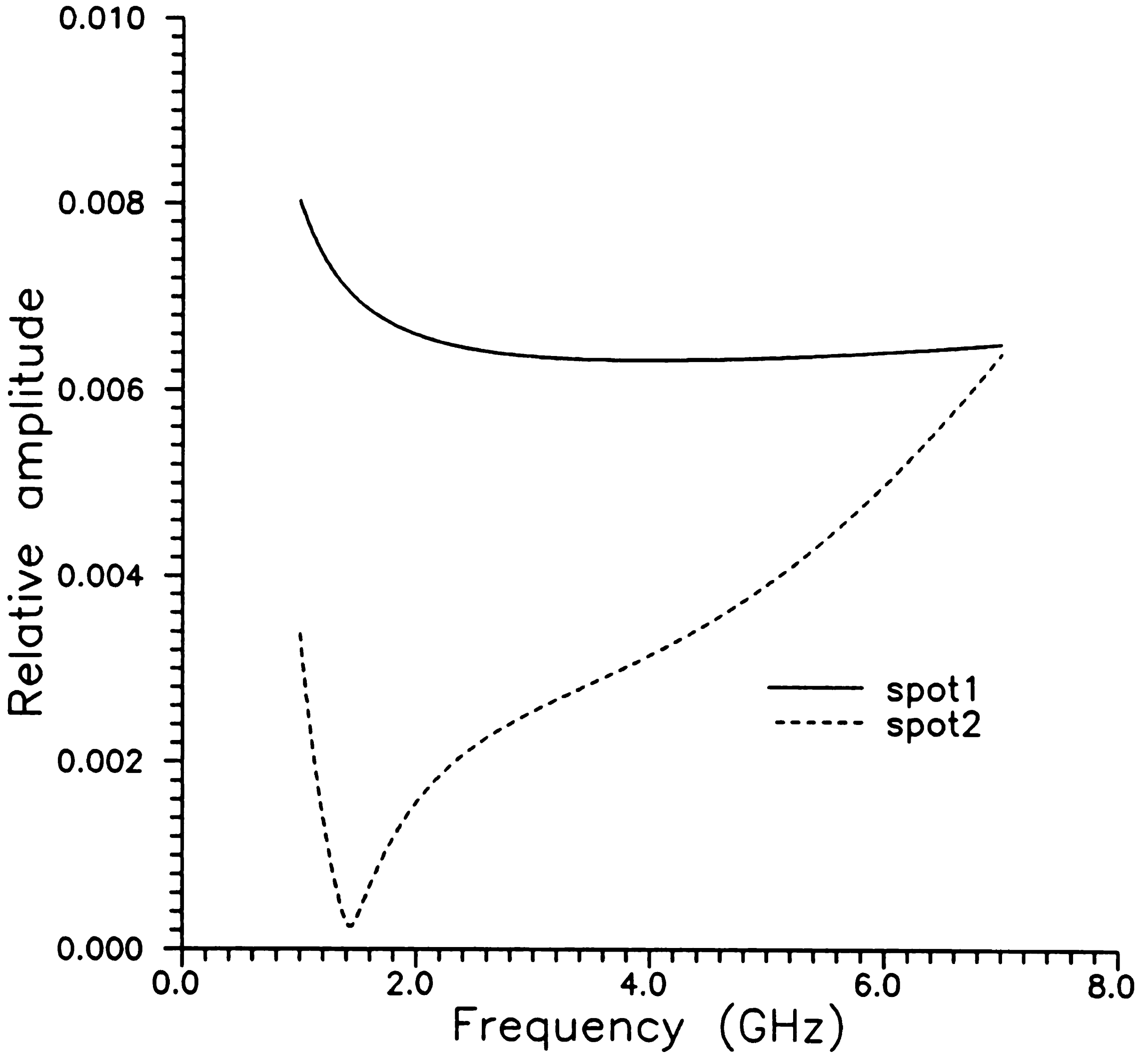

Figure 3.17 Transfer functions of two specular points.

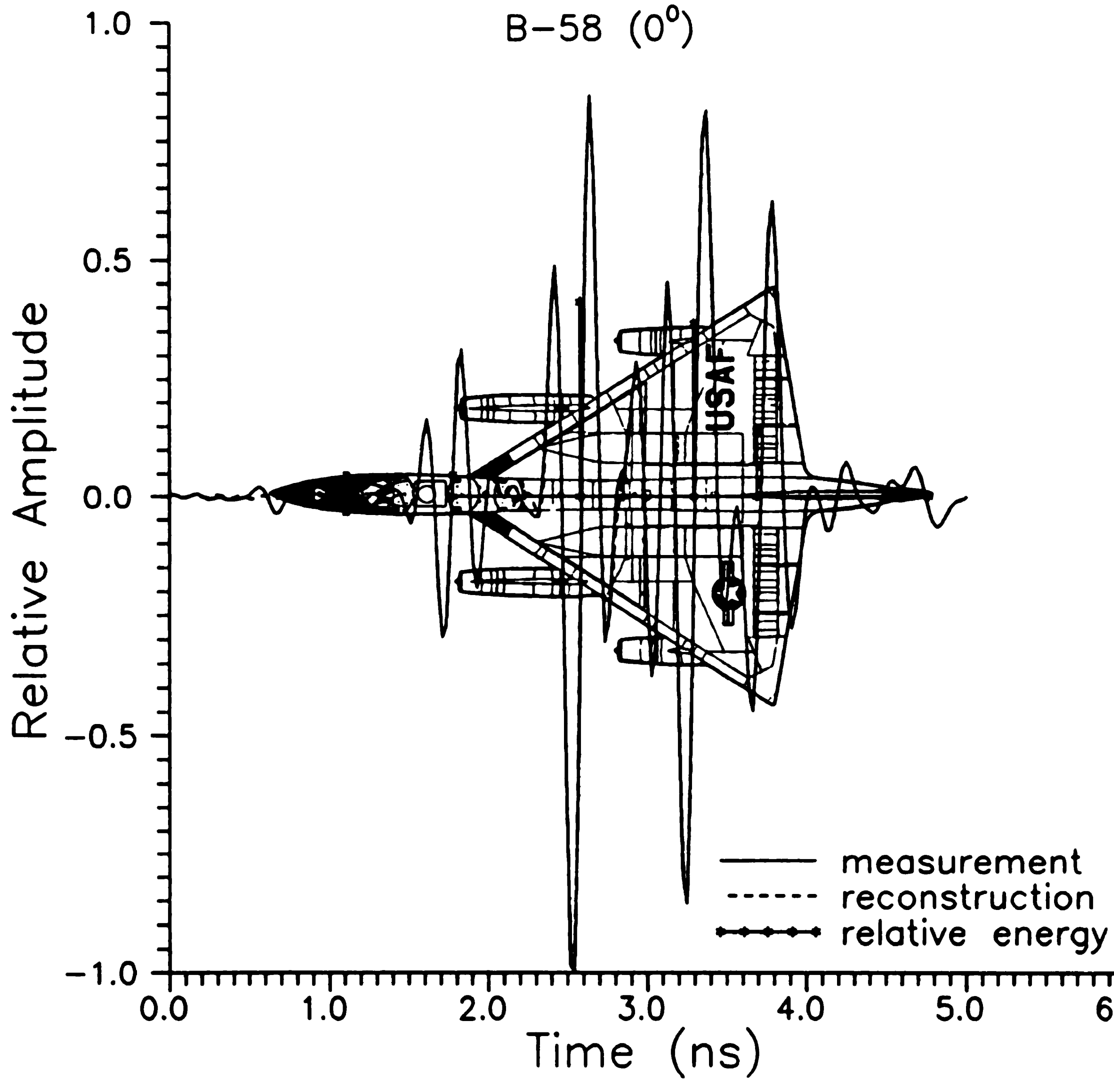

Figure 3.18 Response of 0^0 B-58 measured in the band 1-7 GHz, and reconstructed response using genetic algorithm, and n=-2,-1,...,2, and K=600, L=80, and 30 generations.

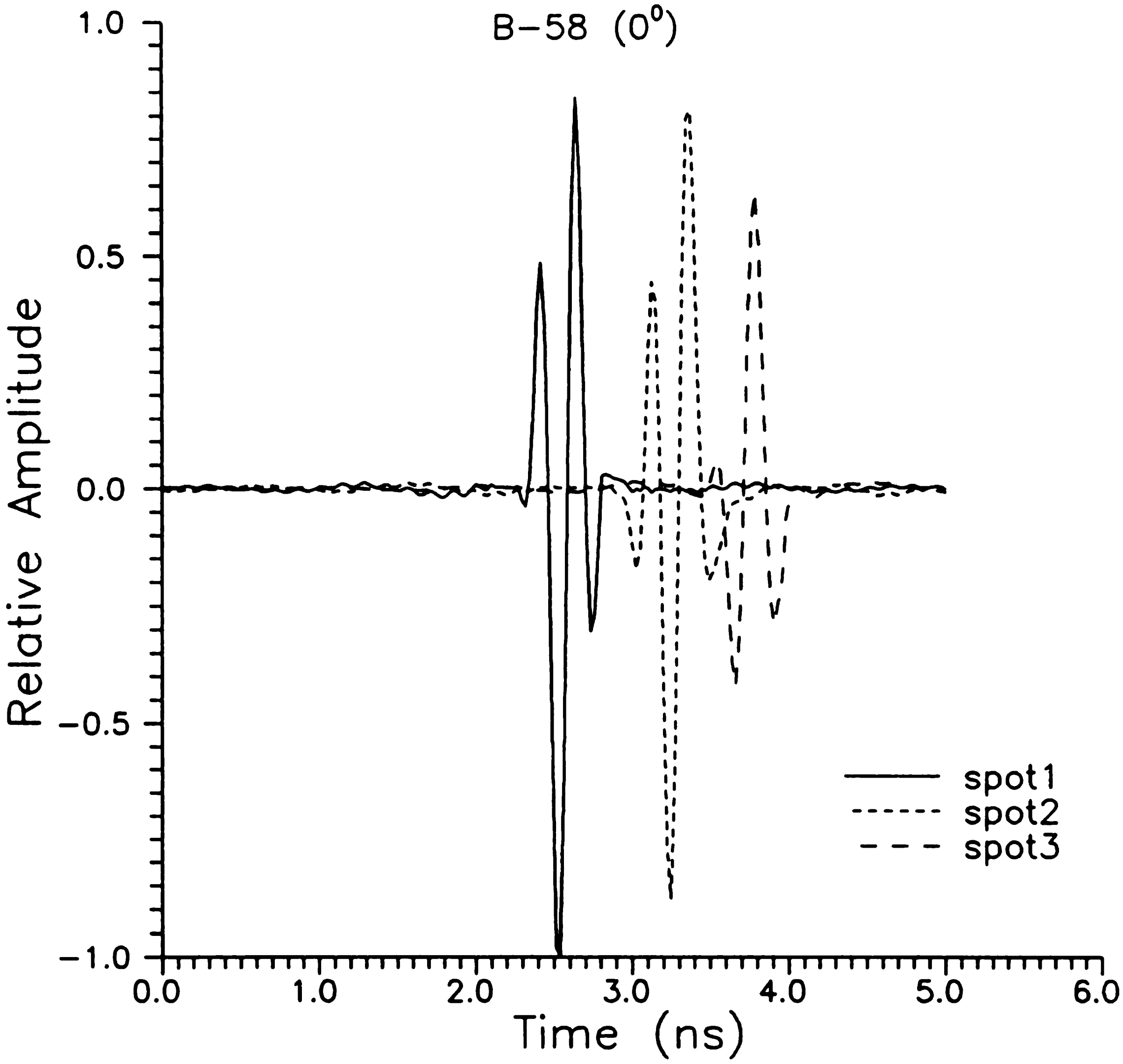

Figure 3.19 Pulse responses of 1st, 2nd, and 3rd specular points obtained using genetic algorithm.

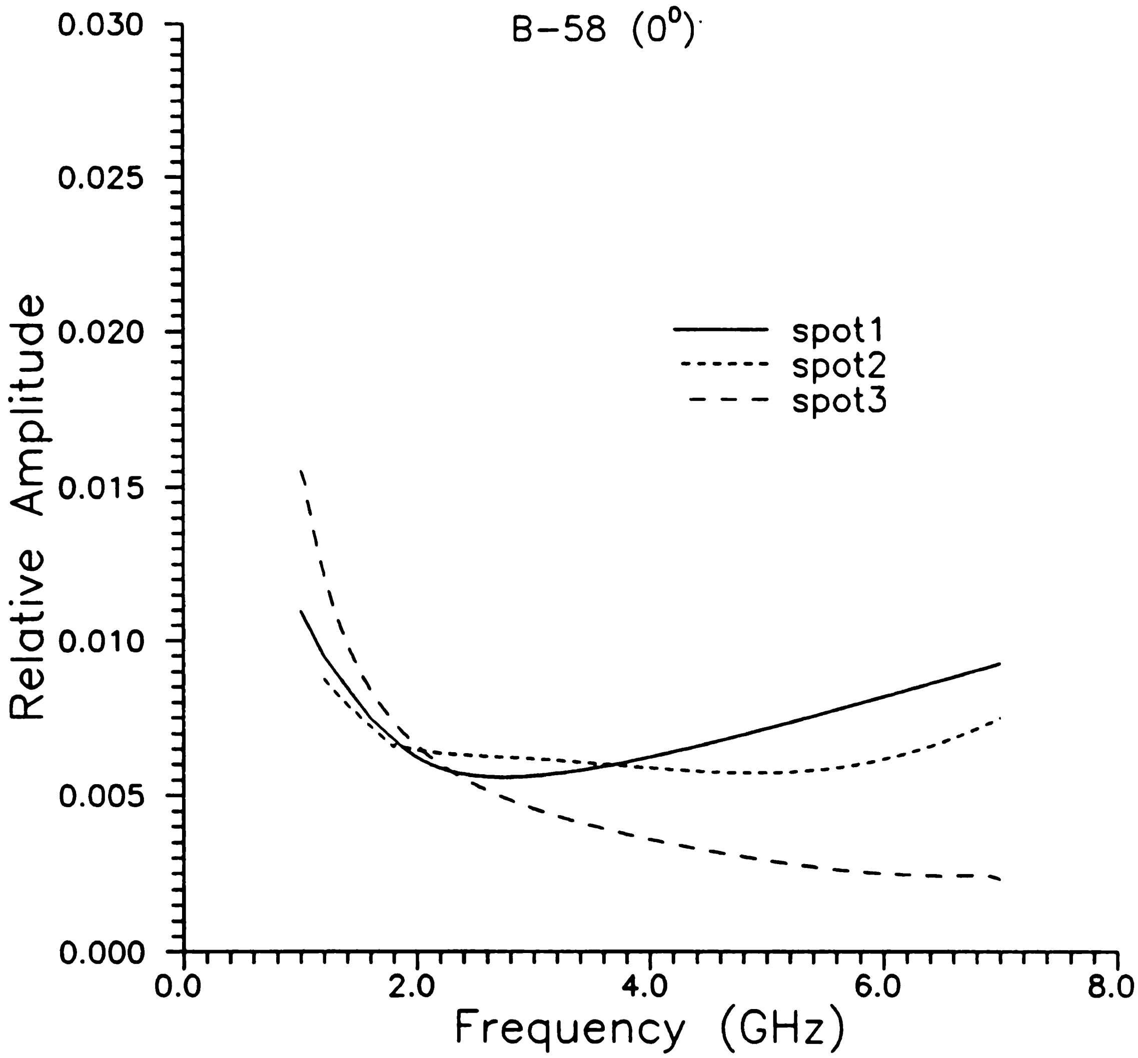

Figure 3.20 Transfer functions of 1st, 2nd, and 3rd specular points obtained using genetic algorithm.

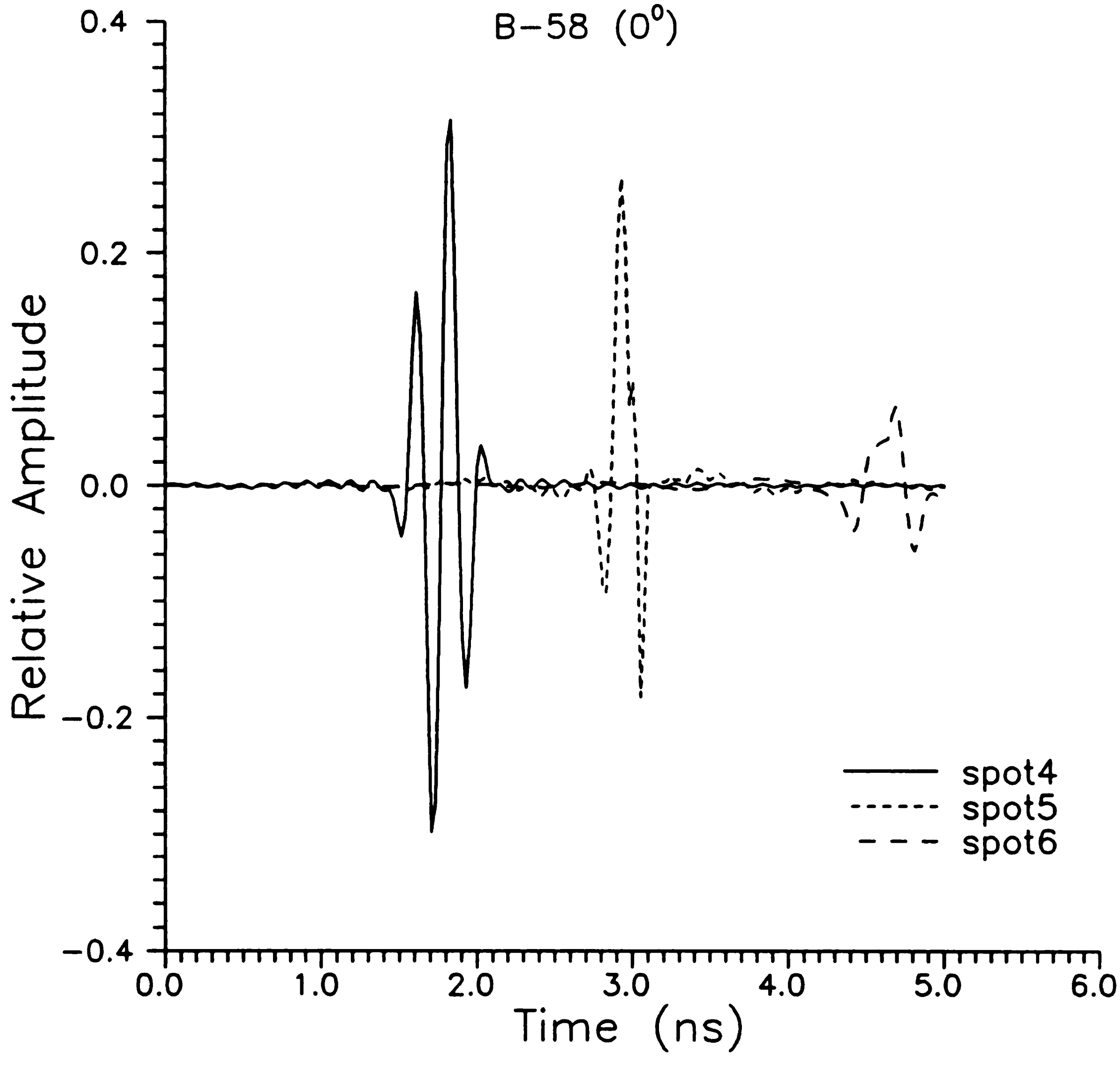

Figure 3.21 Pulse responses of 4th, 5th, and 6th specular points obtained using genetic algorithm.

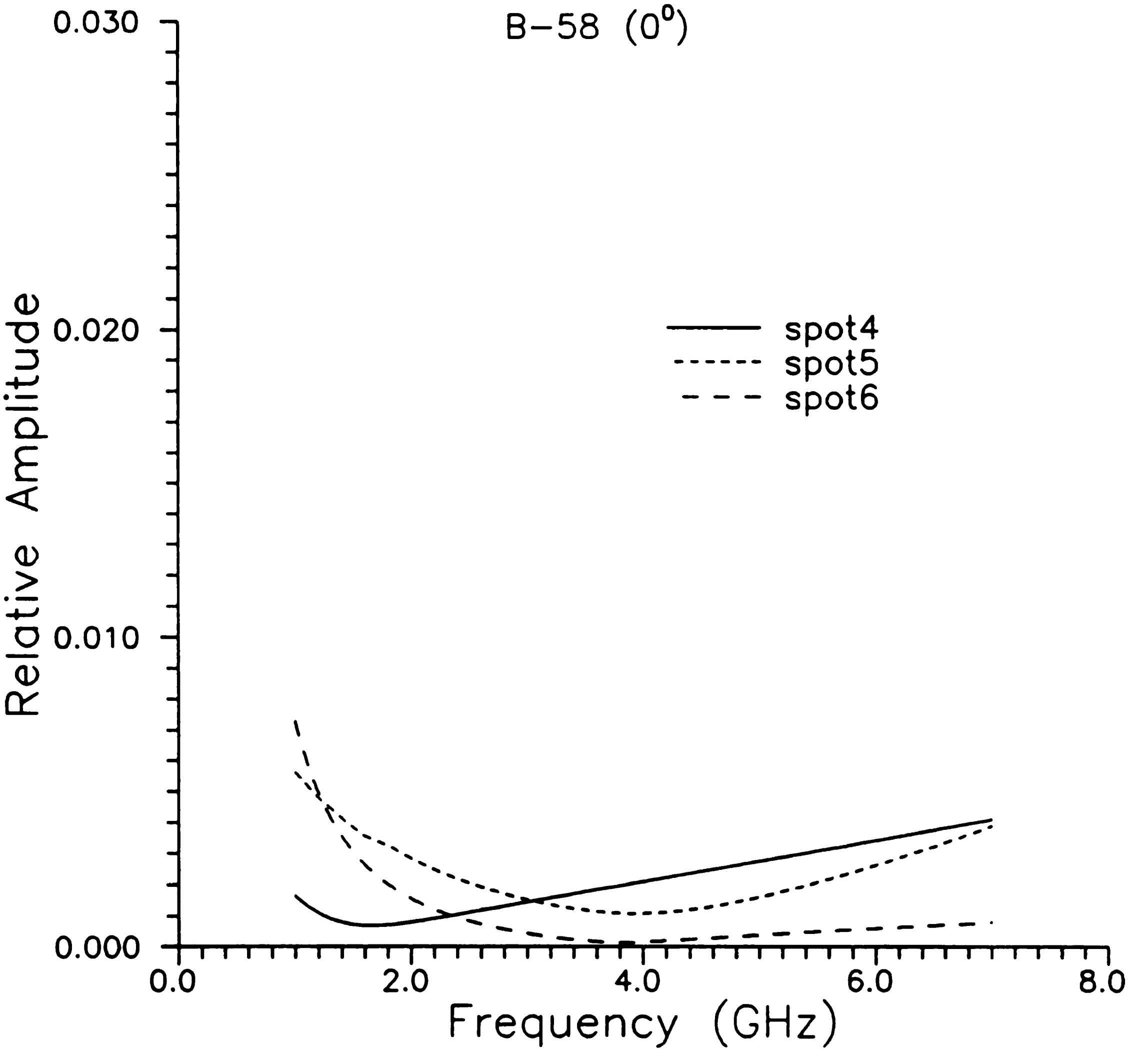

Figure 3.22 Transfer functions of 4th, 5th, and 6th specular points obtained using genetic algorithm.

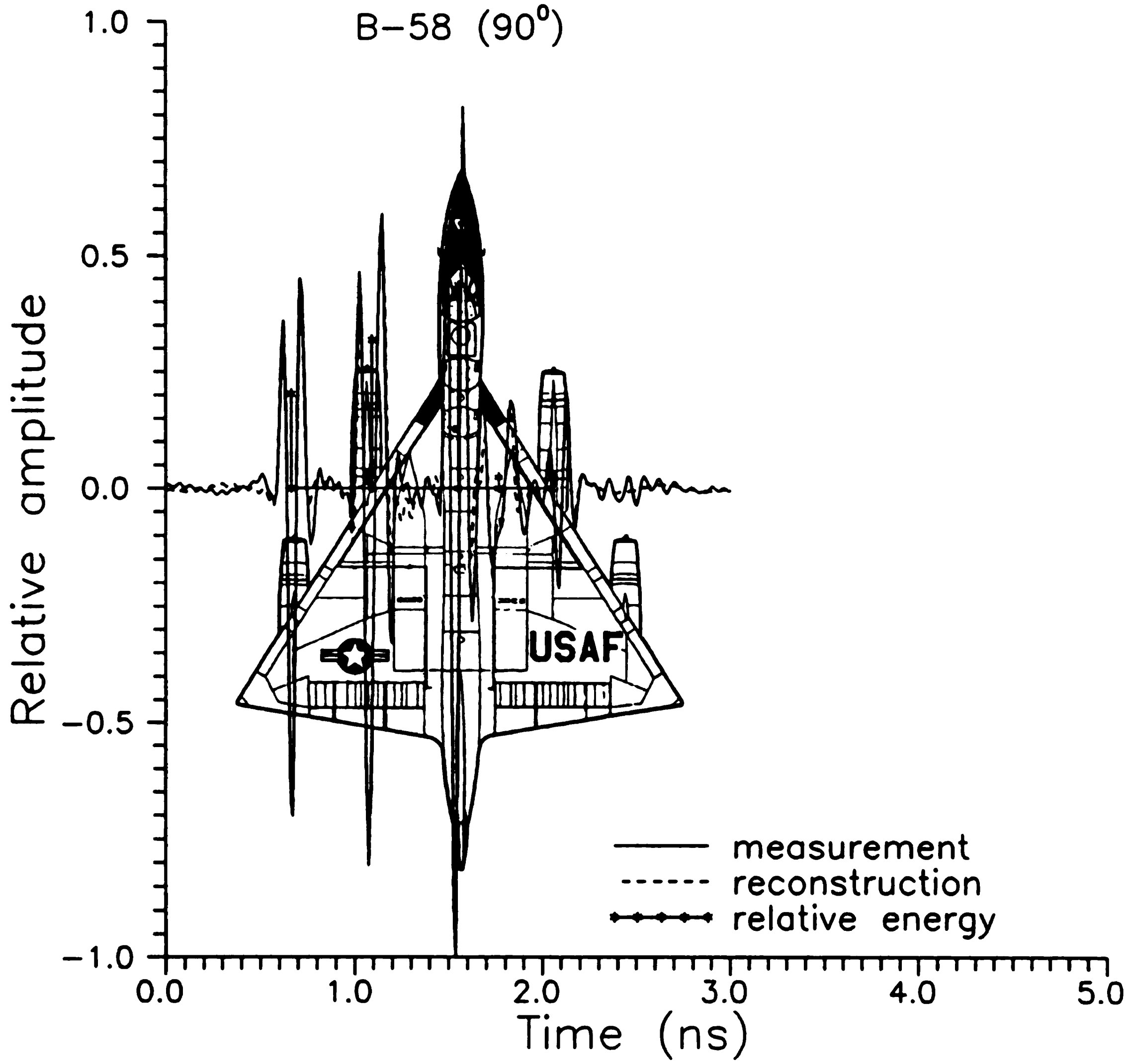

Figure 3.23 Response of 90° B-58 measured in the band 2-18 GHz, and reconstructed response using genetic algorithm, and n=-2,-1,...,2, and K=600, L=80, and 30 generations.

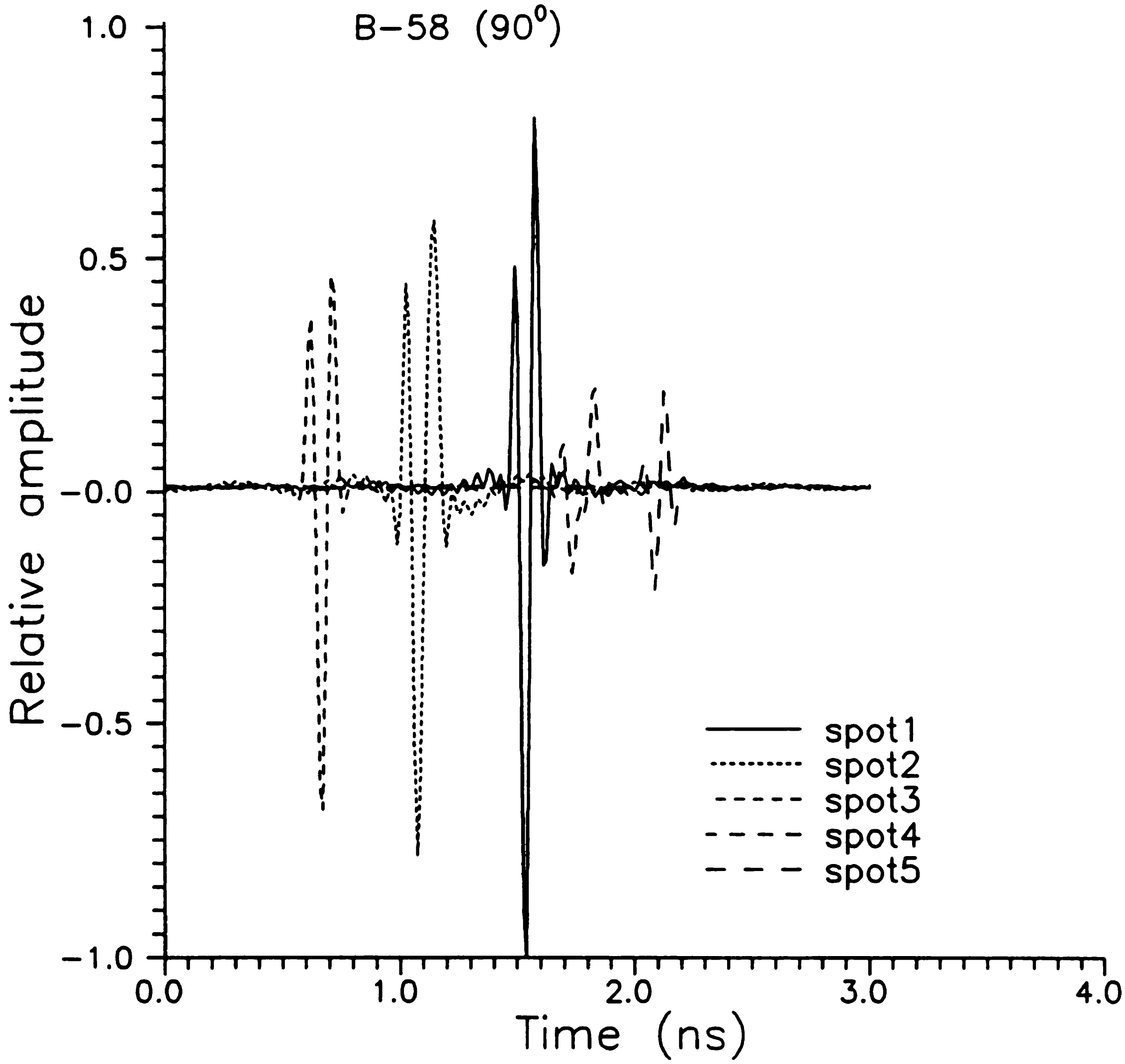

Figure 3.24 Pulse responses of 1st, 2nd, 3rd, 4th, and 5th specular points obtained using genetic algorithm.

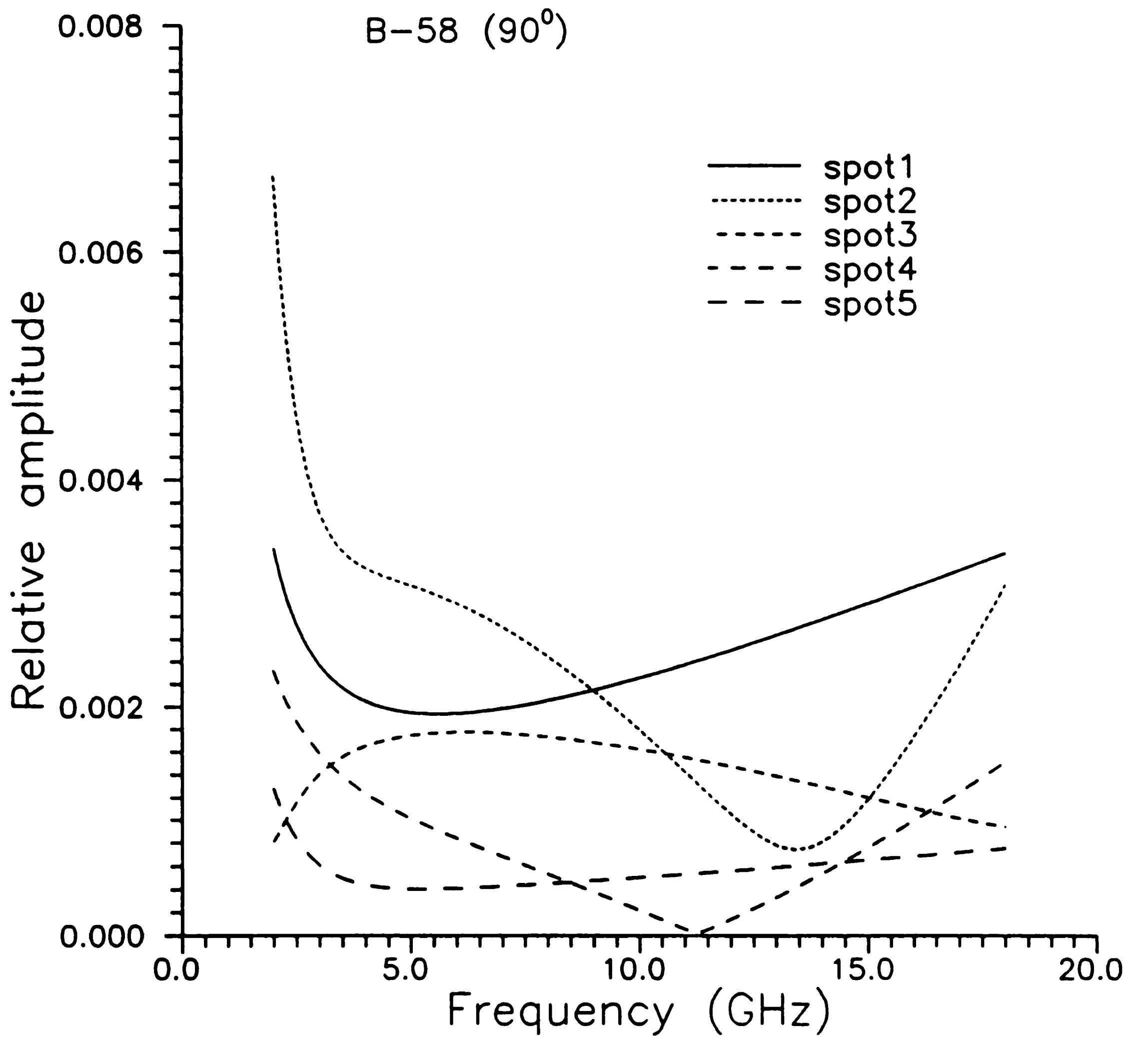

Figure 3.25 Transfer functions of 1st, 2nd, 3rd, 4th, and 5th specular points obtained using genetic algorithm.

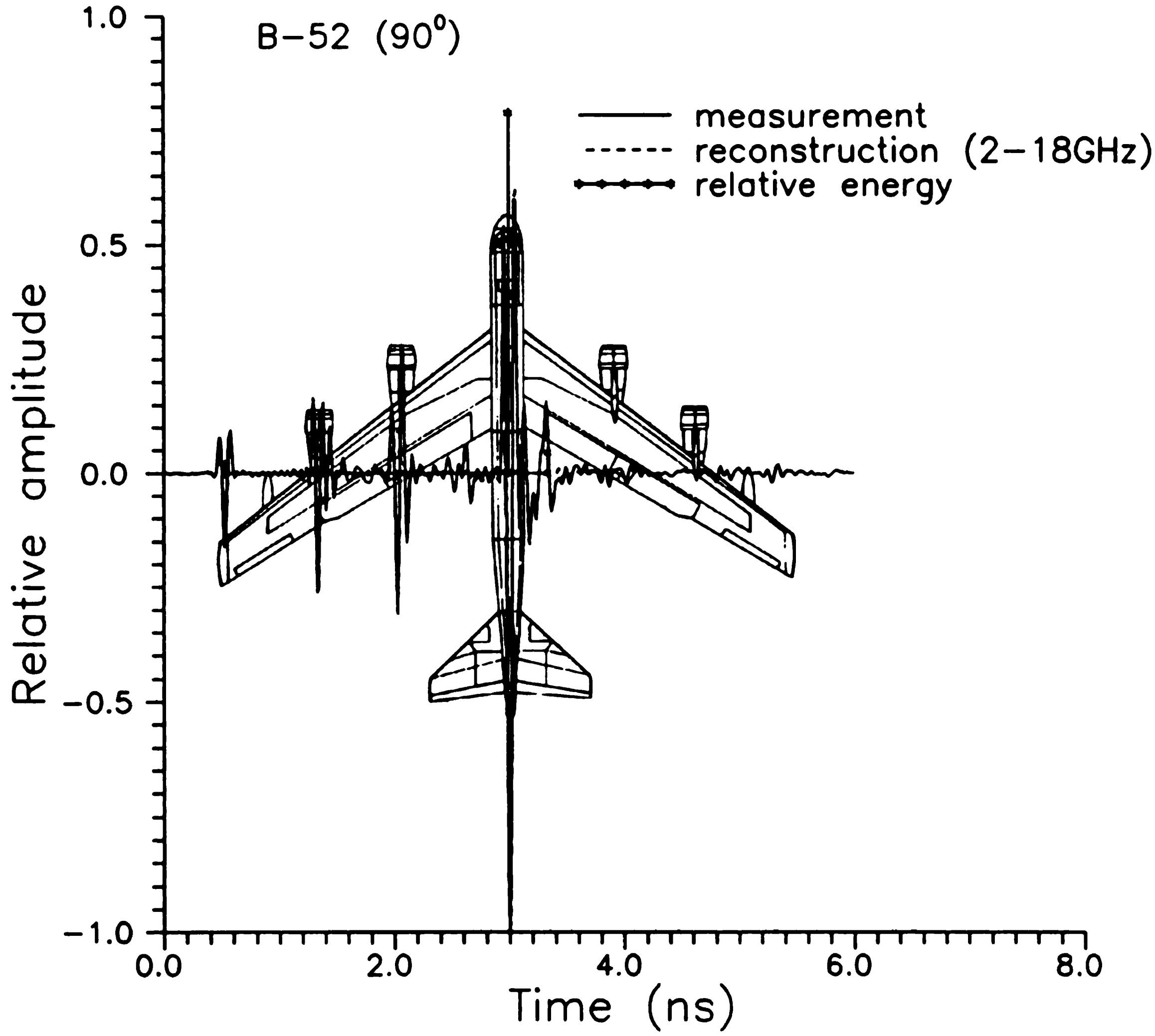

Figure 3.26 Response of 90^0 B-52 measured in the band 2-18 GHz, and reconstructed response using genetic algorithm, and n=-2,-1,...,2, and K=600, L=80, and 30 generations.

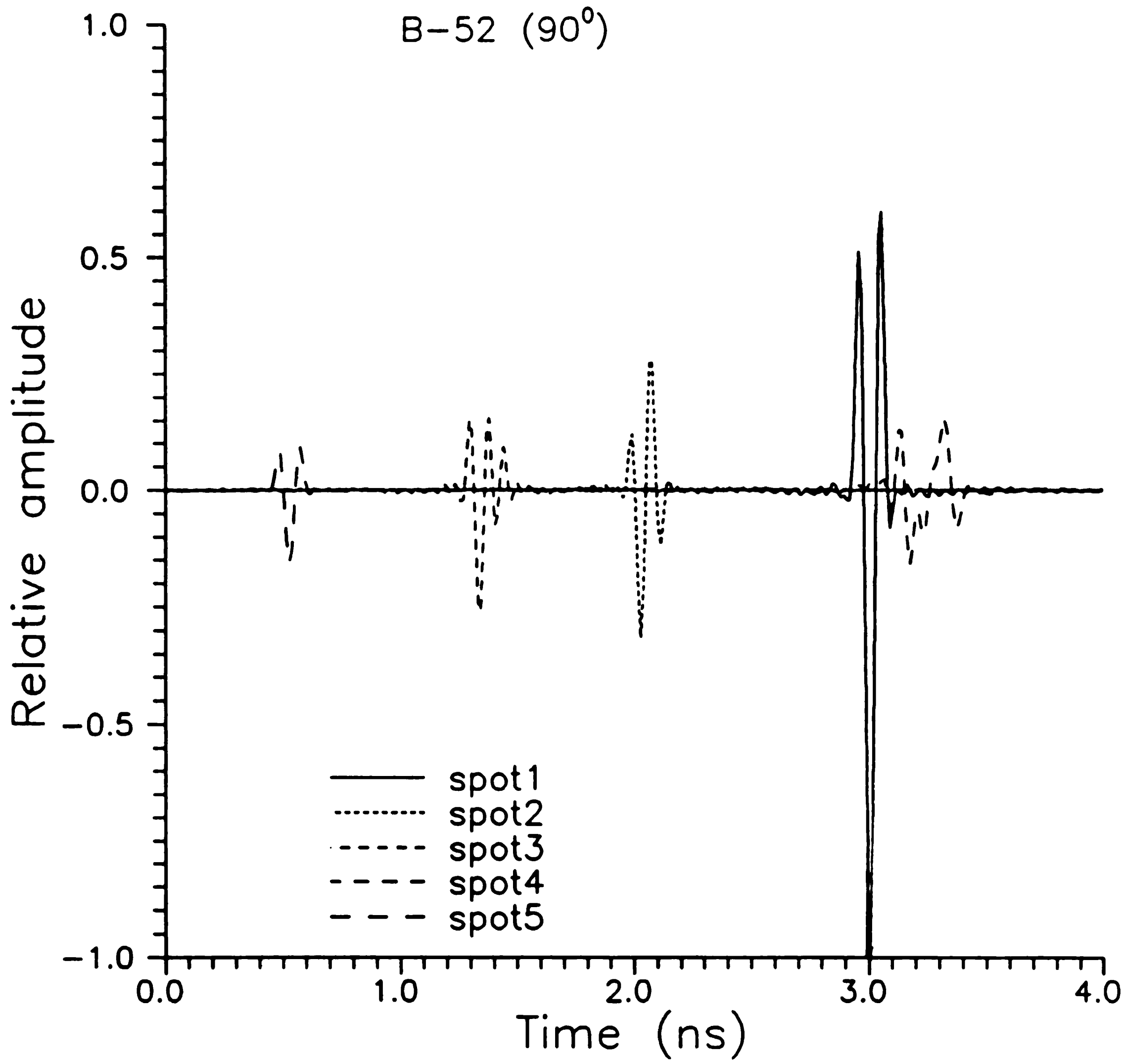

Figure 3.27 Pulse responses of 1st, 2nd, 3rd, 4th, and 5th specular points obtained using genetic algorithm.

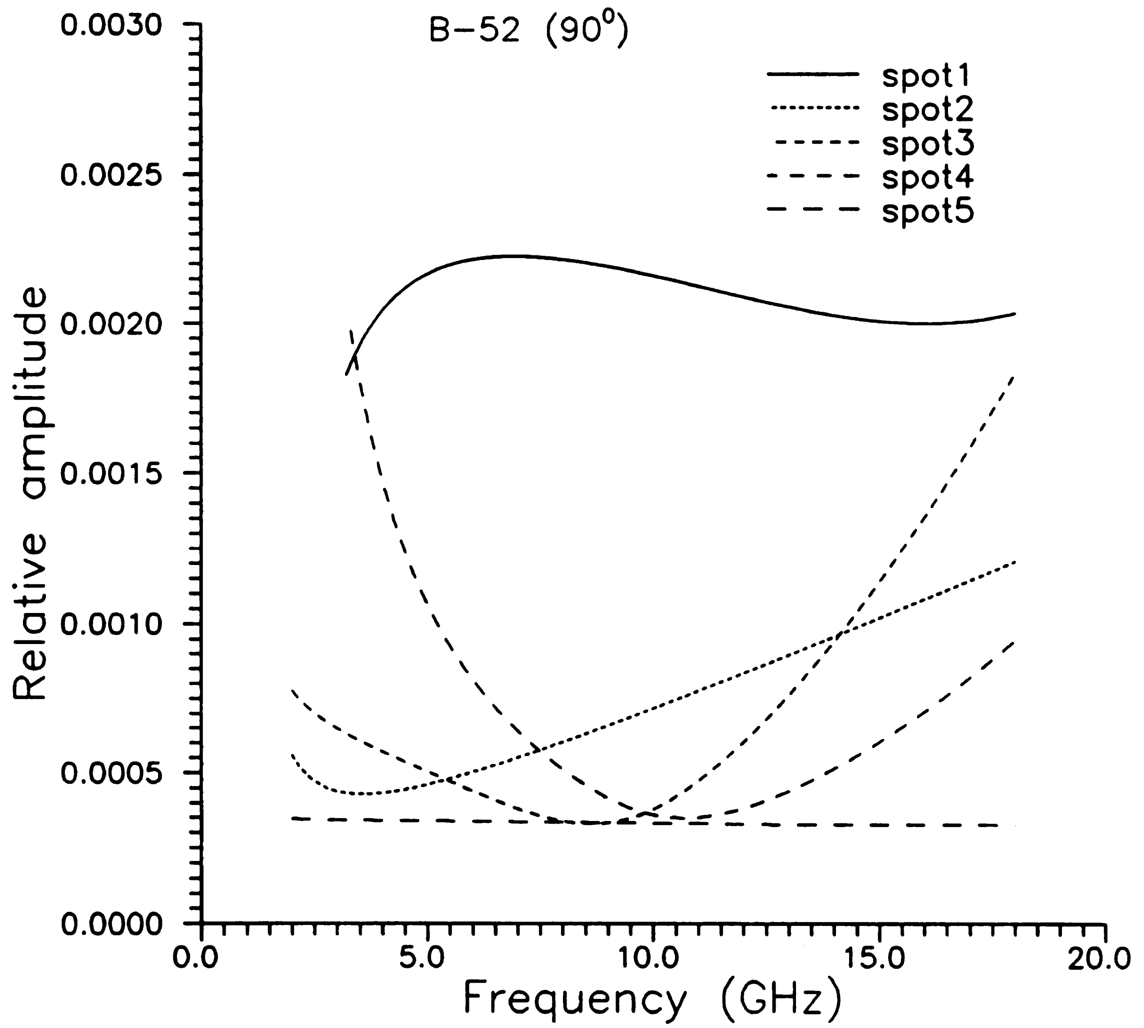

Figure 3.28 Transfer functions of 1st, 2nd, 3rd, 4th, and 5th specular points obtained using genetic algorithm.

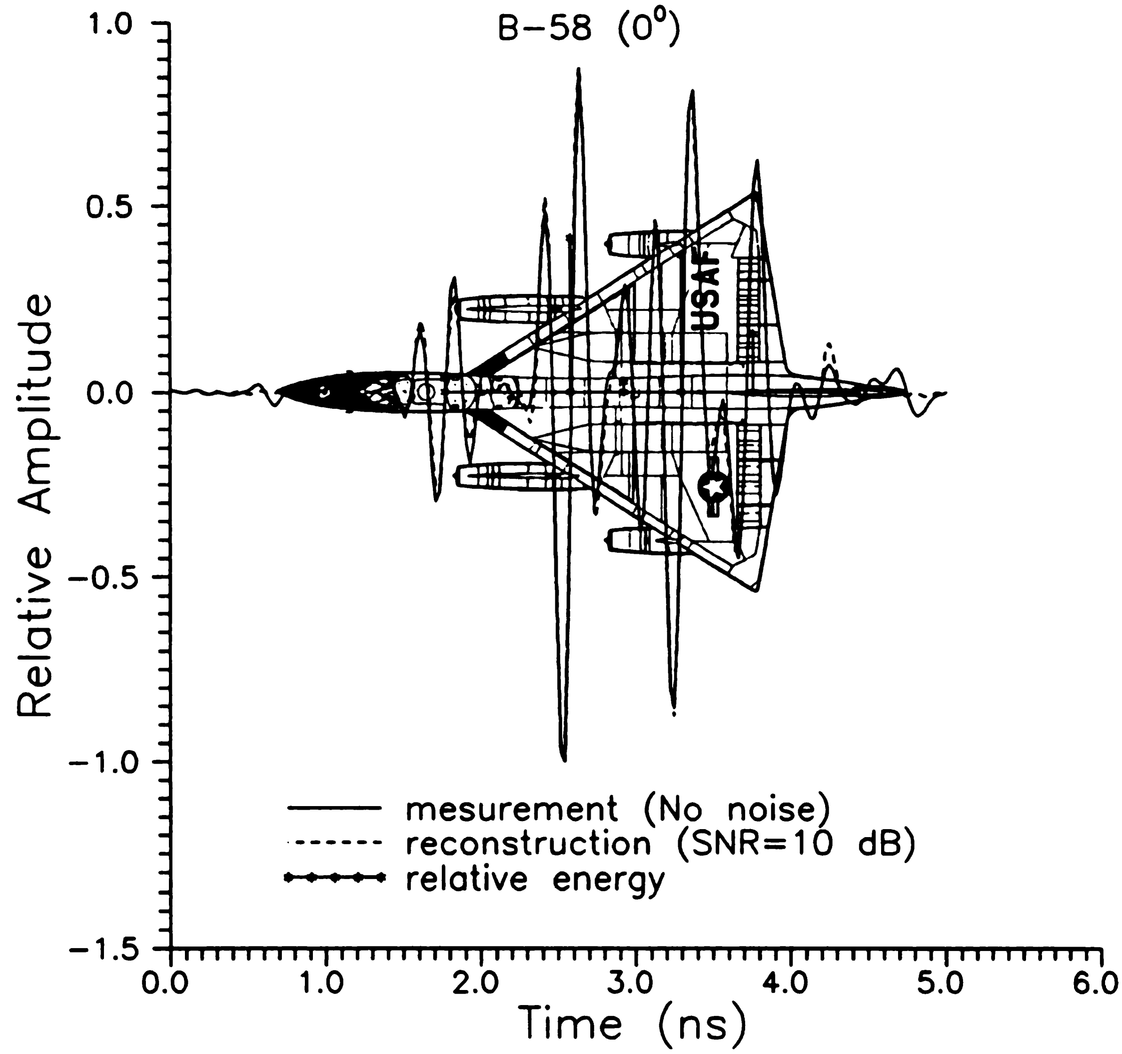

Figure 3.29 Response of 0^0 B-58 measured in the band 1-7 GHz, and reconstructed response with SNR=10 dB using genetic algorithm, and n=-2,-1,...,2, and K=600, L=80, and 30 generations.

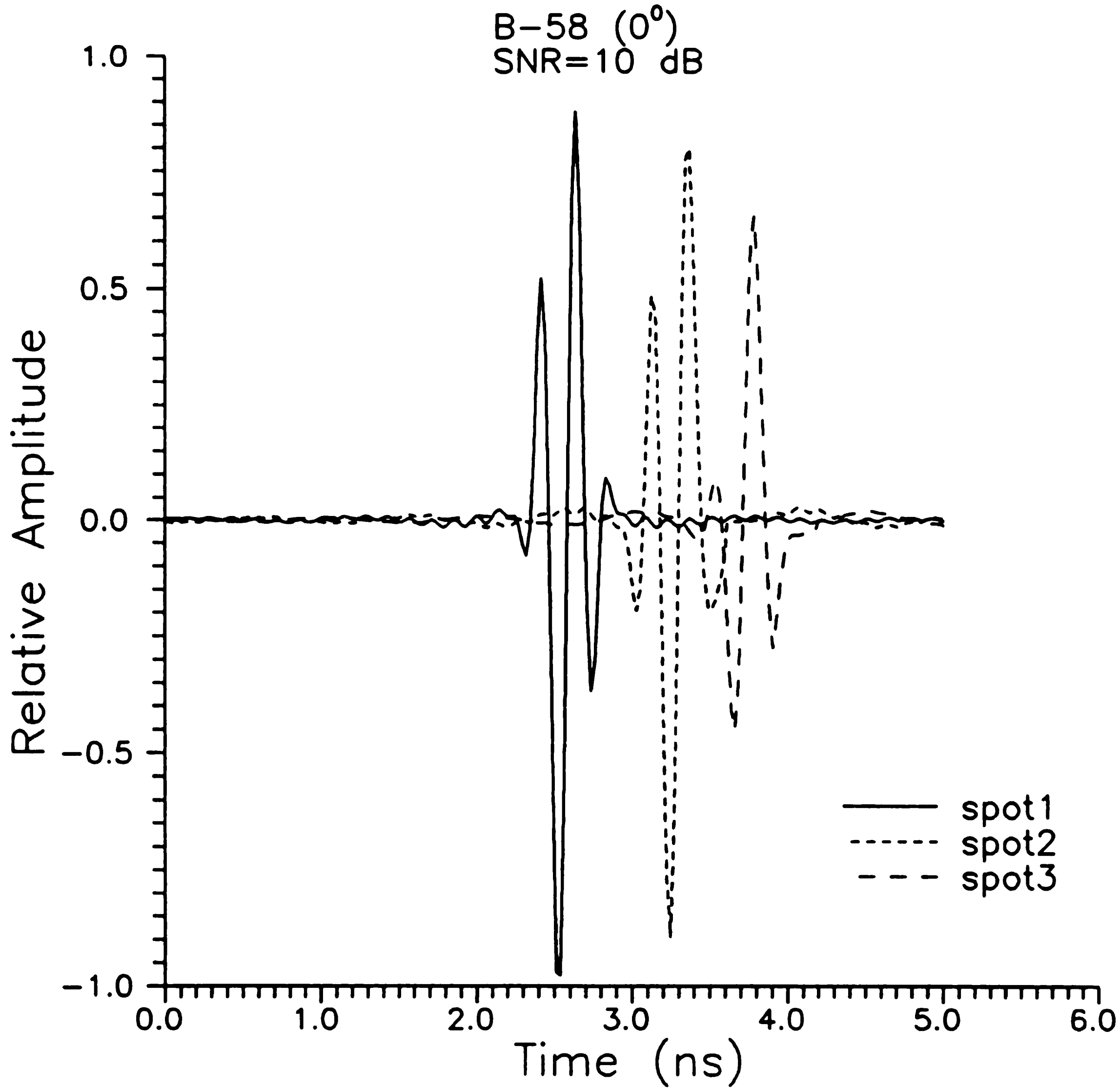

Figure 3.30 Pulse responses of 1st, 2nd, and 3rd specular points obtained using genetic algorithm.

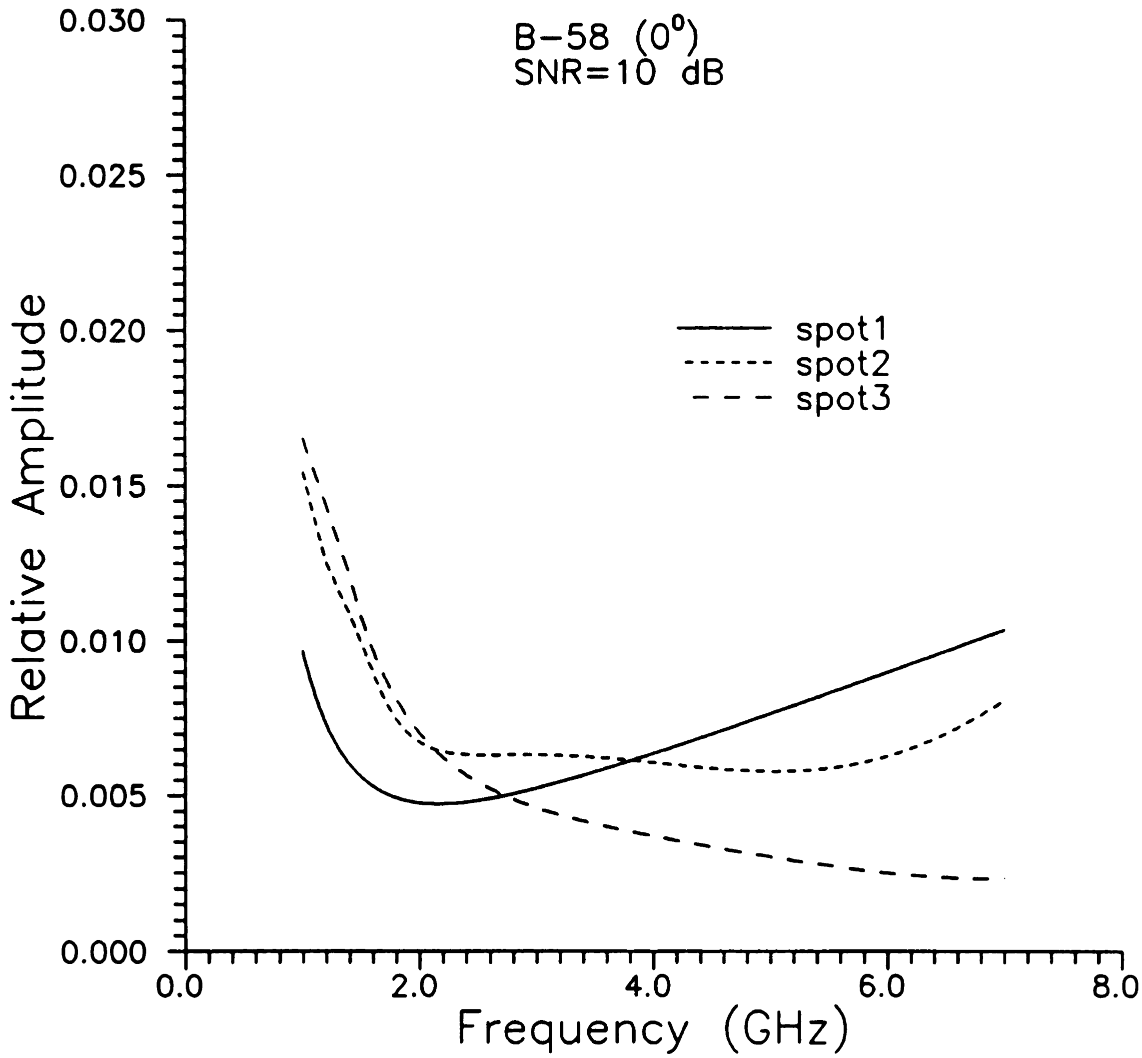

Figure 3.31 Transfer functions of 1st, 2nd, and 3rd specular points obtained using genetic algorithm.

CHAPTER 4

CANONICAL TARGET SCATTERING CENTER ANALYSIS AND EXPERIMENTAL RESULTS

4.1 Introduction

In chapter 2 we introduced a technique called the fitting scheme for studying the temporal positions and transfer functions of individual scattering centers. Recall that using the measured response of B-52 and B-58 aircraft models, we showed that the frequency-domain behavior of individual centers is highly dependent on geometry and aspect angle.

We now wish to verify the accuracy of this technique by comparing the measured transfer functions of a variety of simple canonical targets with the theoretical transfer functions determined by physical optics (PO). Since PO is only accurate when the scatterer is much larger than a wavelength, and both incident and scattered waves are planar, the canonical targets were chosen to be physically large (but not too large), so that PO would be applicable at the lowest frequency and the highest frequency in our sweep. Note that the above two conditions are not exactly satisfied at our lab. Thus, using PO will result in a difference between theory and measurement. Even so, PO is still a very good approximate method.

When the size of targets is much larger than the incident wavelength ($\lambda \to 0$), and the distance between antenna and targets satisfies the far zone condition, the incident and reflected wave can be both considered as plane wave. Physics optics (PO), the geometrical theory of diffraction (GTD) or the physical theory of diffraction (PTD) can be used to calculate the scattered field transfer function of a target. These high frequency techniques are based on localized phenomena (no interactions between scattering components on the target surface), so that each component contributes to the far zone scattered field independently. PO is valid only near the specular reflection region. Beyond this region GTD (or some other high frequency theory) must be used to determine contributions due to edge diffraction, tip diffraction, corner diffraction, etc.

In this chapter we will consider the high frequency responses of three canonical targets: a plate, a 90^0 dihedral corner reflector, and a circular cylinder. People have studied these simple canonical targets to aid in the calculation of target radar cross section (RCS), but have only rarely considered target transfer functions. Reducing RCS by coating targets with lossy material is an important radar stealth technique [19], [20], [21]. We will use a short pulse and the fitting scheme to extract the temporal positions and determine the transfer functions of scattering centers using the measured responses. The experimental results will be compared to those obtained using PO or GTD. First, we will consider the PO formulas for general conducting canonical targets.

4.2 PO Formulas For Simple Canonical Targets

Consider a plane wave incident upon a scatterer along a unit vector $\hat{u}_i$ and polarized along a unit vector $\hat{e}_0$. The incident field can be written as

$$\vec{E}^i = \vec{E}_0 e^{-j\vec{k}^i \cdot \vec{r}'} = E_0 \hat{e}_0 e^{-jk\hat{u}_i \cdot \vec{r}'} = E_0 \hat{e}_0 e^{jk\hat{u}_0 \cdot \vec{r}'} \tag{4.1}$$

where k is the wave number in free space. and $\vec{r}'$ is the position vector in a coordinate system. The unit vector in the backscattering direction is given by

$$\hat{u}_0 = -\hat{u}_i = \alpha_0 \hat{x} + \beta_0 \hat{y} + \gamma_0 \hat{z} \tag{4.2}$$

where the direction cosines are given in terms of incident aspect angles θ_0, ϕ_0, as

$$\begin{aligned} \alpha_0 &= \sin\theta_0 \cos\phi_0 \\ \beta_0 &= \sin\theta_0 \sin\phi_0 \\ \gamma_0 &= \cos\theta_0 \end{aligned} \tag{4.3}$$

Now, let the target surface in rectangular coordinates be parameterized as a single valued function with differential derivatives of first and second order

$$z = \xi(x,y) \tag{4.4}$$

Here we assume that the current in the illuminated region is nonzero but null in the dark region. let $\hat{n}$ be the unit vector normal to the surface as given by

$$\hat{n} = \frac{\nabla\phi}{|\nabla\phi|} = n_x \hat{x} + n_y \hat{y} + n_z \hat{z} \tag{4.5}$$

where $\phi = z - \xi(x, y)$, and n_x, n_y, n_z are three components of $\hat{n}$. Similarly, the unit vector in the direction of reflection is

$$\hat{u}_r = \alpha \hat{x} + \beta \hat{y} + \gamma \hat{z} \tag{4.6}$$

where

$$\begin{aligned} \alpha &= \sin\theta \cos\phi \\ \beta &= \sin\theta \sin\phi \\ \gamma &= \cos\theta \end{aligned} \tag{4.7}$$

and θ, ϕ are the aspect angles of the reflected (scattered) wave.

In the physical optics approach, the surface current density $\vec{K}$ is approximated by

$$\vec{K} \approx 2\hat{n}\times\vec{H}^{i} \tag{4.8}$$

Using the far zone formula

$$\vec{E} = -j\omega\vec{A}_{T} \tag{4.9}$$

where $\vec{A}_T = \vec{A} - \hat{r}\,(\hat{r}\cdot\vec{A})$ is the transverse vector potential, the electric field in the far zone is given by [22]

$$\vec{E} = j2\pi E_0 \frac{e^{-jkr}}{kr}\frac{1}{\lambda^2}\iint_S \frac{\hat{u}_r\times(\hat{n}\times\hat{e}_0)}{n_z}\exp[jkg(x,y)]\,dx\,dy \tag{4.10}$$

where

$$g(x,y) = (\alpha+\alpha_0)x + (\beta+\beta_0)y + (\gamma+\gamma_0)\xi(x,y) \tag{4.11}$$

Note that the incident field vector $\hat{e}_0$ can be written as

$$\hat{e}_0 = e_{0x}\hat{x} + e_{0y}\hat{y} + e_{0z}\hat{z} = e_{0x}\hat{x} + e_{0y}\hat{y} - (\frac{\alpha_0}{\gamma_0}e_{0x} + \frac{\beta_0}{\gamma_0}e_{0y})\hat{z} \tag{4.12}$$

The above equation is obtained using the orthogonal relationship $\hat{e}_0 \cdot \hat{u}_0 = 0$. Finally, the transfer function of the target is defined by

$$H(\omega) = \frac{\vec{E}\cdot\hat{e}_r}{E_0} = \frac{\vec{H}\cdot\hat{h}_r}{H_0} \tag{4.13}$$

where $\hat{e}_r$ and $\hat{h}_r$ are the receiver polarization unit vectors.

Each of three canonical problems is analyzed using (4.10). We only choose those aspect angles at which specular reflection dominates. The following sections will determine transfer functions from measured data using the fitting scheme and give the comparison between theory and measurement. Note that equation (4.10) considers bistatic aspect angles and predicts better results since the scattered field of the plate and cylinder changes sharply with aspect angles. We must be very careful to determine them.

4.3 Plate

The first canonical problem is a rectangular plate, as shown in Figure 4.1. Substituting the equation for a plate into (4.10) gives the electric field [23]

$$\vec{E} = -j8\pi E_0 \frac{e^{-jkr}}{kr} \frac{ab}{\lambda^2} sinc[\frac{2(\alpha+\alpha_0)a}{\lambda}] sinc[\frac{2(\beta+\beta_0)b}{\lambda}]$$
$$[e_{0x}\gamma\hat{x} + e_{0y}\gamma\hat{y} - (\alpha e_{0x} + \beta e_{0y})\hat{z}] \tag{4.14}$$

where

$$sinc(x) = \frac{\sin(\pi x)}{\pi x} \tag{4.15}$$

The transfer function can then be found by using (4.13). Note that PO can't account for edge diffraction and thus the scattered field is polarization insensitive. To obtain more accurate results, GTD can be used to determine the contribution of the edge to the scattered field in the far zone. GTD assumes that the location of the scattering is at points defined by abrupt geometrical discontinuities. It further assumes that the current distribution in the neighborhood of a scattering center is obtained from that of a known case of similar local geometry. For a plate, edge diffraction is found using the known results of an infinite half plane. Depending on polarization, the results are applied to both edges of a perfectly conducting, infinitely thin, infinite strip of width *2a* and height $2b \rightarrow \infty$, yielding the backscattered field when the incident wave propagates within the X-Z plane [24]

$$u_v = \frac{E_0 e^{-jkr-j(\pi/4)}}{2\sqrt{2\pi}(kr)^{1/2}}\left\{\left[1+\frac{1}{\sin\theta}\right]e^{j2ka\sin\theta}+\left[1-\frac{1}{\sin\theta}\right]e^{-j2ka\sin\theta}\right\}$$
$$+\left\{\frac{E_0 e^{jk(-r-2a)}}{2\pi(kr)^{1/2}(2ka)^{3/2}\cos\theta}+\frac{E_0 e^{jk(-r-4a)+j\frac{\pi}{4}}}{8\pi\sqrt{2\pi}(kr)^{1/2}(2ka)^3}\right.$$
$$\left.\left[\frac{1+\sin\theta}{(1-\sin\theta)^2}e^{j2ka\sin\theta}+\frac{1-\sin\theta}{(1+\sin\theta)^2}e^{-j2ka\sin\theta}\right]\right\} \tag{4.16}$$

for vertical polarization and

$$u_h = -\frac{E_0 e^{-jkr-j(\pi/4)}}{2\sqrt{2\pi}(kr)^{1/2}}\left\{\left[1-\frac{1}{\sin\theta}\right]e^{j2ka\sin\theta}+\left[1+\frac{1}{\sin\theta}\right]e^{-j2ka\sin\theta}\right\}$$
$$-\left\{\frac{2E_0 e^{jk(-r-2a)-j(\pi/4)}}{\pi(kr)^{1/2}(2ka)^{1/2}\cos\theta}-2E_0\frac{e^{jk(-r-4a)-j(3\pi/4)}}{2\pi\sqrt{2\pi}(kr)^{1/2}(2ka)}\right.$$
$$\left.\left[\frac{e^{j2ka\sin\theta}}{1-\sin\theta}+\frac{e^{-j2ka\sin\theta}}{1+\sin\theta}\right]\right\} \tag{4.17}$$

for horizontal polarization. Here u_v and u_h are related to three-dimensional electric field by introducing the formula which relates two-dimensional electric field and three-dimensional electric field [25]

$$E_{v,h} = \frac{2b}{\sqrt{r\lambda}}e^{-j\frac{\pi}{4}}u_{v,h} \tag{4.18}$$

Therefore, the transfer function is

$$H_{v,h}(\omega) = \frac{E_{v,h}}{E_0} \tag{4.19}$$

These include contributions from single diffraction, double diffraction, and triple diffraction. Thus, GTD accounts for the polarization dependence of the scattered field. Note that GTD results are similar to those from PO when plate aspect angles are near normal incidence.

Using the above results we will compare the experimental determination of scattering center transfer functions to theory. PO is used as a theoretical baseline for each of three canonical targets. All data has been collected in the frequency domain within the band 1-7 GHz, calibrated using techniques described in chapter 2, and inverse transformed into the time domain using a Gausian-modulated cosine window function centered at 4 GHz (an equivalent pulse width of about 0.4 ns) and a 4096 point FFT. Only the early-time portion is compared with theory. A small late-time component is excited in each case, but suppressed using time windowing.

The technique described in chapter 2 is used to extract the scattering center transfer functions. Each transfer function is represented as a polynomial with a certain number of terms retained. In our experience, a range of powers on omega from -3 to +3 or -2 to +2 gives good results.

Because of the physical separation of the transmitting and receiving antennas within the MSU anechoic chamber, the measured scattered field will arise from a slightly bistatic situation. We must consider bistatic aspect angles due to the sharply varying nature of the canonical target response. Figure 4.2 shows the theoretical transfer function of a rectangular plate 58.5 cm x 40.7 cm in size at normal incidence obtained using PO and GTD. We would expect the edge diffraction to become more important as we move away from normal incidence and the agreement between the techniques to be worse. However, the experimental aspect angles of $\theta \approx 4.7^0$, $\phi \approx 45^0$ for the transmitter and $\theta \approx 4.7^0$, $\phi \approx 225^0$ for the receiver are near enough to normal that we will restrict our comparison to PO.

Figure 4.3 shows the response of a 58.5 cm x 40.7 cm rectangular plate measured in the frequency band 1-7 GHz. The lowest resonant frequency is about 0.25 GHz for the larger edge and 0.4 GHz for the smaller edge. The steep response around 1 GHz may be caused by a higher-order resonance. Figure 4.4 shows the corresponding time domain response of the plate via the inverse FFT, and the reconstructed early-time response obtained using one scattering center. We can see the reconstructed waveform matches quite well. The magnitude of the corresponding transfer function of the plate is shown in Figure 4.5 along with that found using PO. The results match well except near 6 GHz. PO theory predicts a null at 5.8 GHz, but the measurement only attains a minimum value. This is due to some unaccounted edge diffraction and a failure to satisfy the far zone condition. Note that the dramatic difference between this bistatic case and normal incidence shown in Figure 4.2. This demonstrates the significant dependence of scattering center transfer functions on aspect angle, thus the scattered field waveform.

Now, we must also consider the phase of the transfer function. As we mentioned before, it is very difficult to compare the phase directly due to the different time reference points between measurement and PO. One method is to minimize the mean square error of phase using a genetic algorithm, the other method is to match pulse responses obtained using measurement and theory, and then take the Fourier transform. The second method is utilized in this chapter.

Figure 4.6 shows the phase of the plate determined by fitting scheme, and the phase found using (4.14). The match is quite good.

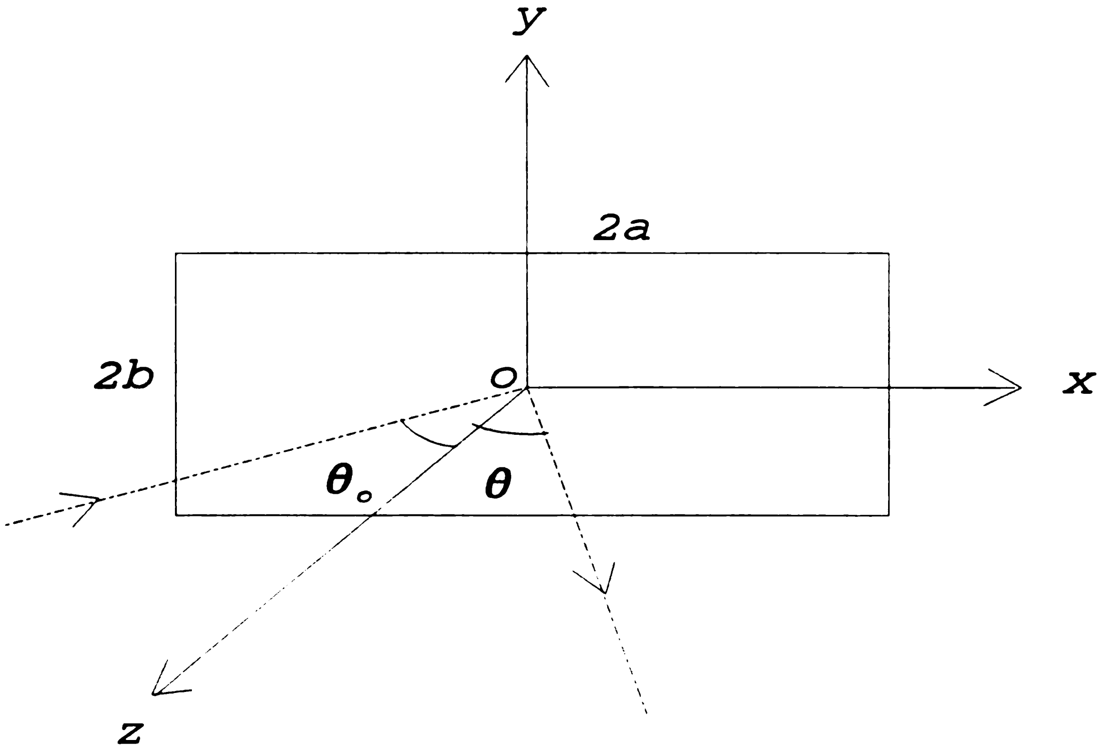

Figure 4.1 Excitation geometry for scattering from a thin rectangular plate.

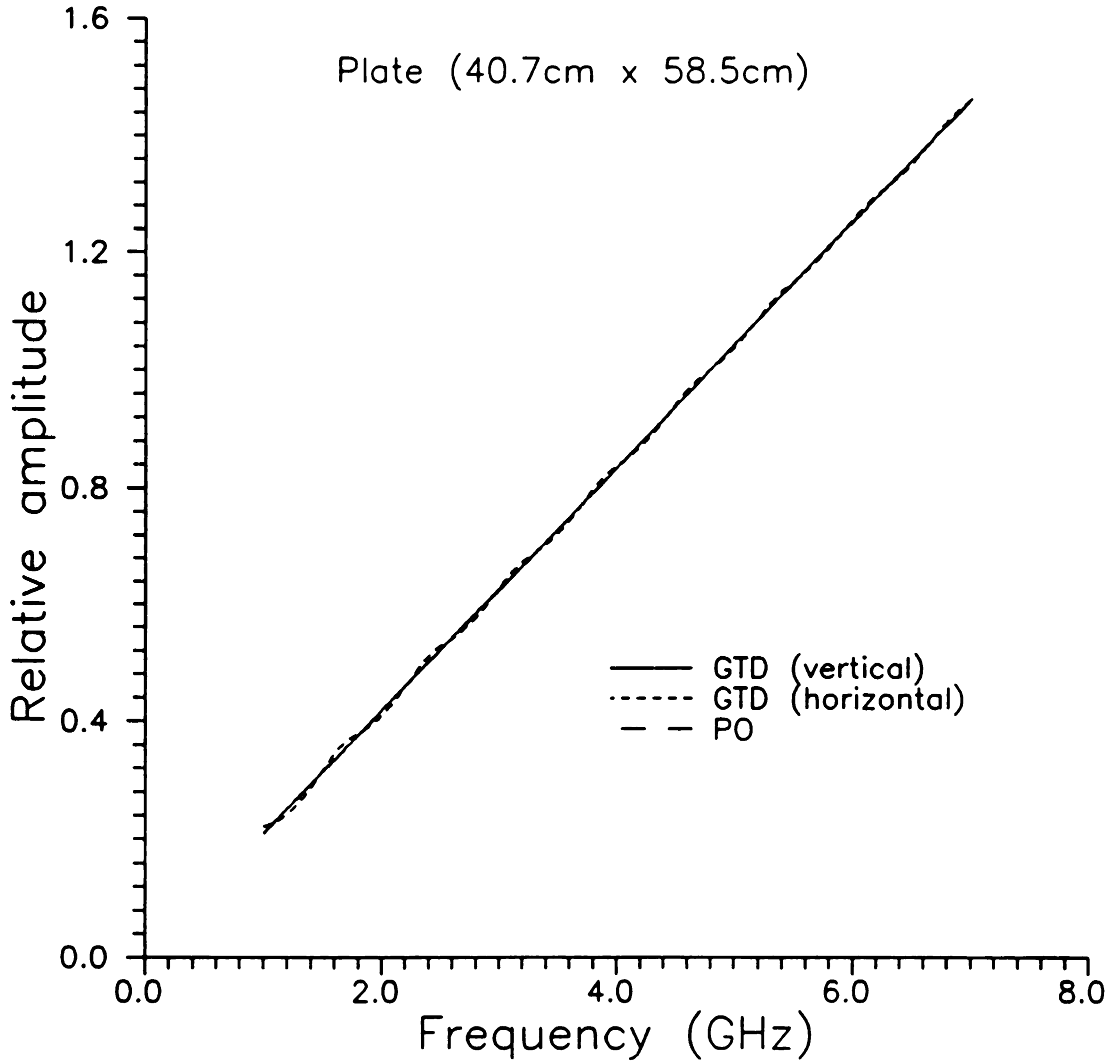

Figure 4.2 Theoretical transfer function of a flat rectangular plate found using both PO and GTD.

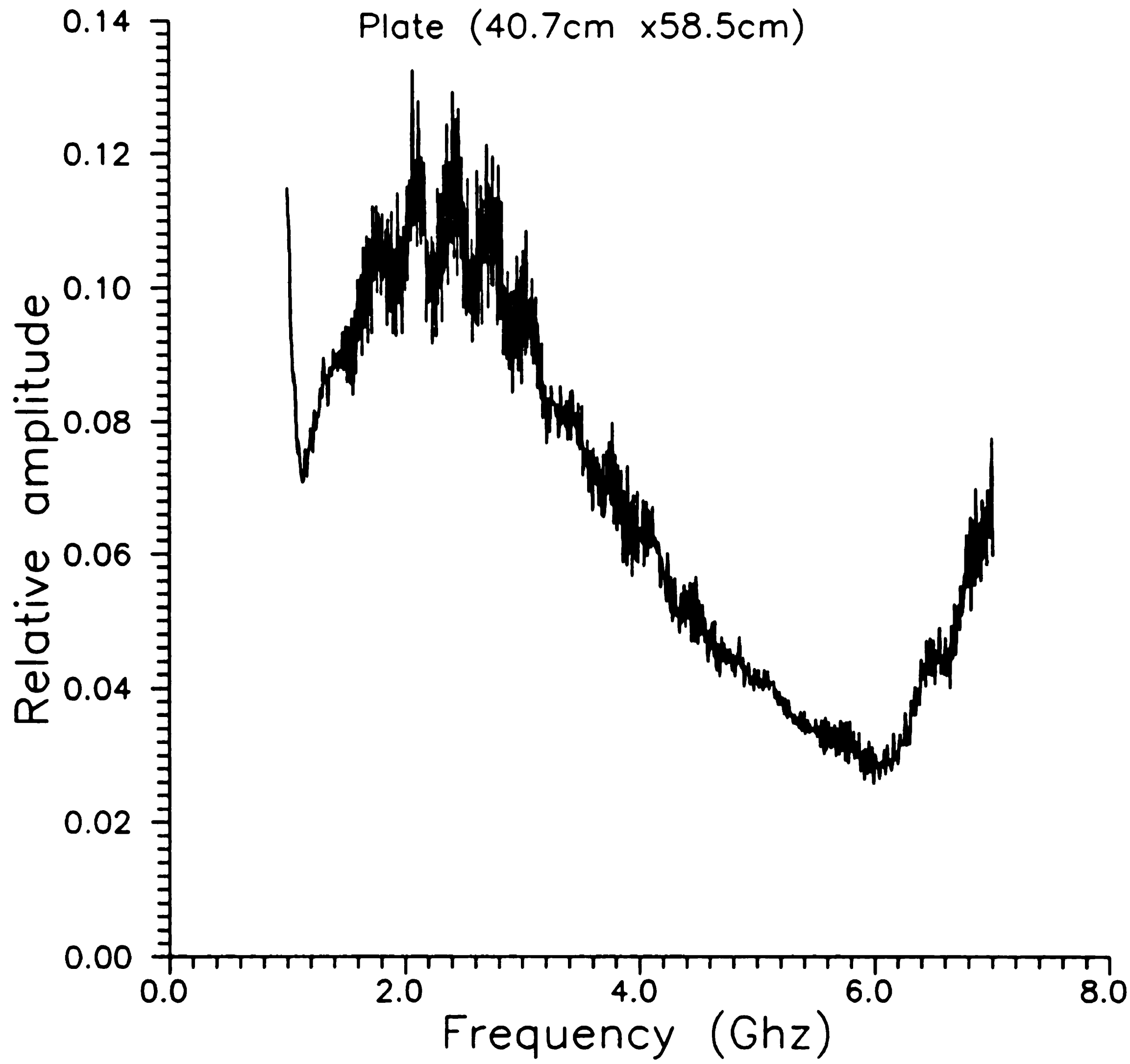

Figure 4.3 Response of a flat rectangular plate measured in the frequency band 1-7 GHz.

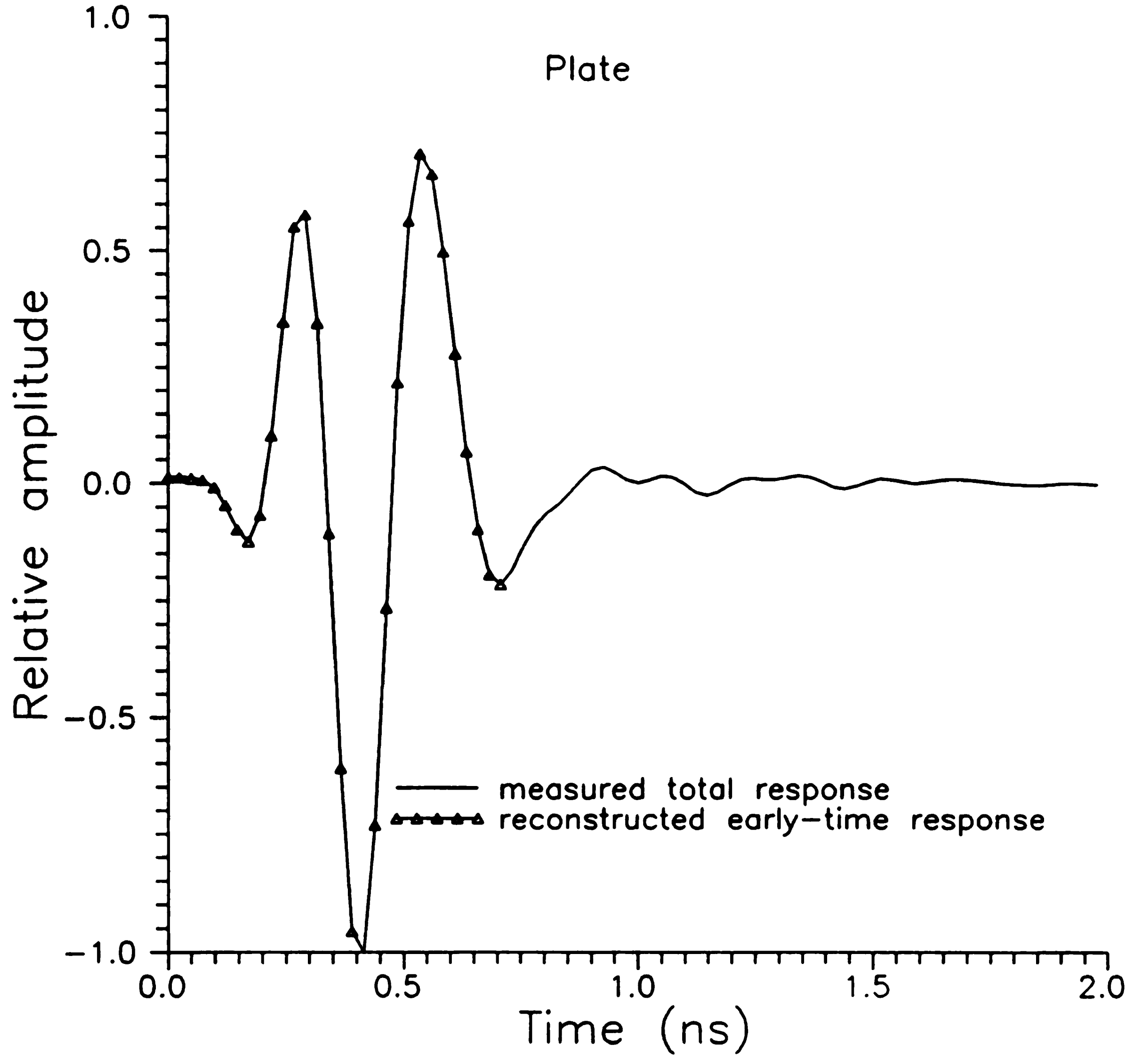

Figure 4.4 Temporal response of rectangular plate and reconstructed early-time response found using one scattering center.

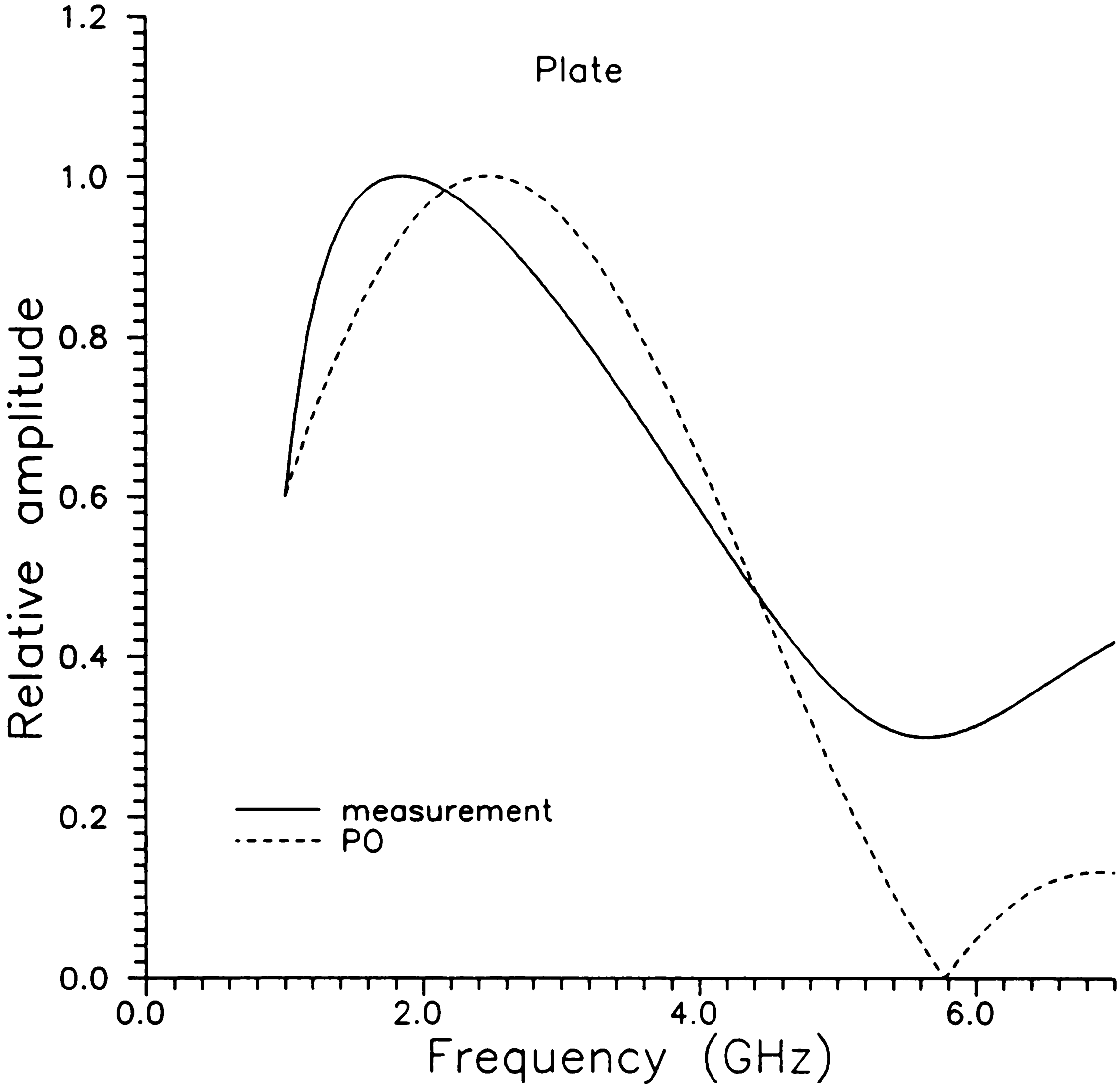

Figure 4.5 Magnitude of transfer function of plate scattering center obtained from measurements and theoretically from PO.

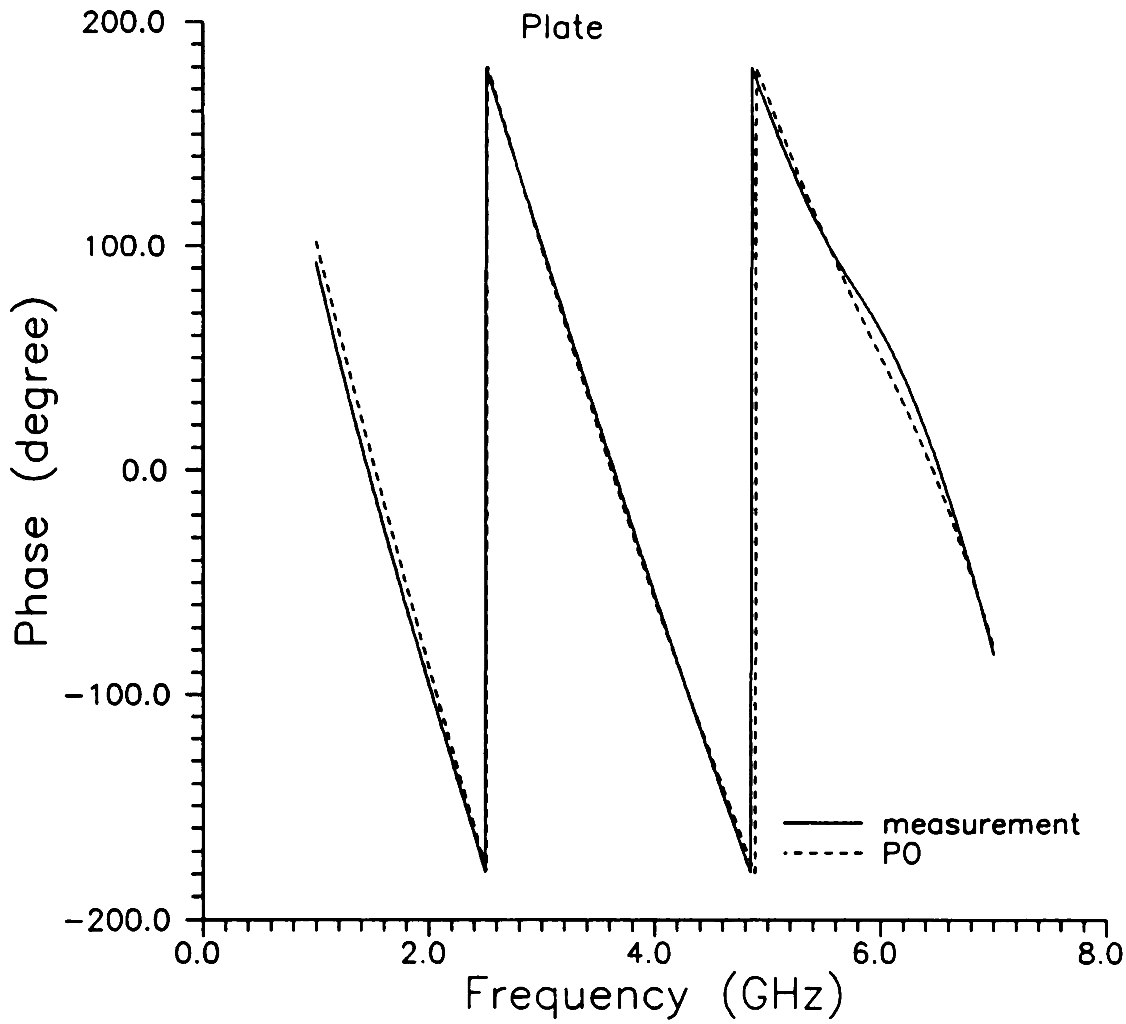

Figure 4.6 Phase of transfer function of plate scattering center obtained from measurements and theoretically from PO.

4.4 90° Dihedral Corner Reflector

Figure 4.7 shows a 90° dihedral corner reflector structure. For edge-on incidence, the scatted field includes contributions mainly from the flat surface of plate II and the outer edge of plate I. So there are two scattering centers in the down range sense for this case. The transfer function of plate II is obtained using (4.14) and the transfer function of the edge of plate I is a constant for both polarizations [26]. We concentrate on edge-on incidence to reduce the interaction between the scattering centers. After some coordinate adjustment, the backscattered field of the outer edge of plate I is approximated by

$$\vec{E} = \hat{y}\frac{E_0}{2\pi}\frac{e^{-jkr}}{r}\left[-\frac{1}{2}(1-\frac{1-\sin\psi}{\cos\psi})\right]be^{-jka\cos\psi} \tag{4.20}$$

for horizontal polarization and

$$\vec{H} = \hat{y}\frac{H_0}{2\pi}\frac{e^{-jkr}}{r}\left[-\frac{1}{2}(1+\frac{1-\sin\psi}{\cos\psi})\right]be^{-jka\cos\psi} \tag{4.21}$$

for vertical polarization, where

$$\psi = \frac{\pi}{4}-\theta \tag{4.22}$$

Figure 4.8 shows the measured response of a 90° dihedral corner reflector measured in the frequency domain. The rapid variation of spectral magnitude is caused by the time delay between the outer edge of one plate and the flat surface of the other plate. The early time response reconstructed using two specular points, shown in Figure 4.9, matches quit well with the measured data except in the latter part of waveform where there is a small late-time component. Figure 4.10 shows the pulse response and relative energy of each scattering center. The two-way transit time between two scattering centers is about 3.5 ns, This gives a separation distance of 52.5 cm, which agrees well with the actual 51.5 cm separation. The individual transfer functions of the scattering centers are shown in Figure 4.11. Note that there is a slight anomaly near 5.2 GHz since edge contribution is not accounted for. A better comparison to PO might be obtained if bigger plates and a wider measurement band were to be used, but the far zone condition is not satisfied in our chamber.

To compare the phases of transfer functions obtained by measurement and theory, the pulse responses obtained using both methods are shifted and matched first, then they are transformed using FFT. The phases of the individual scattering centers are shown in Figure 4.12 and Figure 4.13. We observe that the matches are quite good.

4.5 Circular Cylinder

The last canonical problem is scattering from a circular cylinder. First, we consider the excitation field incident on the side of the cylinder as shown in Figure 4.14. In this case, the equation of cylinder surface is

$$y^2 + z^2 = a^2 \tag{4.23}$$

then

$$\xi(x,y) = a\sqrt{1 - \frac{y^2}{a^2}} \tag{4.24}$$

Here we only consider the illuminated region contribution when using PO, the sign in the above equation is taken as positive. Thus, PO does not account for contributions from the late-time creeping wave. Using (4.10) scattered field is [23]

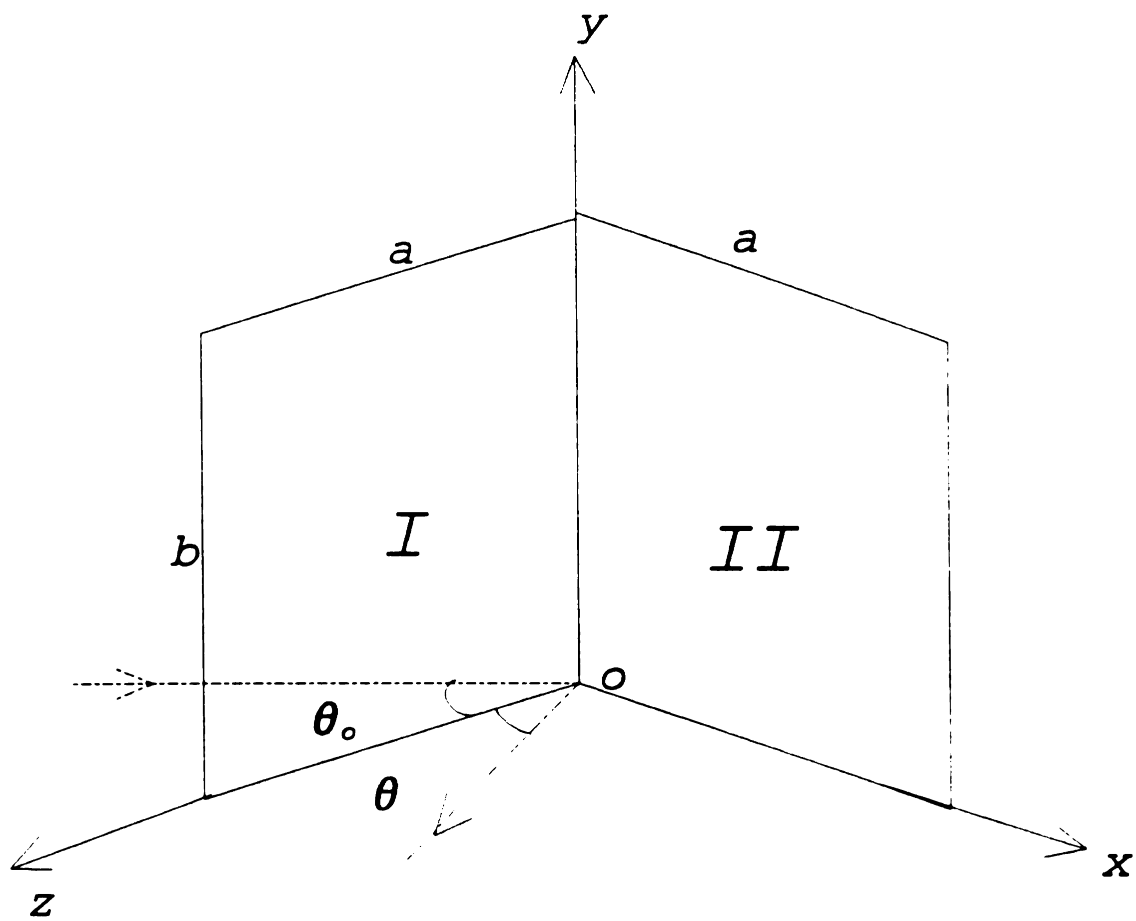

Figure 4.7 Excitation geometry for scattering from a thin dihedral corner reflector.

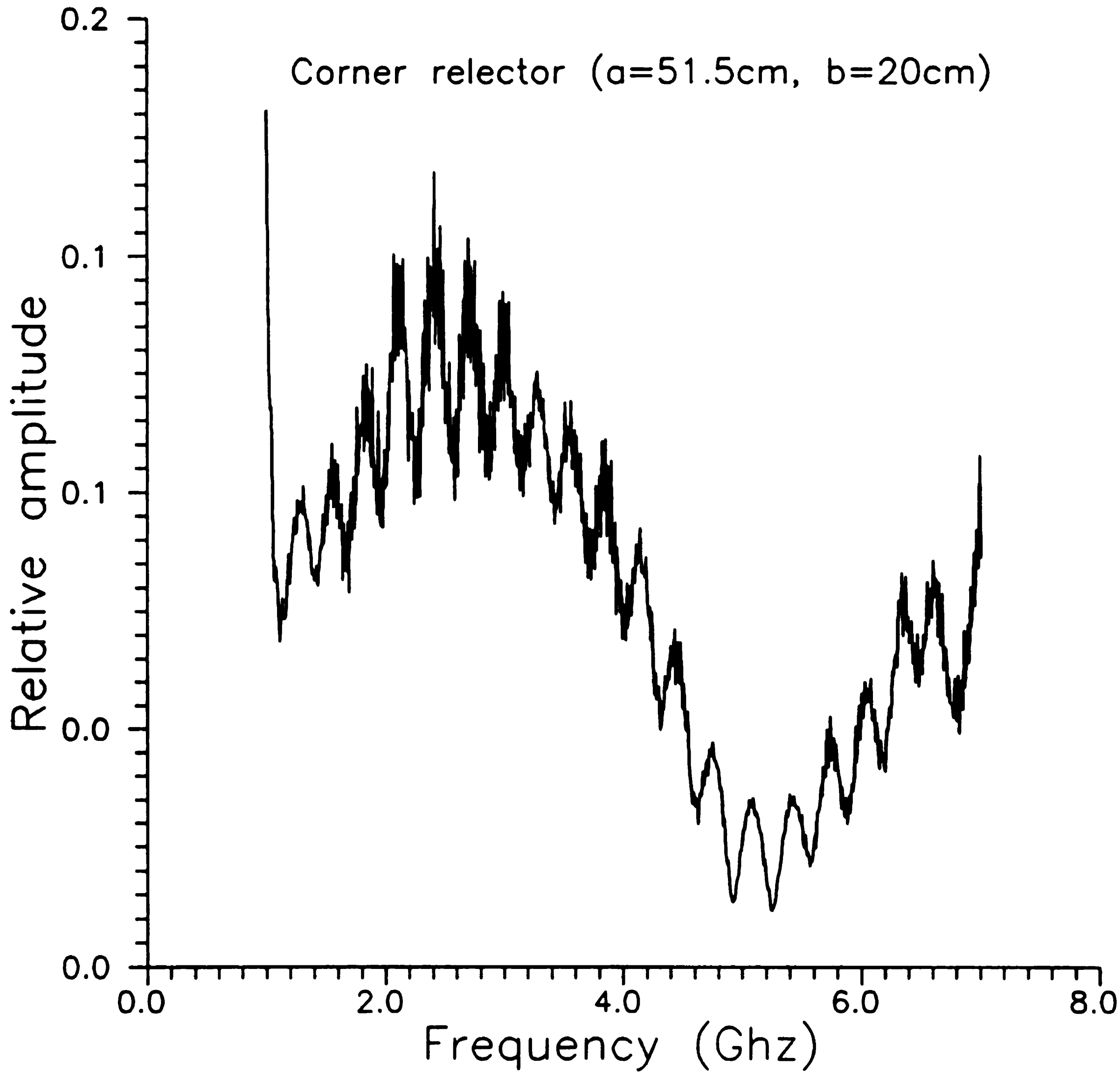

Figure 4.8 Response of a dihedral corner reflector measured in the frequency band 1-7 GHz.

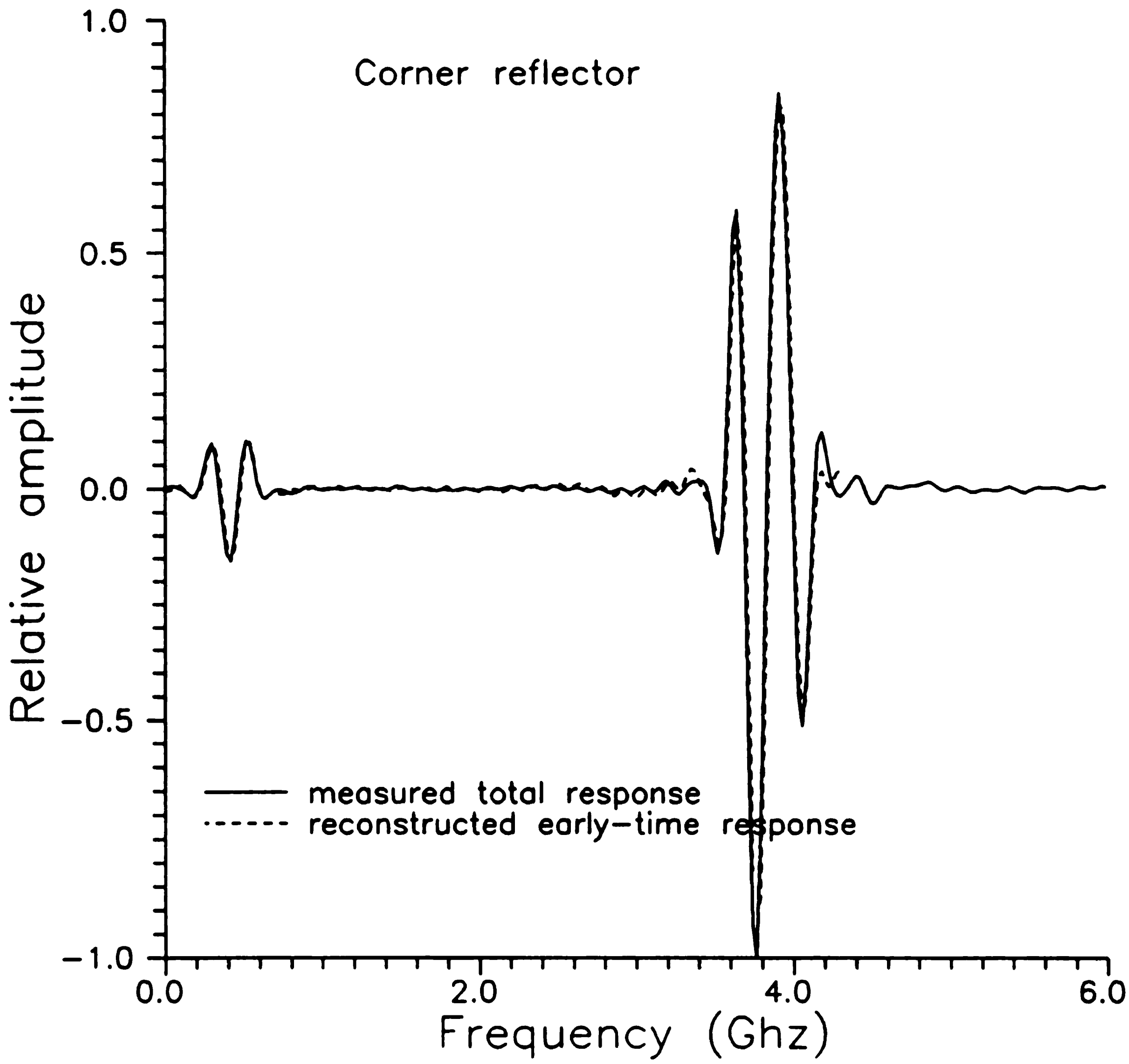

Figure 4.9 Temporal response of dihedral corner reflector and reconstructed early-time response found using two scattering centers.

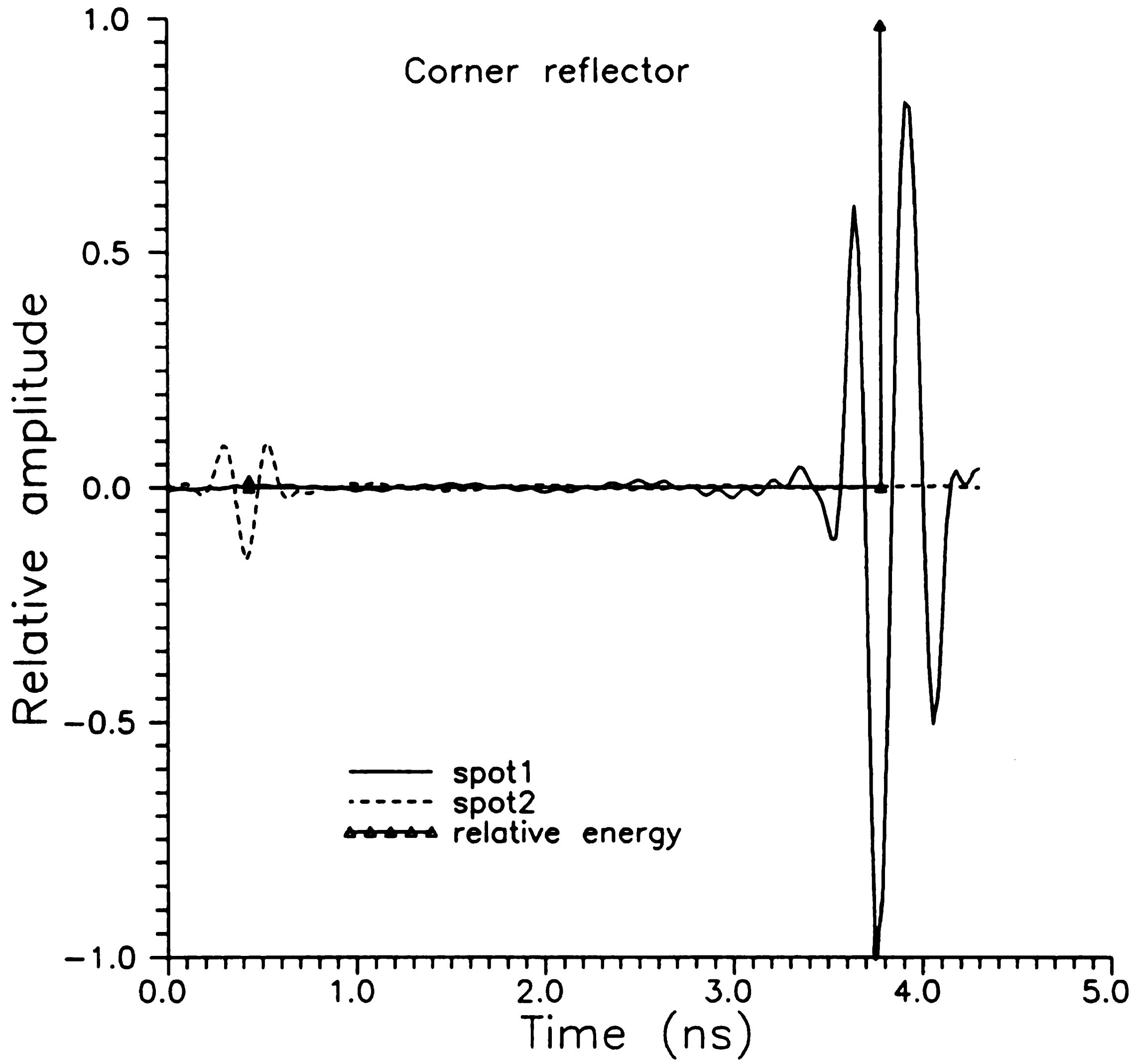

Figure 4.10 Scattering center pulse responses and waveform energies for corner reflector found using two scattering centers.

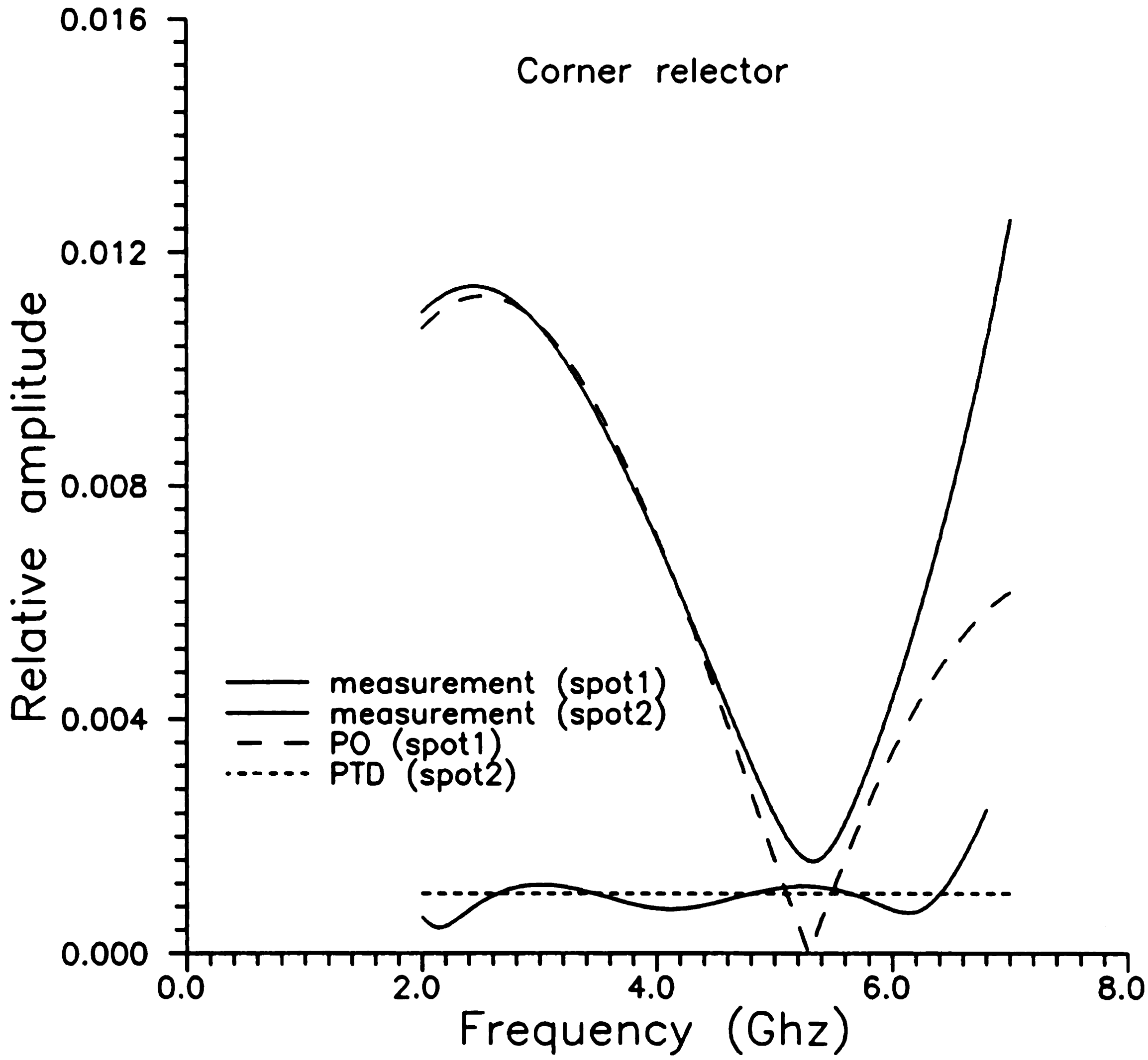

Figure 4.11 Magnitude of transfer functions of corner reflector scattering centers obtained from measurement, from PO, and from PTD.

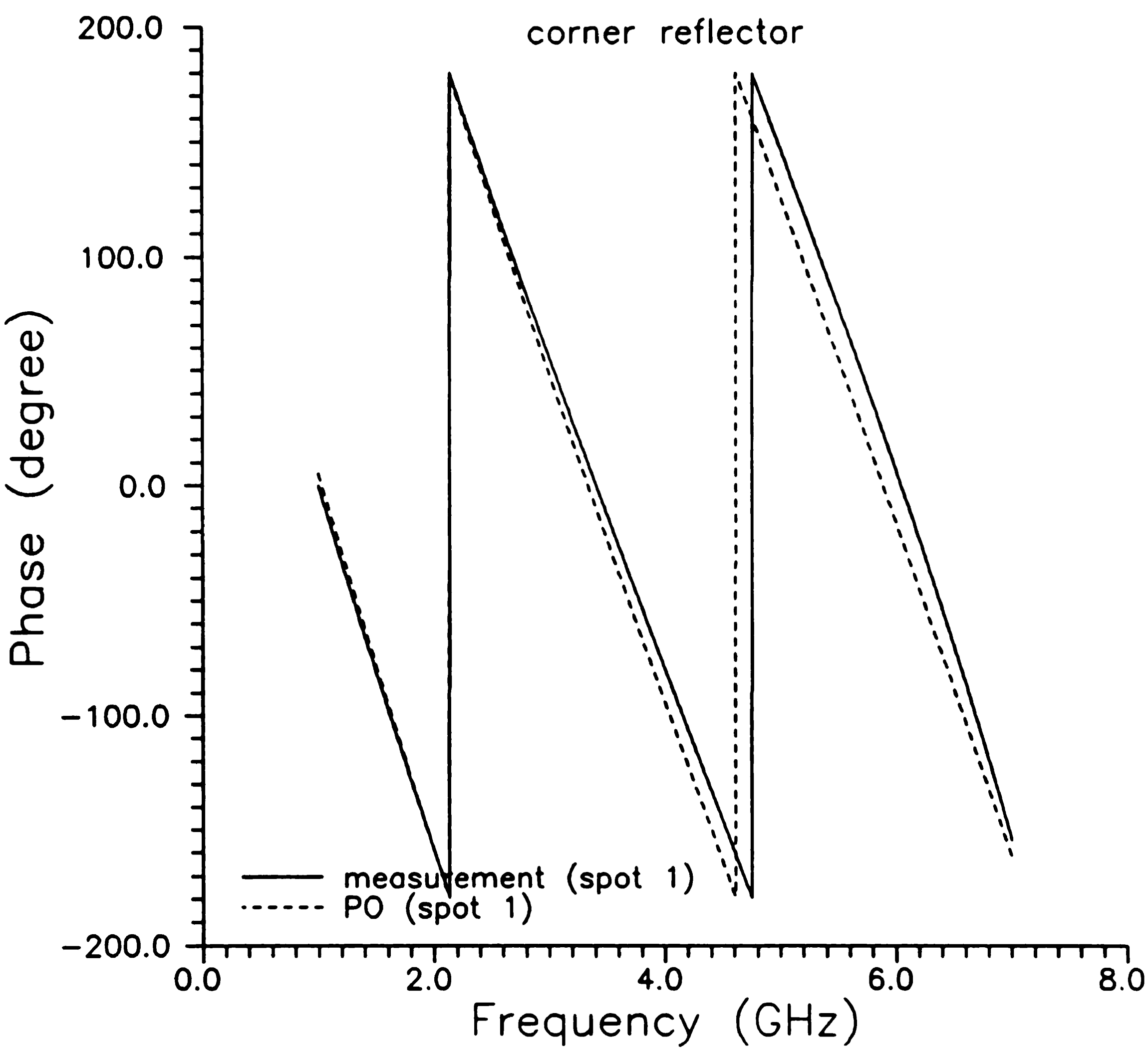

Figure 4.12 Phase of transfer functions of first scattering center obtained from measurement, and from PO.

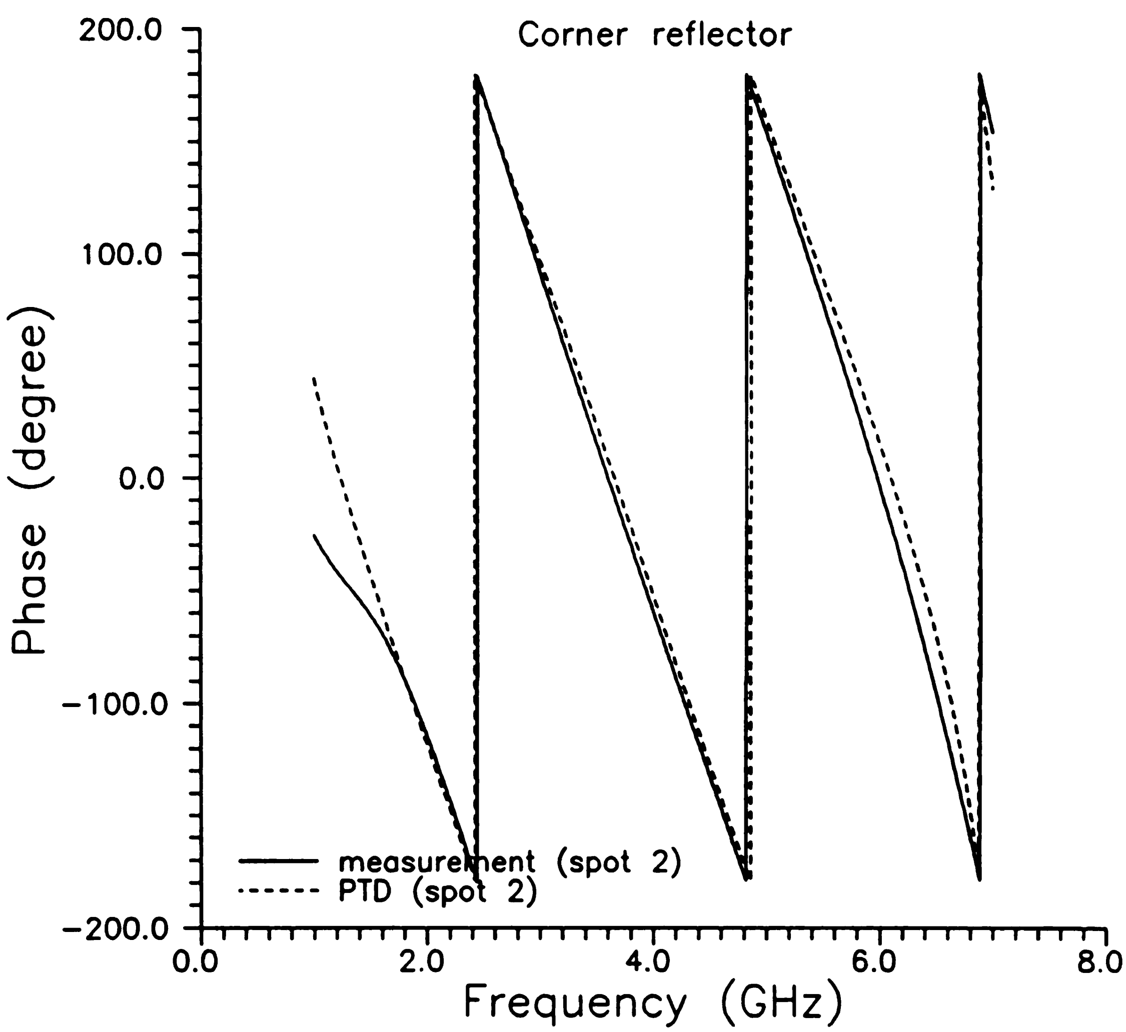

Figure 4.13 Phase of transfer function of second scattering center obtained from measurement, and from PTD.

$$\vec{E}=j2\pi E_0\frac{e^{-jkr}}{kr}\frac{l}{\lambda^2}sinc\frac{[(\alpha_0+\alpha)l]}{\lambda}\int_{-a}^{a}\frac{\hat{u}_r\times(\hat{n}\times\hat{e}_0)}{n_z}e^{jk[(\beta_0+\beta)y+(\gamma_0+\gamma)\sqrt{a^2-y^2}]}dy \tag{4.25}$$

where l is the length and a is radius of the circular cylinder. Now, using the change of variables $y = a\,sin(t)$ allows (4.25) to be written in a form more convenient for calculations

$$\vec{E}=-j2\pi E_0\frac{e^{-jkr}}{kr}\frac{l}{\lambda^2}sinc\frac{[(\alpha_0+\alpha)l]}{\lambda}\int_{-\frac{\pi}{2}}^{\frac{\pi}{2}}(A\hat{x}+B\hat{y}+C\hat{z})e^{jka[(\beta_0+\beta)\sin t+(\gamma_0+\gamma)\cos t]}dt \tag{4.26}$$

where

$$\begin{aligned} A &= e_{0x}\beta a\sin t+e_{0x}\gamma a\cos t \\ B &= e_{0y}\gamma a\cos t+(\frac{\alpha}{\gamma}e_{0x}+\frac{\beta}{\gamma}e_{0y})\gamma a\sin t-e_{0x}\alpha a\sin t \\ C &= -(\frac{\alpha}{\gamma}e_{0x}+\frac{\beta}{\gamma}e_{0y})\beta a\sin t-e_{0x}\alpha a\cos t-e_{0y}\beta a\cos t \end{aligned} \tag{4.27}$$

Again, the PO result is polarization independent due to PO limitations.

The circular cylinder measured is 4 inches in diameter and 12 inches in length. Aspect angles $\theta_0\approx\theta\approx3^0$, $\phi_0\approx45^0, \phi\approx225^0$ were used in all of the cylinder measurements. Figure 4.15 shows the measured response of the cylinder for the excitation field incident on the side of the cylinder with the incident electric field polarized parallel to the cylinder axis. Figure 4.16 shows the reconstructed early-time pulse response of the cylinder found using one scattering center. The magnitude and phase of scattering center transfer function are shown in Figure 4.17 and Figure 4.19. Fairly good agreements with PO are seen. The match procedure of pulse responses is shown in Figure 4.18. Figure 4.20 shows the measured response of the cylinder for the excitation field incident on the side of the cylinder with the incident electric field polarized normal to the cylinder axis. Figure 4.21 shows the reconstructed early-time pulse response found using a single scattering center. The second blip at about 1.3 ns corresponds to the creeping wave returning from one transit around the cylinder and is a late-time phenomenon. To show how phases of transfer functions are obtained and compared, Figure 4.23 demonstrates the pulse responses obtained using fitting scheme and PO. The magnitude and phase of transfer function of the scattering center are shown in Figure 4.22 and Figure 4.24, and good agreements with PO are again observed. The difference is caused by PO conditions are not satisfied, such as far zone condition, $\lambda \to 0$, etc.

The second case is that the excitation field incident on the end of the cylinder as shown in Figure 4.25. The result is similar to scattering from a flat plate, as given by [23]

$$\vec{E} = -j2\pi E_0 \frac{e^{-jkr}}{kr} \frac{1}{\lambda^2}[e_{0x}\gamma\hat{x} + e_{0y}\gamma\hat{y} - (\alpha e_{0x} + \beta e_{0y})\hat{z}]\, V \tag{4.28}$$

where

$$V = 2a^2 \int_{-\pi/2}^{\pi/2} \cos^2 t \, sinc\left[\frac{2a(\alpha + \alpha_0)\cos t}{\lambda}\right] \exp[jka(\beta + \beta_0)\sin t]\, dt \tag{4.29}$$

Figure 4.26 shows the measured response of the cylinder with the excitation field incident from the cylinder end. The reconstructed pulse response using one scattering center and two match pulse responses are shown in Figure 4.27 and Figure 4.29, and the transfer function in Figure 4.28 and Figure 4.30. Again, good agreements with PO are observed.

The pulse response of the cylinder illuminated from the end was used as a test of the sensitivity of pulse response reconstruction to the number of terms used in the polynomial expansion of the transfer function. Figure 4.31 shows the transfer function of the cylinder scattering center found using various numbers of terms. For n=-1,0,1 the results is poor since the pulse response cannot be reproduced using so few terms. As the number of terms increases, the agreement with PO improves. We can't choose too many terms since the pulse response tries to match the late-time portion, each scattering center cannot be represented well.

This chapter shows that the transfer function of a particular scattering center is highly dependent on both the aspect angle of the excitation field and on the physical properties of the surface at the specular point. It also tests the fitting scheme using three canonical targets. Good results are demonstrated. This technique can be used to adequately model the behavior of the specular reflection.

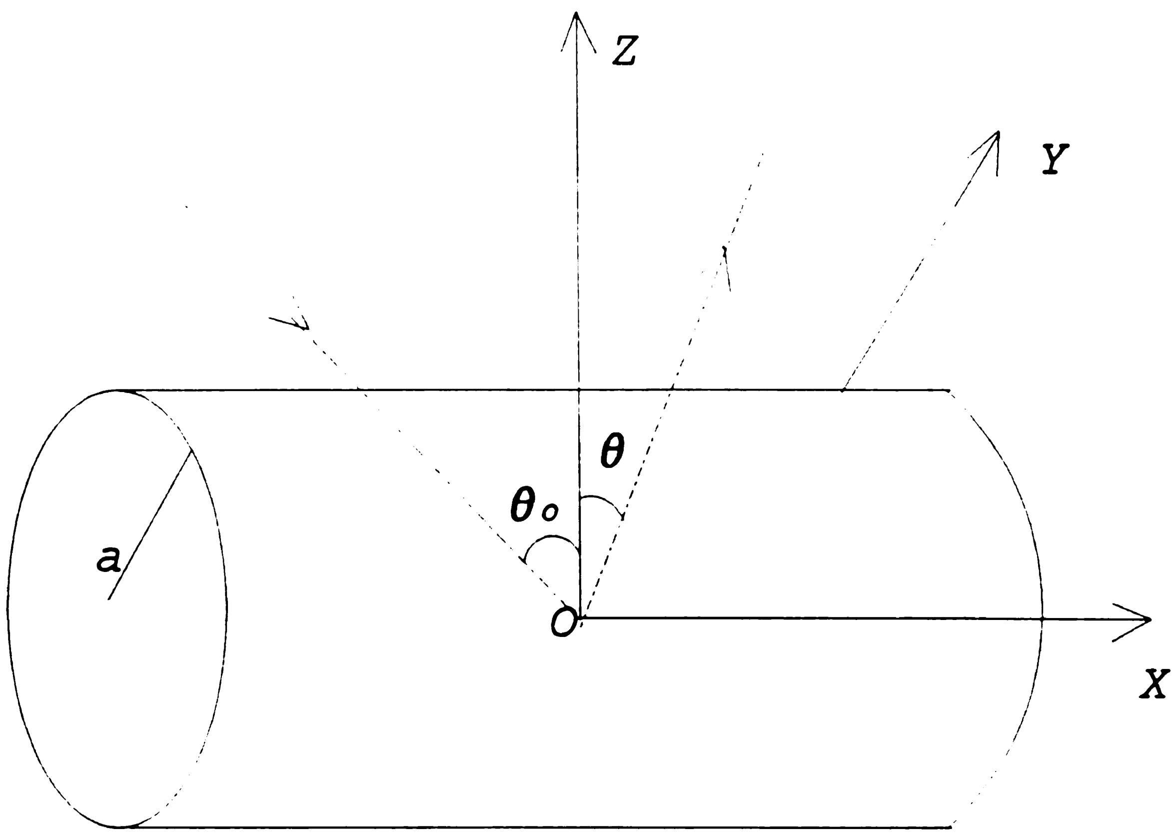

Figure 4.14 Excitation geometry for scattering from the side of a thick cylinder.

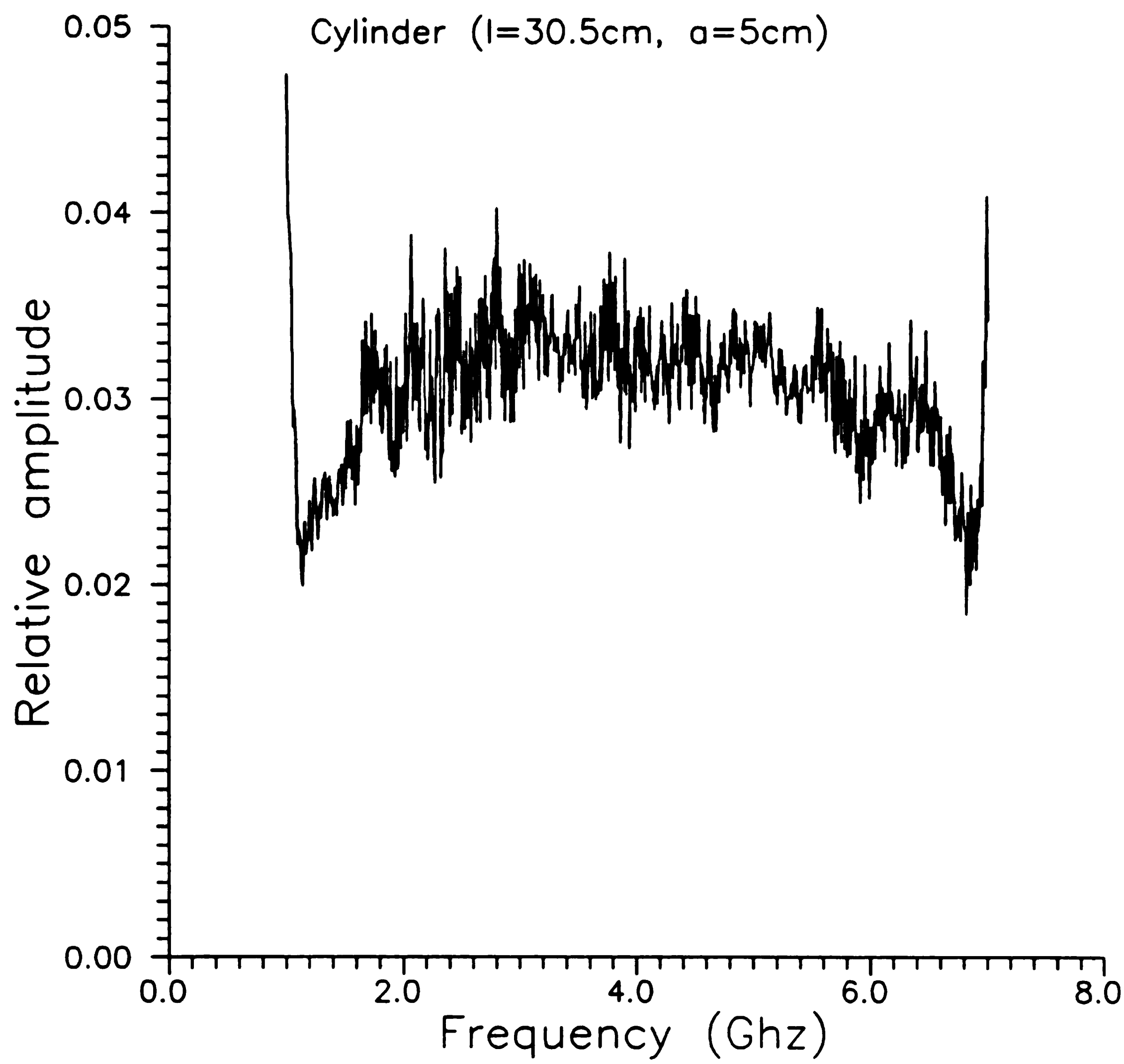

Figure 4.15 Response of cylinder with excitation field incident on the cylinder side and electric field polarized parallel to cylinder axis measured in the frequency band 1-7 GHz.

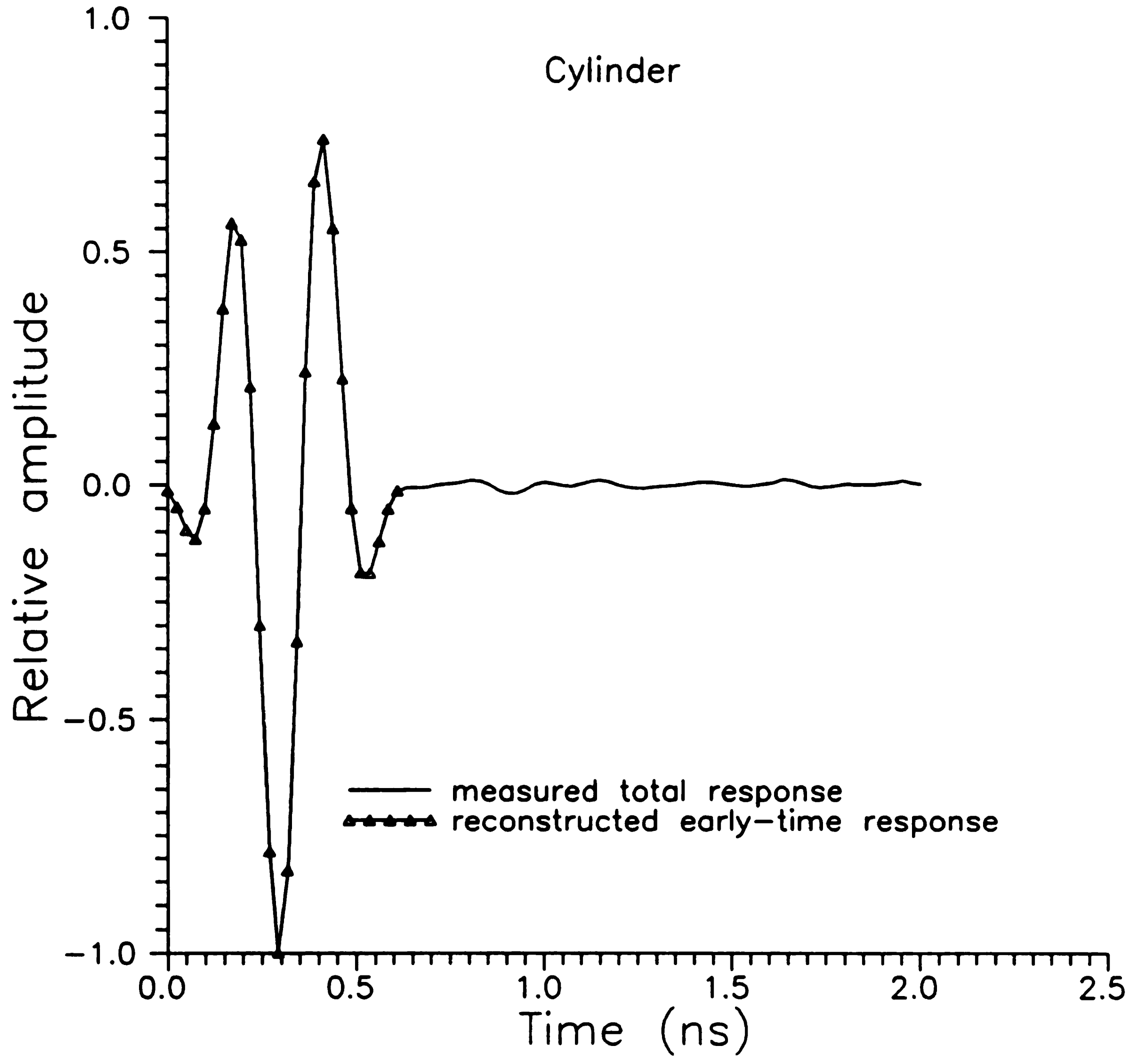

Figure 4.16 Time domain response of cylinder with side incidence and parallel polarization, and early-time response reconstructed using one scattering center.

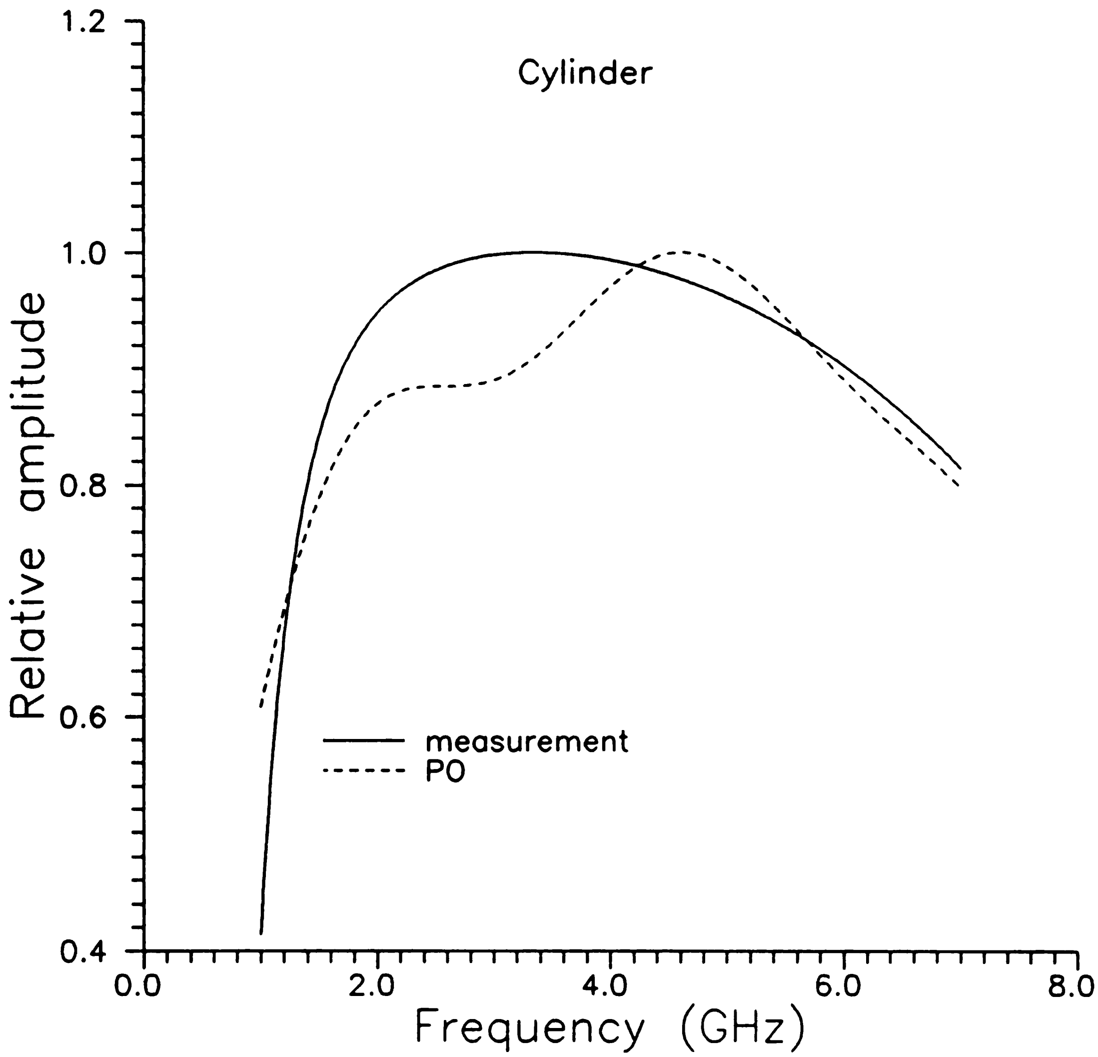

Figure 4.17 Magnitude of transfer function of single scattering center of cylinder with side incidence and parallel polarization.

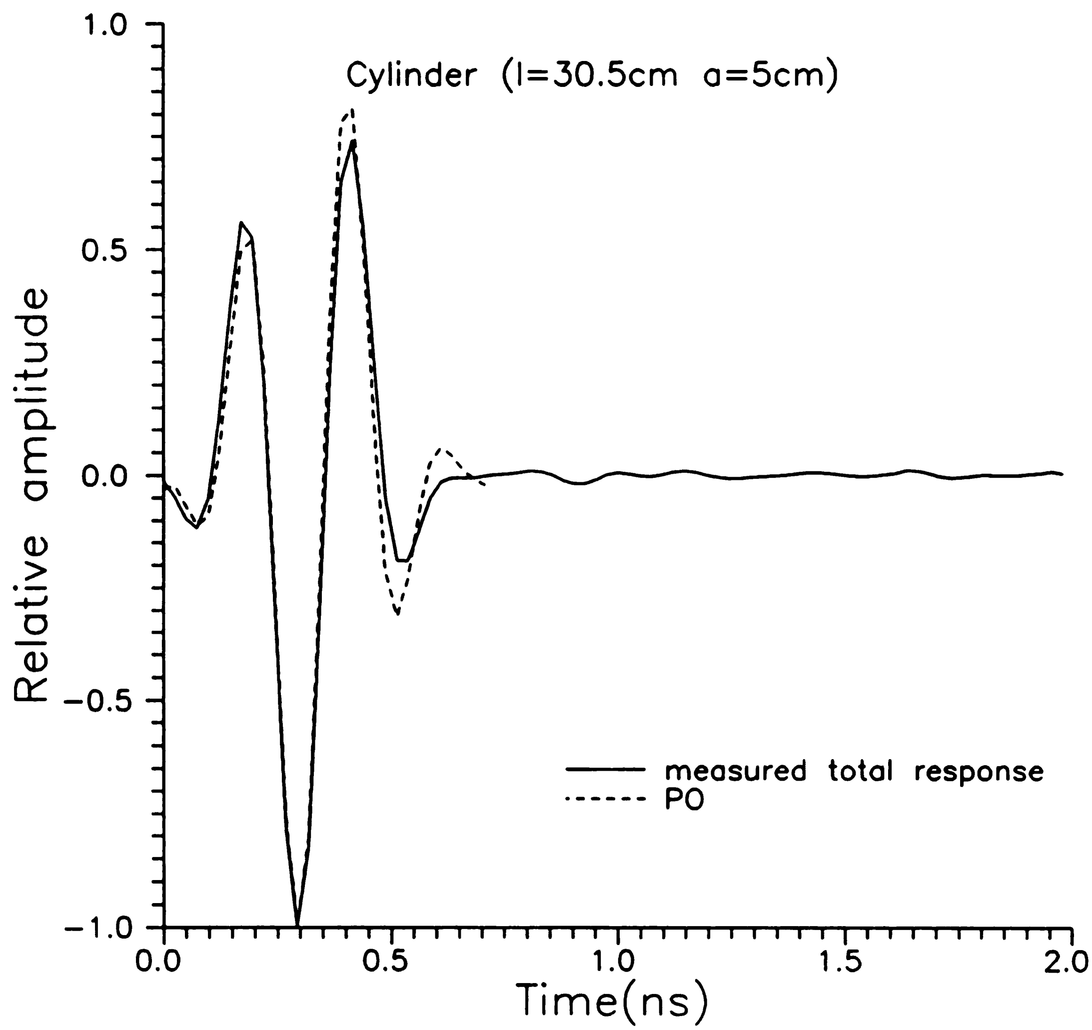

Figure 4.18 Time domain responses of cylinder with side incidence and parallel polarization obtained from measurement and PO.

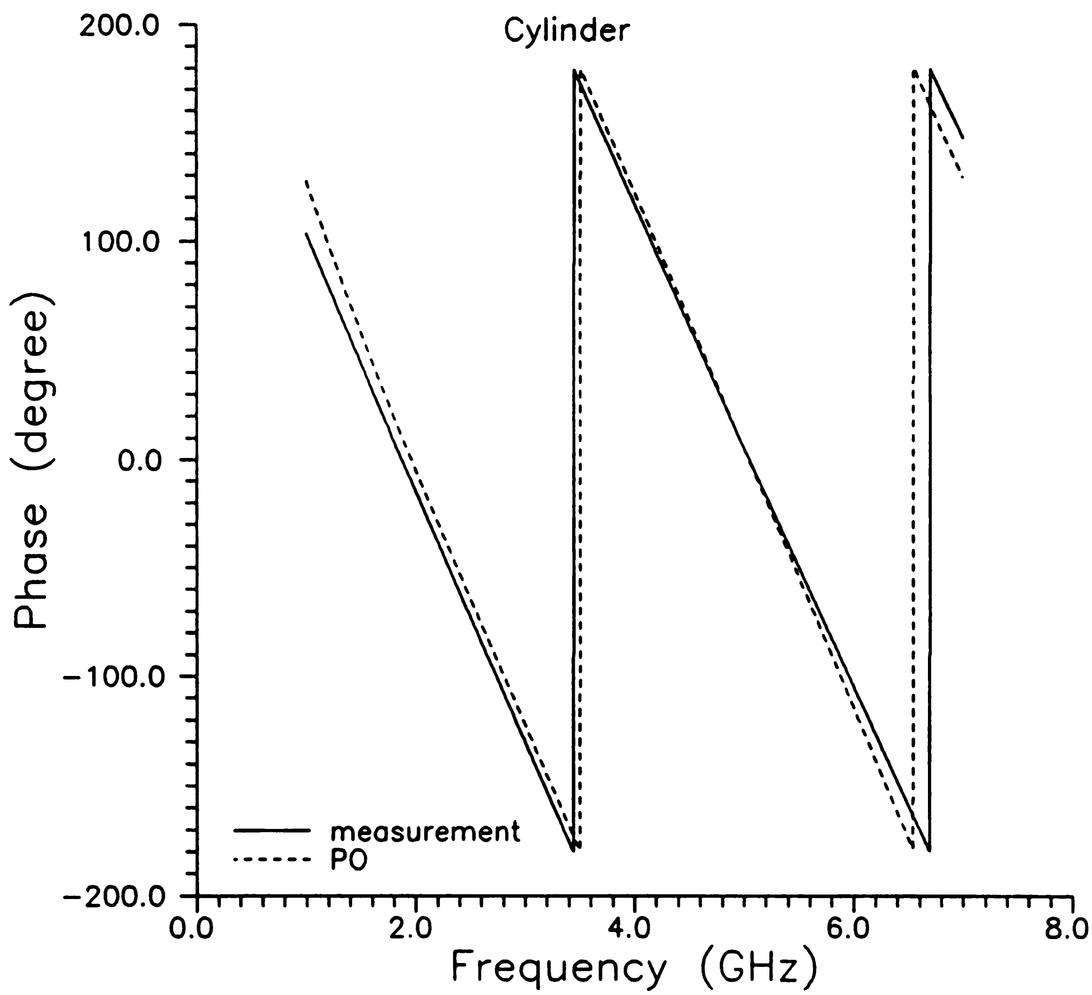

Figure 4.19 Phase of transfer function of single scattering center of cylinder with side incidence and parallel polarization.

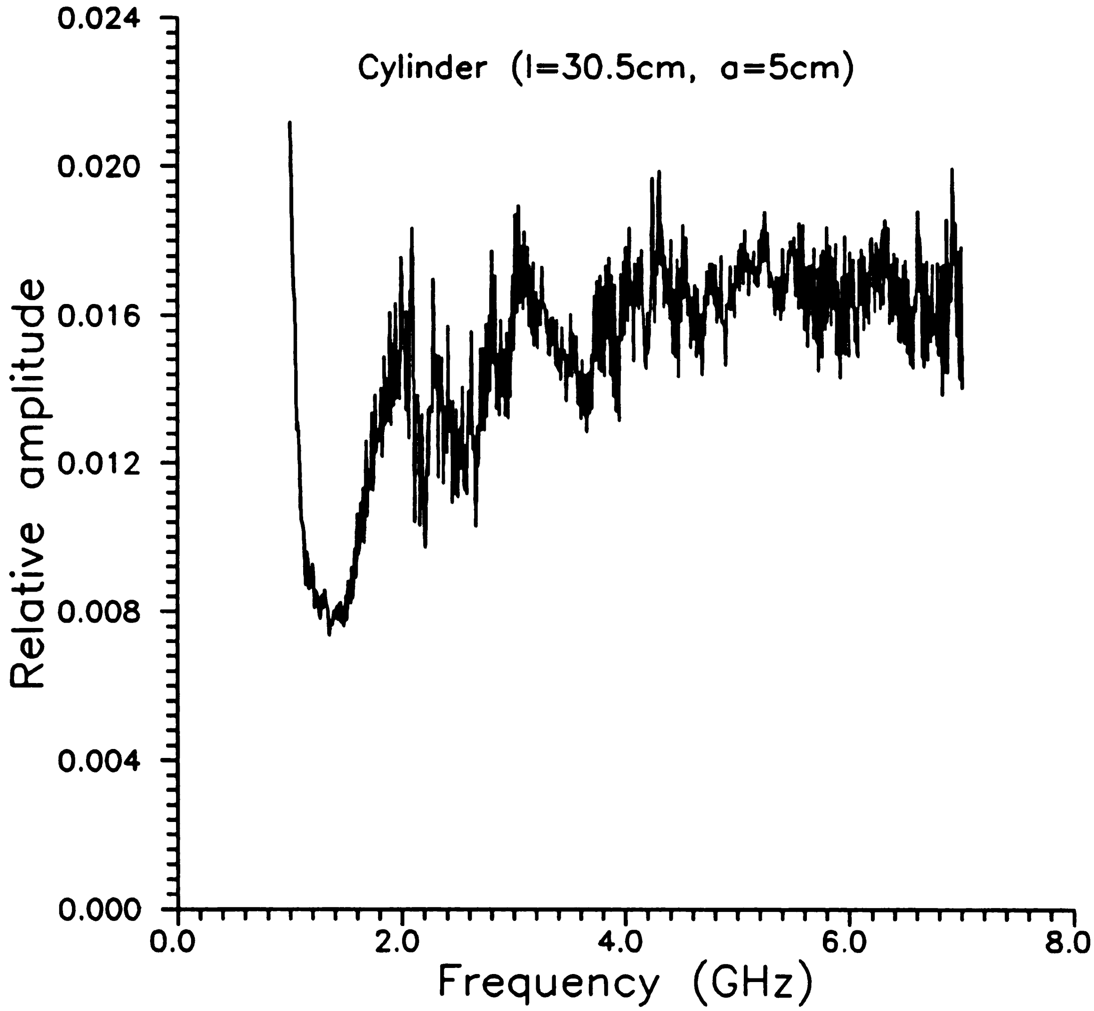

Figure 4.20 Response of cylinder with excitation field incident on the cylinder side and electric field polarized perpendicular to cylinder, measured in the frequency band 1-7 GHz.

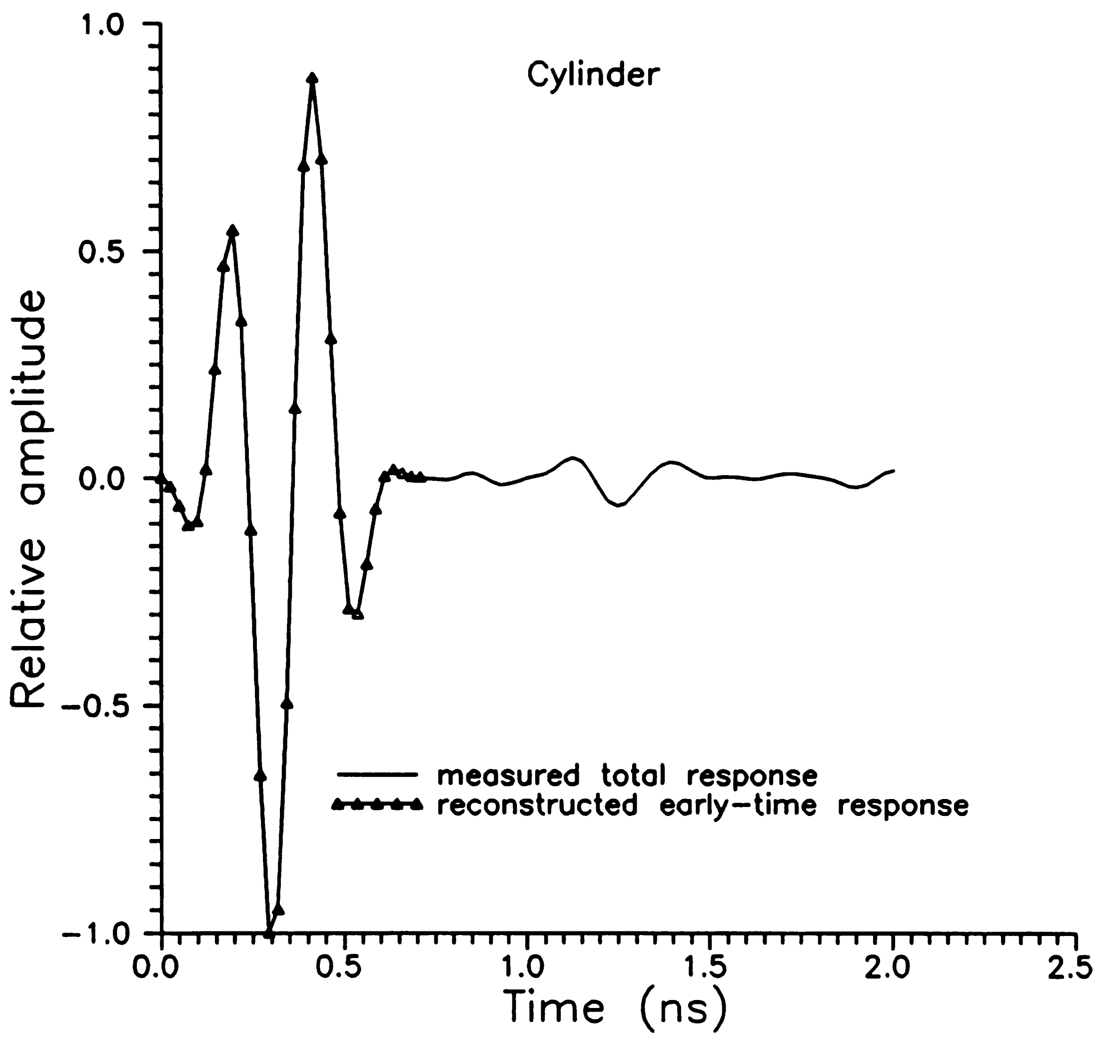

Figure 4.21 Time domain response of cylinder with side incidence and perpendicular polarization, and early-time response reconstructed using a single scattering center.

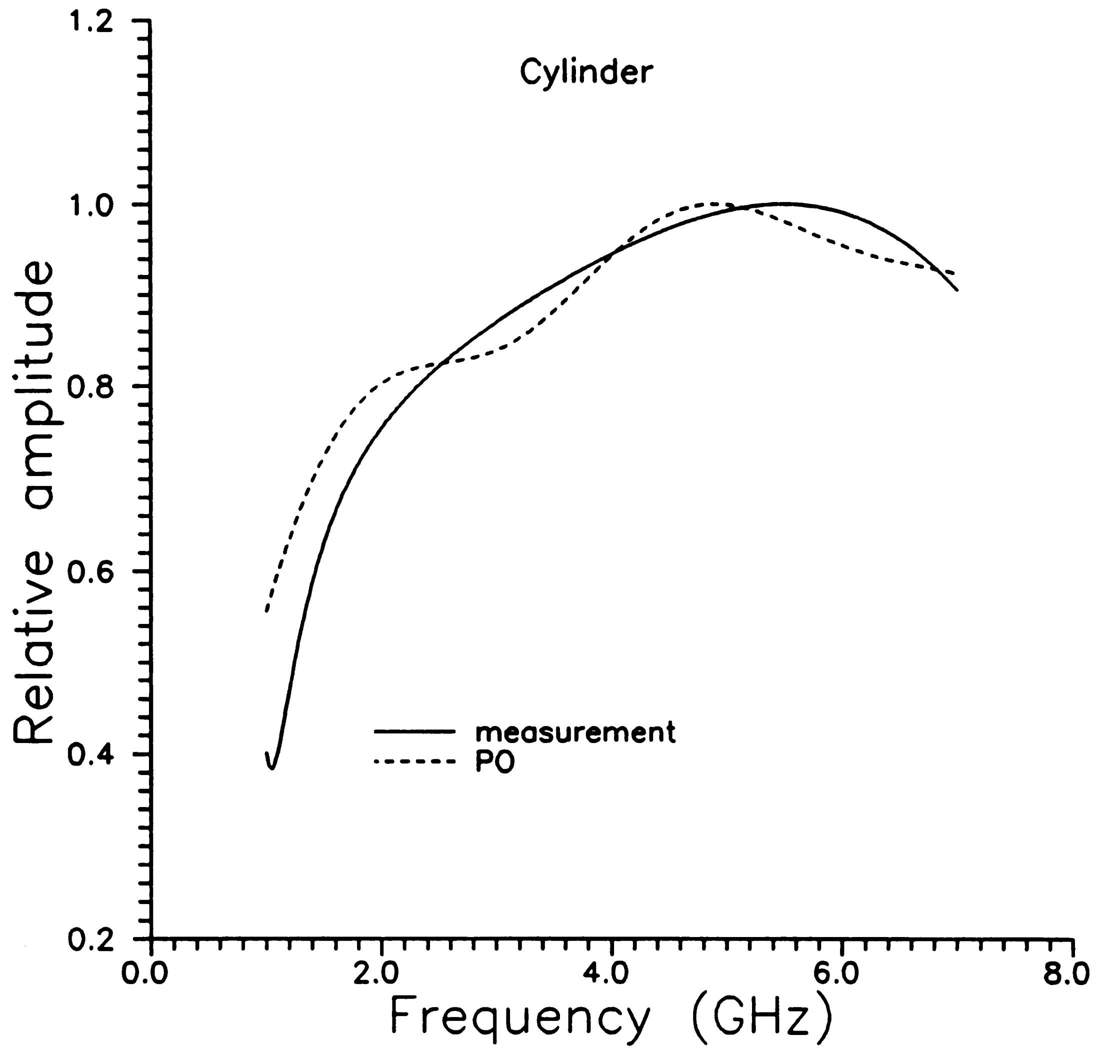

Figure 4.22 Magnitude of transfer function of single scattering center of cylinder with side incidence and perpendicular polarization.

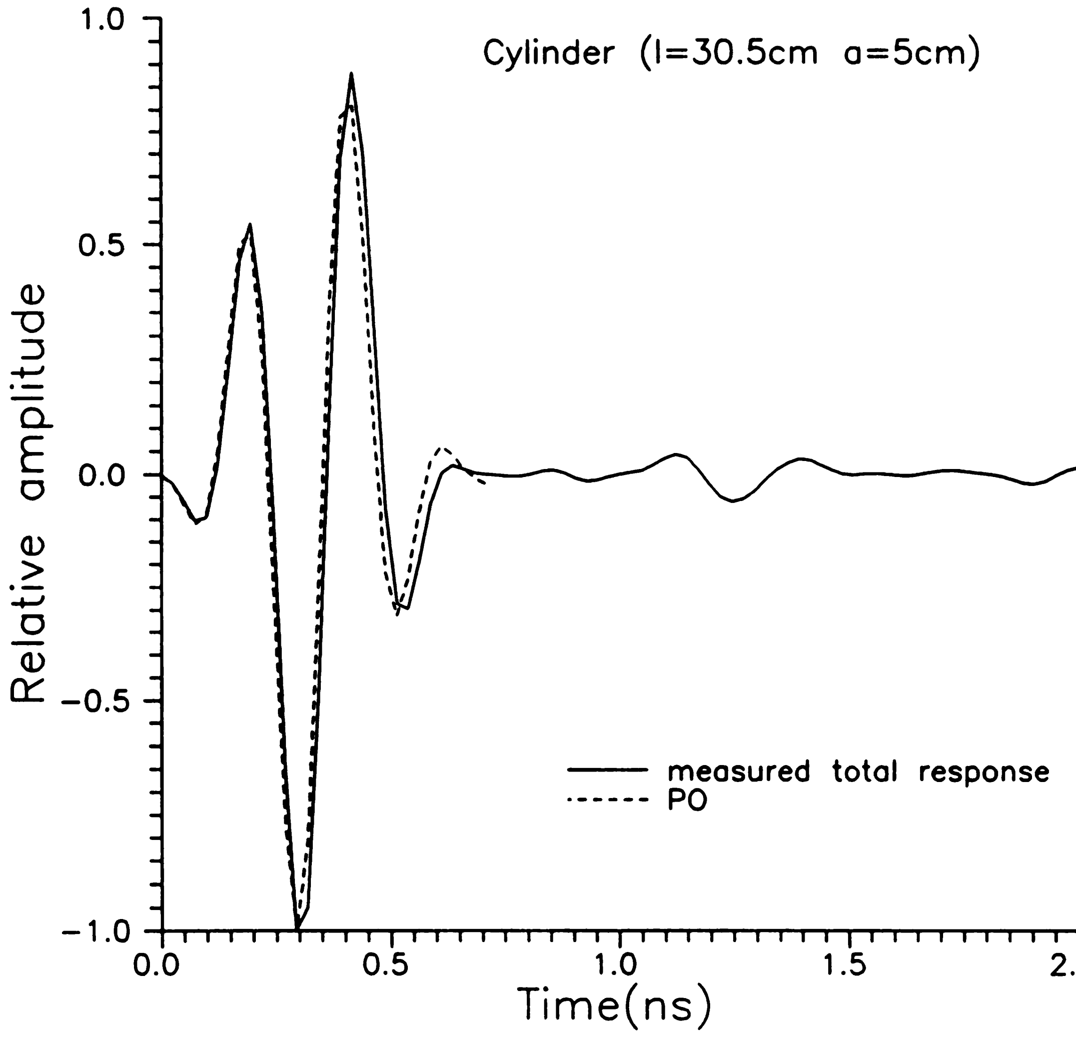

Figure 4.23 Time domain response of cylinder with side incidence and perpendicular polarization, and theoretical response using PO.

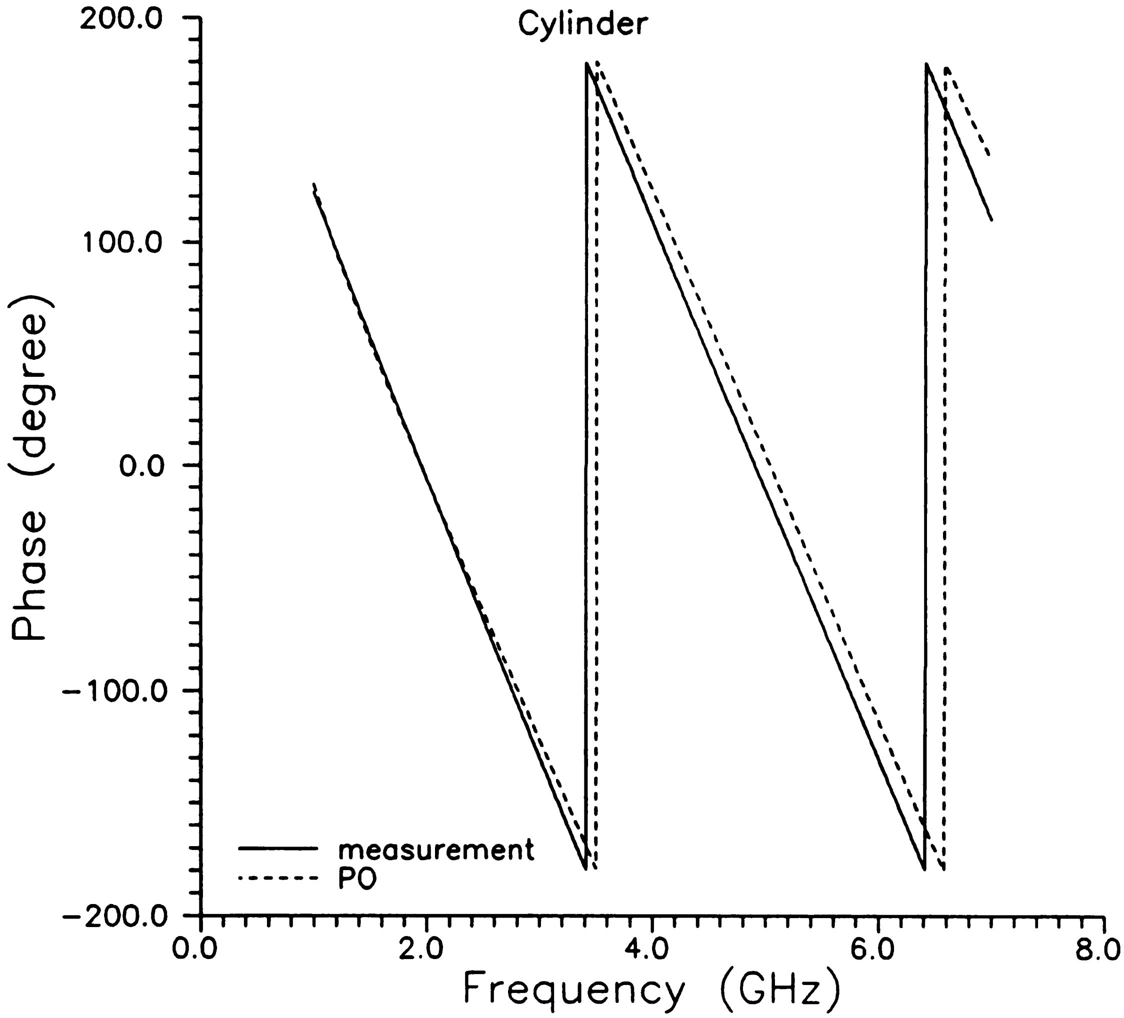

Figure 4.24 Phase of transfer function of single scattering center of cylinder with side incidence and perpendicular polarization.

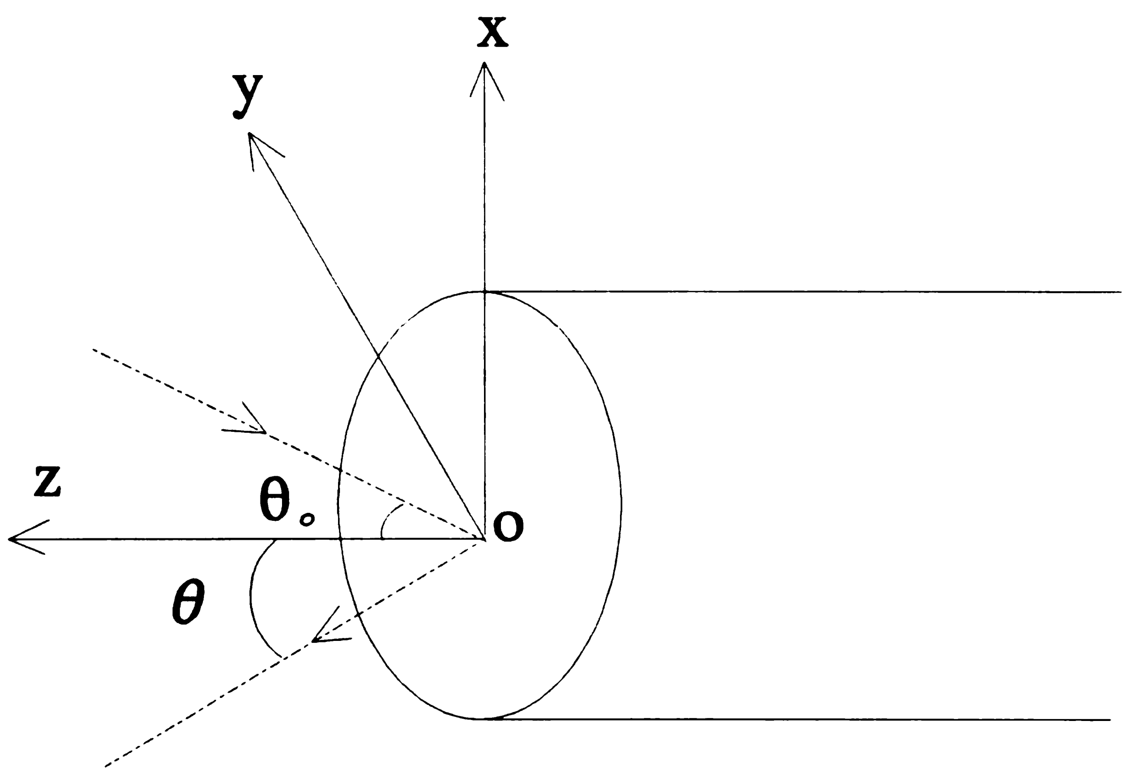

Figure 4.25 Excitation geometry for scattering from the end of a thick cylinder.

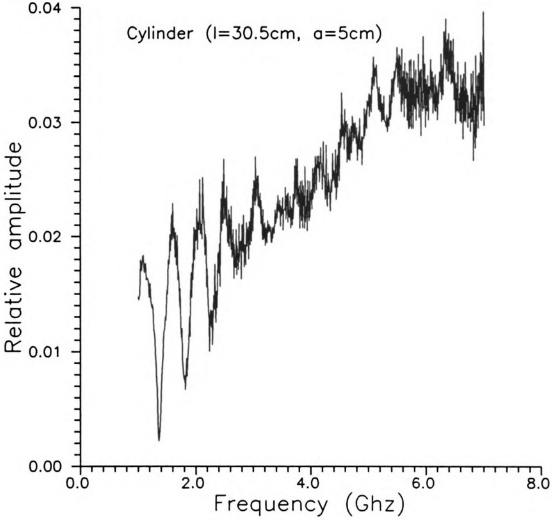

Figure 4.26 Response of cylinder with excitation field incident from end and parallel polarization measured in the frequency band 1-7 GHz.

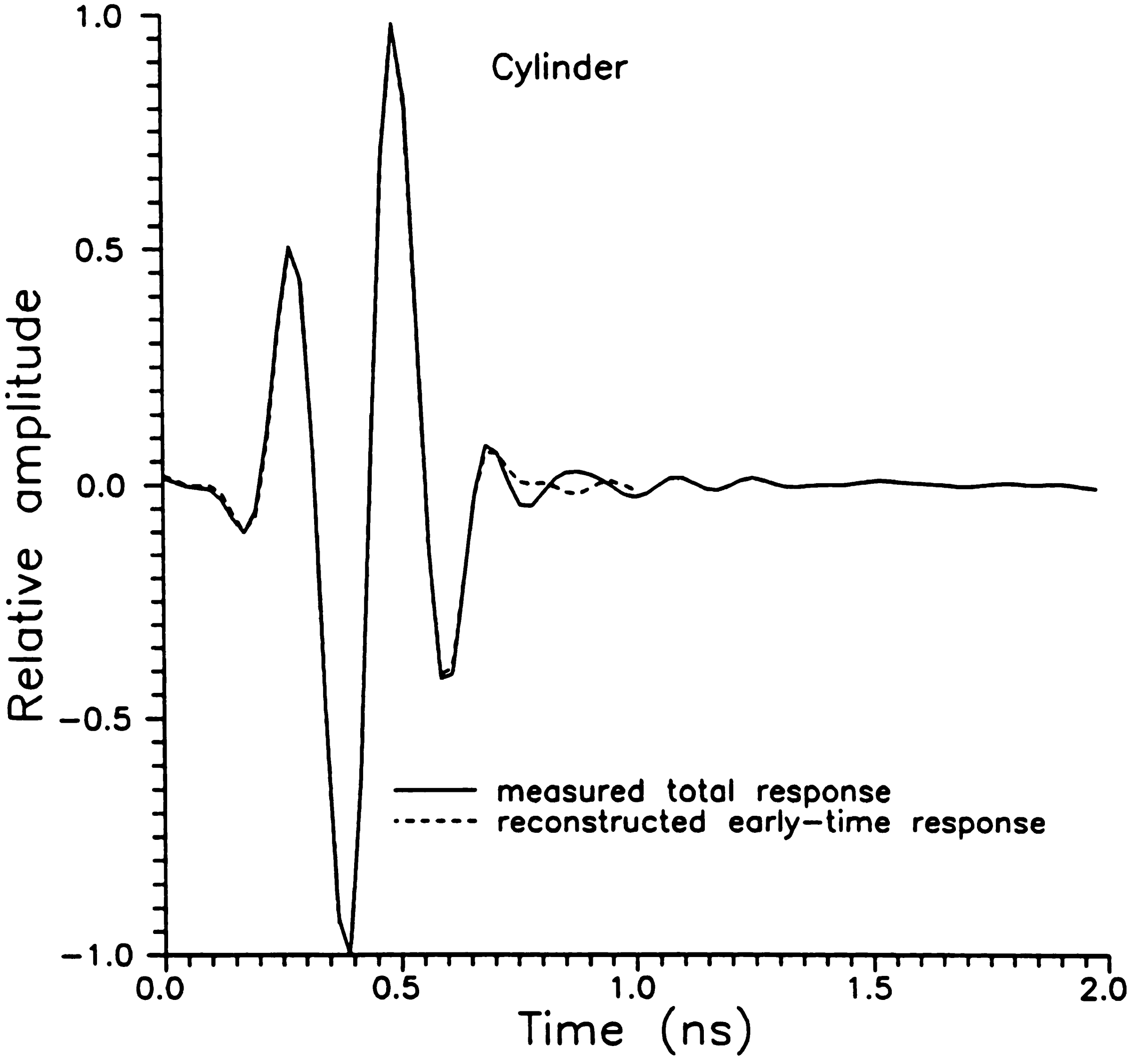

Figure 4.27 Time domain response of cylinder with end incidence and early-time response reconstructed using one scattering center.

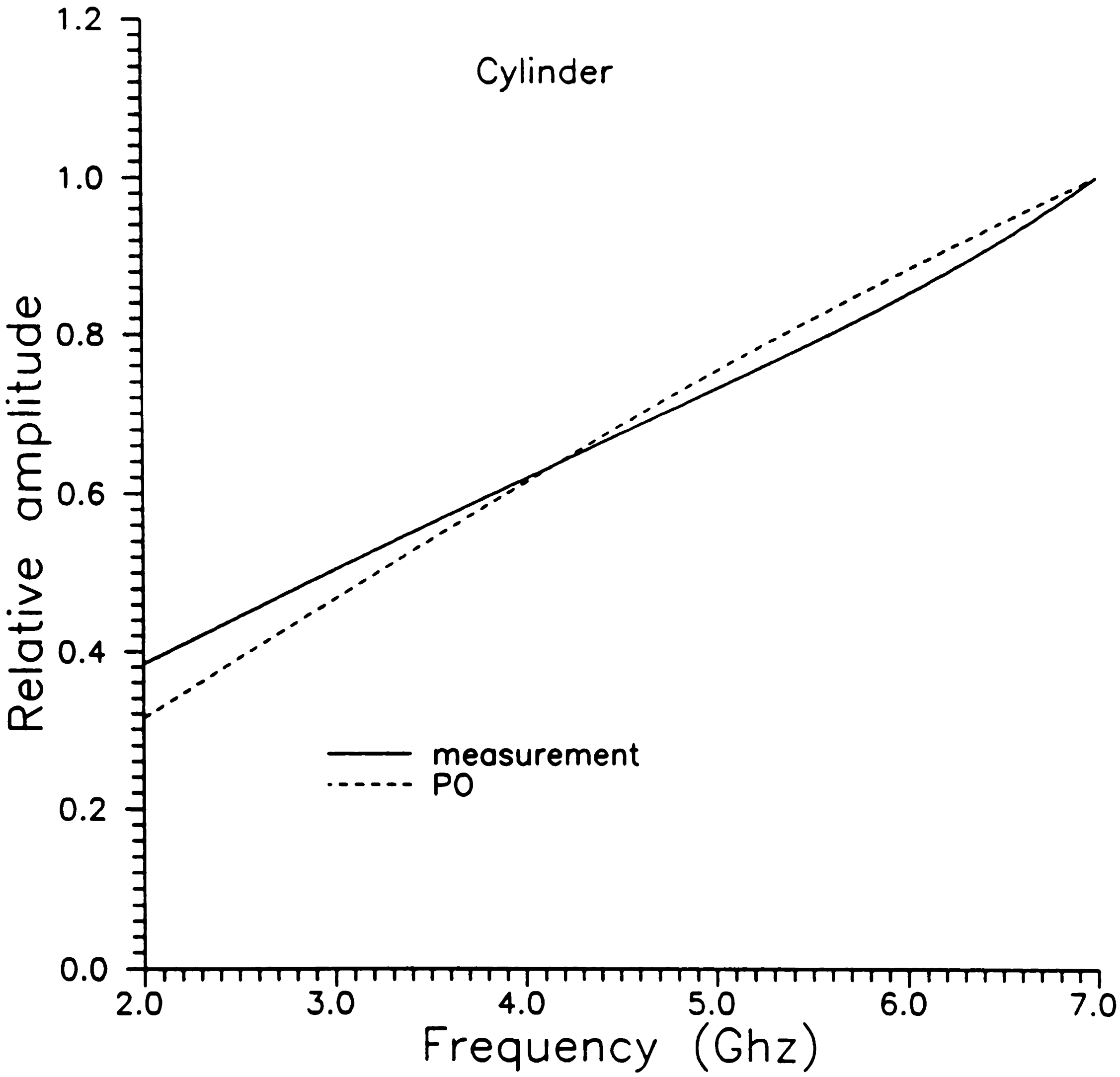

Figure 4.28 Magnitude of transfer function of dominant scattering center of cylinder with excitation incidence from the end.

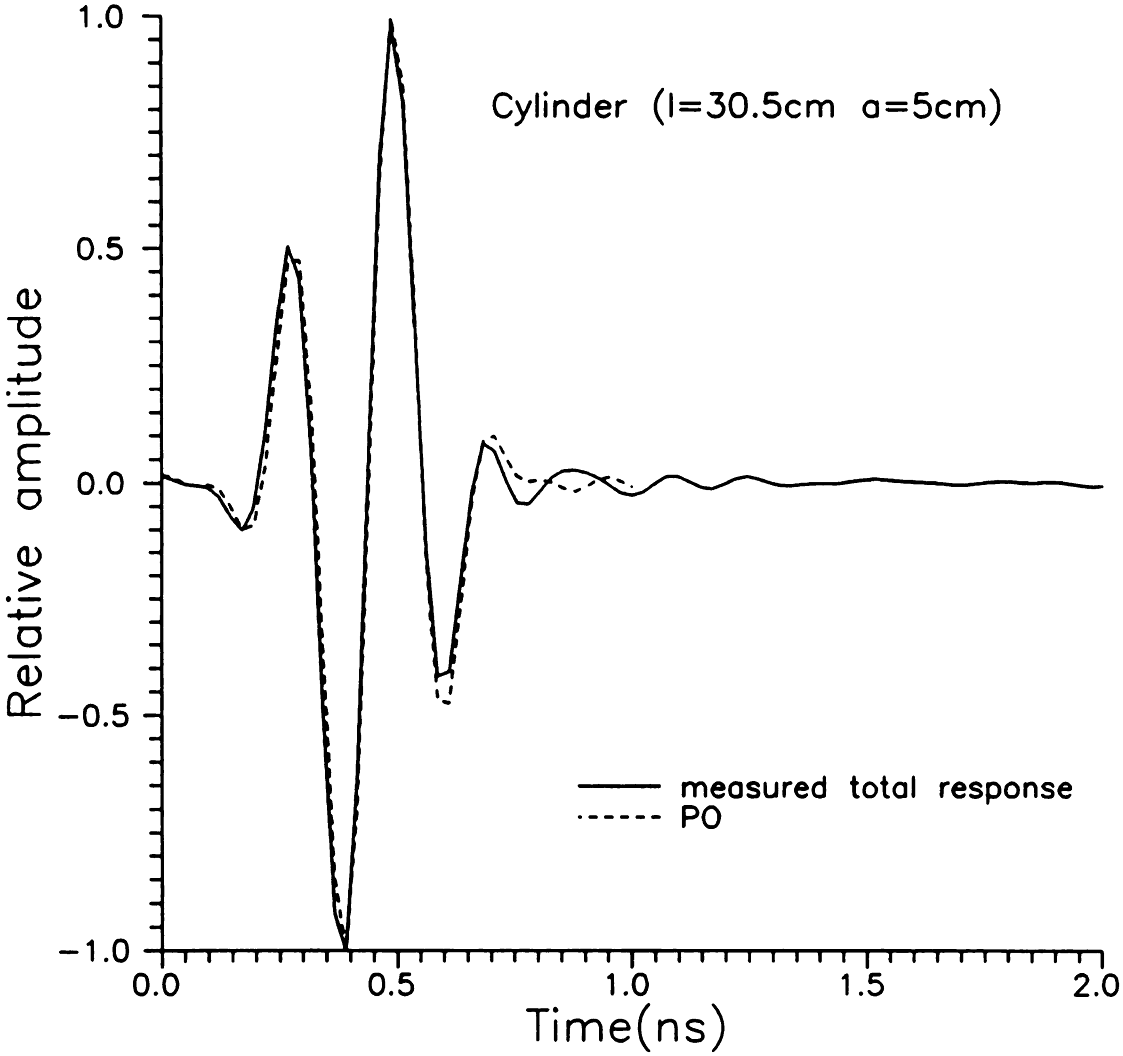

Figure 4.29 Time domain responses of cylinder with end incidence and parallel polarization obtained from measurement and PO.

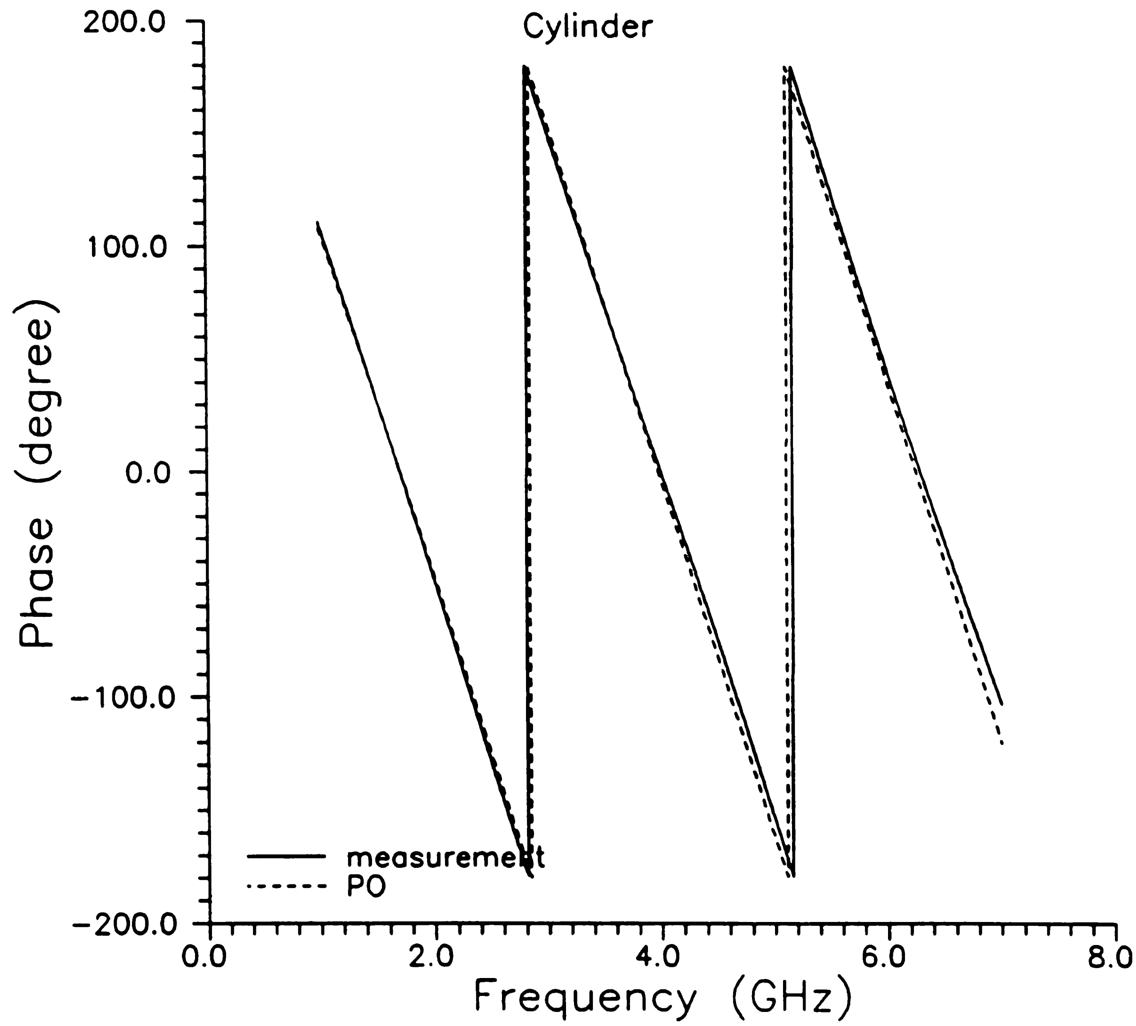

Figure 4.30 Phase of transfer function of dominant scattering center of cylinder with end incidence and parallel polarization obtained from measurement and PO.

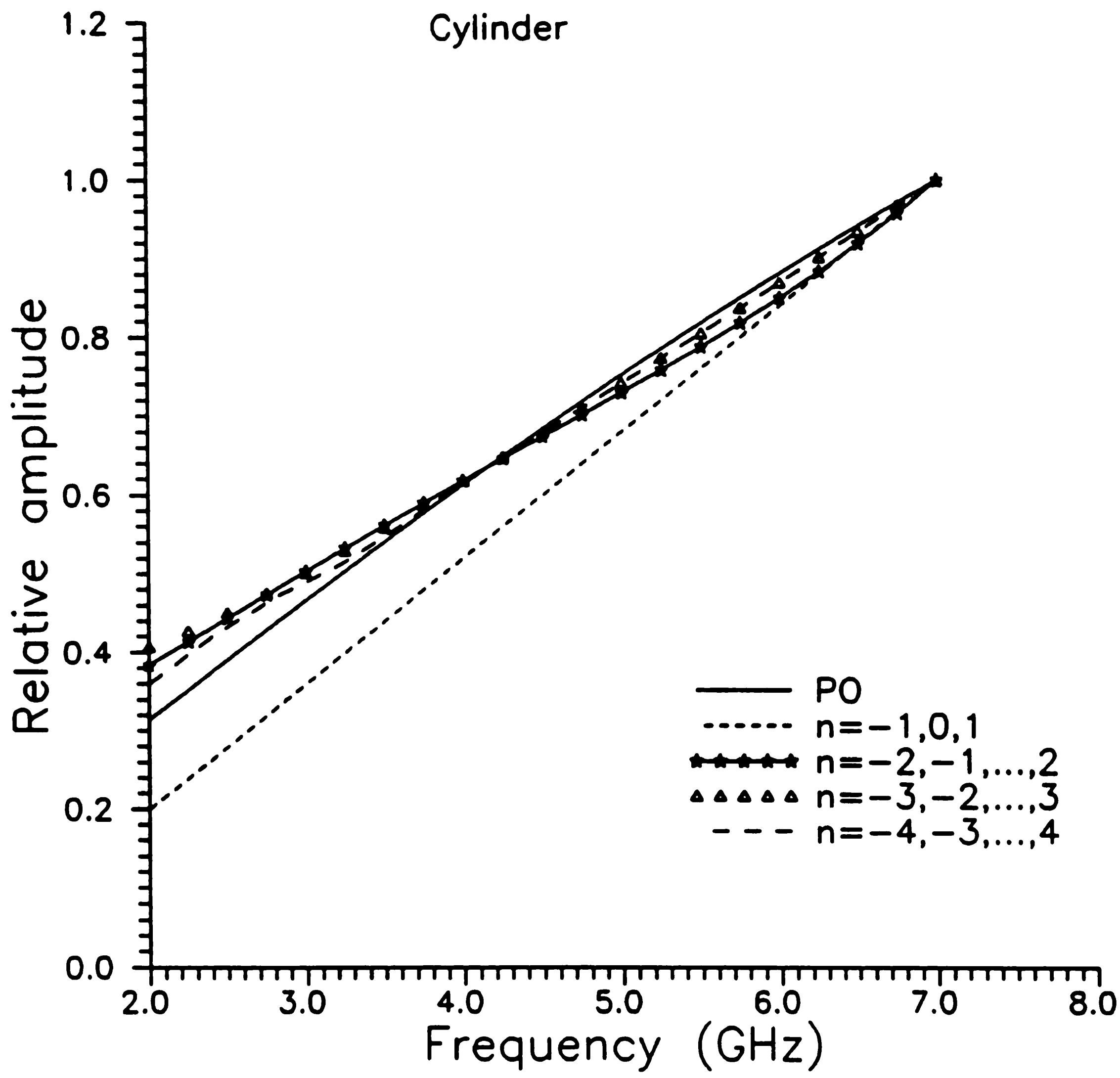

Figure 4.31 Transfer function of single scattering center for cylinder with end-incident excitation determined using various numbers of terms in the polynomial expansion.

5.1

has bee

subject

natural c

al. deve

measured

method i

single-m

has been

Another

[2]. K-p.

complex

of each c

U

excited b

CHAPTER 5

RADAR TARGET DISCRIMINATION USING EARLY-TIME AND LATE-TIME E-PULSE TECHNIQUES

5.1 Introduction

The problem of discriminating and identifying radar targets using radar echoes has been of interest as long as radars have existed. Numerous research studies on this subject have been investigated. Target discrimination schemes based on the late-time natural oscillation behavior of conducting targets have been proposed. K. M. Chen et. al. developed a scheme to extract the natural frequencies of a radar target from a measured response using late-time E-pulse technique and developed a discrimination method involving convolution of the radar return with extinction pulses (E-pulses) and single-mode extraction signals (S-pulses) [3-6], [12], [28]. Resonance mode extraction has been demonstrated with both theoretical and measured transient data [27], [29], [30]. Another technique using the K-pulse has also been shown in many research papers [1], [2]. K-pulses and E-pulses are quite similar except that a K-pulse annihilates all the complex natural resonances, and the duration of the K-pulse is minimal. An advantage of each of the above schemes is their aspect-independence.

Unfortunately, for low Q or targets whose dominant natural resonances are not excited by the interrogating waveform, due to the much smaller amount of signal energy in th

We

usab

targe

the s

reflec

algori

aspect

proces

discrim

a schen

late-tim

amount

5.3 pres

5.4 sho

5.5 dem

and dev

perform

combina

in the late-time response, discrimination using the late-time E-pulse technique is difficult. We must develop a new technique called the early-time E-pulse technique, which is usable with waveforms arising from specular scattering or early-time responses of radar targets. This technique uses resonance cancellation in the frequency domain to eliminate the sinusoidal functions arising from the aspect-dependent temporal positions of specular reflections. Target discrimination using early-time information is then possible using an algorithm identical to that using late-time data, with the exception that discrimination is aspect-dependent [10].

For targets with both strong early-time and late-time responses, the discrimination process will combine both early-time and late-time E-pulse techniques to improve discrimination capabilities or make high-confidence identification decisions. We propose a scheme based on the E-pulse technique which will use information obtained from the late-time portion of the response to narrow the number of possible targets so that the amount of effort expended using the early-time data is decreased markedly.

Section 5.2 reviews early-time E-pulse technique notations and procedure. Section 5.3 presents quantification of radar target discrimination using E-pulse technique. Section 5.4 shows some numerical examples based on the early-time E-pulse technique. Section 5.5 demonstrates how to combine the early-time E-pulse and late-time E-pulse techniques and develop a new discrimination scheme called the combined E-pulse technique. The performance of this technique is also illustrated in section 5.5. The effective of the combined scheme is verified using the measured responses of a B-52, B-58, and F-14.

5.2

dom

the i

local

"part

pulse

cance

It is b

is a d

respon

techniq

from th

respons

of the s

can be

as

where

n^{th} targ

depend

5.2 Summaries of Late-Time and Early-Time E-Pulse Techniques

When a short-duration pulse interacts with a radar target, it produces a time domain scattered field waveform consisting of the effects of two distinct phenomena. As the interrogating pulse passes across the target, specular reflections are returned from localized scattering centers, producing an impulse-like "early-time" component along with "partial resonances". It also establishes the target global resonances after the interrogating pulse has passed the target completely.

The late-time E-pulse radar target discrimination scheme is a natural resonance cancellation technique grounded in the late-time behavior of the transient scattered field. It is based on target natural frequencies and is aspect-independent. We know that there is a duality between the temporal behavior of the late-time component of the transient response and the spectral behavior of the early-time component. The early-time E-pulse technique amounts to a cancellation of the frequency domain sinusoidal functions arising from the aspect-dependent temporal positions of the specular reflections.

In the early 1970's Baum [31] proposed a model of the late-time transient response, and devised a means to calculate the relevant parameters from the geometry of the scatterer. According to his model, the time domain backscattered field response can be written as a sum of the aspect-independent natural resonance modes of the target as

$$r(t) = \sum_{n=-N}^{N} A_n e^{s_n t} \qquad t>T_L \tag{5.1}$$

where $s_n = \sigma_n + j\omega_n$. s_n is the aspect-independent complex resonant frequency of the n^{th} target mode occurring in complex-conjugate pairs (i.e., $s_{-n}=s_n^*$), A_n is the aspect-dependent complex amplitude of the n^{th} mode, N is the number of modes excited by the inc

of l

whe

max

meas

the de

time E

the ea

of the

here p

the m^{th}

where A

p(t). H

expone

incident pulse, and T_L designates the beginning of the late-time period. For the usual case of backscattering measurements, this time is given by

$$T_L = T_b + 2T_{tr} + T_p \tag{5.2}$$

where T_b is the time when incident wave strikes the leading edge of the target, T_{tr} is maximum one-way transient time along the line of sight, and T_p is pulse width used in measurement system. (5.1) can also be written in an alternative form as

$$r(t) = \sum_{n=1}^{N} a_n e^{\sigma_n t} \cos(\omega_n t + \phi_n) \tag{5.3}$$

The aspect-independent nature of the natural resonance frequencies has prompted the development of several target discrimination schemes, including the K-pulse and late-time E-pulse techniques. Although these techniques are aspect-independent, they ignore the early-time component of the transient response, which often contains a large portion of the signal energy.

Altes [11] has proposed a simple model for the early-time response

$$r_E(t) \approx \sum_{m=1}^{M} p(t) * h_m(t - T_m) \quad t < T_L \tag{5.4}$$

here $p(t)$ is the incident pulse and $h_m(t)$ is the localized impulse response originating at the m^{th} scattering center at time T_m. In the frequency domain this response becomes

$$R_E(\omega) = \mathscr{F}[r_E(t)] \approx \sum_{m=1}^{M} P(\omega) H_m(\omega) e^{-j\omega T_m} \tag{5.5}$$

where $H_m(\omega)$ is the transfer function of m^{th} scattering center and $P(\omega)$ is the spectrum of p(t). Hurst and Mittra [8] suggest that the transfer function can be approximated as an exponential function of frequency. Assuming that $P(\omega)$ is a slowly varying function then give

wher

cente

relate

numb

term

proces

contril

Moses

the spe

late-tim

respons

where c

and x r

early-ti

when c

In parti

gives

$$R_E(\omega) \approx \sum_{m=1}^{M} B_m e^{\tau_m \omega} \tag{5.6}$$

where $\tau_m = \alpha_m - j\,T_m$ are called "complex times", and are associated with the scattering center impulse responses. Note that M is the number of exponential terms which is related to the number of scattering centers. However, M is not the exact scattering center number, since our measurement system is bandlimited and more than one exponential term may be needed to represent one scattering center. The physics of the scattering process (reflection or diffraction) determines the amplitude of each scattering center contribution in (5.6). We notice that (5.6) is essentially the model used by Carriere and Moses [9] in their Prony method analysis of target scattering centers.

There exists an obvious duality between the temporal late-time response (5.1) and the spectral early-time response (5.6). This duality allows the direct application of the late-time E-pulse technique to spectral early-time data.

In summary, both the temporal late-time response and the spectral early-time response can be expressed in a general exponential form

$$f(x) = \sum_{k=1}^{K} c_k e^{Q_k x} \qquad X_L < x < X_F \tag{5.7}$$

where c_k and Q_k are complex constants, X_L, X_F are the domain of the signal measurement, and x represents time in the case of a late-time response or frequency in the case of an early-time response. An E-pulse $e(x)$ is a real waveform with finite duration X_E which when convolved with $f(x)$ eliminates a preselected component of the exponential series. In particular, the entire series can be eliminated resulting in

The co

cance

where

[29]. [

using t

5.3

pioneer

the earl

betwee

discrim

each E

Discrim

The ED

$$c(x) = e(x)*f(x) = \int_0^{X_E} f(x')e(x-x')dx' \equiv 0 \quad X_L+X_E<x<X_F \tag{5.8}$$

The conditions for obtaining an extinction pulse are presented in the context of resonance cancellation as

$$E(s=Q_k) = E(s=Q_k^*) = 0 \tag{5.9}$$

where $E(s)$ is the Laplace transform of $e(x)$. The E-pulse mode extraction technique [27], [29], [30] can be used to find $e(t)$, Q_k can then be found from (5.9), and c_k is extracted using the least squares method.

5.3 Quantification of Radar Target Discrimination Using E-Pulse Technique

The automation of the late-time E-pulse discrimination method was originally pioneered by Rothwell and Ilavarasan [12], [32]. A similar approach can be applied to the early-time E-pulse discrimination scheme since it is developed based on the duality between spectral early-time response and temporal late-time response. Automated discrimination requires a measure of the amount of signal presented in the waveform for each E-pulse to quantify discrimination. To quantify discrimination an "E-pulse Discrimination Number" (EDN) is defined

$$EDN = \frac{\int_{X_L+X_E}^{X_F} [c(x)]^2 dx}{\int_0^{X_E} [e(x)]^2 dx} \tag{5.10}$$

The EDN is a measure of the deviation from the expected value of zero energy. For a tem

two

unk

in (

E-p

the

vani

iden

diffe

by

There

produc

accura

supplie

sensitiv

spectru

shifting

early-ti

frequen

discrim

shifted

temporal late-time response, the choice of the window duration is usually based on the two-way transient time and signal to noise ratio (SNR) present in the measurement of an unknown target. Note that the convolution energy is normalized by the E-pulse energy in (5.10). To use the EDN for automated discrimination, the EDN is calculated for each E-pulse in the data base. In actual situations, noise and inaccuracies in the estimates of the target Q_k used to construct the E-pulses will prevent the EDN from precisely vanishing when the E-pulse is matched to the unknown target. Thus the target is identified by the E-pulse yielding the minimum EDN. As a quantitative measure of the differences in all the EDN values, the "E-pulse discrimination ratio" (EDR) is defined by

$$EDR\,(dB) = 10.0 \log_{10}\left\{\frac{EDN}{\min(EDN)}\right\} \tag{5.11}$$

Therefore, the E-pulse yielding the smallest EDN has an EDR of 0 dB, while the EDRs produced by the other E-pulses are greater than 0 dB. Note that if the method is working accurately, EDR should be 0 dB when the E-pulse matches the target. Thus, EDR supplies a better measure of radar target discrimination.

The E-pulse discrimination scheme (especially, early-time E-pulse method) is sensitive to the estimation of T_b. Since the early-time E-pulse technique is based on the spectrum of the early-time response, the time shifting in defining T_b will cause the shifting of the complex times of the exponential sinusoidal waveforms that make up the early-time spectrum. This sensitivity to the T_b reference arises when one constructs frequency domain E-pulses for the early-time response and subsequently attempts discrimination using an independently measured response whose beginning time has shifted by an amount τ from the response used to synthesize the E-pulse. We can find that tl

overco

A sim

is not

due t

circum

differe

real pa

be T_b.

discrim

at whic

The thr

limit th

betwee

where

value o

5.4

concen

that the effectiveness of the early-time frequency domain E-pulse is reduced [34]. To overcome this difficulty, we must have a reference feature for each early-time response. A simple reference is the maximal point in the early-time response Unfortunately, this is not enough since there are usually some slight shifts associated with each measurement due to equipment variations or slight changes in the target angular position. To circumvent this problem, the discrimination process is repeated many times for slightly different values of τ. The point at which the convolution of one early-time E-pulse with real part (or imaginary part) of the spectral early-time response is a minimal is taken to be T_b.

Another method to determine the beginning time (commonly used in late-time discrimination process) uses a computer model of a threshold detector [33]. The point at which the target response is greater than the threshold voltage V_T is taken to be T_b. The threshold must be set to be small enough to detect weak signals but large enough to limit the false alarm rate to an acceptable level. For Gaussian white noise, the mean time between false alarms T_f for a given V_T is given by [33]

$$T_f = \frac{1}{B_{IF}} \exp \frac{V_T^2}{2\psi_0} \tag{5.12}$$

where B_{IF} is the IF bandwidth of the measurement system, and ψ_0 is the mean-square value of the noise voltage.

5.4 Performance of Early-Time E-Pulse Discrimination Scheme

Many papers have been published about late-time E-pulse discrimination. We will concentrate on the early-time E-pulse technique in this section. To demonstrate early-time canc

1:72

perfo

pulse

is bas

meas

band

wings

with a

GHz a

early-ti

crosses

Gaussia

constru

on the

reconst

The E-

forced

domain

pulses c

cancellation using early-time target responses, the ultra-wide-band measurements of a 1:72 scale B-52 aircraft model, a 1:48 scale B-58, and a 1:32 scale F-14 are used to perform E-pulse cancellation of early-time scattered field responses. The early-time E-pulses of three targets are created at an increment of 2.7^0. The choice of this increment is based on the "correlation discrimination range" presented in Chapter 6.

Figure 5.1 shows the magnitude of the scattered field response of the B-52 measured at 45.9^0 incidence from nose-on in the anechoic chamber within the frequency band 2-18 GHz, with the incident electric field polarized in the plane of the aircraft wings.

The transient response of the B-52 has been obtained by weighting the spectrum with a Gaussian modulated cosine function with $\tau=0.1$ ns and center frequency of 10.0 GHz and then inverse transformed using the FFT. The result is shown in Figure 5.2. The early-time period is dominated by specular reflections during which the incident pulse crosses the aircraft. The equivalent incident pulse is the inverse Fourier transform of Gaussian modulated cosine weighting function as shown in Chapter 7.

The spectrum of the early-time portion of the response can be canceled by constructing an E-pulse based on the complex times determined by the specular points on the B-52. Figure 5.3 shows the real part of the spectrum of the early-time and its reconstruction using the 25 extracted complex times. The match is seen to be excellent. The E-pulse constructed from the extracted complex times is shown in Figure 5.4. A forced DC-canceling E-pulse has been used here. This E-pulse will cancel the frequency domain sinusoid response.

To test the performance of early-time E-pulse discrimination scheme, all other E-pulses of three targets are also created based on their complex times. Note that the early-time E-pulse duration must be taken within the measurement band limits. The E-pulse duration X_E can be estimated by repeating the program until a reasonable minimal convolution output in (5.8) is obtained. Convolution of the real part of the early-time spectrum shown in Figure 5.3 with each of three E-pulses at the same aspect angle is presented in Figure 5.5, revealing a null response in the "late frequency" range (i.e. after X_L+X_E) after 8.9 GHz for the B-52 target. The B-58 and F-14 show significant components in their late frequency range after 8.4 GHz and 8.5 Ghz. According to the definition of EDR given in (5.11), EDR value is 0 dB for the 45.9^0 B-52, 28.8 dB for 45.9^0 B-58, 24.5 dB for the 45.9^0 F-14. All the values of EDR obtained from each of the E-pulse convolutions are shown Figure 5.6. Note that EDR values have been negative for display purposes. It is easily seen that the correct waveform is identified, with a high level of confidence. It is also observed that the B-52 target can be identified within 41^0-70^0.

To test the effect of various white Gaussian noise levels on the early-time target discrimination scheme, Figure 5.7 shows early-time E-pulse discrimination ratio obtained by convolving the noisy response with SNR=20 dB with each of the three target E-pulses. Again, B-52 is properly identified. The results shown in Figure 5.7 are quite similar to those shown in Figure 5.6 since the target waveform is only slightly distorted at very high SNR. Other results are demonstrated in Figure 5.8, Figure 5.9, Figure 5.10 and Figure 5.11. Obviously, the EDR difference between targets becomes smaller with higher noise level. Therefore, the target discrimination performance becomes worse. It is seen that although the B-52 can still be discriminated at SNR=0 dB, the minimal EDR is at 27^0 instead of 45.9^0 due to the large distortion of the B-52 response.

In summary, the B-52 target can be identified at an SNR of 0 dB. We may test

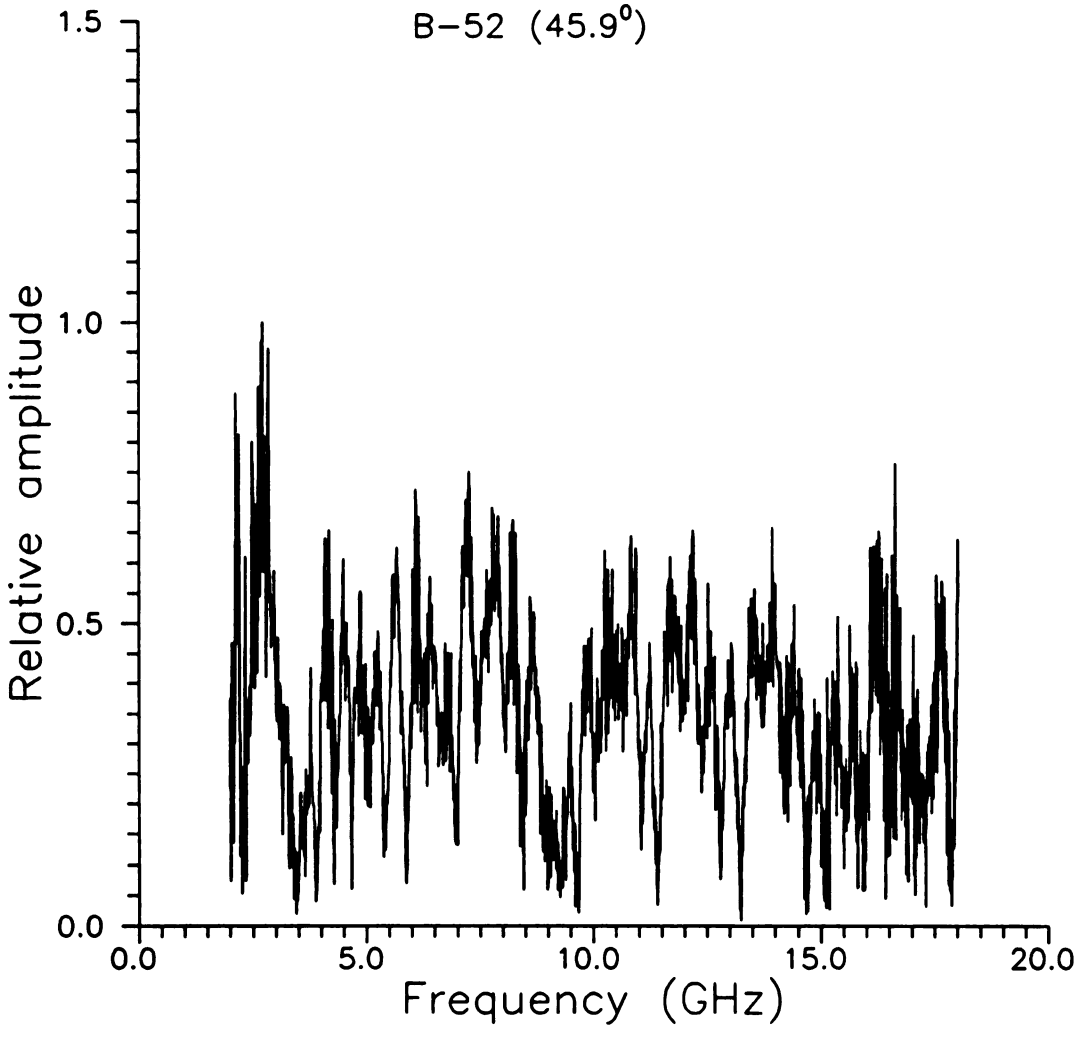

Figure 5.1 Frequency domain scattered-field response of 45.9^0 B-52 aircraft model measured in the band 2-18 GHz.

Figure

Relative amplitude

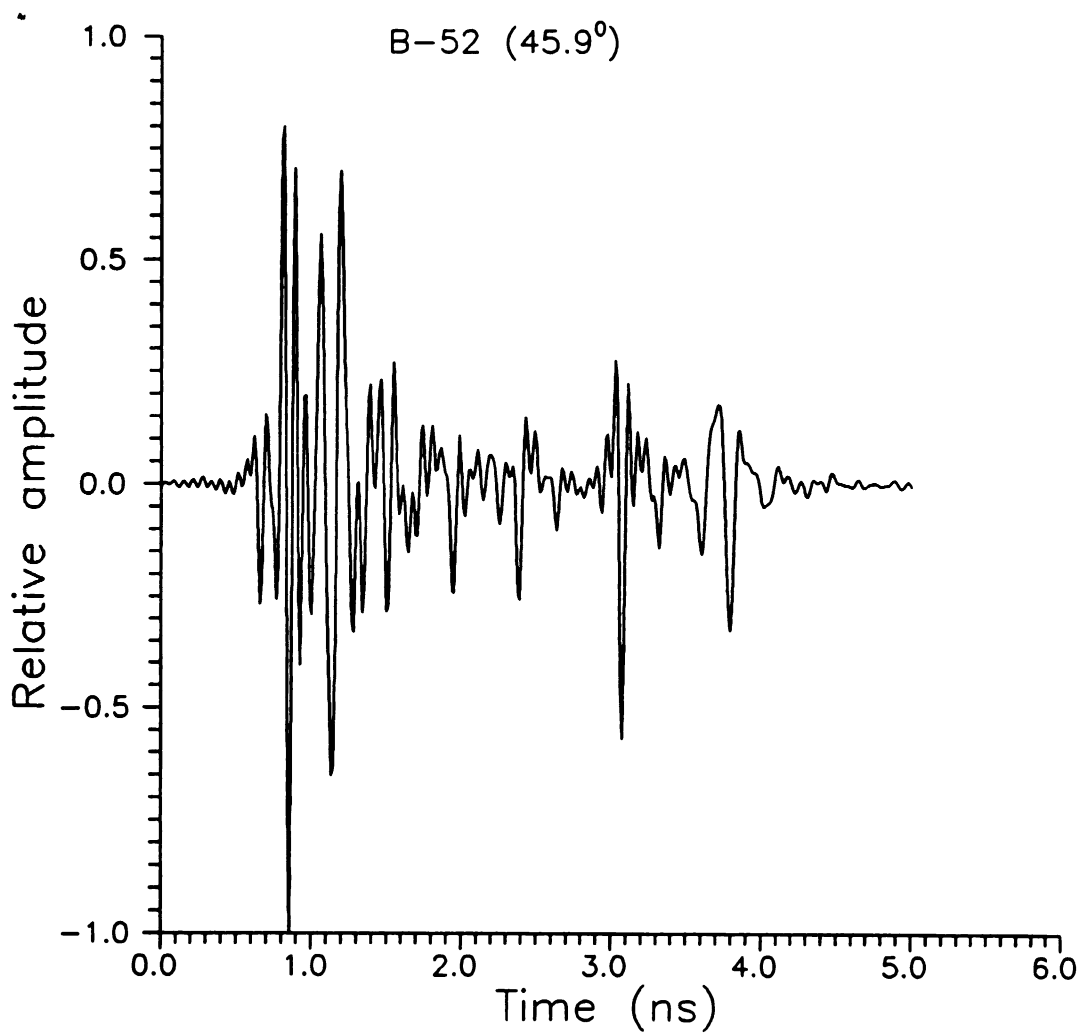

Figure 5.2 Transient response of B-52 aircraft model.

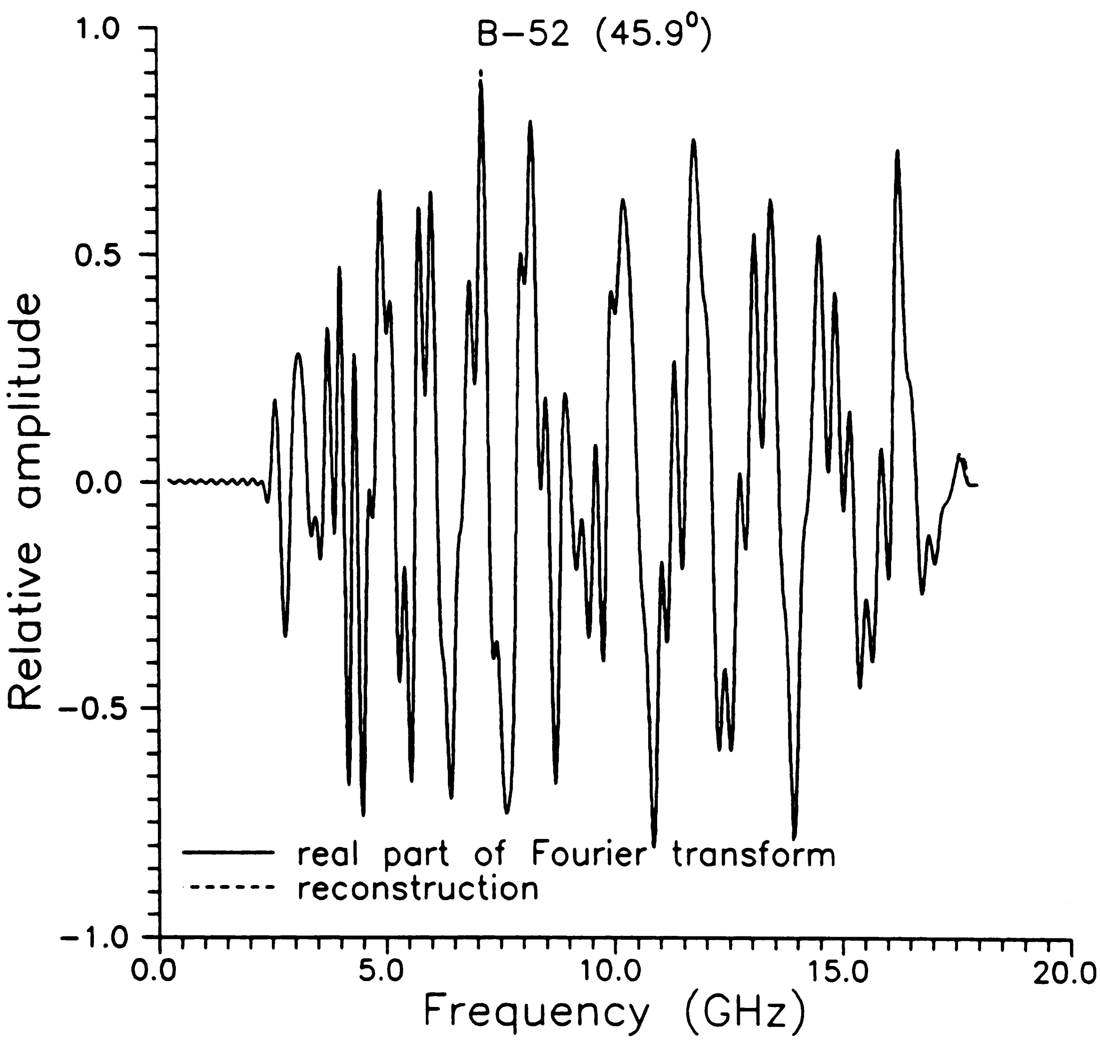

Figure 5.3 Real part of spectrum of early-time portion of B-52 response. Dotted line is reconstruction using 25-term exponential series.

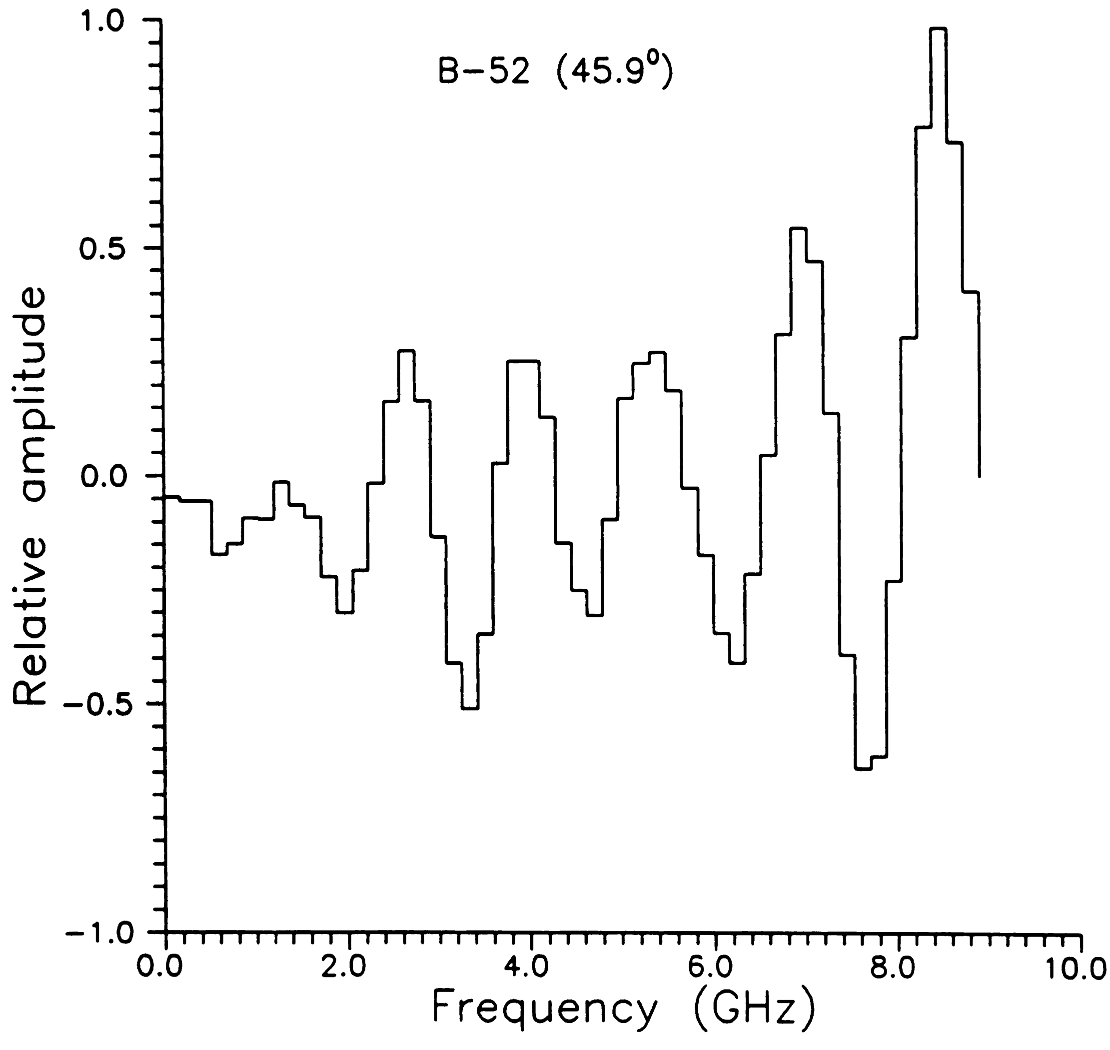

Figure 5.4 Early-time E-pulse constructed to cancel spectrum of early-time B-52 response.

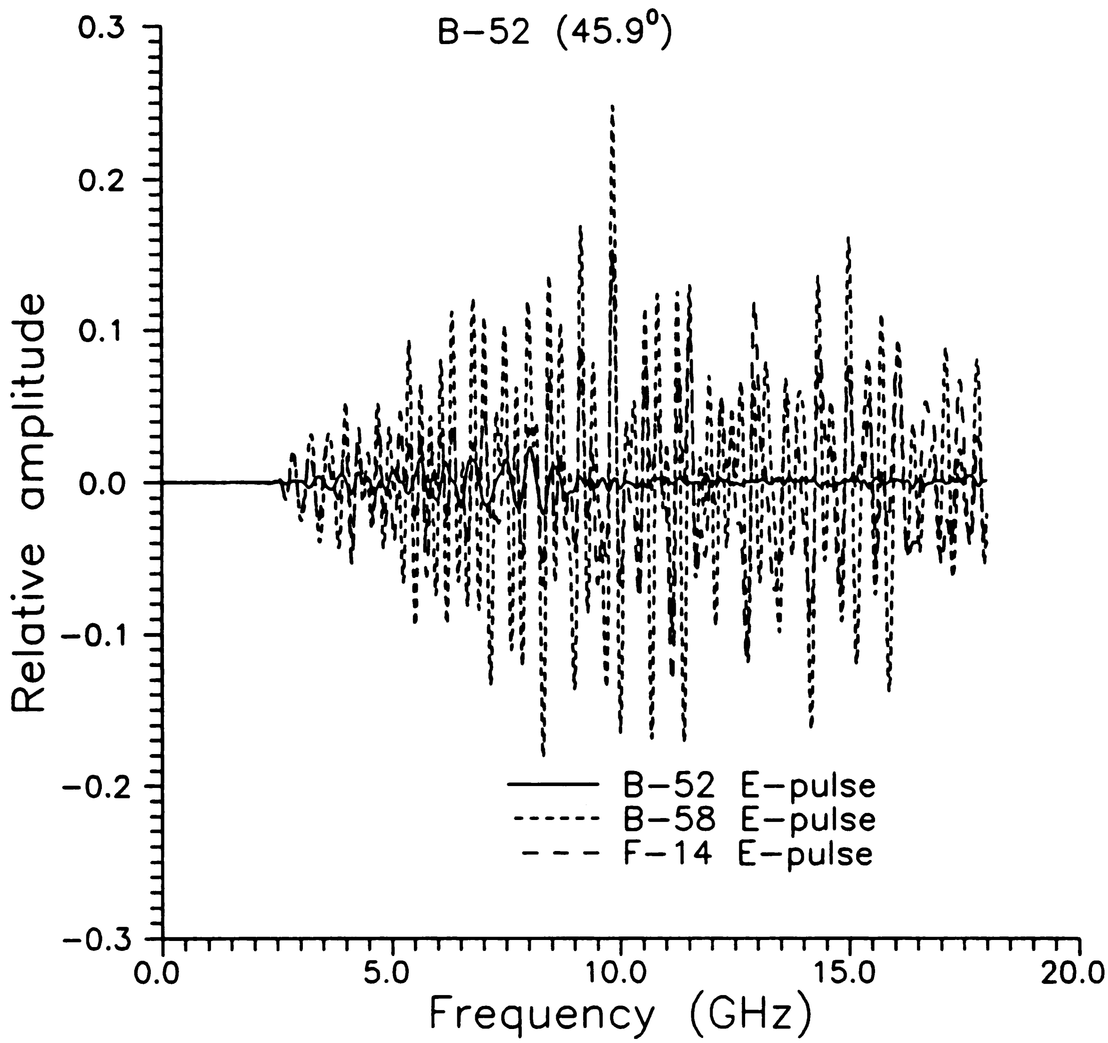

Figure 5.5 Convolution of early-time B-52 response with early-time E-pulses of B-52, B-58 and F-14 at 45.9^0.

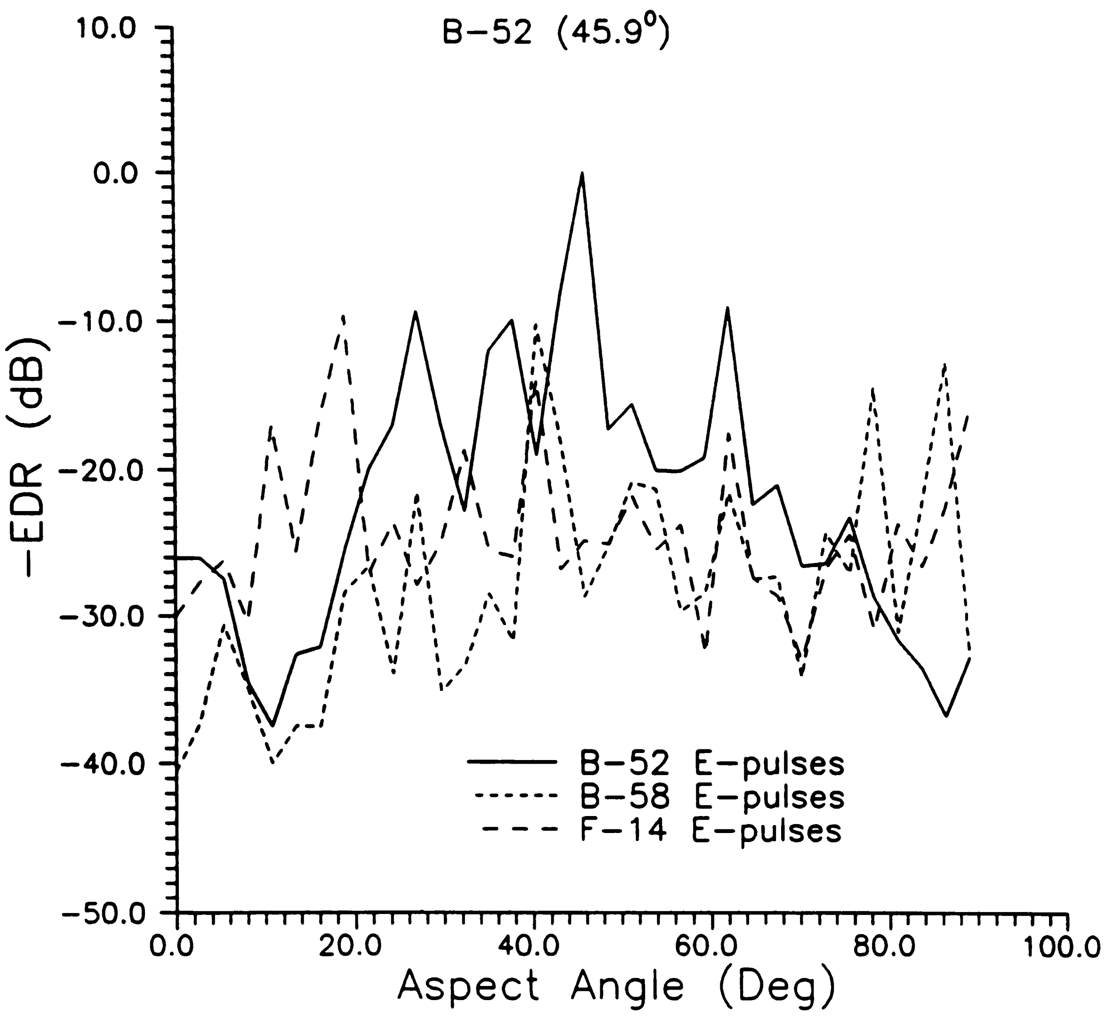

Figure 5.6 Early-time discrimination of B-52 measured at 45.9° aspect angle for different candidate targets, as a function of aspect angle.

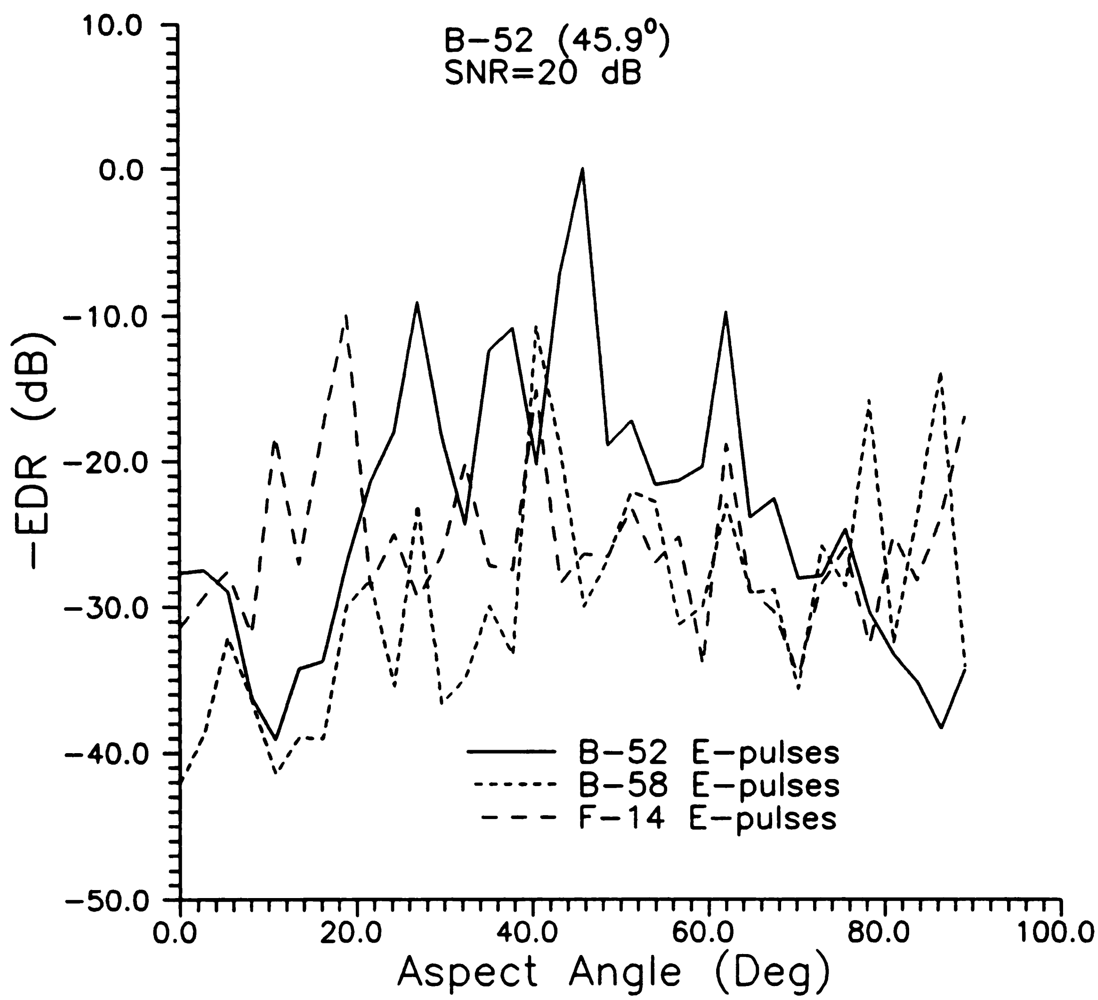

Figure 5.7 Early-time discrimination of the noisy B-52 response measured at 45.9⁰ aspect angle for different candidate targets, as a function of aspect angle. SNR=20 dB.

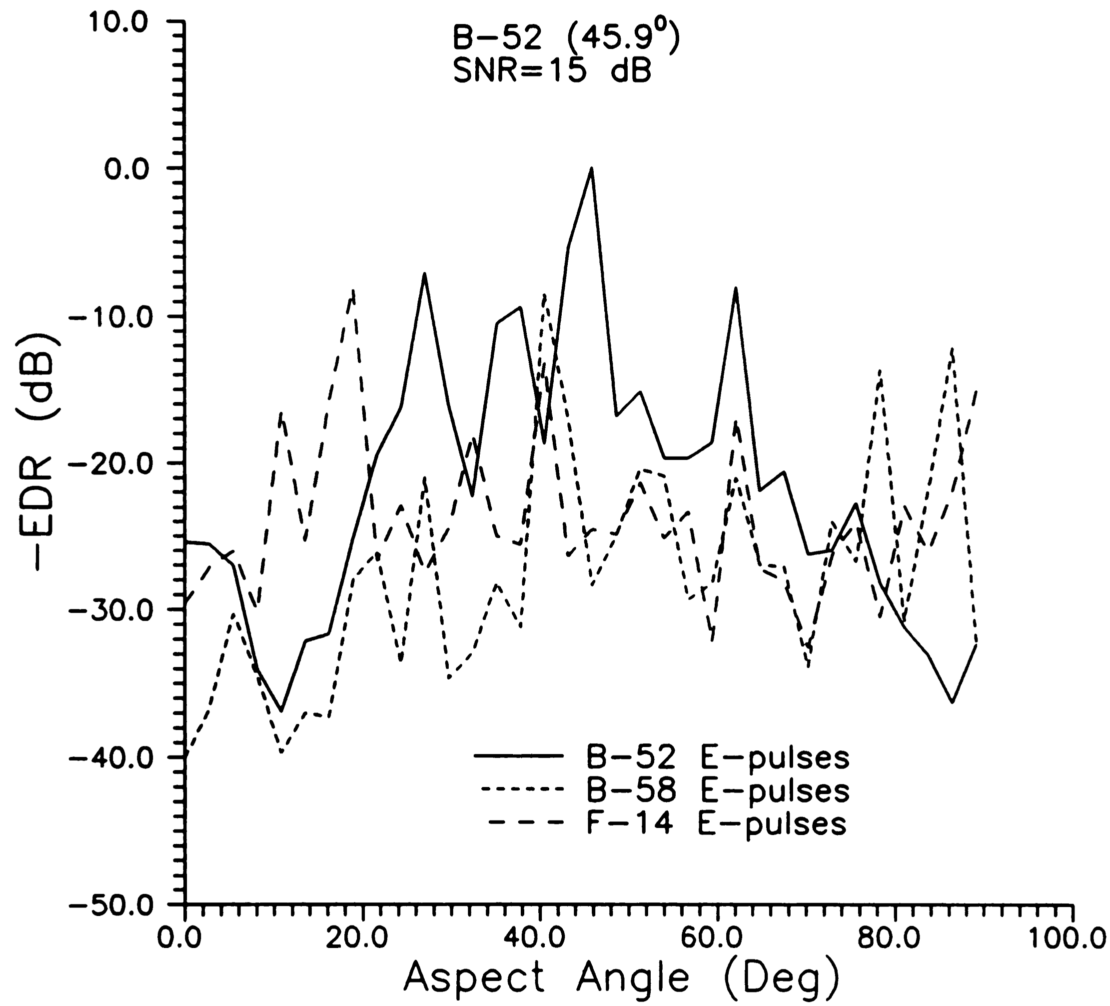

Figure 5.8 Early-time discrimination of the noisy B-52 response measured at 45.9^0 aspect angle for different candidate targets, as a function of aspect angle. SNR=15 dB.

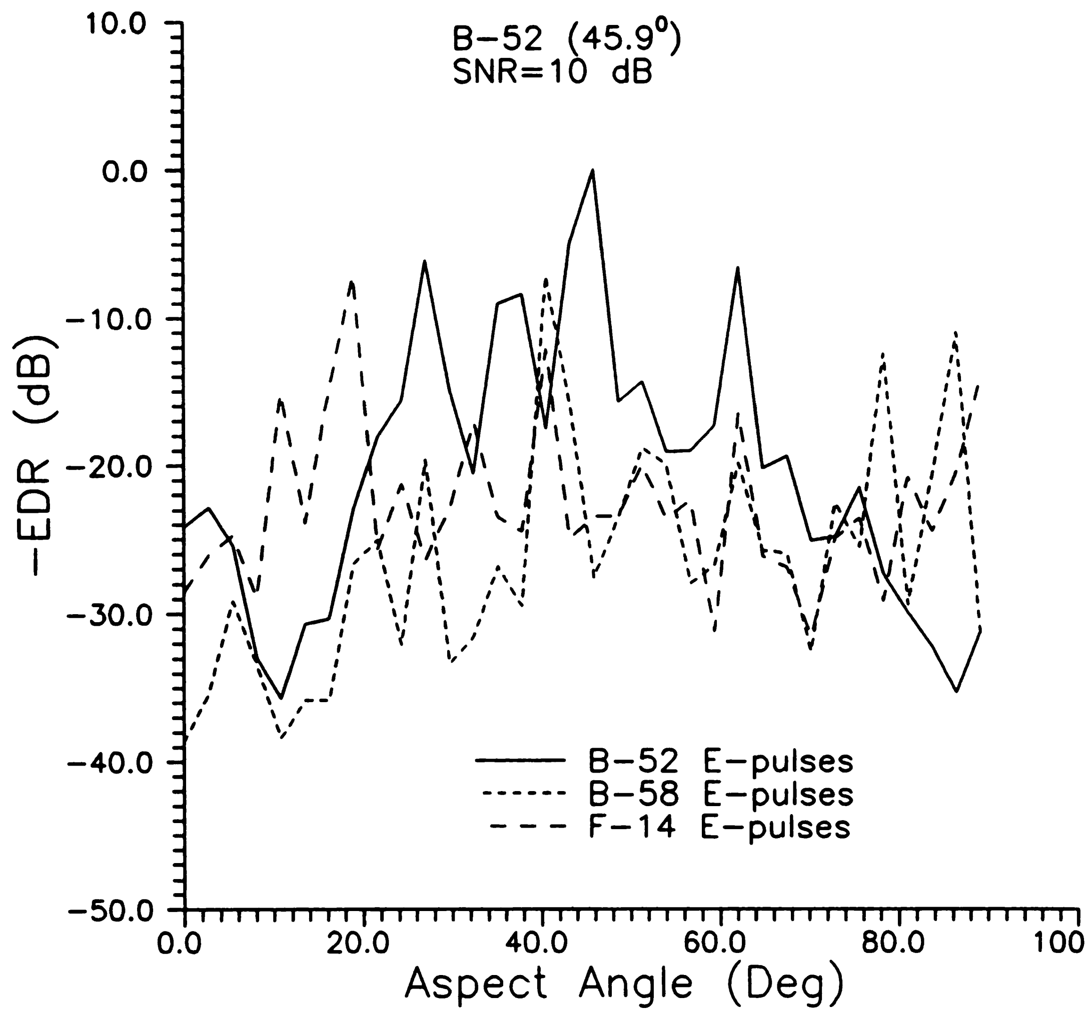

Figure 5.9 Early-time discrimination of the noisy B-52 response measured at 45.9° aspect angle for different candidate targets, as a function of aspect angle. SNR=10 dB.

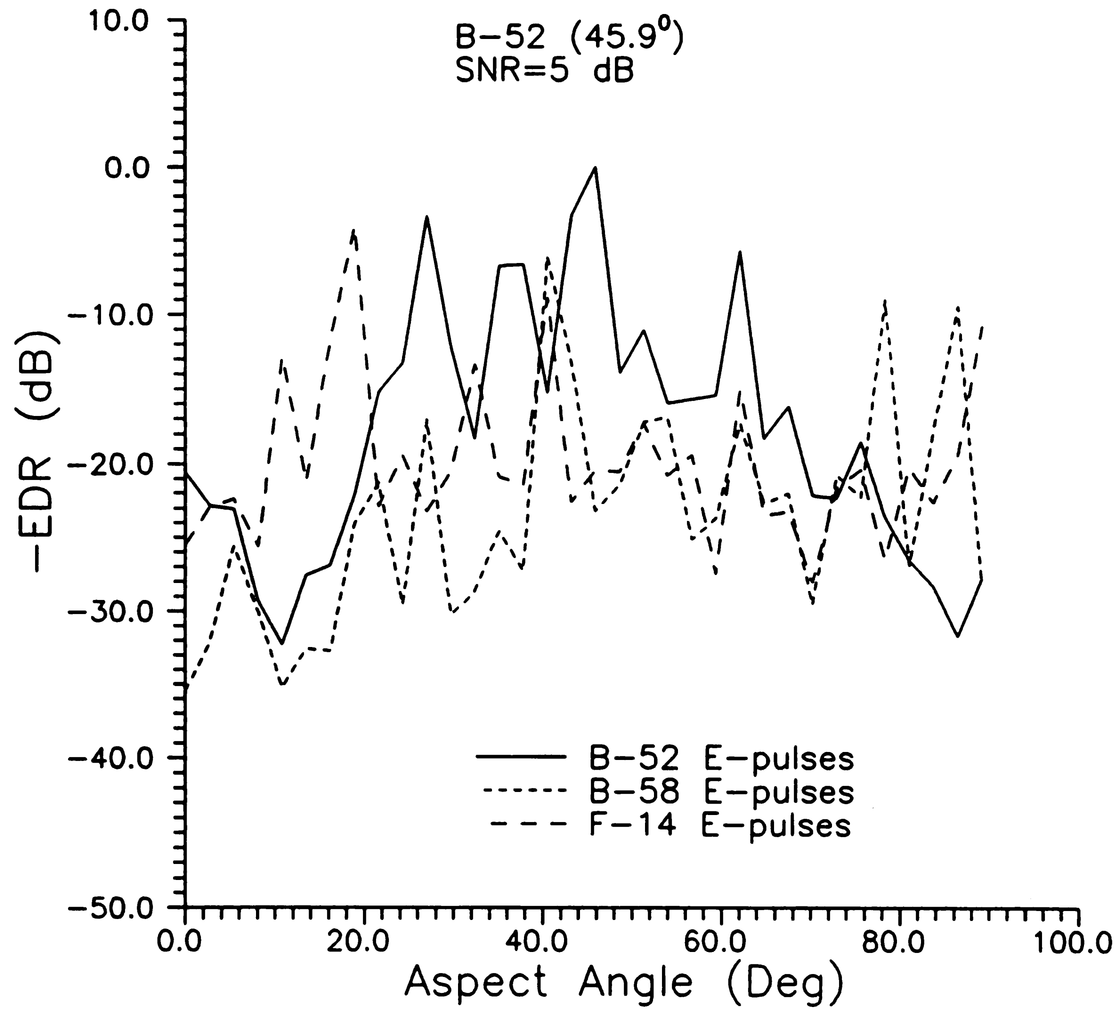

Figure 5.10 Early-time discrimination of the noisy B-52 response measured at 45.9^0 aspect angle for different candidate targets, as a function of aspect angle. SNR=5 dB.

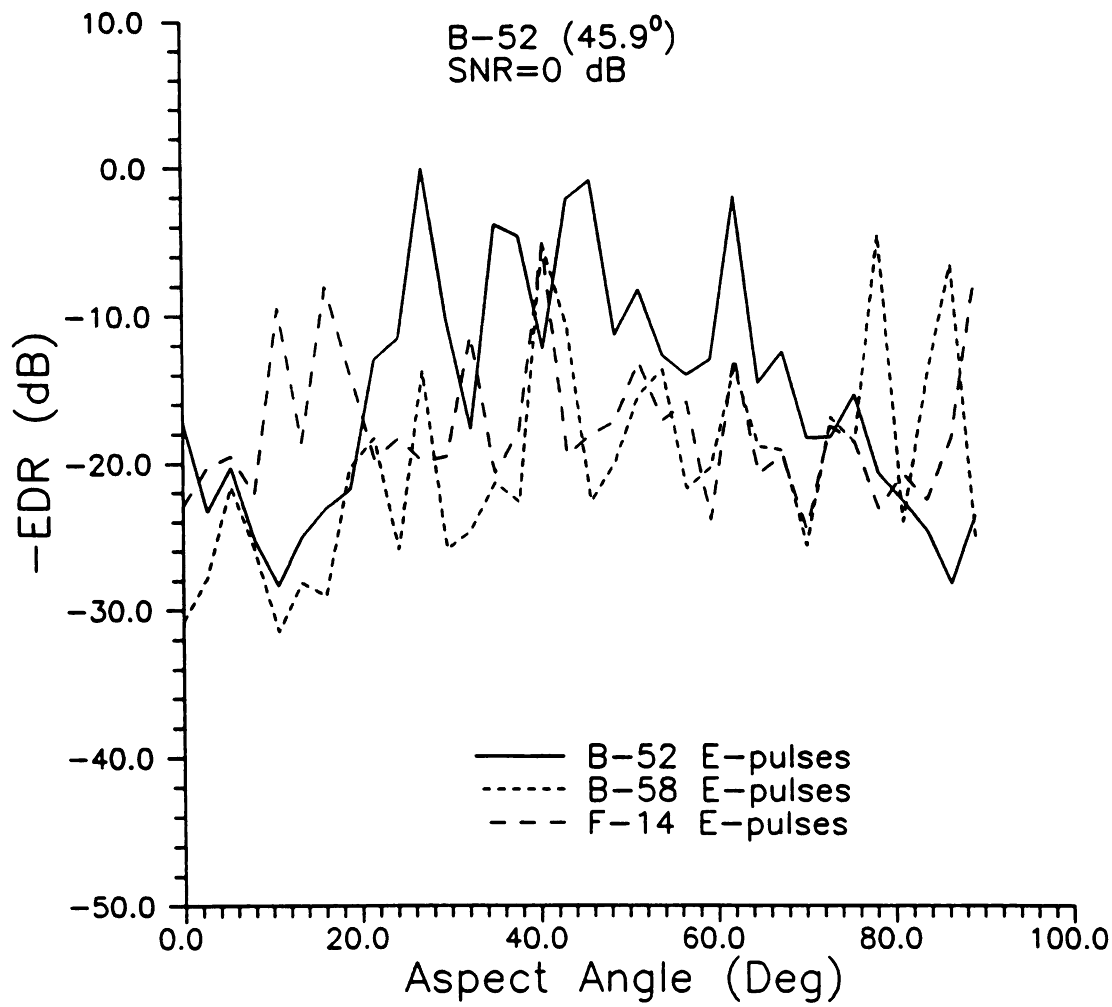

Figure 5.11 Early-time discrimination of the noisy B-52 response measured at 45.9° aspect angle for different candidate targets, as a function of aspect angle. SNR=0 dB.

to see if this is a general conclusion using different targets in a future study.

5.5 Radar Target Discrimination Using Combined E-Pulse Techniques

The previous section describes radar target discrimination using only early-time responses. In those situations where both early and late-time target information are available, both portions of the response can be used to improve discrimination capabilities. A target scheme may attempt to identify the target using early time and late time separately and then combine the results, or it can integrate the information into a single decision process. We propose a scheme called the combined E-pulse technique based on the late-time E-pulse technique which will use information obtained from the late-time portion of the response to narrow down the number of possible targets so that the amount of effort expended using the early-time data is decreased markedly.

It is important to recall that the late-time E-pulse scheme is aspect independent, while the early-time E-pulse scheme is aspect dependent. If only the early-time E-pulse scheme is used, many E-pulses for each target (one for each significant aspect angle) must be convolved with the measured data. On the other hand, only one E-pulse is needed for each target using the late-time E-pulse scheme. Unfortunately, due to the lesser amount of signal energy in the late-time response, results using the late-time E-pulse are sometimes ambiguous. That is, instead of identifying the target, a few targets are separated out as being good candidates for the measured target.

We propose that the late-time aspect independent scheme be used to identify a possible selection of targets. Then, using information stored about the amplitudes and phases of dominant target resonances as a function of aspect angle, the possible range of aspect angle of each candidate target is determined. Finally, the early-time E-pulse scheme is applied over a limited range of aspect angles for each target, resulting in a decreased amount of effort expended by the early-time E-pulse scheme. Thus, the target is identified with strong confidence.

Obviously, if the illuminating waveform has no frequency content in the resonance region of the target to be identified, this approach is not viable, and the early-time technique must be used alone.

The aspect angle of the target is determined by minimizing the squared difference between the measured late-time response and the response of the candidate target reconstructed using the modal amplitudes and phases extracted from laboratory data and saved in a data base. The aspect angle which minimizes the squared error difference is taken to be the angle of the target. We may take for later testing some nearby aspect angles at which the squared error differences are very closed to minimum difference. Note that there is also a scaling factor to be determined, since in the actual measurement the overall amplitude of the measured response will be different from that measured in the lab. Note that we assume that polarizations used in the two measurements are the same. This scaling factor can be computed by least squares at each point in the search for the aspect angle.

The reconstructed waveform for the l^{th} target at the j^{th} aspect angle can be written as

$$r_{l,j} = \sum_{n=1}^{N} a_{l,j,n} e^{\sigma_{l,n} t} \cos(\omega_{l,n} t + \phi_{l,j,n}) \tag{5.13}$$

where $a_{l,j,n}$, the amplitude of the n^{th} mode of target l at aspect j and $\phi_{l,j,k}$, the phase angle, are stored in a data base, as are the aspect-independent natural frequencies, $\sigma_{l,n} + j\,\omega_{l,n}$. The squared error difference between this reconstructed waveform and the measured data is defined as

$$\epsilon_{l,j} = \sum_{i=1}^{M} [m(t_i) - K_{l,j} r_{l,j}(t_i)]^2 \tag{5.14}$$

where t_i is the time at sample point i, M is the number of points in the late-time response, and $K_{l,j}$ is scaling factor. $K_{l,j}$ is determined by minimizing $\epsilon_{l,j}$ as

$$K_{l,j} = \frac{\sum_{i=1}^{M} [m(t_i)\, r_{l,j}(t_i)]}{\sum_{i=1}^{M} r_{l,j}^2(t_i)} \tag{5.15}$$

It is anticipated that $K_{l,j}$ are different for different targets and aspect angles. The most probable scaling factor is determined by minimal SER as defined below.

Since different candidate targets have different late-time periods, a normalized error quantity, the squared error per point (SEPP) is needed. This is defined as

$$SEPP_{l,j} = \frac{1}{M} \frac{\sum_{i=1}^{M} [m(t_i) - K_{l,j}(t_i)\, r_{l,j}(t_i)]^2}{\int_{late-time} m^2(t)\, dt} \tag{5.16}$$

where $\int_{late-time} m^2(t)\, dt$ is the energy in the late-time response. A measure of the quality of the smallest error is given by the "squared error ratio" (SER), defined by

$$SER_{l,j}(dB) = 10.0 \log_{10} \left\{ \frac{SEPP_{l,j}}{\min(SEPP)} \right\} \tag{5.17}$$

Thus, the aspect angle and target producing 0 dB SER is the most probable candidate.

Two sets of antennas must be used to increase bandwidth to allow for both strong early and late-time signals to be measured for a single aircraft at various angles of incidence. A data splicing routine was developed in an effort to accomplish this [34]. In the case of the B-52, a 1:72 scale model was measured over the band 2-18 GHz, while a 1:144 scale model was measured over the band 0.4-4.4 GHz. The orientation and location of the antennas and the targets was maintained throughout the measurements. The amplitude of the low band data was scaled by 2.0 and the frequency step size by a factor of 0.5 by the application of the linearity principle to the measured data because of the known scale ratio of 2 between the model targets. The two data sets were spliced together in the frequency domain at one preselected frequency for all of the measured responses from 0^0-89.1^0 at an increment of 2.7^0. The resulting ultra-wideband frequency data, equivalent to 0.2-18.0 GHz for the larger target, was interpolated down to DC, and then Fourier transformed into the time domain by weighting the frequency domain spectrum with a double gaussian function (the information in the lower frequency won't be lost greatly).

As a comparison to the temporal target response generated from the high frequency data (2-18 GHz) as shown in the previous Figure 5.2, Figure 5.12 shows the scattered time domain response of a B-52 target at 45.9^0 incidence obtained from the spliced frequency data (0-18 GHz). Note that the occurrence of a strong late-time oscillatory component appearing after the excitation signal has passed the target after 6.1 ns, resulting from the low frequency-component of the spliced data.

As a demonstration of the combined E-pulse technique, 1:72 scale B-52, 1:48 scale B-58 and 1:48 F-14 models have been measured within the band 0-18 GHz and inverse transformed into the time domain. Each target has been measured from 0^0 to 89.1^0 at a 2.7^0 increment. Figure 5.13 shows the convolution of the B-52 response measured at 45.9^0 from nose-on with the late-time E-pulses of the B-52, B-58 and F-14.

The beginning of the late-time convolutions of the B-52, B-58 and F-14 are 14.2 ns, 14.1 ns and 13.9 ns, respectively. Using equation (5.11), the B-52 has an EDR of 0 dB, while B-58 and F-14 have an EDR of 20.5 dB and 29.8 dB. In this case the difference is so large that the B-52 can be easily identified. However, we will assume that a verification is required using the early-time E-pulses. Thus, we will attempt to identify the correct aspect angle of the measured target.

To investigate the effect of the scaling factor, the response used to determine the amplitudes and phases of each target is multiplied by a factor of ten before being used in the discrimination process. Figure 5.14 shows the calculated scaling factors (K_{ij}) for the measured B-52 at 45.9^0 for various aspect angles. As expected, the scaling factors are dramatically different for different targets and aspect angles, with the B-52 near 45.9^0 producing a value very close to the actual value of 10.

To assess the effect of random gaussian noise on determining the proper scaling factor, additional noise has been added to the transient response of 45.9^0 B-52 model. Figure 5.15 shows the calculated scaling factors for various aspect angles at SNR=15 dB. Quite similar results are observed as those in Figure 5.14. An approximated value of 10 can still be obtained near 45.9^0 for the B-52 target even in as bad a situation as SNR=0 dB, as shown in Figure 5.16.

Next, we need to determine the proper aspect angle. In a real situation, we don't know the proper scaling factor. We need to calculate the squared error ratio (SER) using the scaling factors determined by (5.15) for measurements at various aspect angles, then the one which leads to minimal squared error ratio is chosen.

Figure 5.17 shows the squared error ratio as a function of aspect angles for B-52, B-58 and F-14 using the scaling factor determined by minimal SER as explained above.

The error is minimized for the correct aspect angle, thus identifying the aspect angle of the measurement. Again, the SER values are negative for display purposes. Squared error ratio can also be used as a means to discriminate targets. It is noticed that the B-52 target can be identified within 28^0 to 66^0 with the high confidence.

The effect of gaussian noise on the squared error ratio is shown in Figure 5.18, Figure 5.19, Figure 5.20, Figure 5.21, and Figure 5.22. In each case, the measured response is from a B-52 at 45.9^0 aspect angle. When the B-52 is the anticipated target, the SER is minimized for the correct angle, 45.9^0, regardless of the noise level. However, the rate at which the SER increases as the aspect angle moves away from 45.9^0 decreases with increasing noise. That is, as the noise gets worse, it is harder to tell with certainty that the aspect angle is 45.9^0. When the B-58 and F-14 are the anticipated targets, the SER values are large around 45.9^0. This is as expected, since the reconstructed B-52 response never matches the measured B-58 and F-14 responses.

Once the candidate targets and their estimated aspect angles have been determined, the early-time E-pulse technique is used to single out the correct target and verify the previous decisions made through late-time E-pulse and SER techniques. This makes us turn to the early-time E-pulse discrimination results as shown in Figure 5.6, Figure 5.7, Figure 5.8, Figure 5.9, and Figure 5.10. It is seen that the B-52 produces a small convolved output for angles near 45.9^0, while the B-58 and F-14 produce a large convolved output. This serves to verify the late-time identification of the B-52.

Obviously, this has been a very limited test of the proposed early-time/late-time technique. We hope to accumulate more target spliced data in the future to test the combined E-pulse technique.

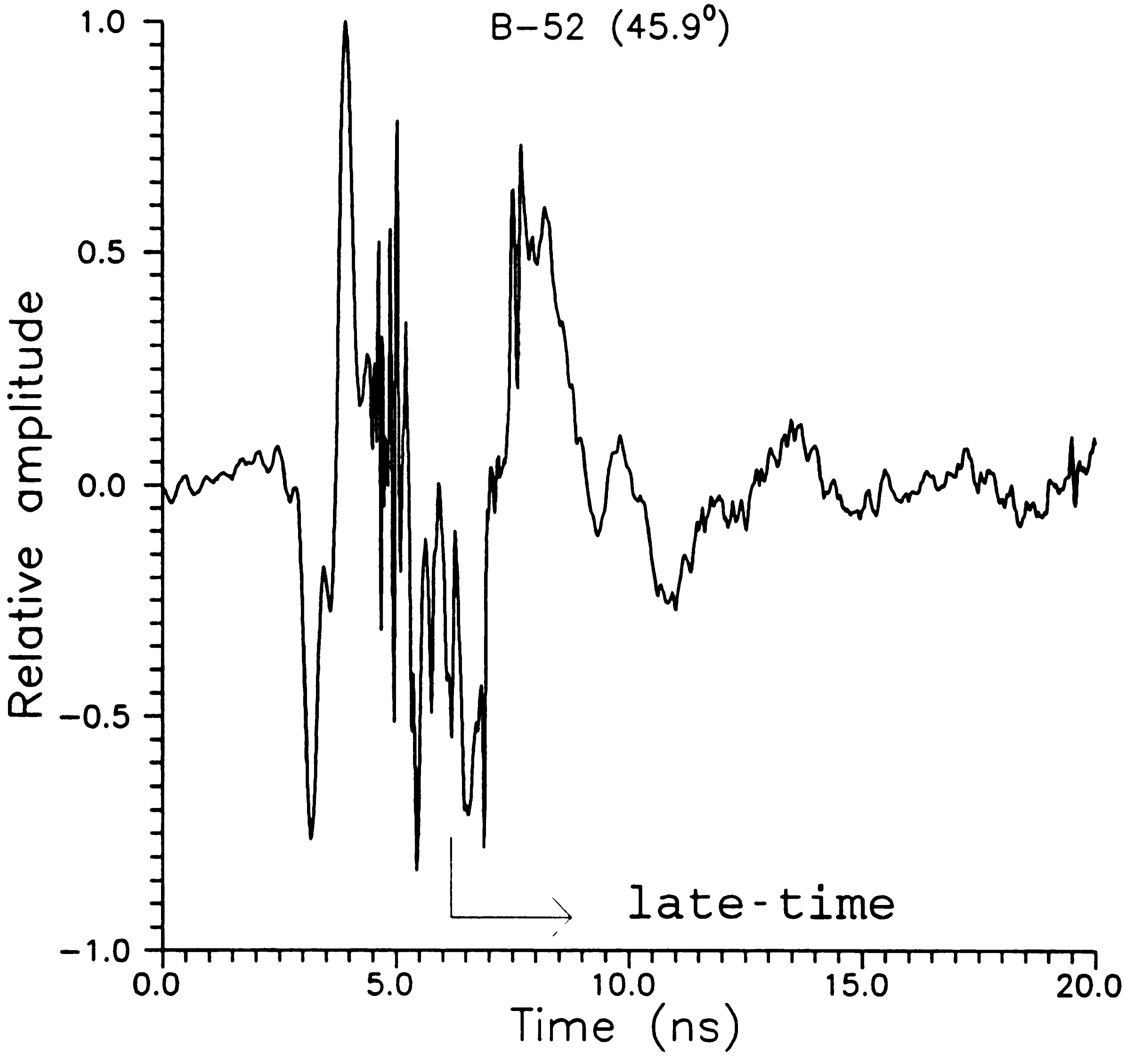

Figure 5.12 Spliced transient response of B-52 aircraft model at 45.9° incidence.

Relative amplitude

Figu

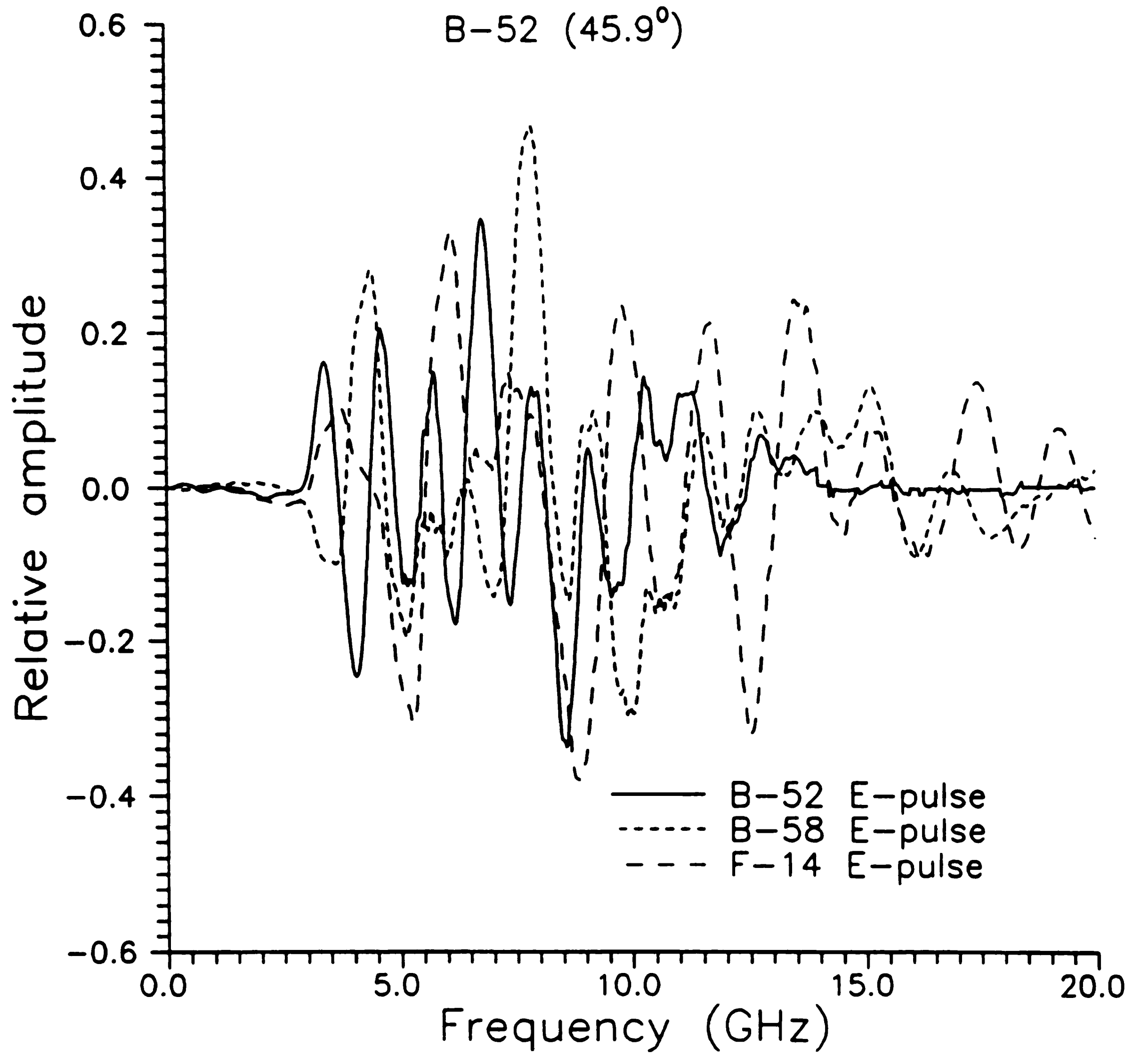

Figure 5.13 Convolution of late-time B-52 response measured at 45.9° generated using spliced data with late-time E-pulses of B-52, B-58 and F-14.

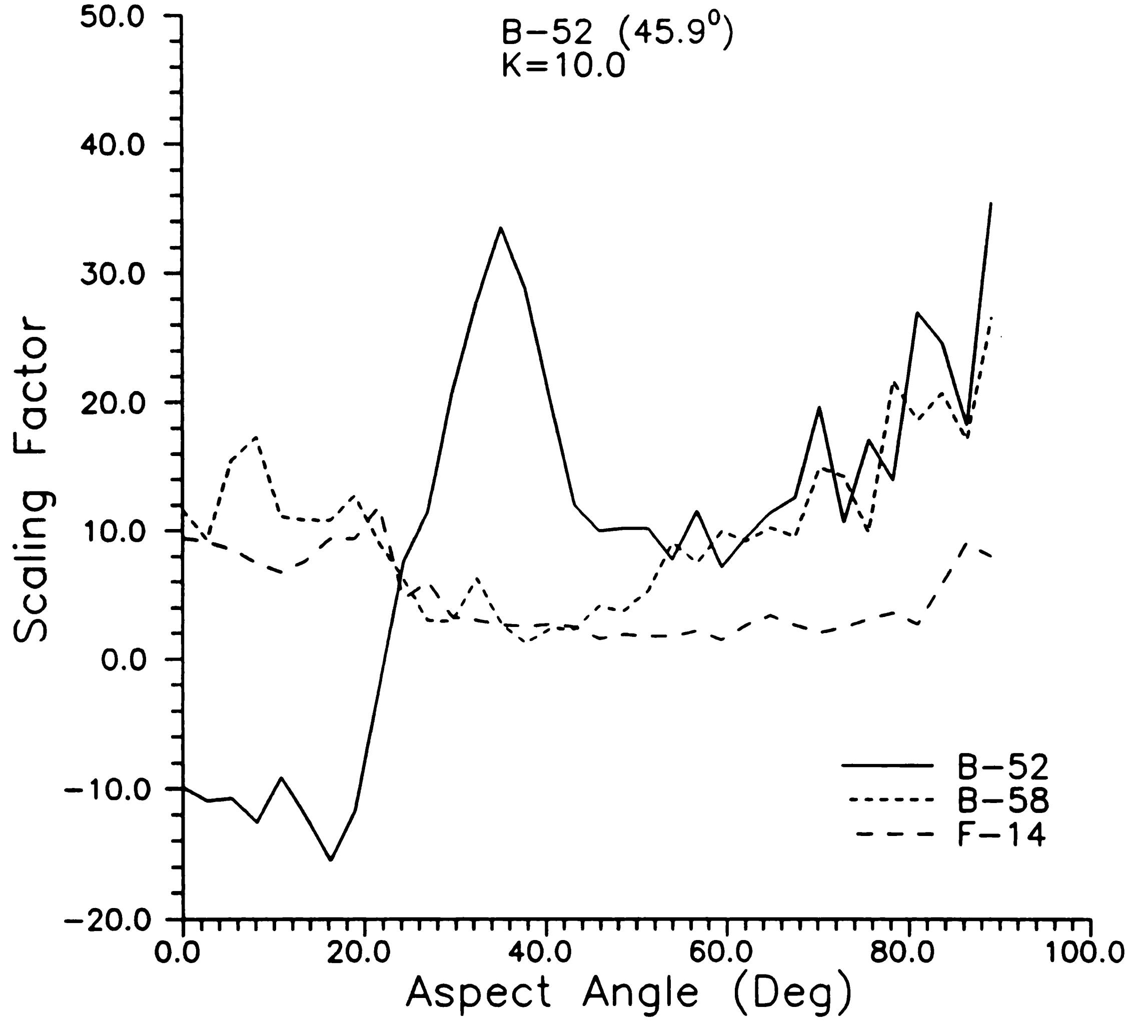

Figure 5.14 Calculated scaling factors of B-52 response measured at 45.9^0 aspect angle for various aspect angles and targets.

Scaling Factor

Figur

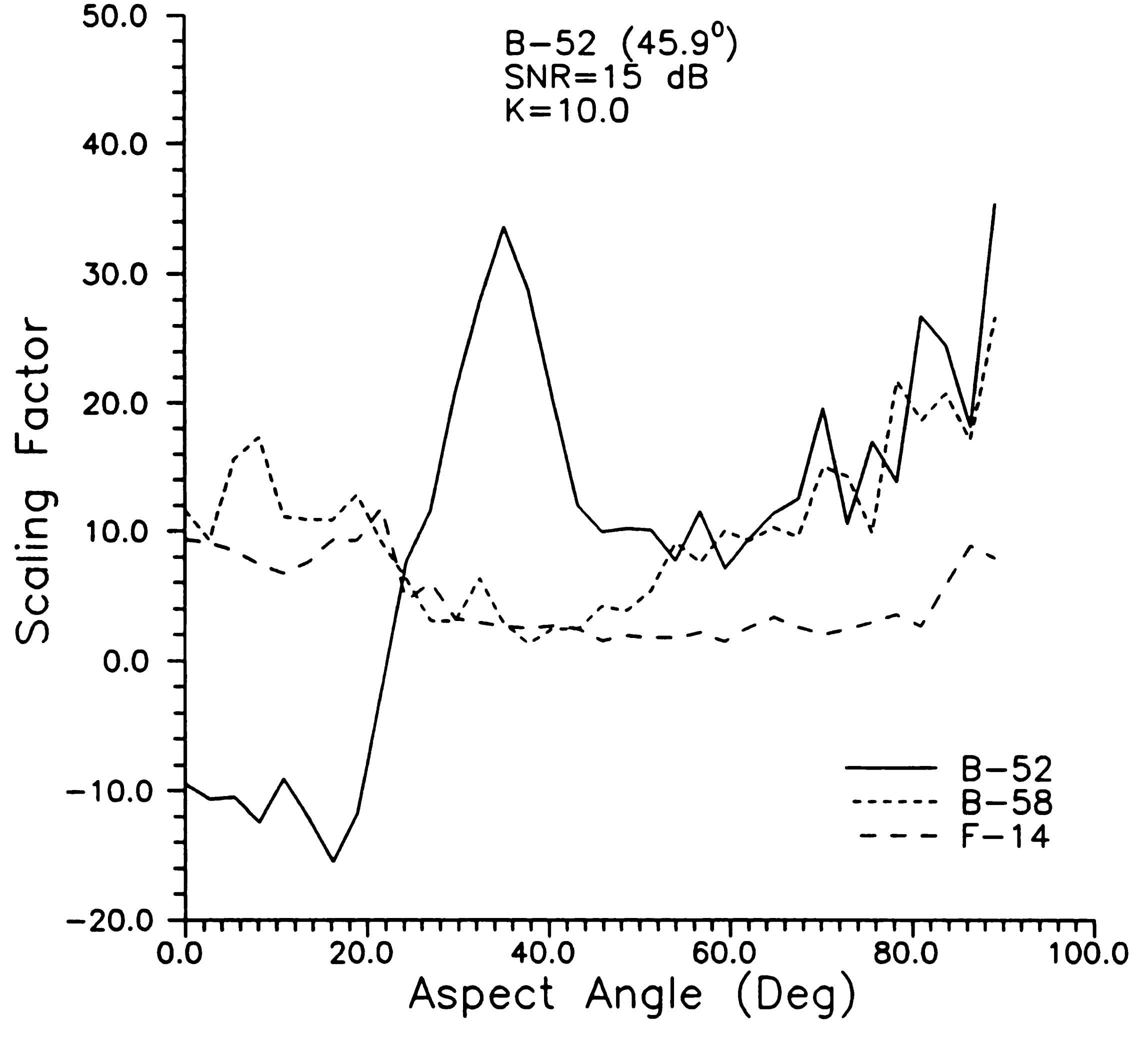

Figure 5.15 Calculated scaling factors of the noisy B-52 response measured at 45.9^0 aspect angle for various aspect angles and targets. SNR=15 dB.

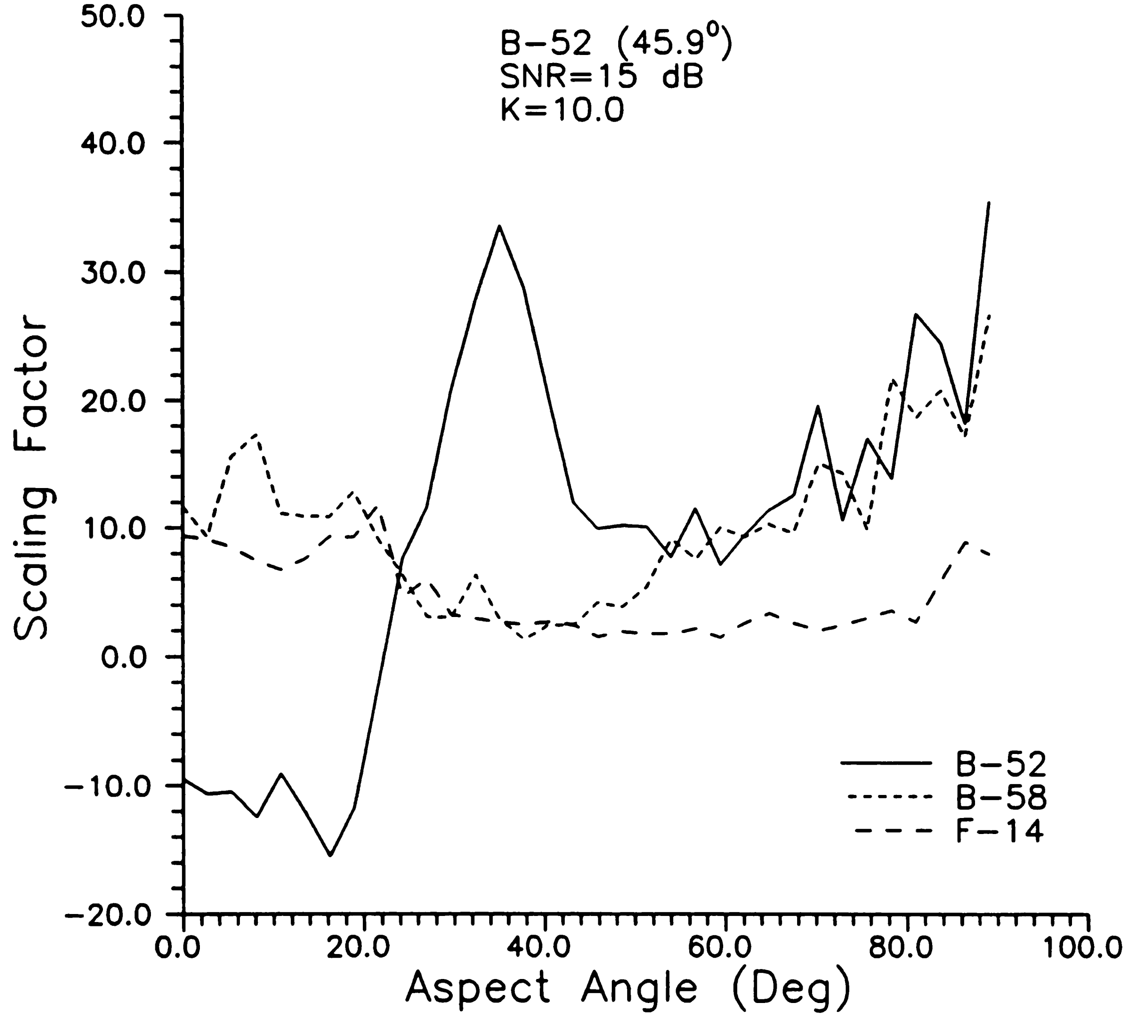

Figure 5.15 Calculated scaling factors of the noisy B-52 response measured at 45.9^0 aspect angle for various aspect angles and targets. SNR=15 dB.

Scaling Factor

Figure

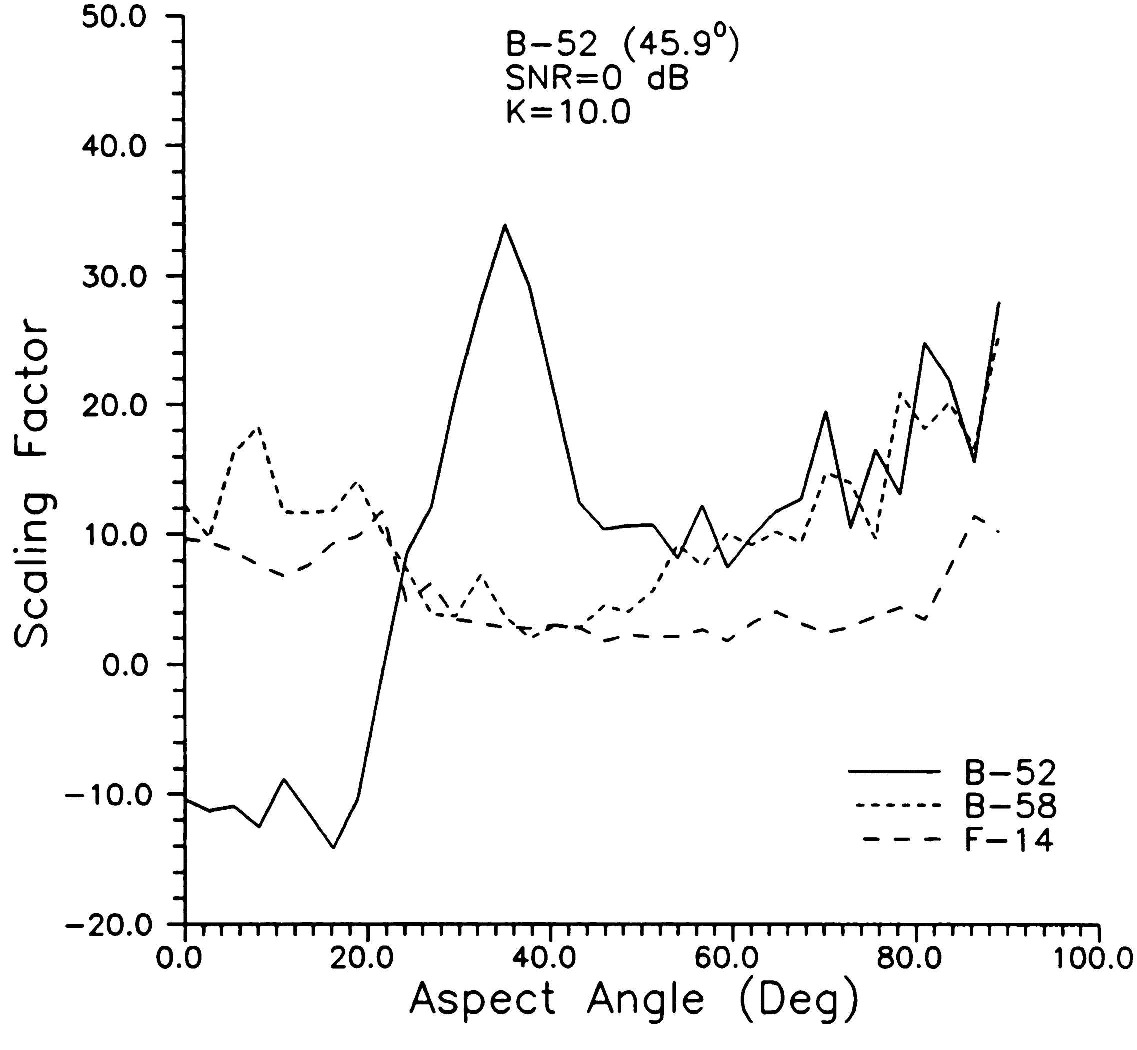

Figure 5.16 Calculated scaling factors of the noisy B-52 response measured at 45.9^0 aspect angle for various aspect angles and targets. SNR=0 dB.

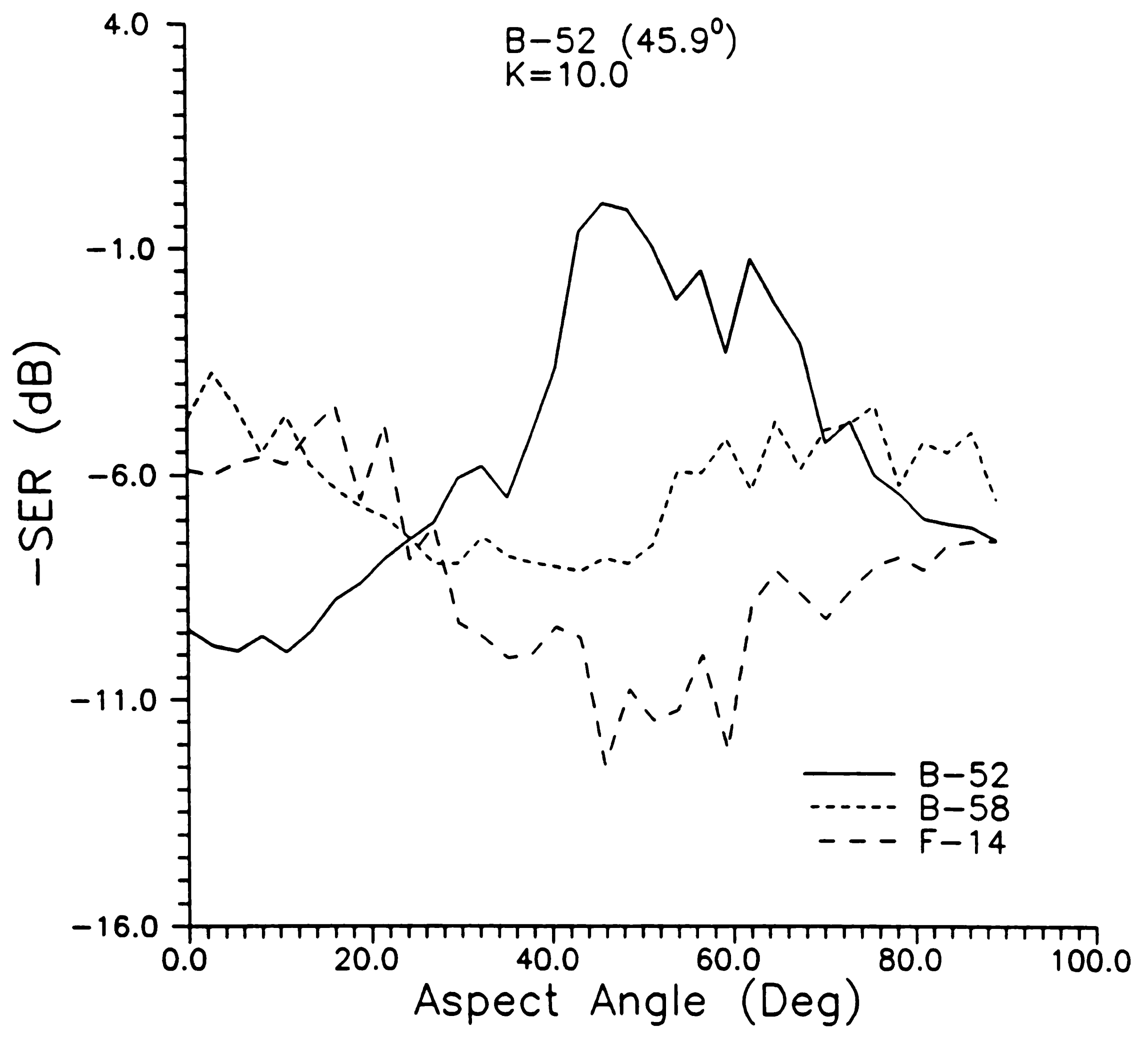

Figure 5.17 Squared error ratio of B-52 response measured at 45.9^0 aspect angle for different candidate targets, as a function of aspect angle.

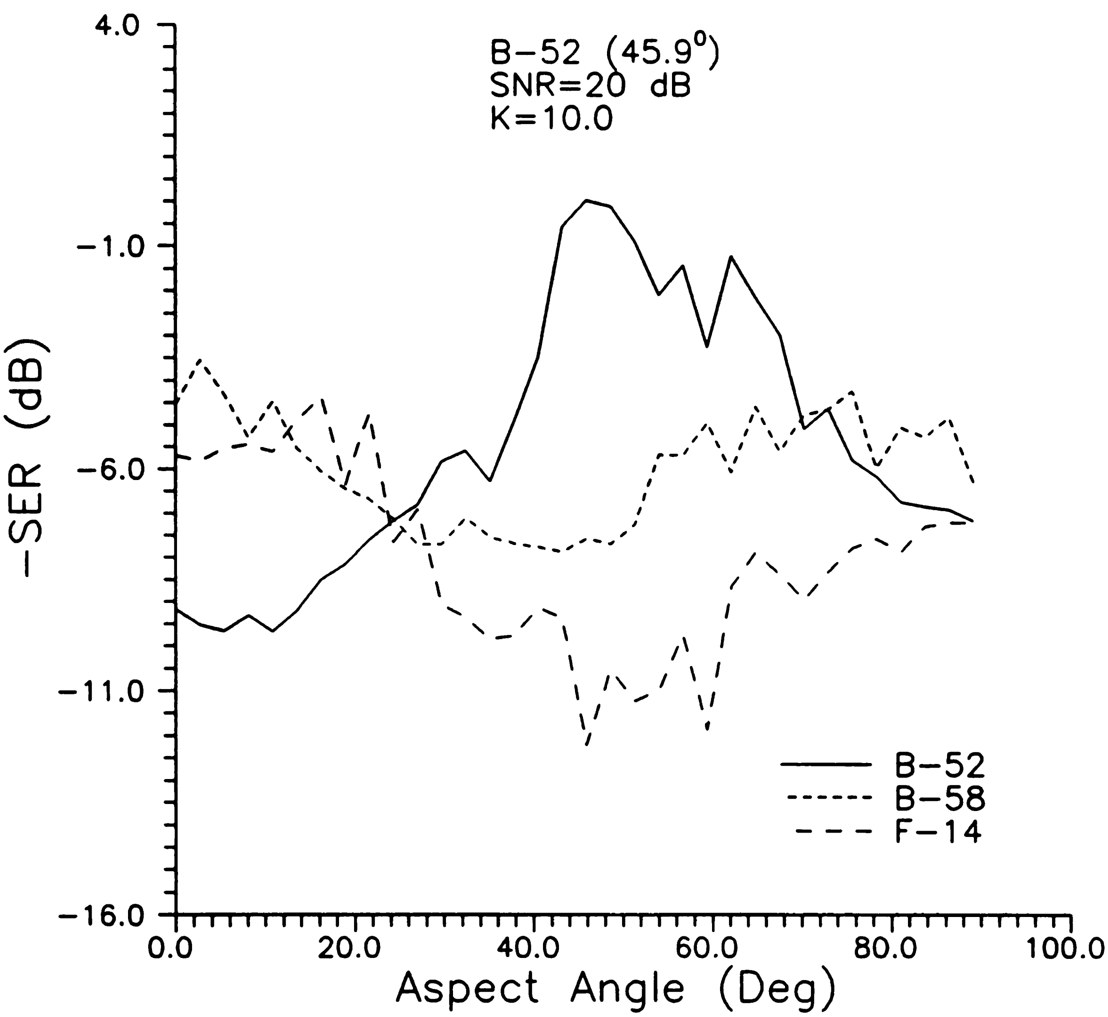

Figure 5.18 Squared error ratio of the noisy B-52 response measured at 45.9^0 aspect angle for different candidate targets, as a function of aspect angle. SNR=20 dB.

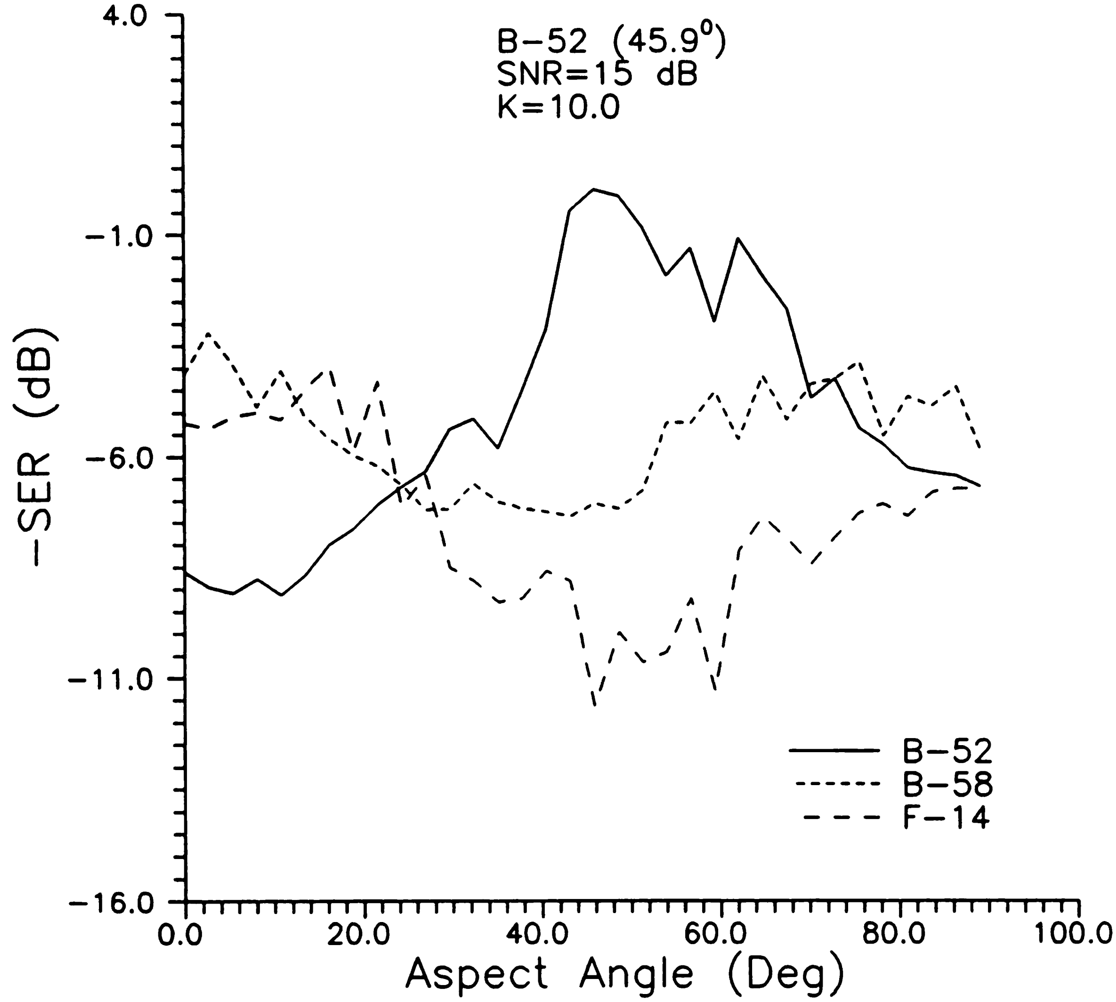

Figure 5.19 Squared error ratio of the noisy B-52 response measured at 45.9^0 aspect angle for different candidate targets, as a function of aspect angle. SNR=15 dB.

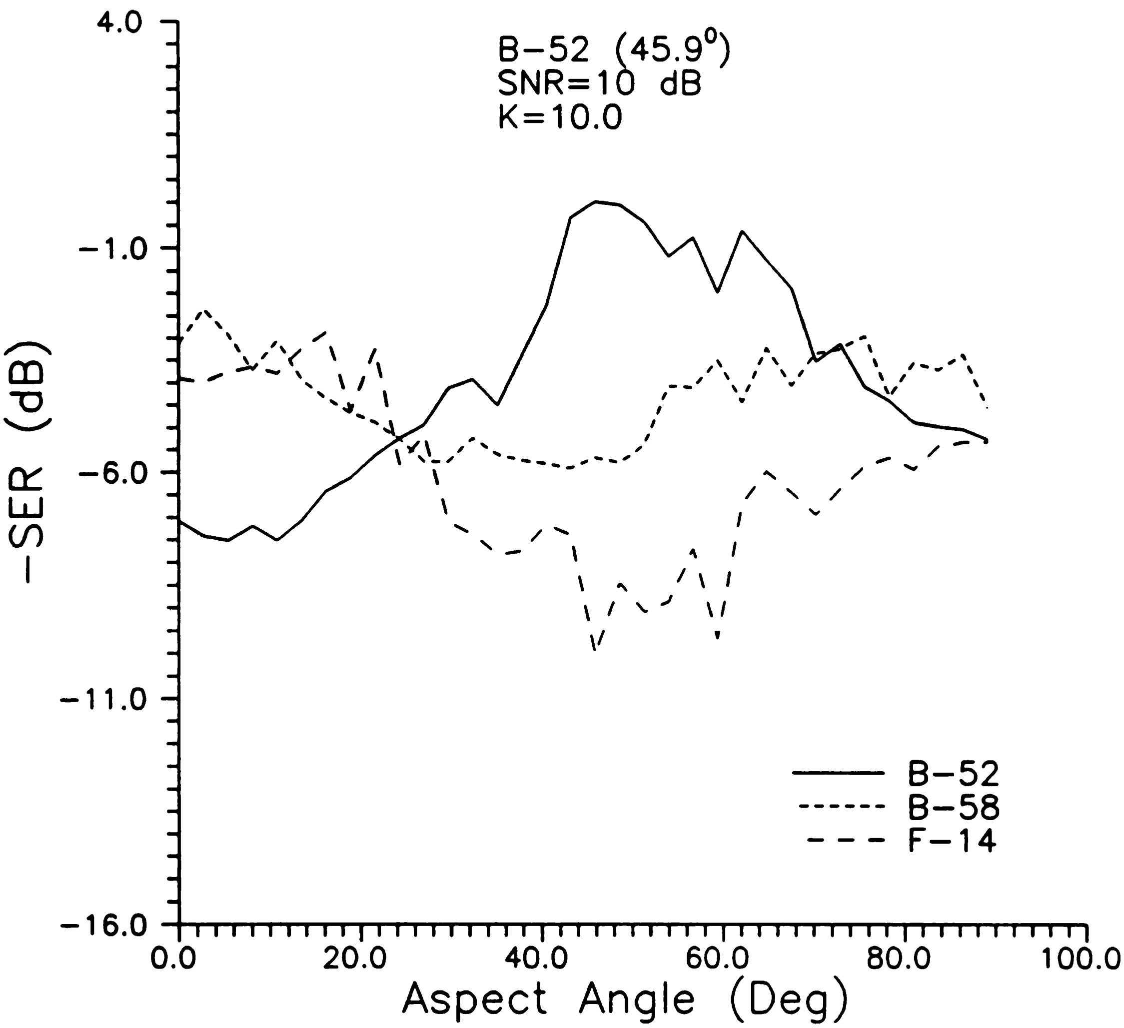

Figure 5.20 Squared error ratio of the noisy B-52 response measured at 45.9^0 aspect angle for different candidate targets, as a function of aspect angle. SNR=10 dB.

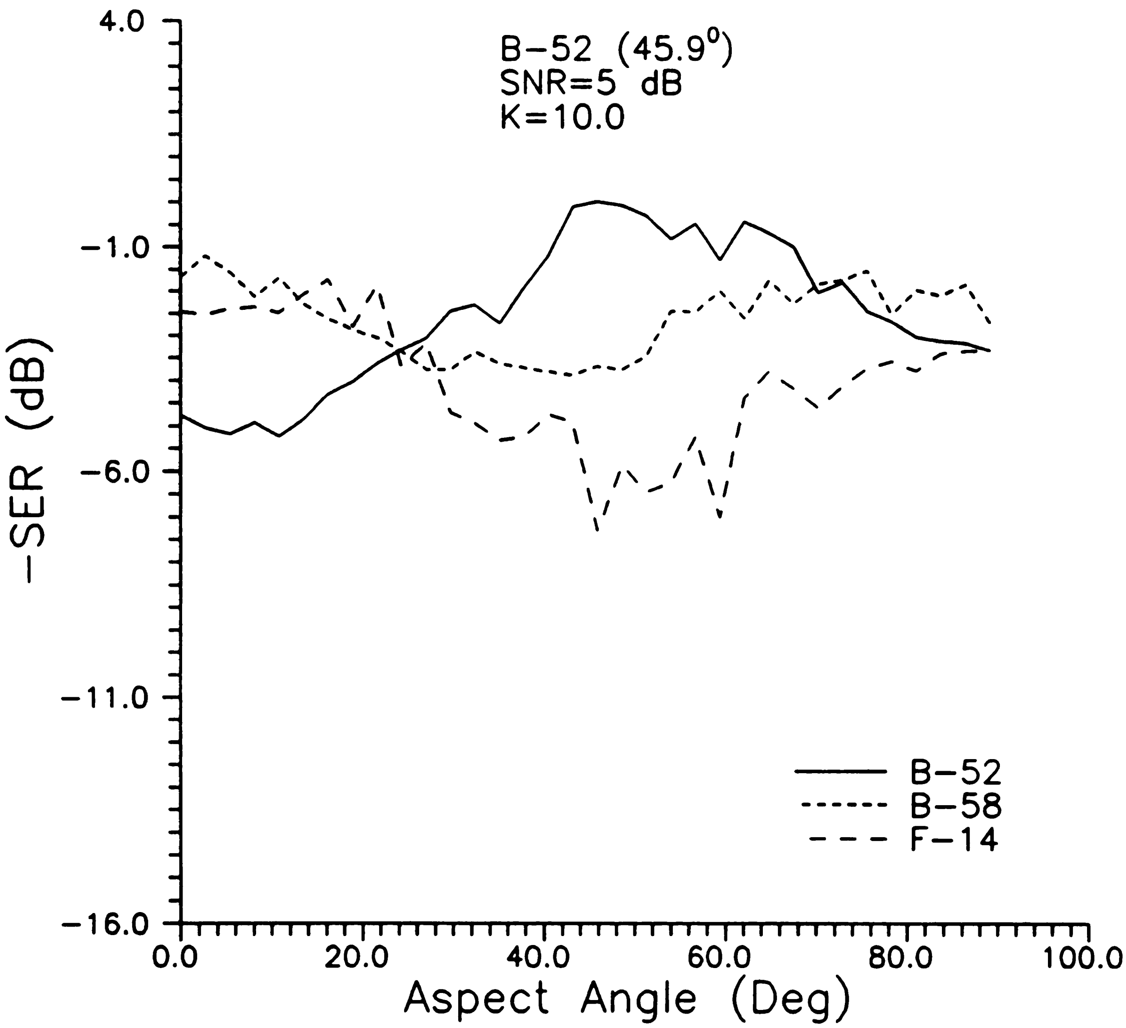

Figure 5.21 Squared error ratio of the noisy B-52 response measured at 45.9^0 aspect angle for different candidate targets, as a function of aspect angle. SNR=5 dB.

Fig

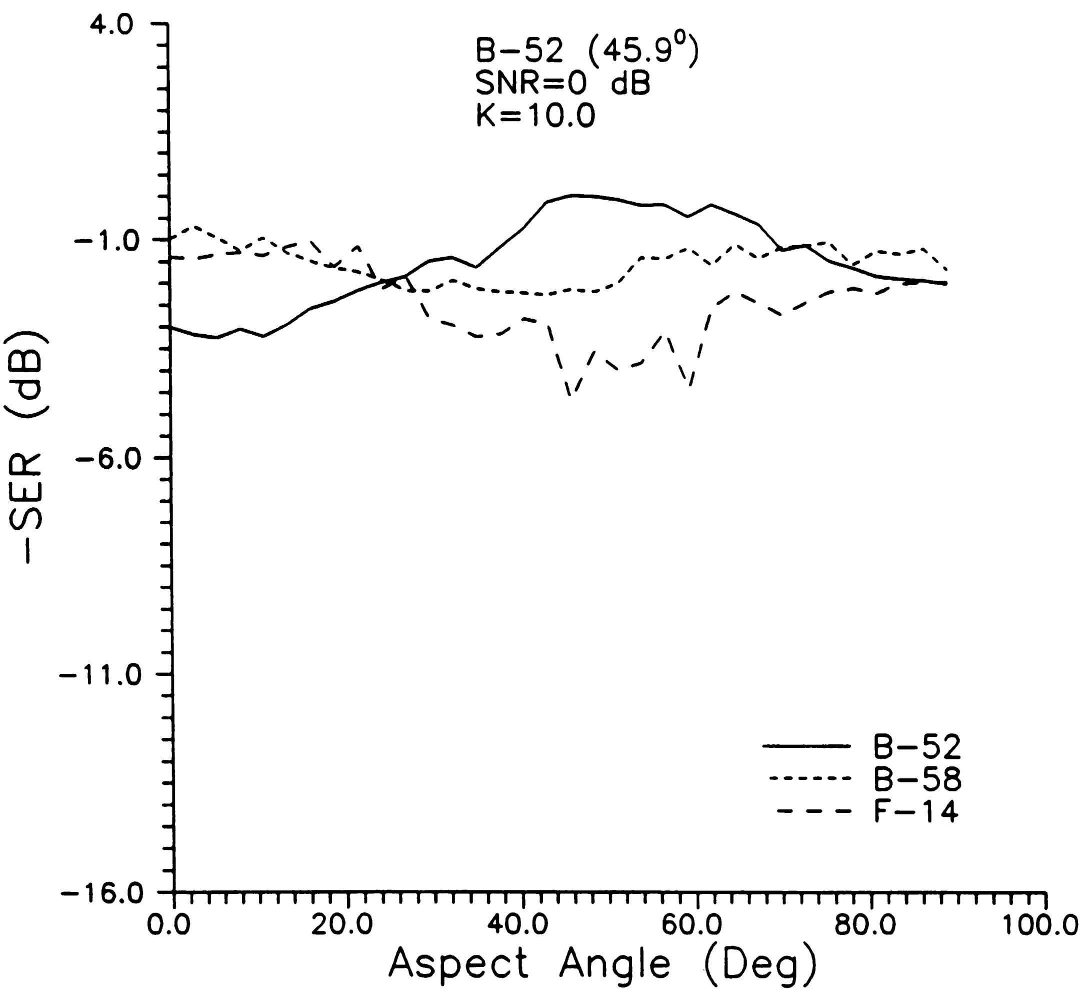

Figure 5.22 Squared error ratio of the noisy B-52 response measured at 45.9^0 aspect angle for different candidate targets, as a function of aspect angle. SNR=0 dB.

CHAPTER 6

RADAR TARGET DISCRIMINATION USING CORRELATION TECHNIQUE

6.1 Introduction

We introduced the E-pulse technique to perform target discrimination in the last chapter. We will discuss another method called correlation-based target discrimination. It is well known that the matched filter maximizes the peak output if a linear system has a pre-specified input in the presence of random noise. In fact, if the matched filter output is properly normalized, that maximum is known a priori to be one. Thus target identification can be performed using a bank of matched filters knowing that the target will be associated with the filter which produces unity output.

The drawback to using a matched filter approach is that since the early-time target response is aspect dependent, a large number of matched filters must be constructed for each expected target. The measured response of each target at many aspect angles would have to be stored, amounting to a significant storage retrieval problem. If the stored information could be parameterized in some way, the information space and retrieval time could be reduced significantly.

To perform correlation-based target discrimination, the measured response of an unknown target is correlated with each reconstructed response stored in terms of parameters. The stored pattern which produces the maximal correlation is thus associated with the unknown target, and the target is identified.

There are several methods to reduce data storage. Rothwell demonstrated how the discrete wavelet transform technique could be used to finish this job [35], [36], [37]. He also showed the results of discrimination among five aircraft models using data measured at a 0.45^0 aspect angle increment. A discrimination ratio for correlation-based processing was introduced, and the aspect angle "window" in which a target would be identified was examined. H. J. Li and S. H. Yang used range profiles as feature vectors for data representation and established a decision rule based on the matching scores to identify aerospace objects [38]. Other methods using neural networks and imaging techniques have been proposed [39], [40], [41], [42].

To properly reduce the storage space, we need to determine the appropriate increment size of aspect or frequency. This thesis does not discuss frequency discretization. Interested persons may see [43]. If the increment size is too small, the database will occupy too much memory space; if the size is too large, target identification may be impossible. A "discrimination range" will be introduced to determine the range of aspect angles over which a correct decision is possible. This range describes the aspect angle discretization required for data storage.

In section 6.2 we review the quantification of correlation discrimination. In section 6.3 we discuss a "frequency-domain" method, which is based on frequency-domain representation of the data. In section 6.4 we describe a "time-domain" method since the information is done using the time-domain representation of the data. We also demonstrates the effects of spatial resolution and Gaussian noise level on radar target discrimination performance.

6.2 Quantification of Correlation-Based Discrimination

Correlation-based discrimination is carried out by computing the cross correlation, $g(t)$, of a reconstructed stored waveform with the measured response of an unknown target, $r(t)$. The normalized correlation is given by

$$C_k(t) = \frac{g(t)}{\sqrt{\frac{1}{2\pi}\int_{-\infty}^{\infty} |R(\omega)|^2 d\omega \ \frac{1}{2\pi}\int_{-\infty}^{\infty} |F_k(\omega)|^2 d\omega}} \tag{6.1}$$

For computational efficiency the correlation is performed in frequency domain using the FFT as

$$g(t) = \mathcal{F}^{-1}\{F_k(\omega)\, R(\omega)\} \tag{6.2}$$

Here $R(\omega)$ is the spectrum of the measured response of an unknown target, and $F_k(\omega)$ is the k^{th} reconstructed spectrum in a series of data sets. By Schwartz inequality, $C_k(t)$ will attain a maximum value of unity only if

$$|R(\omega)| = |F_k(\omega)| \ or \ |R(\omega)| = K\,|F_k(\omega)| \tag{6.3}$$

where K is a constant. The most probable target is identified as that which produces a maximum correlation.

To describe the quality of target discrimination, a "discrimination ratio" is defined as the largest correlation ideally from the right target, divided by the next largest one from a different target. In a similar fashion, it is helpful to quantify the range of aspects over which a specific target may be identified. This also provides a measure of the density of aspect angles required for stored waveforms. A "discrimination range" (with units of degrees) is defined as the range of angles over which a specific target response produces the maximum correlation among all the targets.

6.3 Performance of Correlation-Based Discrimination Scheme With Frequency-Domain Storage

In Chapter 5 we demonstrated that the early-time waveform could be represented as a series of complex exponentials in the frequency domain, and that the "complex times" associated with the scattering centers could be determined using the E-pulse technique. The reconstructed data can be used in correlation-based discrimination. Because extraction of the scattering center information is accomplished using the frequency domain representation of the data, this will be referred to as a "frequency-domain" method.

Remember that the response is reconstructed in the frequency domain according to

$$F_k(\omega) = \sum_{n=1}^{N} a_{nk} e^{Q_{nk}\omega} \tag{6.4}$$

The quantities Q_{nk} represent complex times associated with the temporal positions of scattering centers. They are extracted in the frequency domain using the E-pulse technique. This process was described previously.

To demonstrate target discrimination performance using the frequency domain method, we will use the responses of five different target models: B-52 (1:72 scale), B-58 (1:48), TR-1 (1:48), F-14 (1:48), and M-29 (1:48). These measurements were taken over the band 1-7 GHz at a 0.01 GHz sampling increment, weighted using a Gaussian modulated cosine (GMC) function centered at 4 GHz, and inverse transformed into the time-domain using the FFT. The pulse duration is approximately 0.4 ns. Each target was measured at 68 aspect angles from 0^0 (nose-on) to 30.15^0 with a 0.45^0 aspect angle increment.

Figure 6.1 shows total pulse response of the B-52 at 18^0 aspect. Because the dominant resonances of the target lie below 1 GHz, there is only a very small late-time signal (beginning at about 5 ns). Several early-time events are seen, including the initial scattering from the nose of the aircraft. The complex times associated with these events are determined by using the E-pulse technique to fit the real (or imaginary) part of the complex exponential series in (6.4) to the real (imaginary) part of the Fourier transform of the response shown in Figure 6.1. Figure 6.2 shows the real part of the frequency domain response, and the response reconstructed using 14 exponential terms. Since agreement is good, the 14 complex amplitudes and 14 complex times represent an efficient means for storing the data in coded form. Using the spectrum waveform of the response in Figure 6.1 as the response of an unknown target, and correlating it with the stored responses of all other targets, gives the results shown in Figure 6.3. Here the maximum correlation is plotted versus aspect angle. Since we only care about maximum correlation, and since any time shift present when we determine the beginning time of the early-time response only leads to a time position shift of the resulting maximum correlation, our discrimination scheme is much less sensitive to determination of the beginning time of the signal than E-pulse discrimination scheme. At 18^0 a unity maximum correlation is obtained, since identical responses are being correlated. Note that the maximum correlation of the unknown target response is largest for the B-52 over a range of angles from about 17^0 to 20^0, corresponding to 3^0 discrimination range over which the B-52 can be identified. Since the maximum correlation of all the wrong targets is 0.84, the discrimination ratio is 1.2 for the 18^0 B-52 response. Similar results for the other four targets at various aspect angles are illustrated in Figure 6.4, Figure 6.5 , Fig

the

whi

def

of 1

whe

than

of t

Fig

but

resu

Fig

com

of th

the

the

Figu

expe

corre

Figur

Figure 6.6, and Figure 6.7. The largest discrimination range is observed in the case of the TR-1. This target can be identified within a range of 10^0 surrounding 22.5^0 aspect.

In order to show the effects of random noise on target discrimination, zero-mean white Gaussian noise is artificially added to the unknown target response. SNR was defined in Chapter 2.

Figure 6.8 shows the pulse response of the B-52 model at 18^0 aspect with an SNR of 10 dB. As we have seen before, noise has a greater influence on late-time response where signal is very small. This suggests that using only the early-time response is better than using the total response or only the late-time response. Performing the correlation of this signal spectrum with the reconstructed waveforms gives the results shown in Figure 6.9. The maximum correlation has dropped to 0.98 with the addition of the noise, but the discrimination range is only slightly reduced from the noise-free case. Similar results are shown for higher noise levels for various targets shown in Figure 6.10, Figure 6.11, Figure 6.12, and Figure 6.13. Note that 28 complex amplitudes and complex times are required to represent the data using the frequency domain technique.

Figure 6.14 shows the correlation of the B-52 response with 10 dB SNR with each of the target responses reconstructed using just 7 exponential terms in (6.4). As expected, the discrimination ratio is decreased, since the lesser number of terms can not reproduce the original measured data as faithfully.

A summary of the effects of noise on discrimination is shown in Figure 6.15 and Figure 6.16. The effect of noise on discrimination range is shown in Figure 6.15. As expected, when the measured signal becomes noisier, the range of angles over which correct identification can be performed becomes narrower (except with the F-14). Figure 6.16 shows the discrimination ratio as a function of noise level. It also indicates a reduced ability to discriminate among targets as noise level becomes higher. With the definition used in the current thesis, it is possible to discriminate accurately with an SNR as low as -10 dB (within 0^0 to 30.15^0 aspects). Conservatively, a 2^0 discrimination range is observed. This may suggest that the extracted parameters can be stored at a increment of 2^0 aspect to reduce storage space further.

New wideband AEL H-1498 horn antennas with a rated bandwidth from 2 to 18 GHz allow the effective resolution of our measurements to be increased by a factor of 2.67. The enhanced measurement system produces higher resolution scattering data from scale model aircraft which will now be used in this section to study correlation-based target discrimination. The theory and procedure are exactly same as presented above.

We will use the responses of five different target models: B-52 (1:72 scale), B-58 (1:48), TR-1 (1:48), F-14 (1:48), and A-10 (1:48). These measurements were taken over the band 2-18 GHz at a 0.01 GHz sampling increment, weighted using a Gaussian modulated cosine (GMC) function centered at 10 GHz, and inverse transformed into the time-domain using the FFT. The pulse duration is approximately 0.2 ns. Each target was measured at 201 aspect angles from 0^0 (nose-on) to 180^0 with a 0.9^0 aspect angle increment.

Figure 6.17 shows the pulse response of the B-52 at 18^0 aspect. The wider bandwidth of the new measurement system provides greater temporal resolution and thus detail in the early-time response than that shown in Figure 6.1. The complex times associated with scattering centers are determined by using the E-pulse technique to fit the complex exponential series in (6.4) to the Fourier transform of the response in Figure 6.17. Figure 6.18 illustrates the real part of the frequency domain response, and the reconstructed waveform using 25 exponential terms. The agreement is good.

Compared to 14 exponential terms used previously, the amount of required data storage is increased by just about a factor of 2. Using the spectrum of the response in Figure 6.17 as the response of an unknown target, and correlating it with the stored responses of all other targets, gives Figure 6.19. At 18^0 a nearly unity maximum correlation is obtained, and the target is identified over a 3^0 range of aspect angles (discrimination range). Although this range has not increased, the discrimination ratio has increased by approximately a factor of 2 over the whole 180^0 range, and thus discrimination performance is better. Similar results for the B-58 at various aspect angles are demonstrated in Figure 6.20.

To see the effects of random noise on target discrimination, zero-mean white Gaussian noise is again added to the measured response. Performing the correlation of 18^0 B-52 response with the reconstructed waveforms gives the results shown in Figure 6.21. The discrimination range is only slightly reduced from the noise-free case. The discrimination ratio is still higher than that shown in Figure 6.3. Similar results are shown for another SNR level for B-58 target in Figure 6.22.

A summary of effects of noise on discrimination is shown in Figure 6.23. As expected, when the measured signal becomes noisier, the range of angles over which correct identification can be performed becomes narrower. The target can be identified with SNR as low as -5 dB. In our case, higher resolution provides better discrimination performance, but it requires more storage space and more parameter extracting time. Note that 50 complex amplitudes and complex times are required to represent the data using frequency domain technique. Obviously, the required parameters to be saved are increased by about twice compared to those before.

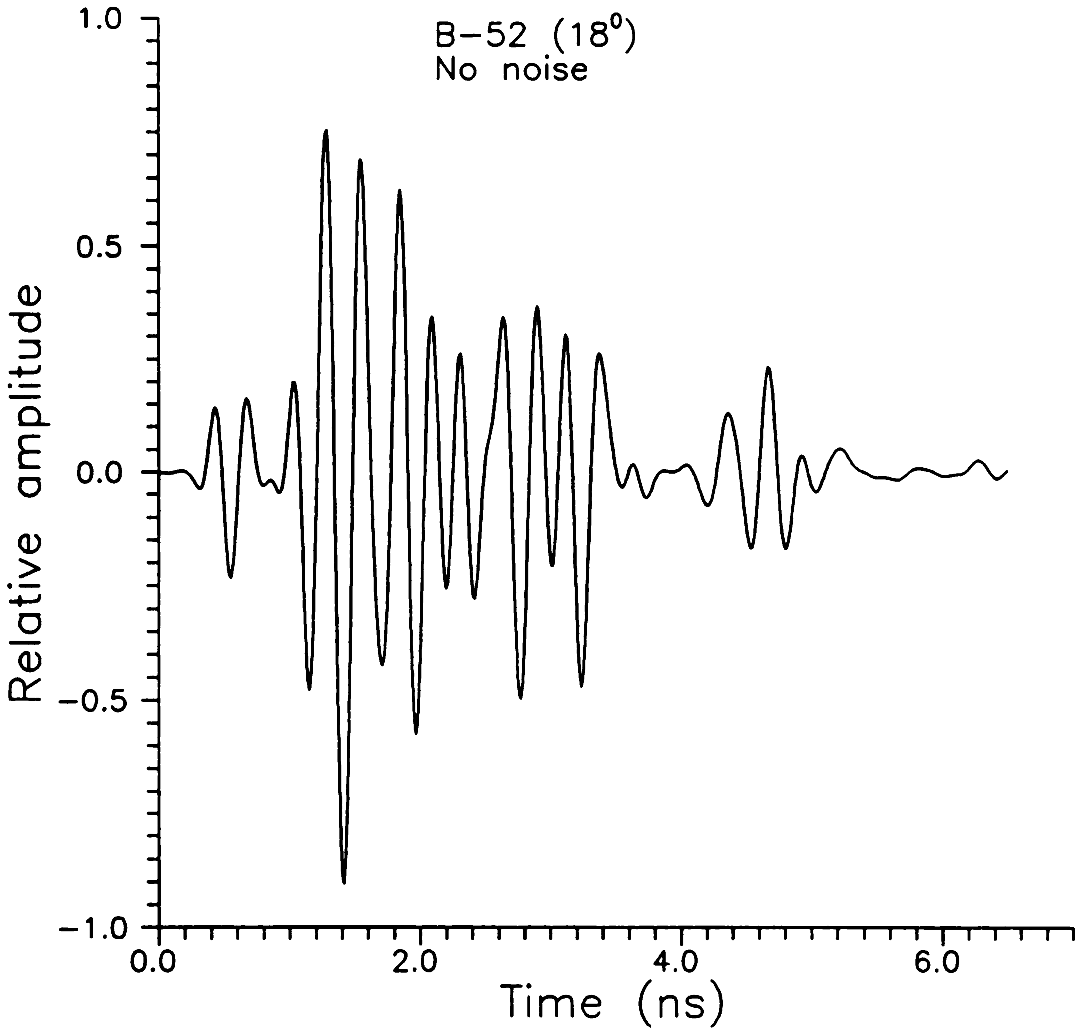

Figure 6.1 Pulse response of B-52 aircraft model measured at 18^0 aspect angle in the band 1-7 GHz.

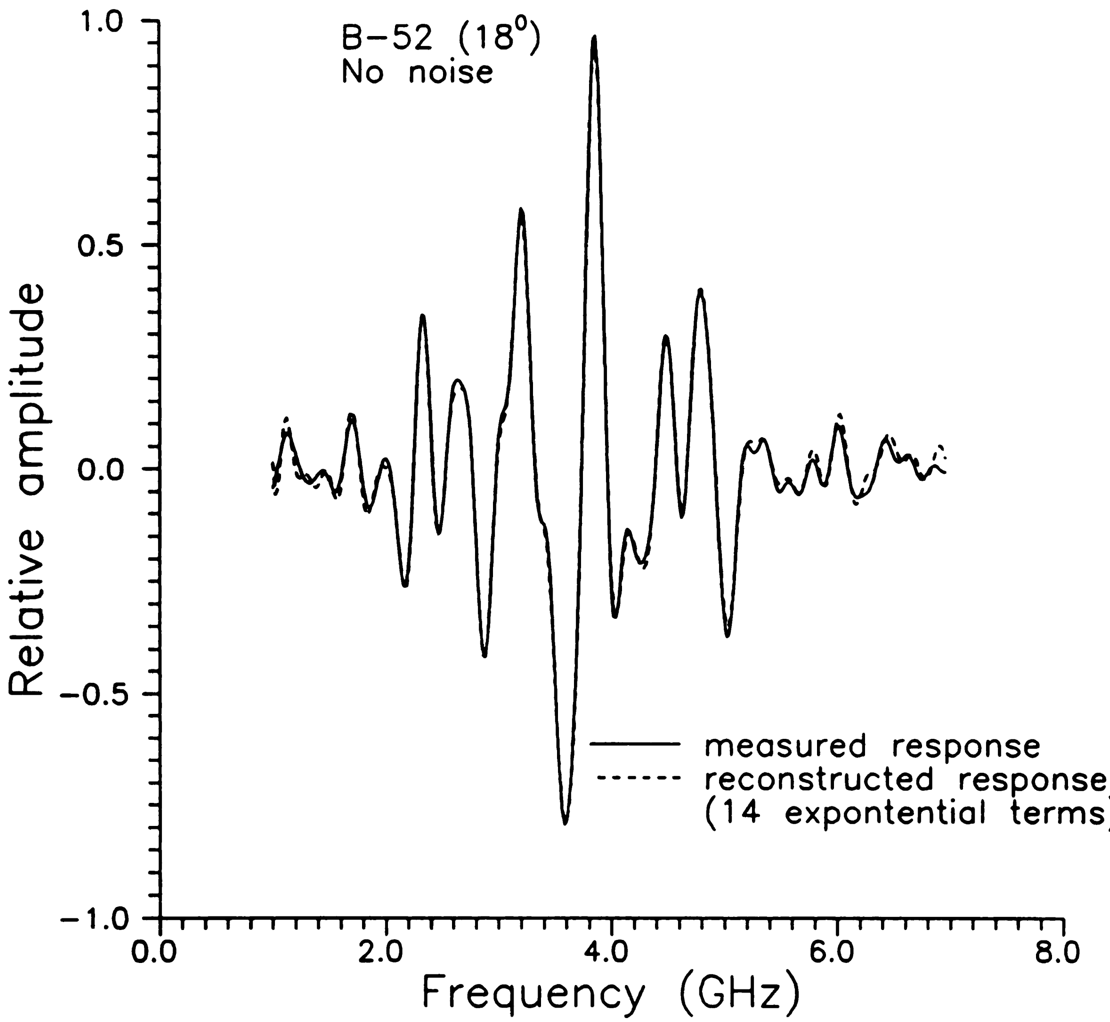

Figure 6.2 Measured real part of Fourier transform of early-time response of 18^0 B-52, and reconstructed response using 14 exponential terms determined by E-pulse technique.

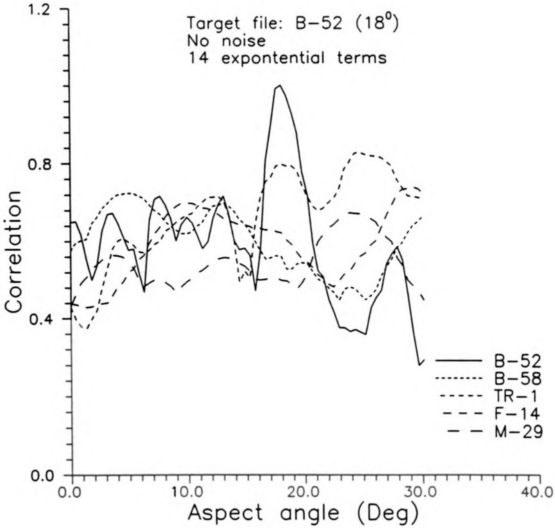

Figure 6.3 Maximum correlation of 18^0 B-52 response with responses from various targets reconstructed from 14 term frequency domain representation.

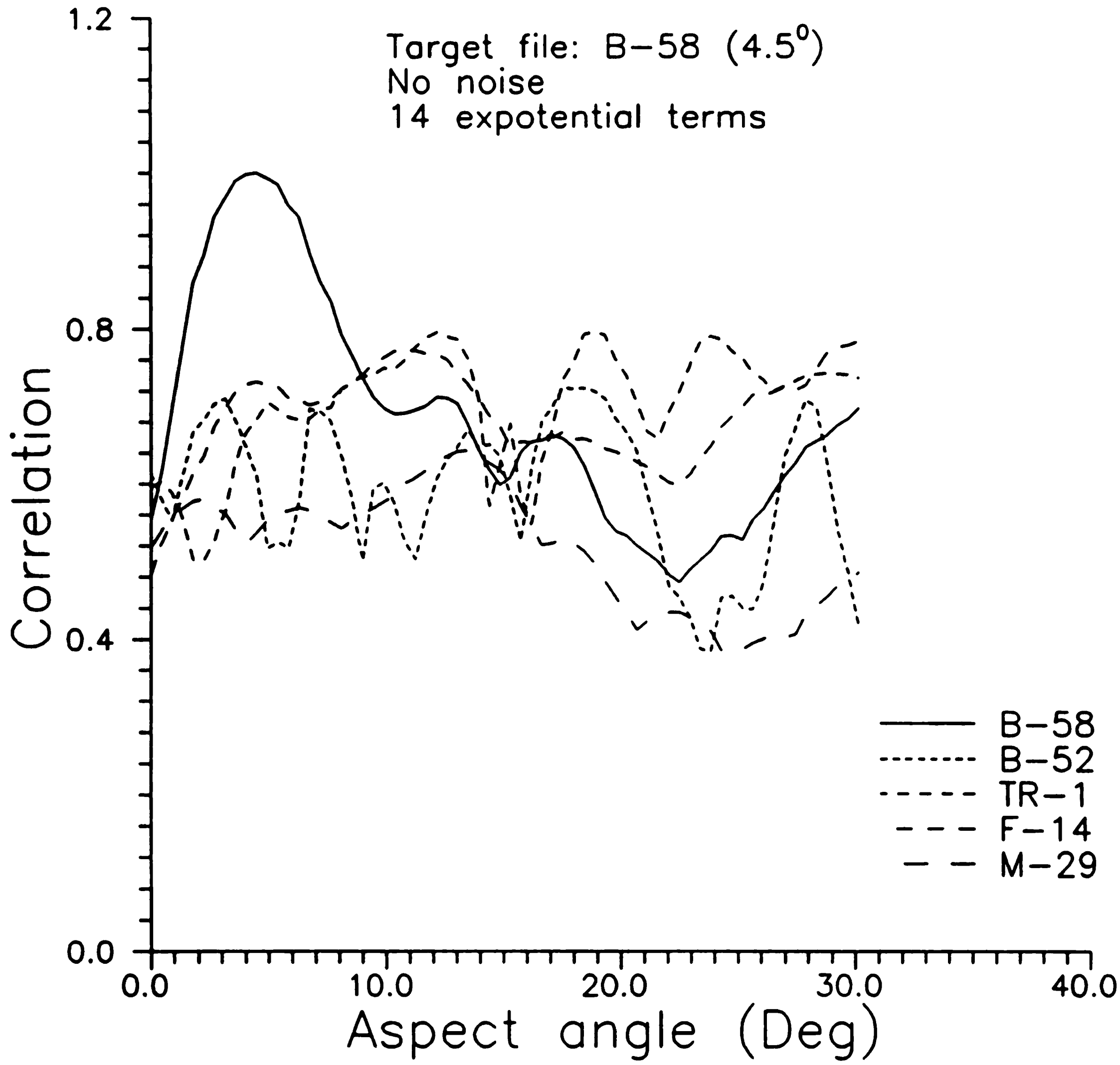

Figure 6.4 Maximum correlation of 4.5^0 B-58 response with responses from various targets reconstructed from 14 term frequency domain representation.

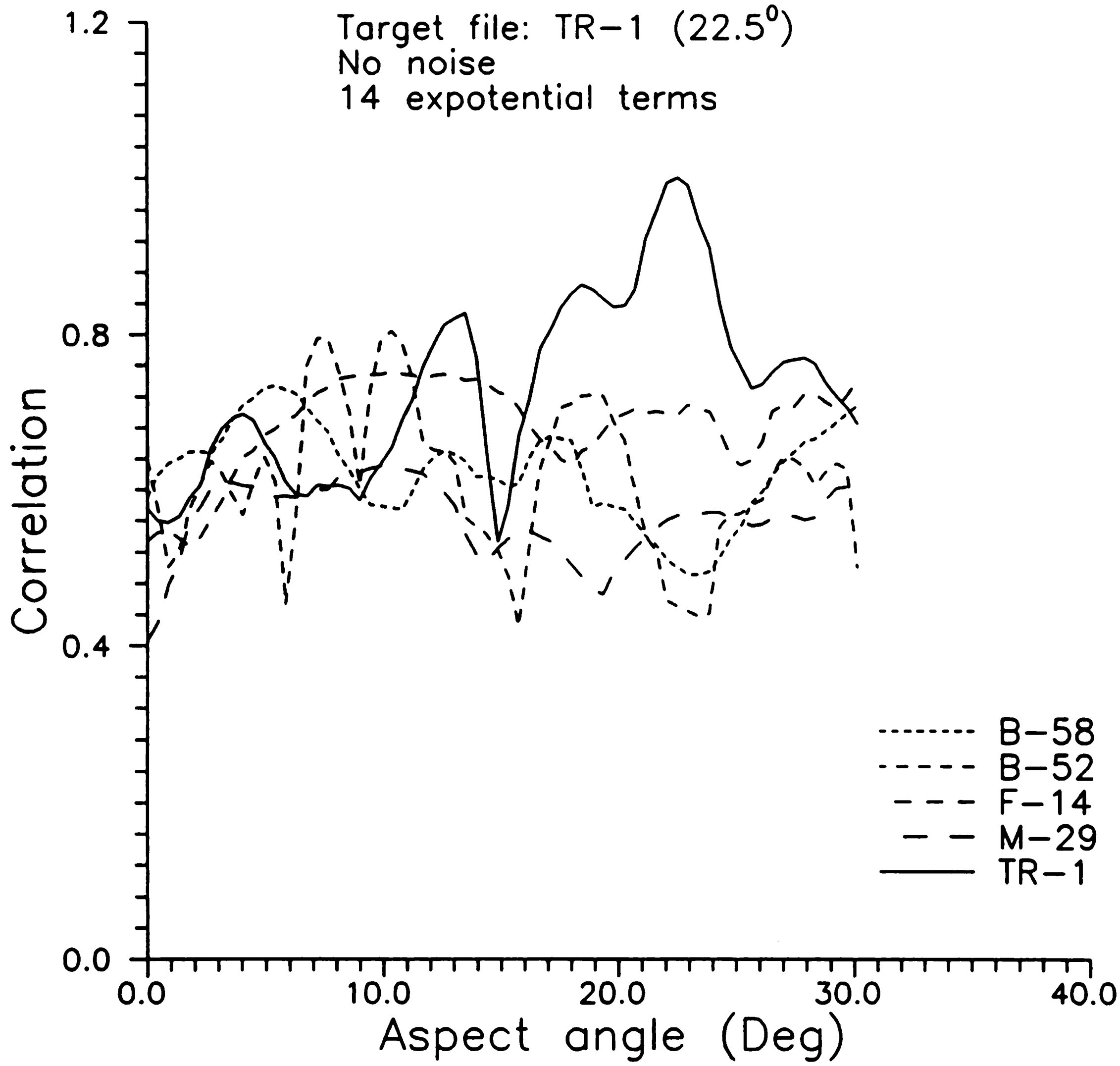

Figure 6.5 Maximum correlation of 22.5° TR-1 response with responses from various targets reconstructed from 14 term frequency domain representation.

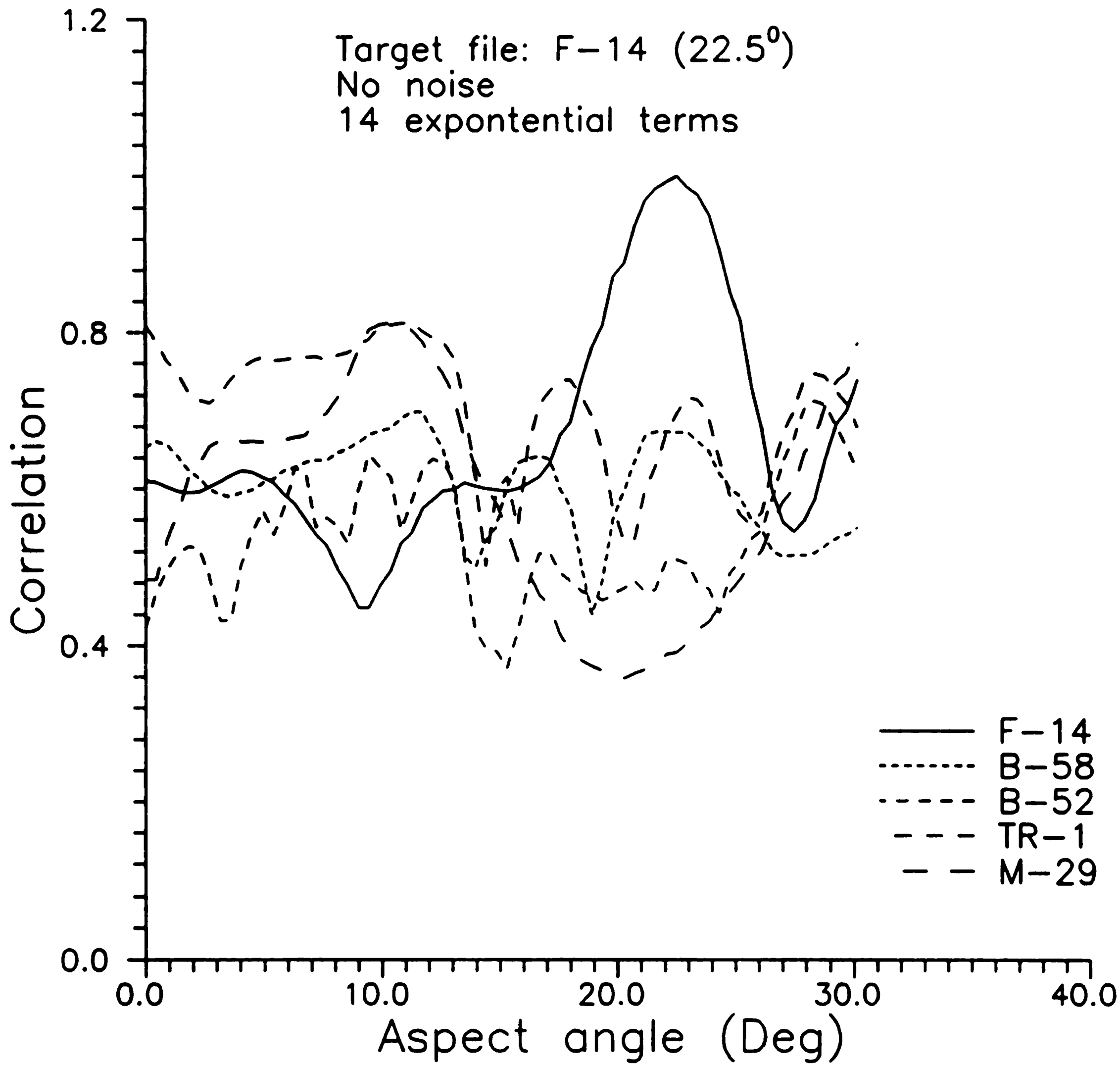

Figure 6.6 Maximum correlation of 22.5° F-14 response with responses from various targets reconstructed from 14 term frequency domain representation.

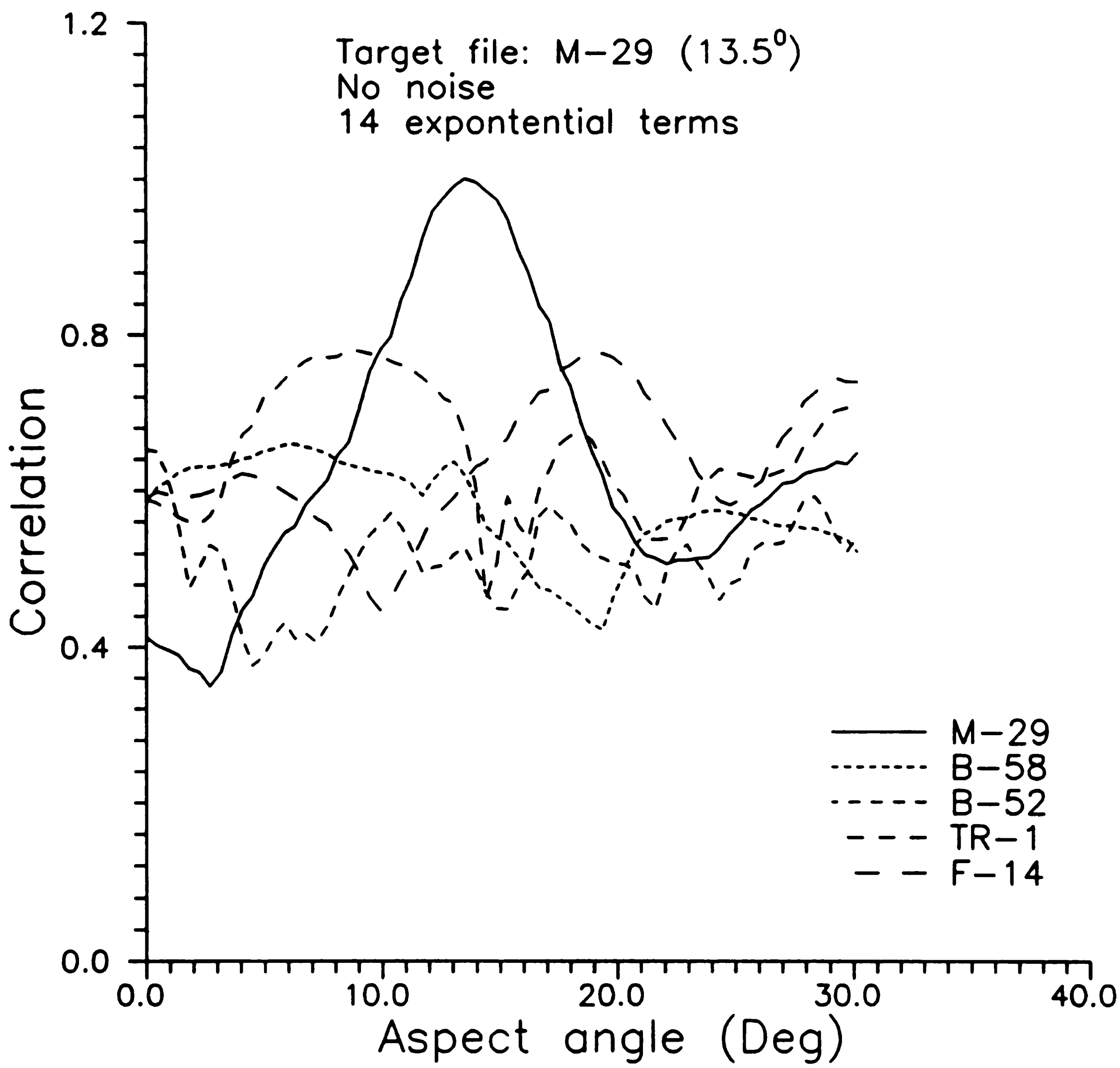

Figure 6.7 Maximum correlation of 13.5⁰ M-29 response with responses from various targets reconstructed from 14 term frequency domain representation.

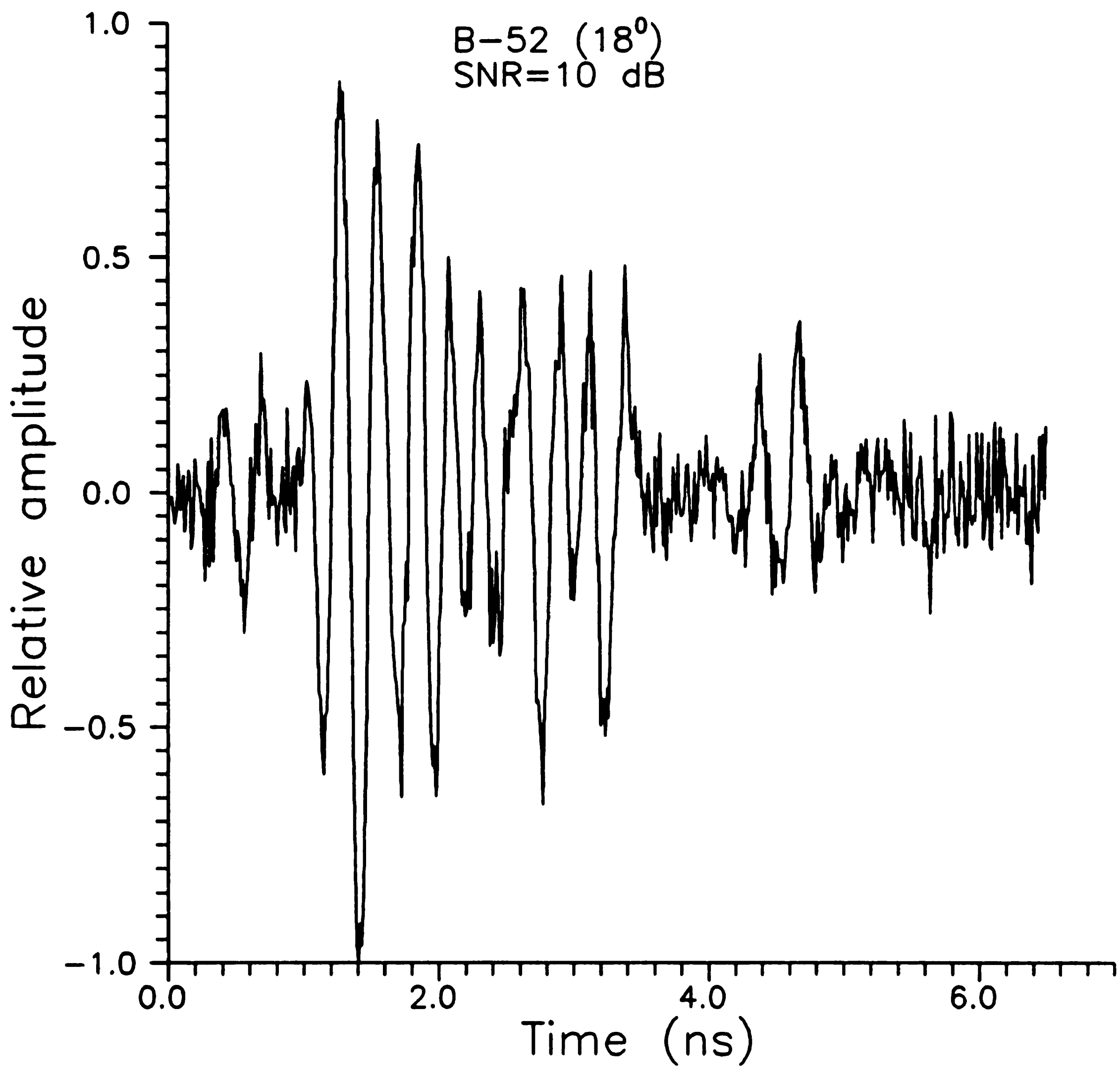

Figure 6.8 Response of 18^0 B-52 aircraft model with zero-mean white Gaussian noise added. SNR = 10 dB.

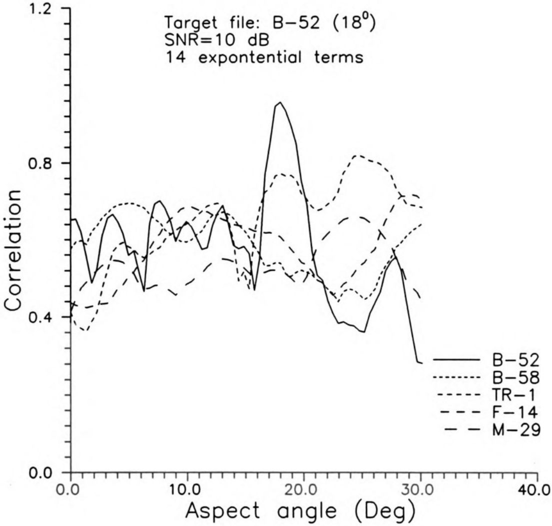

Figure 6.9 Maximum correlation of noisy 18^0 B-52 response with responses from various targets reconstructed from 14 term frequency domain representation. SNR=10 dB.

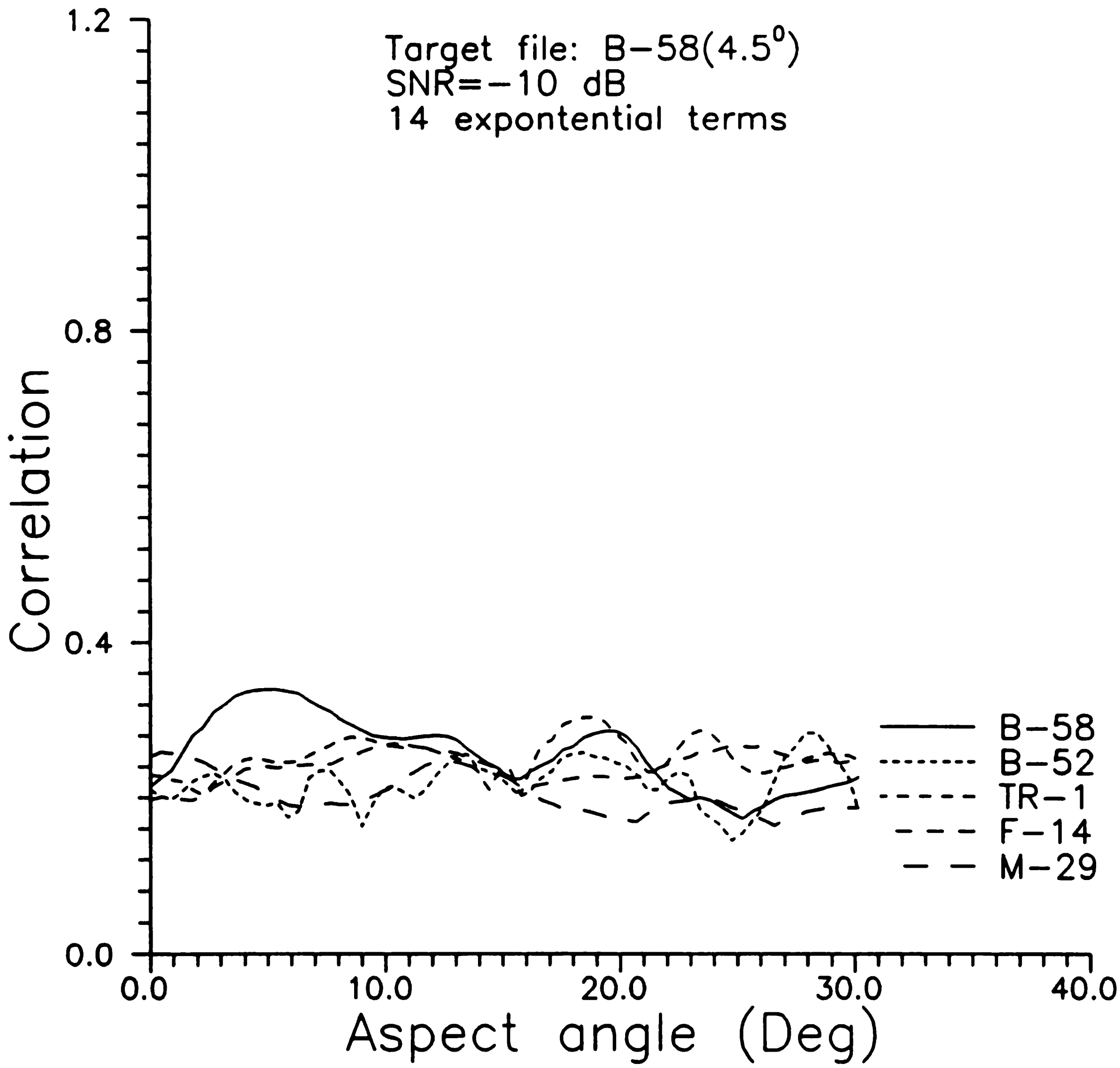

Figure 6.10 Maximum correlation of noisy 4.5^0 B-58 response with responses from various targets reconstructed from 14 term frequency domain representation. SNR=-10 dB.

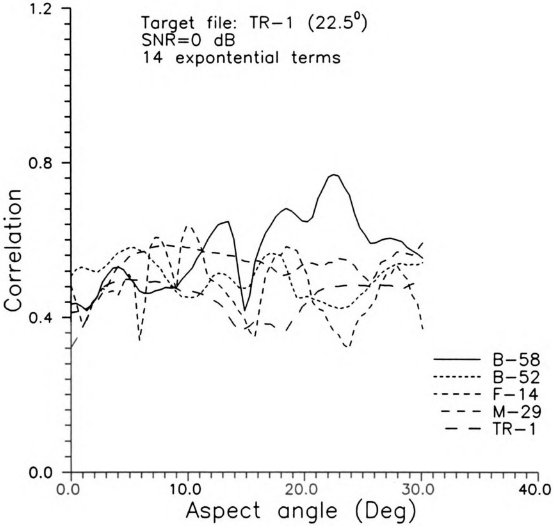

Figure 6.11 Maximum correlation of noisy 22.5^0 TR-1 response with responses from various targets reconstructed from 14 term frequency domain representation. SNR=0 dB.

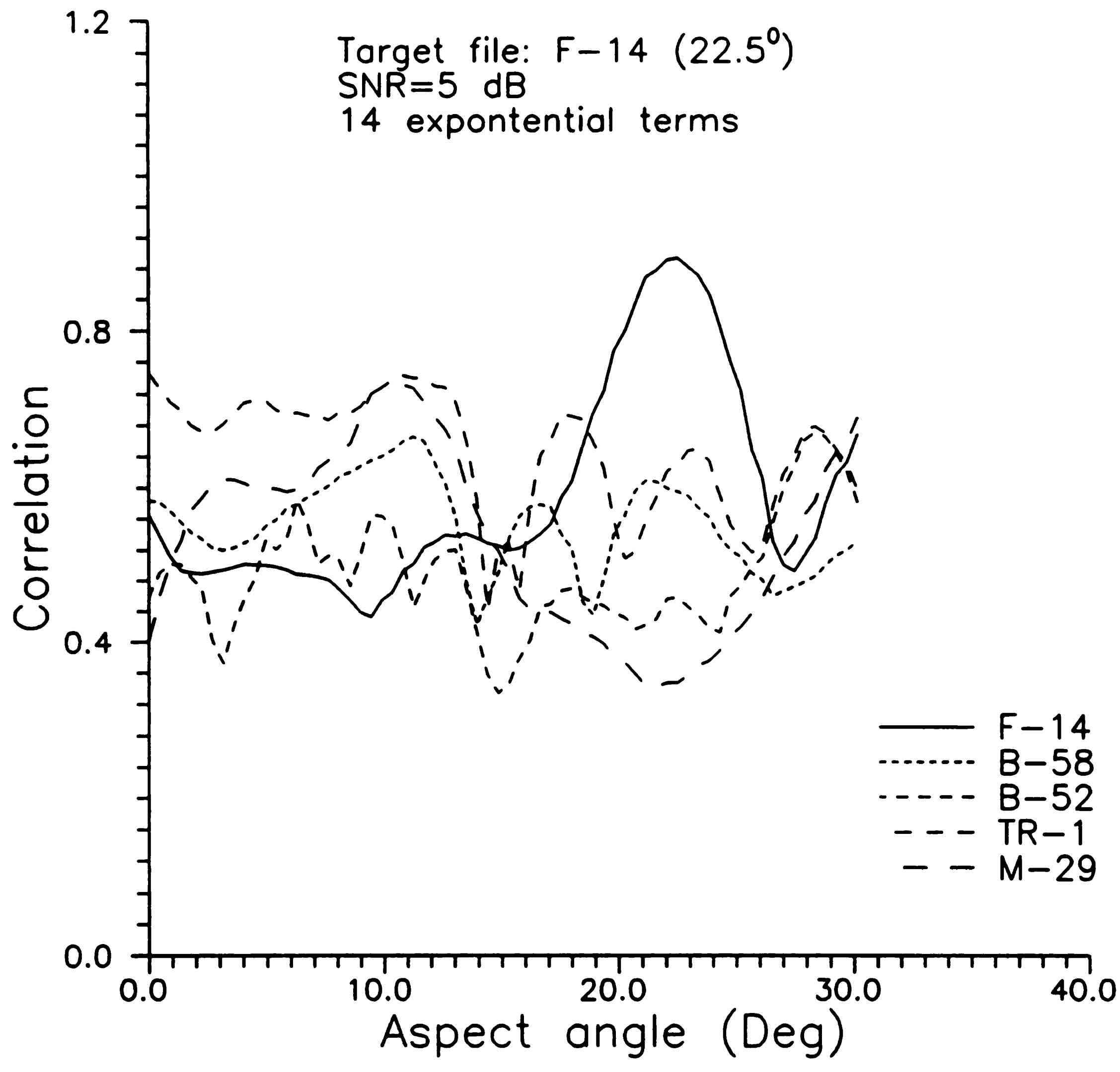

Figure 6.12 Maximum correlation of noisy 22.5° F-14 response with responses from various targets reconstructed from 14 term frequency domain representation. SNR=5 dB.

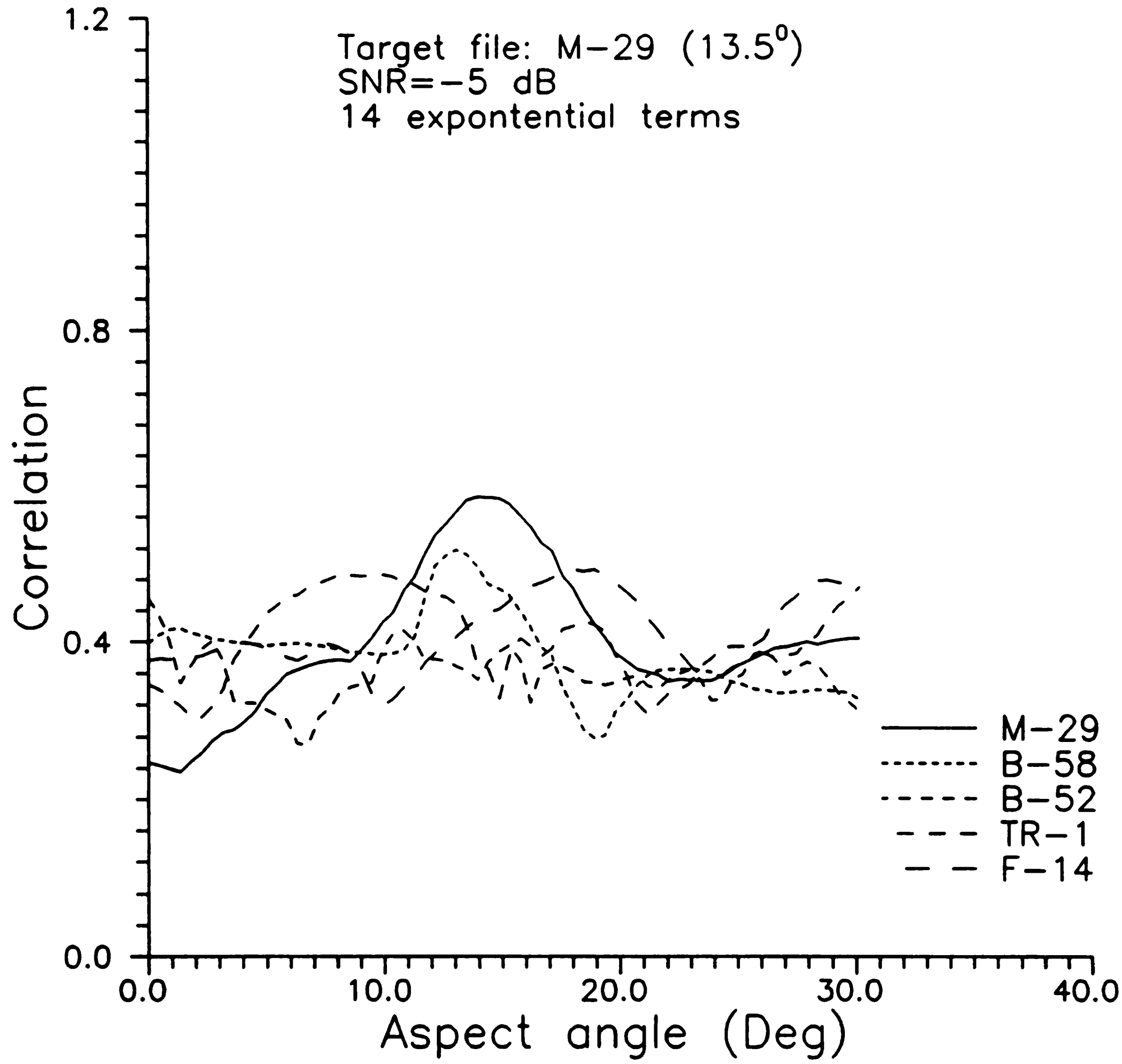

Figure 6.13 Maximum correlation of Noisy 13.5^0 M-29 response with responses from various targets reconstructed from 14 term frequency domain representation. SNR=-5 dB.

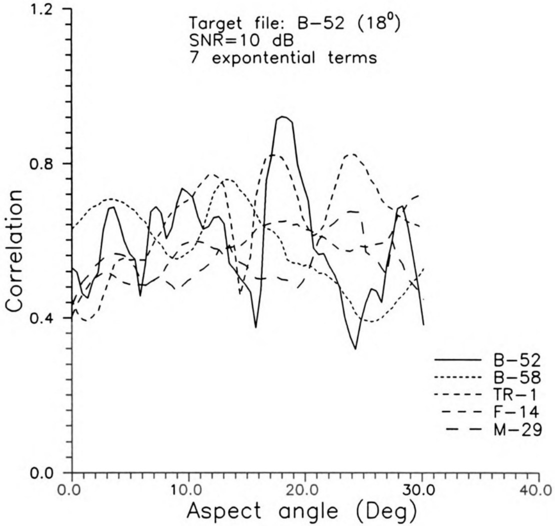

Figure 6.14 Maximum correlation of noisy 18^0 B-52 response with responses from various targets reconstructed from 7 term frequency domain representation. SNR=10 dB.

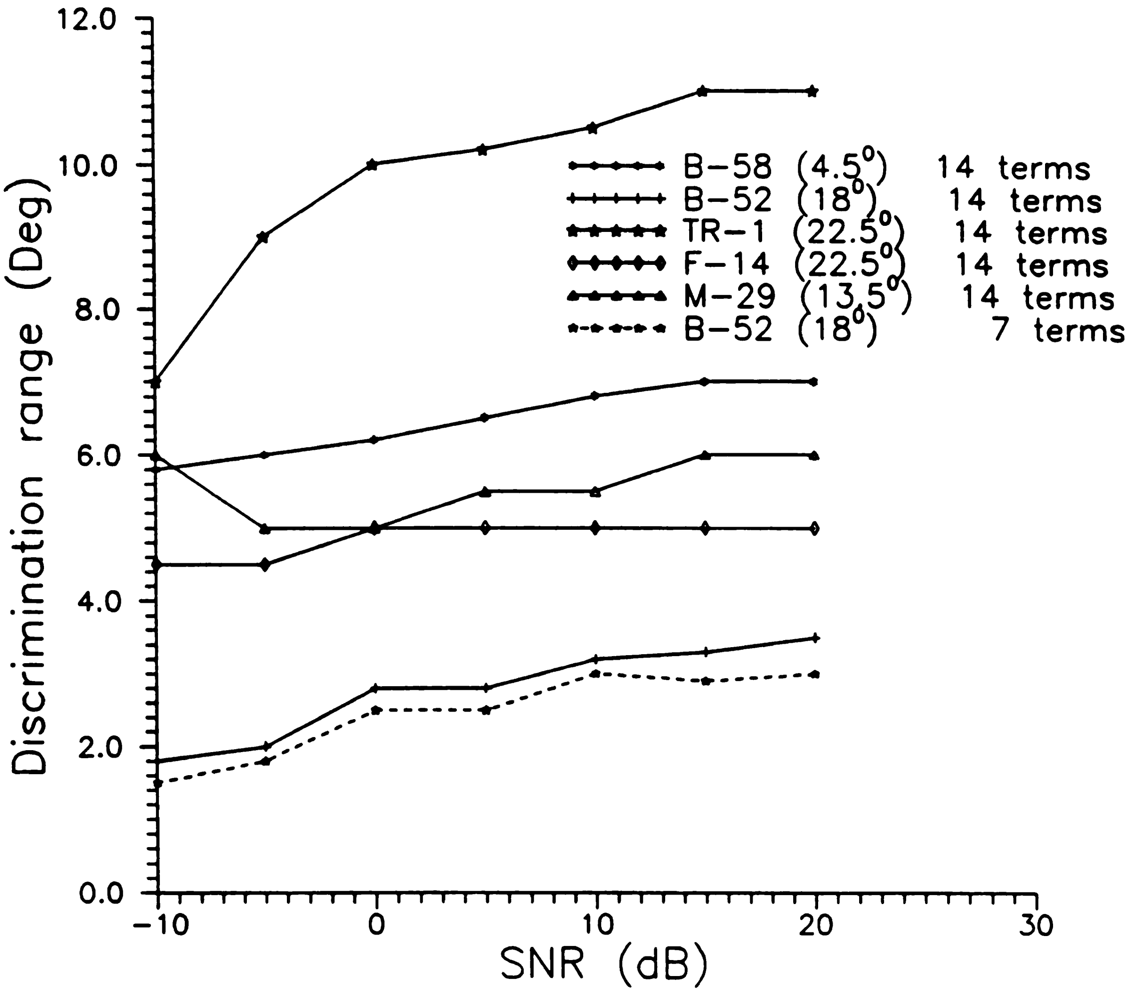

Figure 6.15 Discrimination range of various aircraft targets as a function of noise level. Frequency-domain technique used.

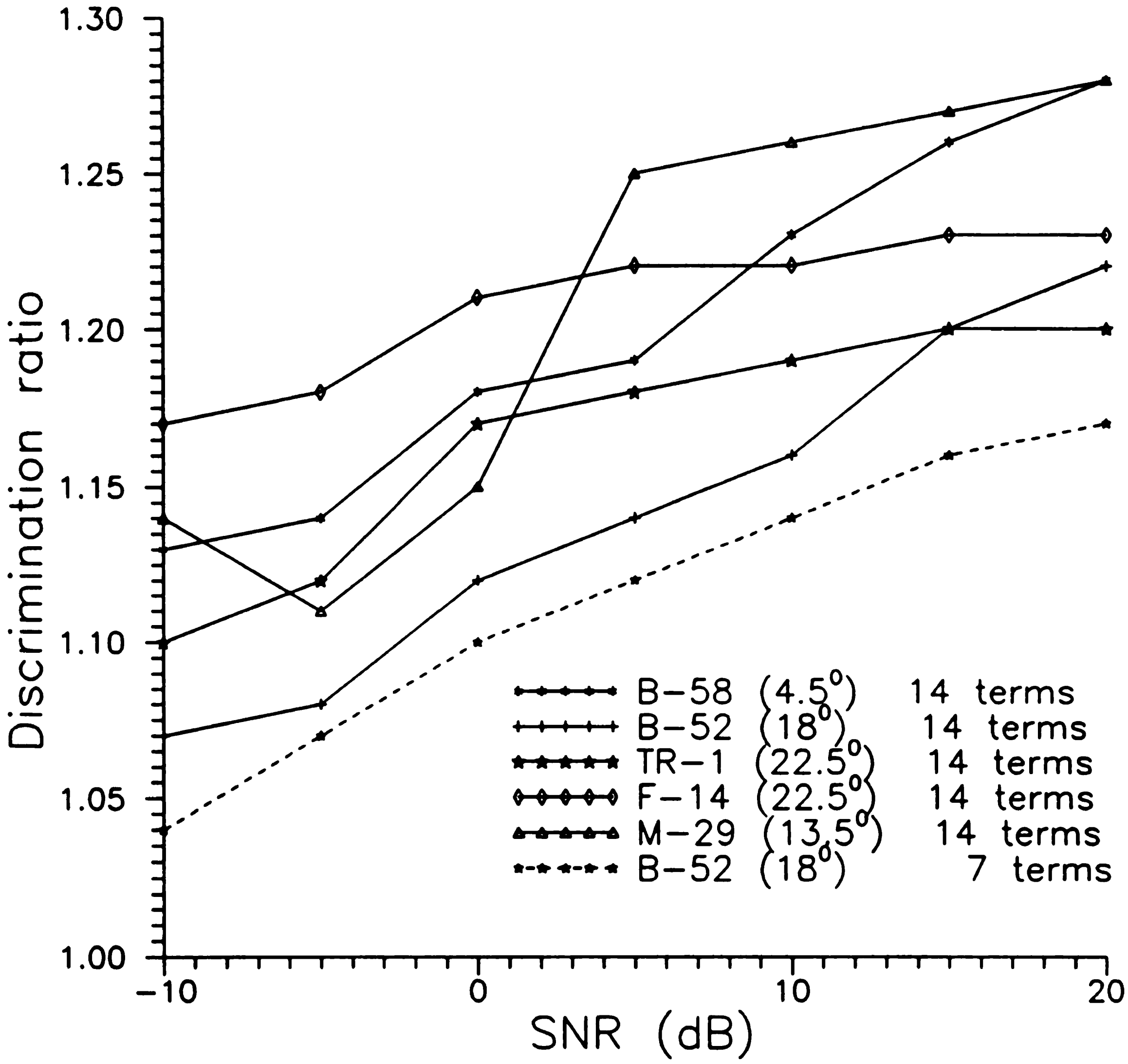

Figure 6.16 Discrimination ratio of various aircraft targets as a function of noise level. Frequency-domain technique used.

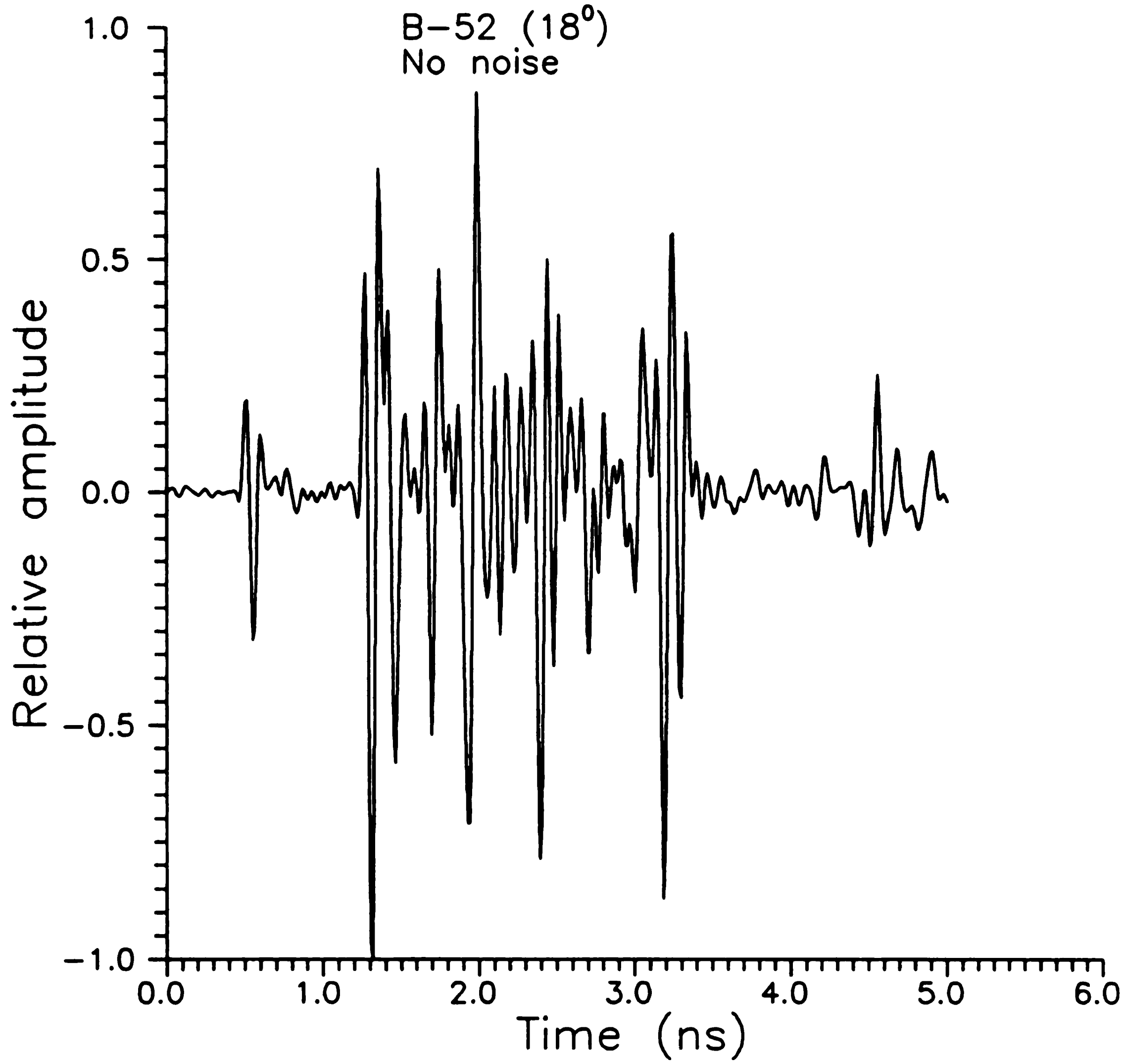

Figure 6.17 Pulse response of B-52 aircraft model measured at 18° aspect angle in the band 2-18 GHz.

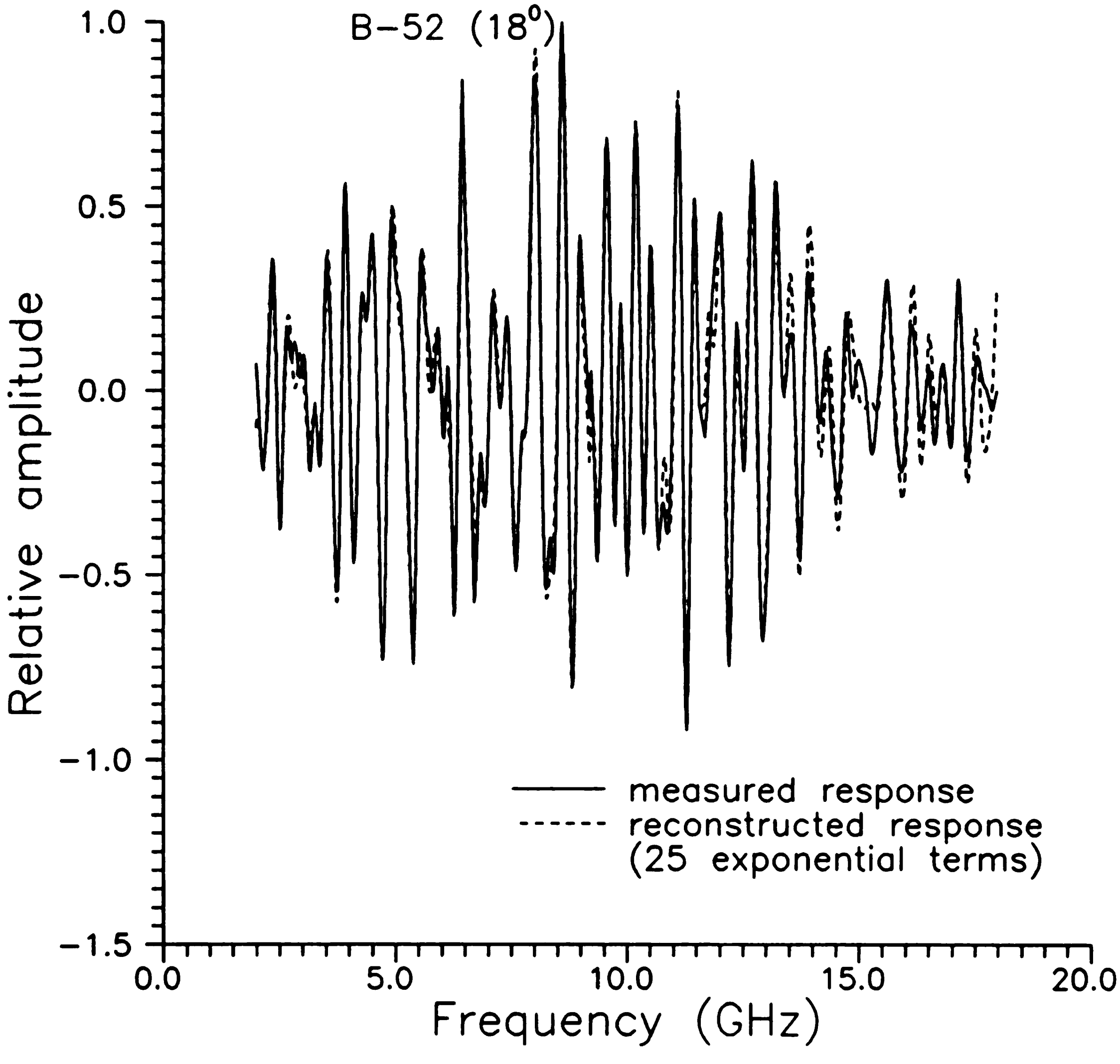

Figure 6.18 Measured real part of Fourier transform of early-time response of 18^0 B-52, and reconstructed response using 25 exponential terms determined by E-pulse technique.

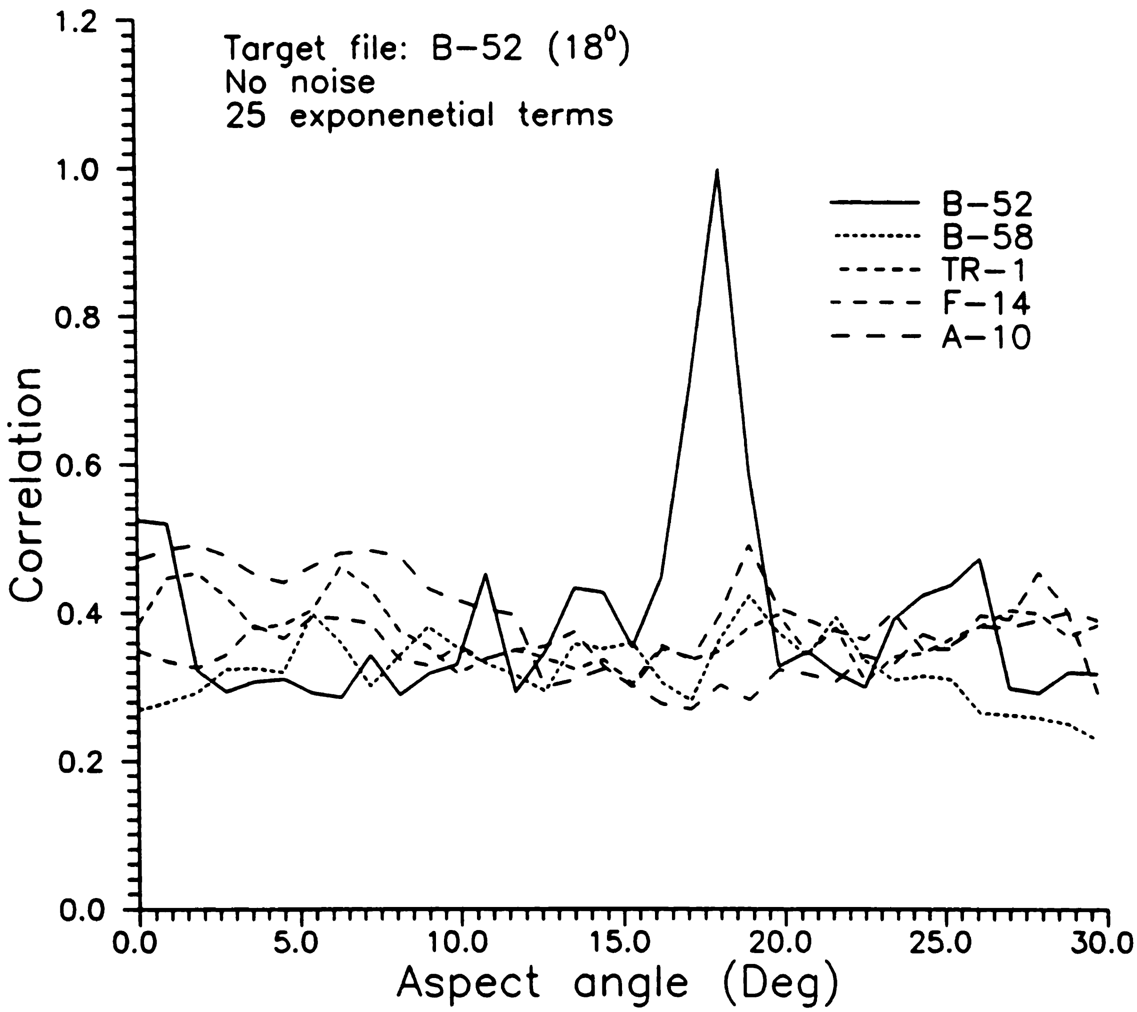

Figure 6.19 Maximum correlation of 18^0 B-52 response with responses from various targets reconstructed from 25 term frequency domain representation.

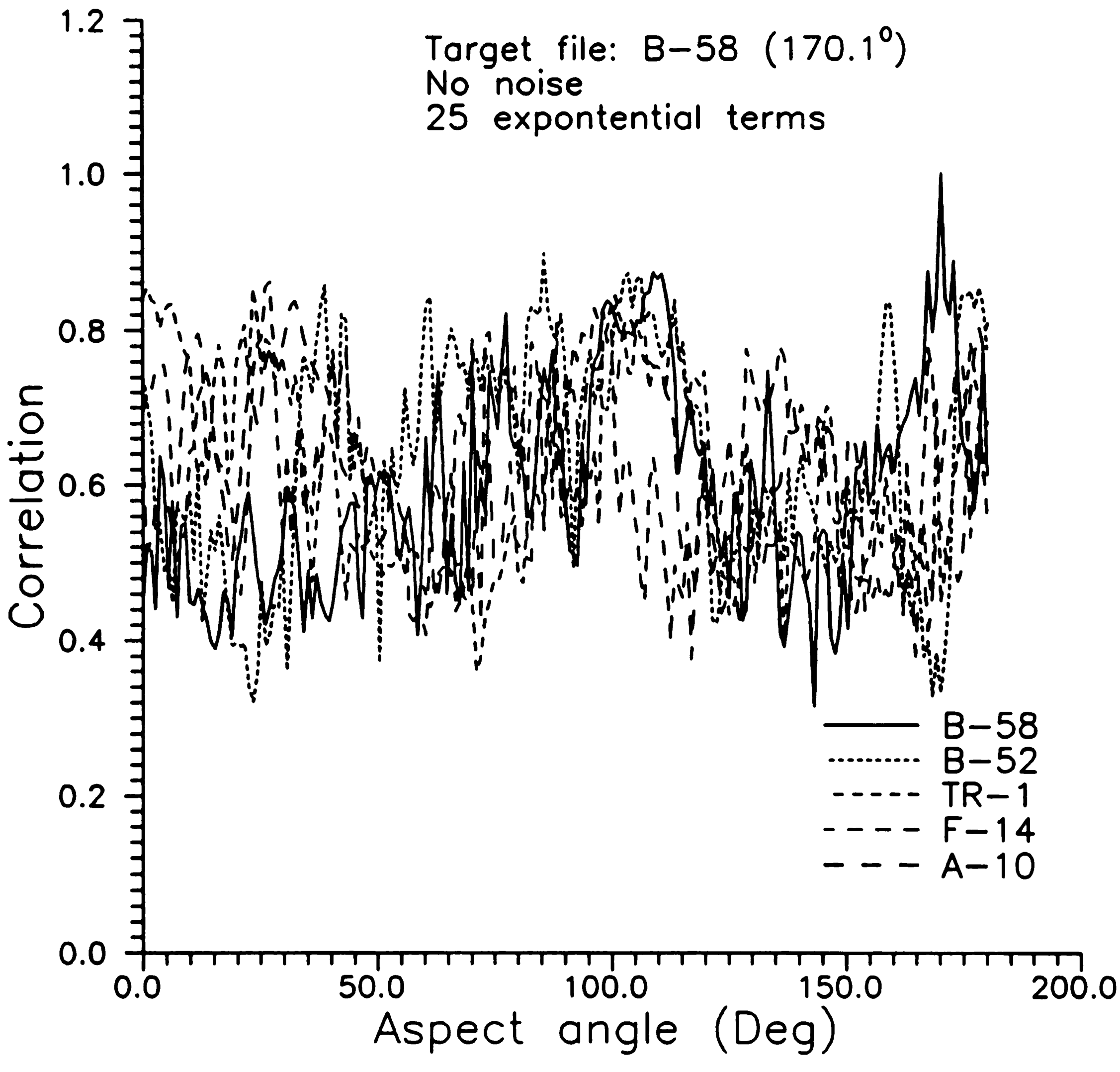

Figure 6.20 Maximum correlation of 170.1^0 B-58 response with responses from various targets reconstructed from 25 term frequency domain representation.

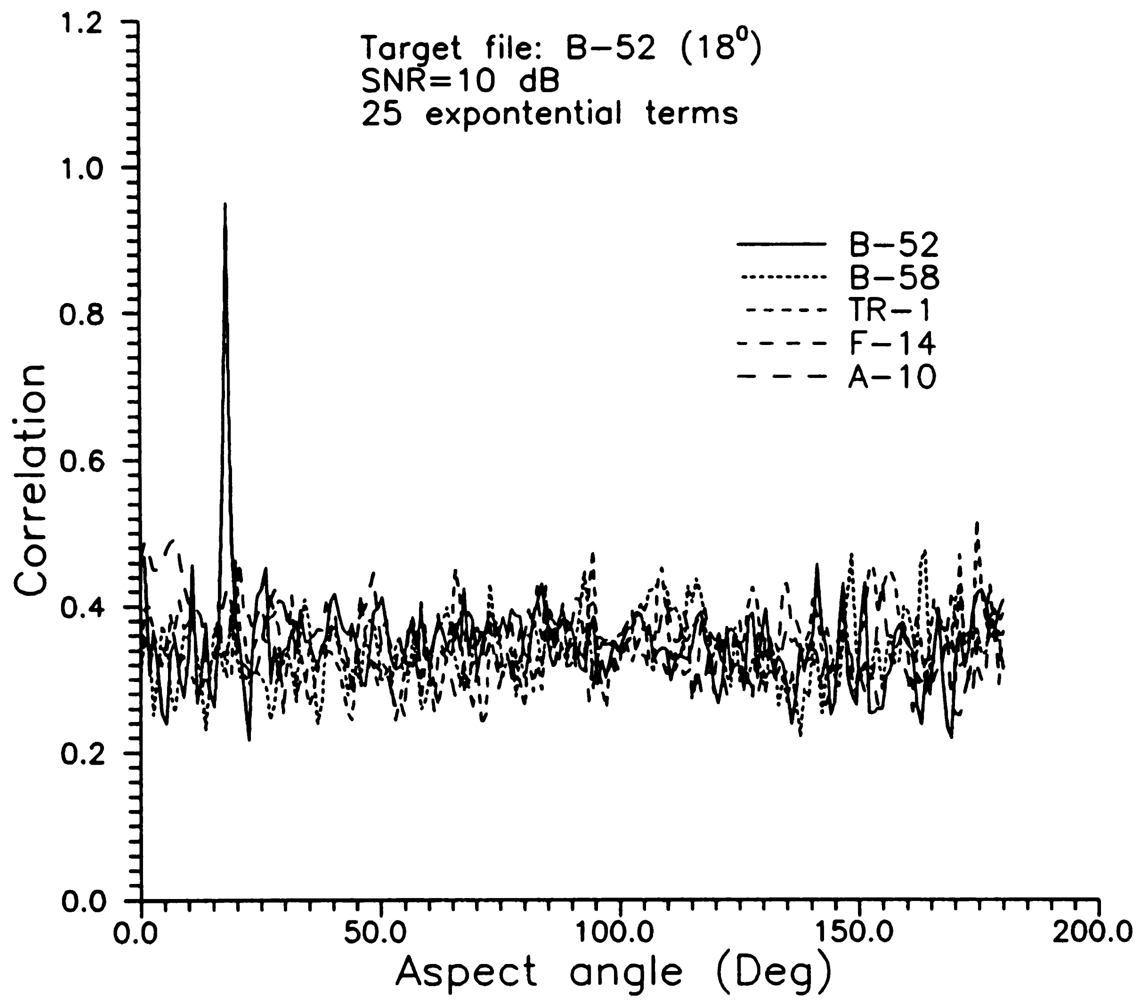

Figure 6.21 Maximum correlation of noisy 18^0 B-52 response with responses from various targets reconstructed from 25 term frequency domain representation. SNR=10 dB.

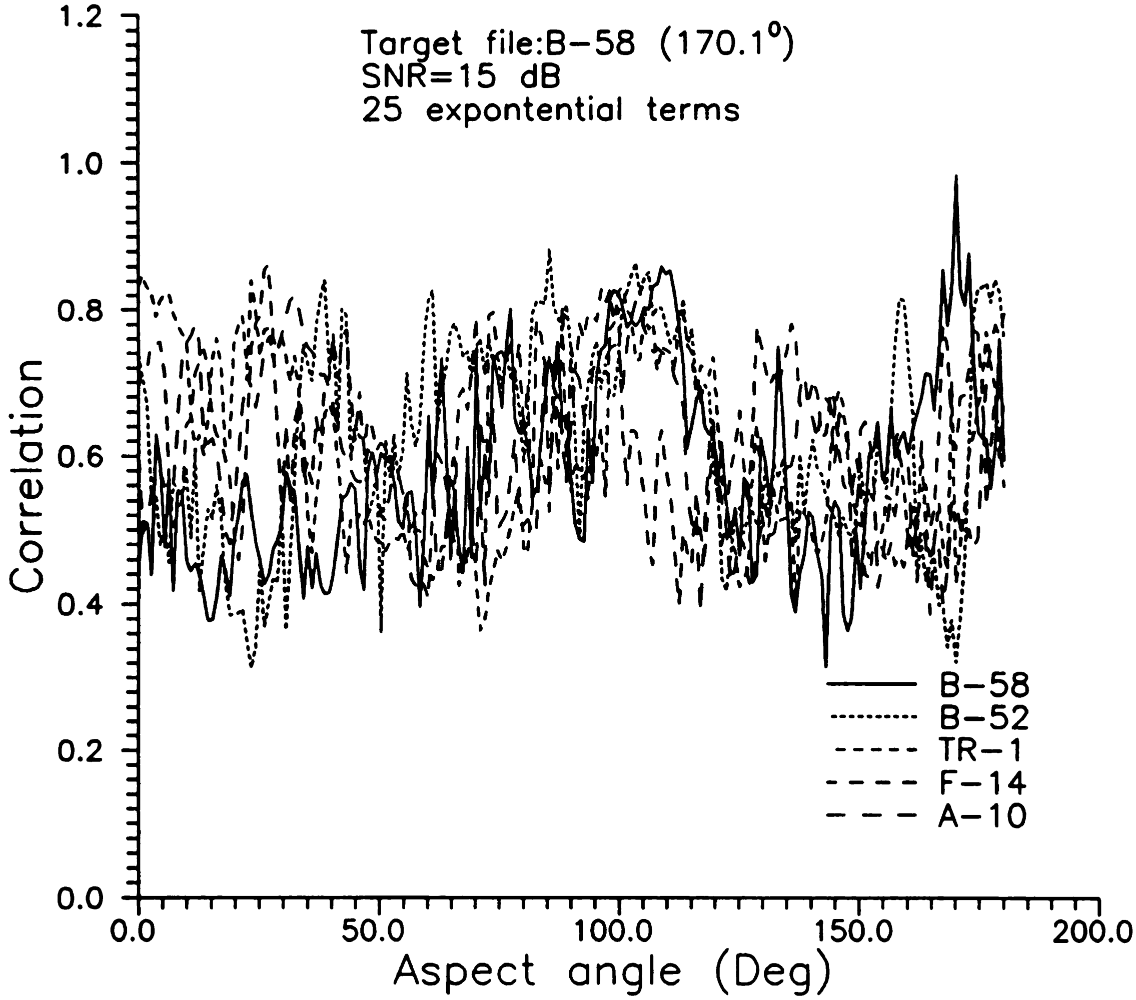

Figure 6.22 Maximum correlation of noisy 170.1^0 B-58 response with responses from various targets reconstructed from 25 term frequency domain representation. SNR=15 dB.

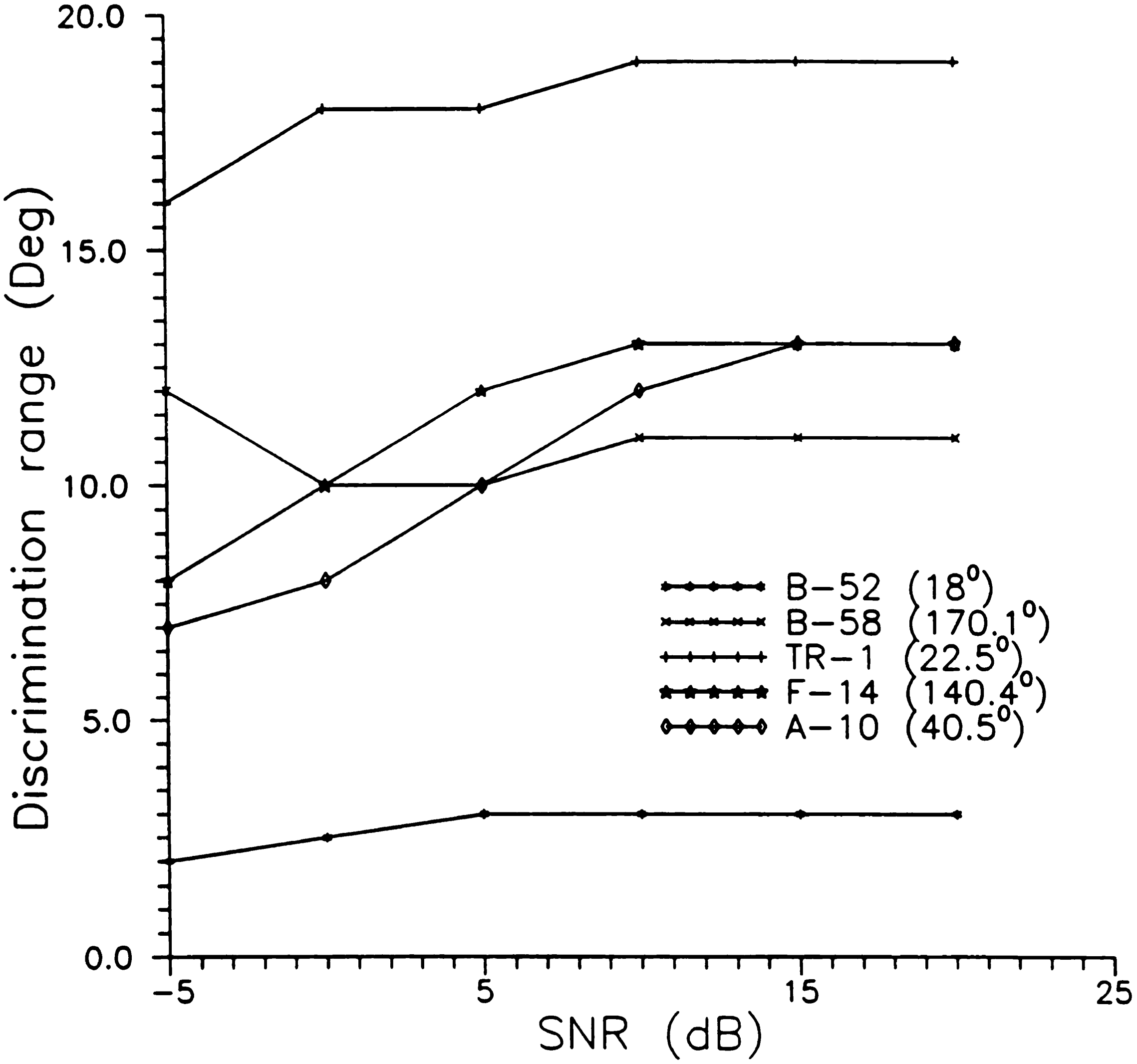

Figure 6.23 Discrimination range of various aircraft targets as a function of noise level. Frequency-domain technique used. The measured frequency band is 2-18 GHz.

6.4 Performance of Correlation-Based Discrimination Scheme With Time-Domain Storage

In this section we will present a technique for locating the scattering centers in the time domain. Because extraction of the scattering center information is done using the time domain representation of the data, this is referred to be a "time-domain" method.

To review, the time-domain method assumes that the early-time transient response of a radar target at k^{th} aspect angle, $f_k(t)$, consists of distinct specular reflections arising from scattering centers on the targets. Temporal "hot spot" positions $\{T_m\}$ and amplitudes $\{a_{mn}\}$ are extracted by the least squares method and stored in the computer. The early-time pulse response is reconstructed in the form of

$$f_k(t) = \sum_m f_{km}(t) \approx \sum_m p(t) * h_{km}(t) \tag{6.5}$$

where

$$h_{km}(t) = \sum_{n=-\infty}^{\infty} a_{kmn} \delta^{(n)}(t - T_{km}) \tag{6.6}$$

Here p(t) is the transmitted pulse waveform, and $h_{km}(t)$, $f_{km}(t)$ are the impulse response and pulse response of the m^{th} scattering center at k^{th} aspect angle, respectively. By storing just the values of T_{km} and a_{kmn} for a subset of the scattering centers, a significant reduction in storage space is achieved.

To demonstrate target discrimination using the time-domain approach, we use the responses of the same five different target models used in section 6.3: B-52 (1:72 scale), B-58 (1:48), TR-1 (1:48), F-14 (1:48), and M-29 (1:48). These measurements were taken over the narrower band 1-7 GHz.

Figure 6.24 shows the measured 18^0 B-52 response, and the reconstructed response using 9 scattering centers, each with a seven term expansion of the localized pulse response ($n=-3,-2,\ldots,3$). The agreement is good. Using this measured response as the response of an unknown target, and correlating it with the stored responses of all targets, gives the maximum correlation results shown in Figure 6.25. Here the maximum correlation is plotted versus aspect angle. At 18^0 a unity maximum correlation is obtained, and the B-52 target is identified over a 3^0 range of aspects, called the "discrimination range". A similar result was shown in Figure 6.3. The plots are nearly identical because the time and frequency domain approaches each do a good job of representing the measured waveform.

Similar results for other targets at various aspect angles are illustrated in Figure 6.26, Figure 6.27, and Figure 6.29. Again the largest discrimination range is observed in Figure 6.27. This target can be identified within a range of 11^0 around 22.5^0. These results are very similar to those found by frequency-domain method. Figure 6.28 shows the measured response of 22.5^0 F-14, and reconstructed response. The match is very good.

To test the effects of random noise on target discrimination, zero-mean white Gaussian noise is again added to the unknown target responses as before.

Correlating the early-time response shown in Figure 6.8 with the reconstructed responses from various targets gives the results shown in Figure 6.30. The maximum correlation is reduced due to noise, but the B-52 can still be identified with a 3^0 discrimination range. Similar results are demonstrated for other noise levels in Figure 6.32, Figure 6.33, and Figure 6.34. Figure 6.31 shows pulse response of the B-

58 model with a very severe SNR of -10 dB. It is obvious that signal is distorted completely. Upon correlation with the stored responses from all the targets, the maximum correlation has been reduced greatly, but the B-58 can still be identified accurately.

Figure 6.35 shows the result of using fewer scattering centers and fewer *n* terms in the representation of each scattering center response. Here the measured response of the 22.5^0 TR-1 is compared with the reconstructed response using 3 scattering centers and $n=-2,-1,\ldots,2$. Figure 6.36 shows the correlation of the measured 22.5^0 TR-1 response (with 0 dB SNR) with each of reconstructed responses, using 3 scattering centers and $n=-2,\ldots,2$. As expected, the discrimination range is decreased since less information is included in the reconstructed responses.

To summarize discrimination performance, Figure 6.37 shows the discrimination range of five targets as a function of noise level. All targets are identified with noise level as low as SNR=-10 dB (within 0^0 to 30.15^0 aspects). Compared with Figure 6.15, Figure 6.37 shows comparable ranges.

We still use five different target models to test the effects of the enhanced measurement band on the time-domain correlation-based discrimination: B-52 (1:72), B-58 (1:48), TR-1 (1:48), F-14 (1:48),and A-10 (1:48). These measurements were taken over the wider band 2-18 GHz.

Figure 6.38 shows the measured 22.5^0 TR-1 response, and the reconstructed response using 13 scattering centers, each with a seven term expansion of the localized pulse response ($n=-3,-2,\ldots,3$). The agreement is very good. Figure 6.39 shows the maximum correlation of this measured response with the stored responses of all targets as a function of aspect angles. About an 18^0 discrimination range is observed and the target can also be identified between 0^0 and 10^0. This shows improved discrimination results. Similar results for other targets are seen in Figure 6.40 and Figure 6.41.

Performing the correlation of the noisy 22.5^0 TR-1 response with the reconstructed waveforms gives the results shown in Figure 6.42. The discrimination range is only slightly reduced from the noise-free case. Similar results are shown for other SNR levels for F-14 and A-10 targets in Figure 6.43, and Figure 6.44.

A summary of effects of noise on discrimination is shown in Figure 6.45. We can compare Figure 6.45 with Figure 6.23. Both show comparable results since both approaches can represent the measured waveform well. The target can be identified with SNR as low as -5 dB (within 0^0 to 180^0 aspects). It is found that when the resolution is increased by more than two times, the ability to discriminate targets is enhanced. Note that a total of 104 parameters are required to represent the data (91 amplitudes and 13 scattering locations) with time domain technique. Obviously, the two methods and the wavelet technique [35] require roughly the same amount of storage space.

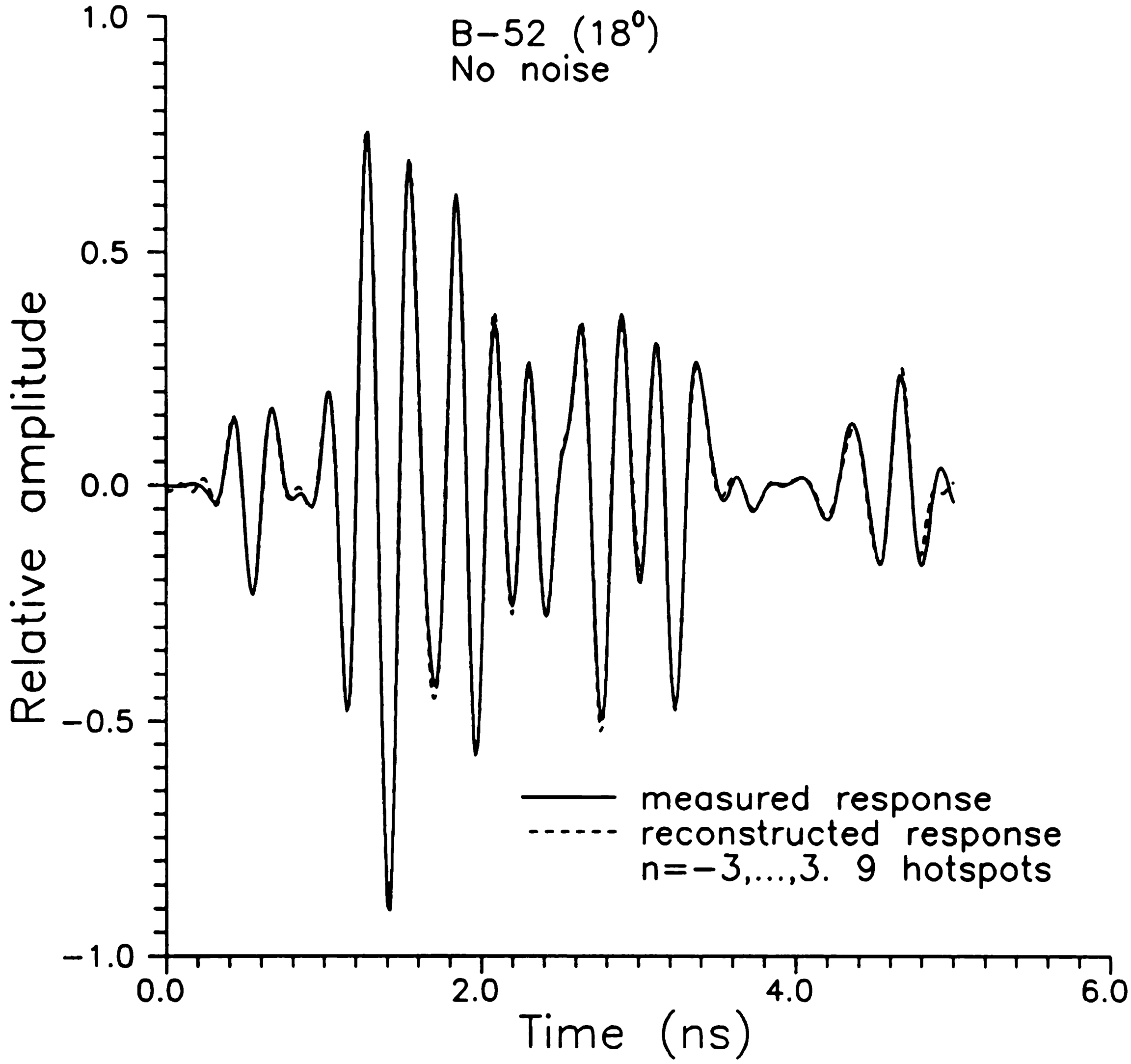

Figure 6.24 Measured early-time response of 18^0 B-52, and reconstructed response using 9 scattering centers and n=-3,...3.

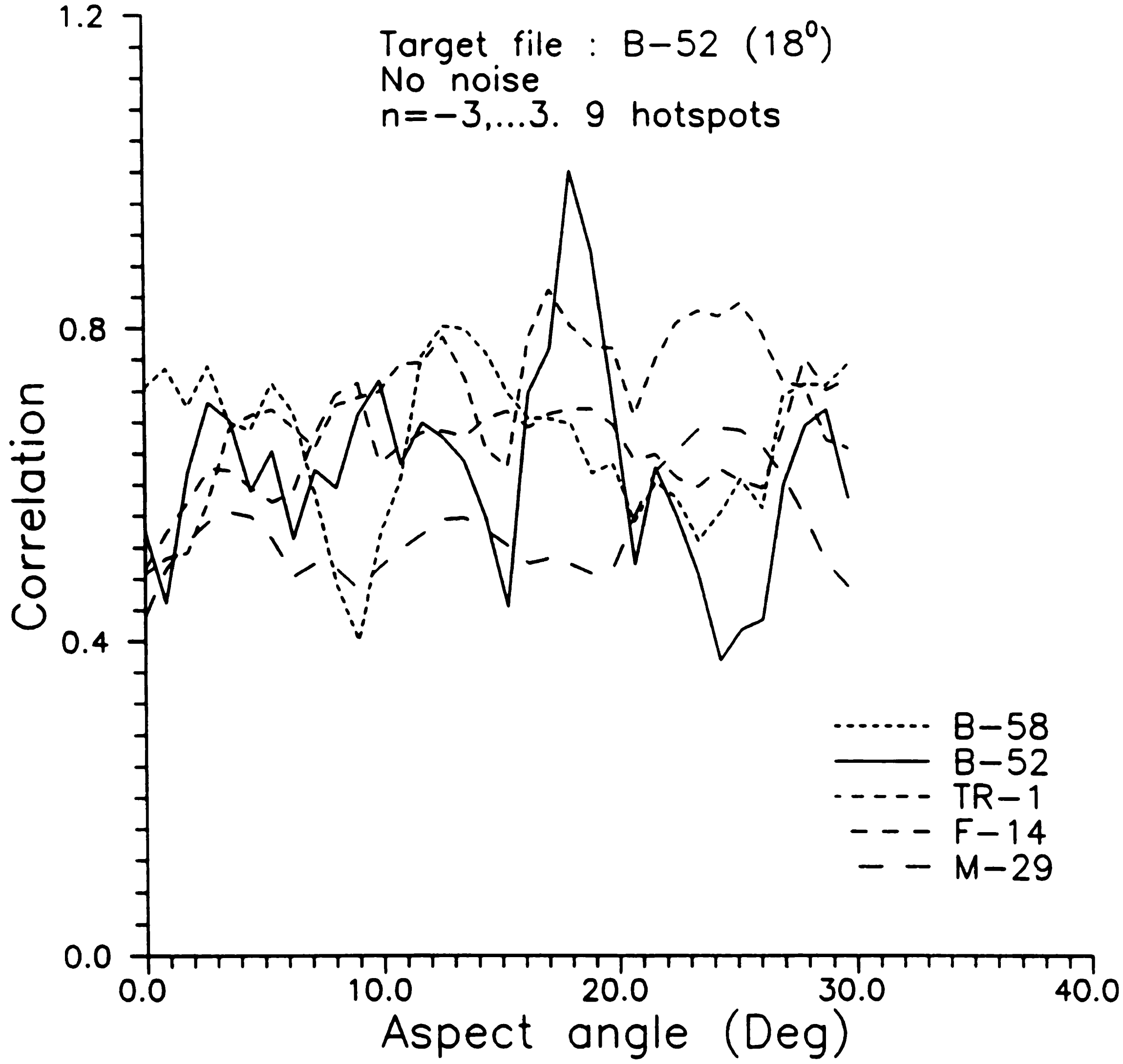

Figure 6.25 Maximum correlation of 18^0 B-52 response with responses from various targets reconstructed from time-domain representation using 9 scattering centers and n=-3,-2,...3.

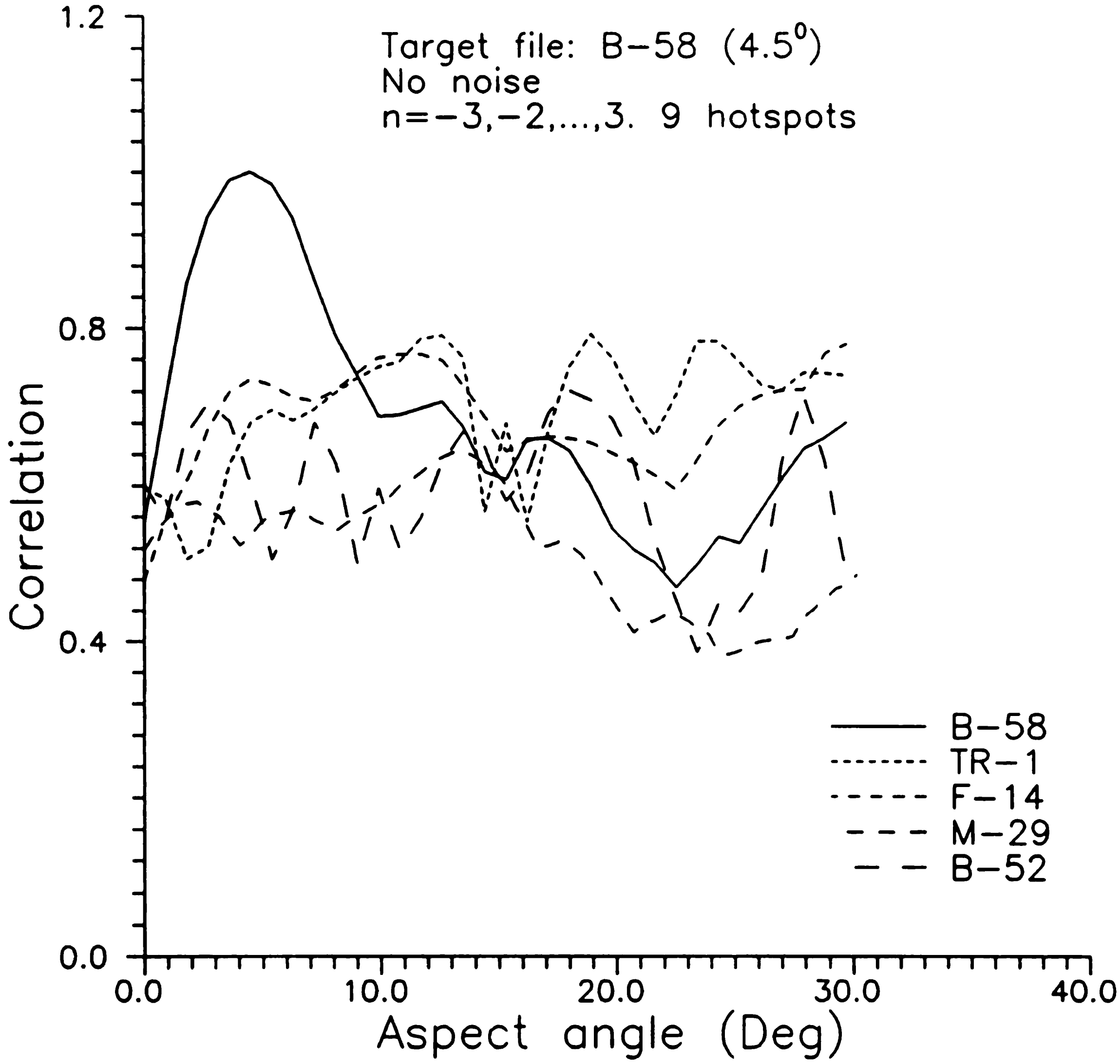

Figure 6.26 Maximum correlation of 4.5^0 B-58 response with responses from various targets reconstructed from time-domain representation using 9 scattering centers and n=-3,-2,...3.

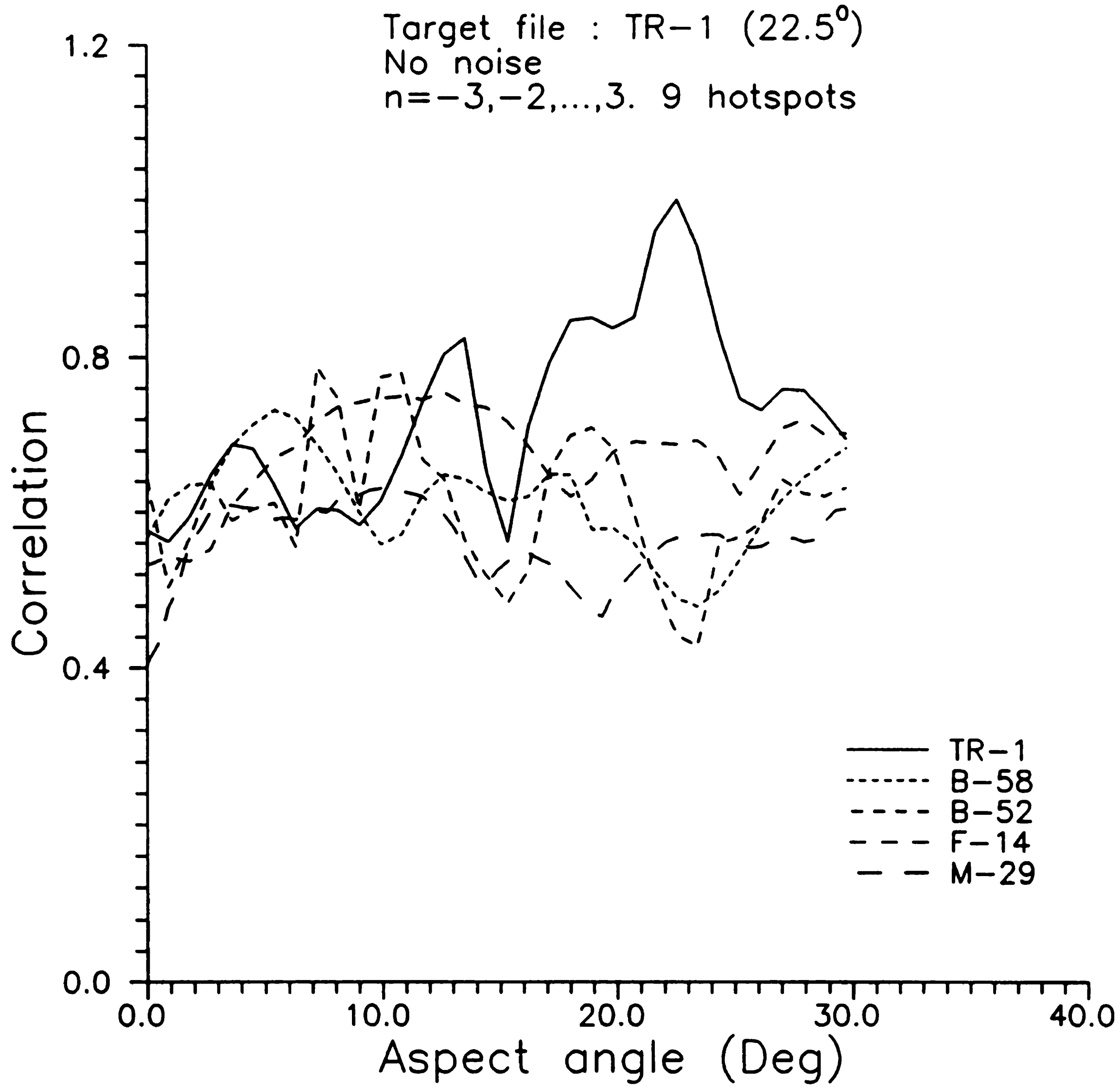

Figure 6.27 Maximum correlation of 22.5^0 TR-1 response with responses from various targets reconstructed from time-domain representation using 9 scattering centers and n=-3,-2,...3.

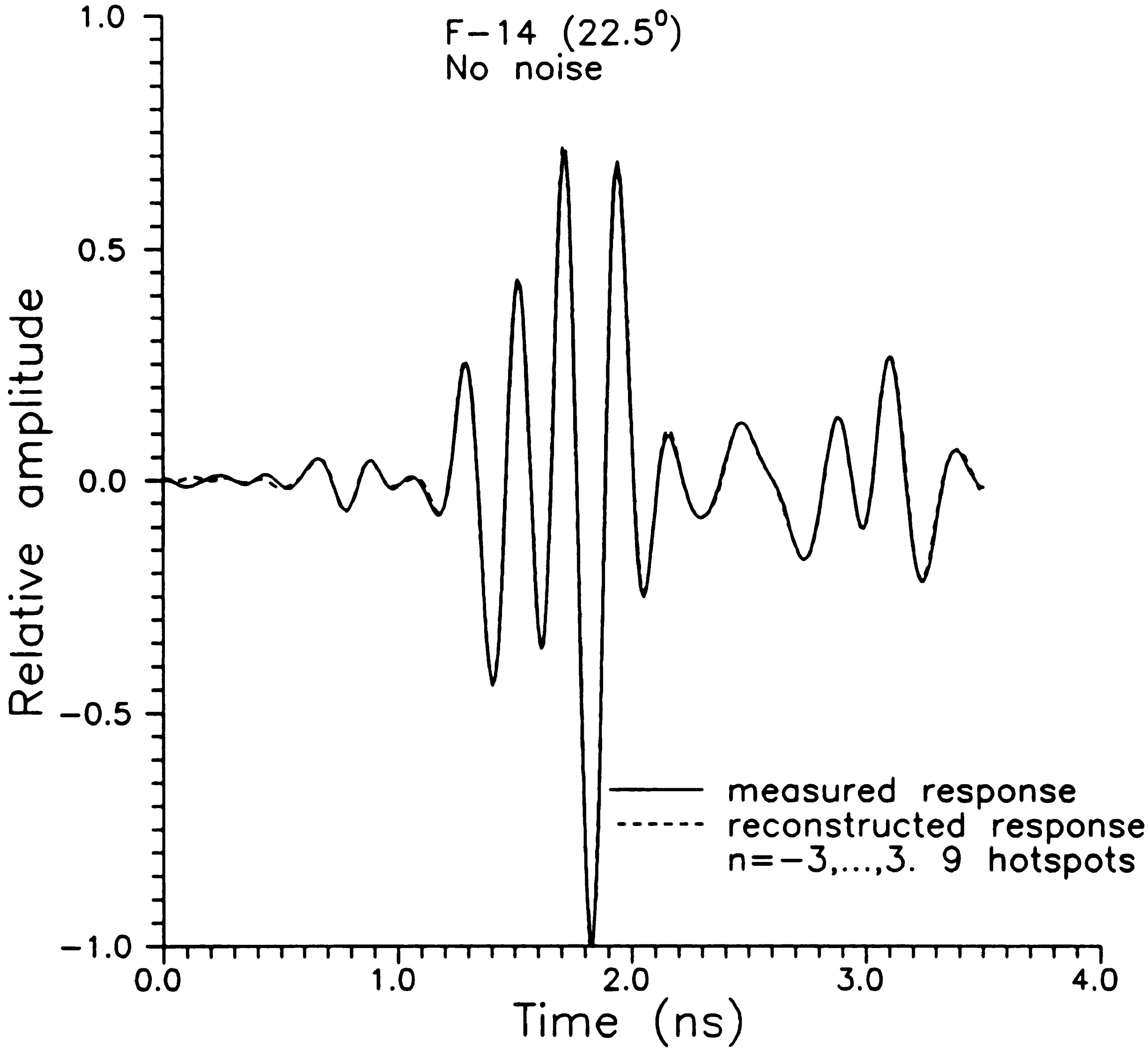

Figure 6.28 Measured early-time response of 22.5^0 F-14, and reconstructed response using 9 scattering centers and n=-3,...3.

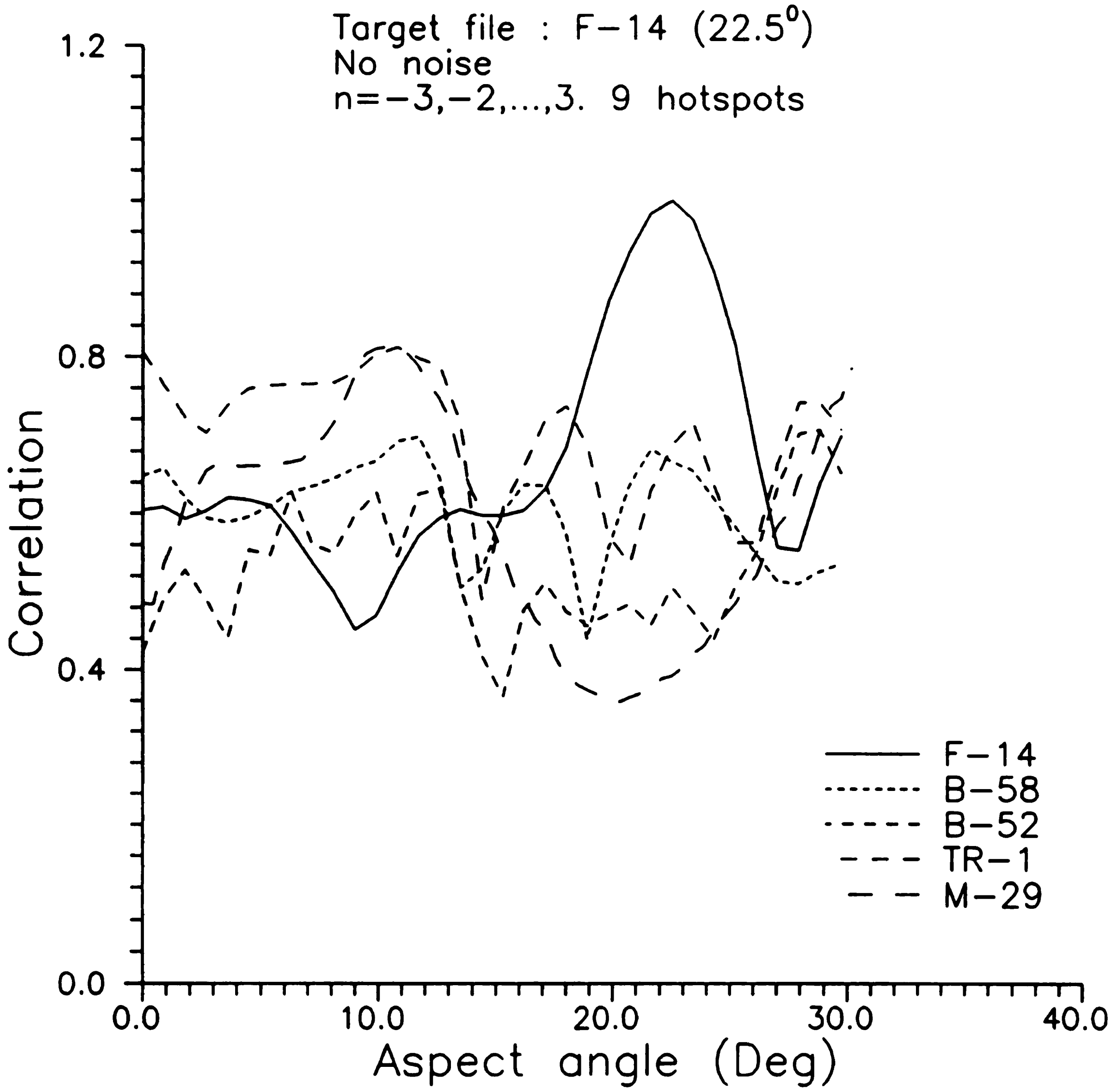

Figure 6.29 Maximum correlation of 22.5° F-14 response with responses from various targets reconstructed from time-domain representation using 9 scattering centers and n=-3,-2,...3.

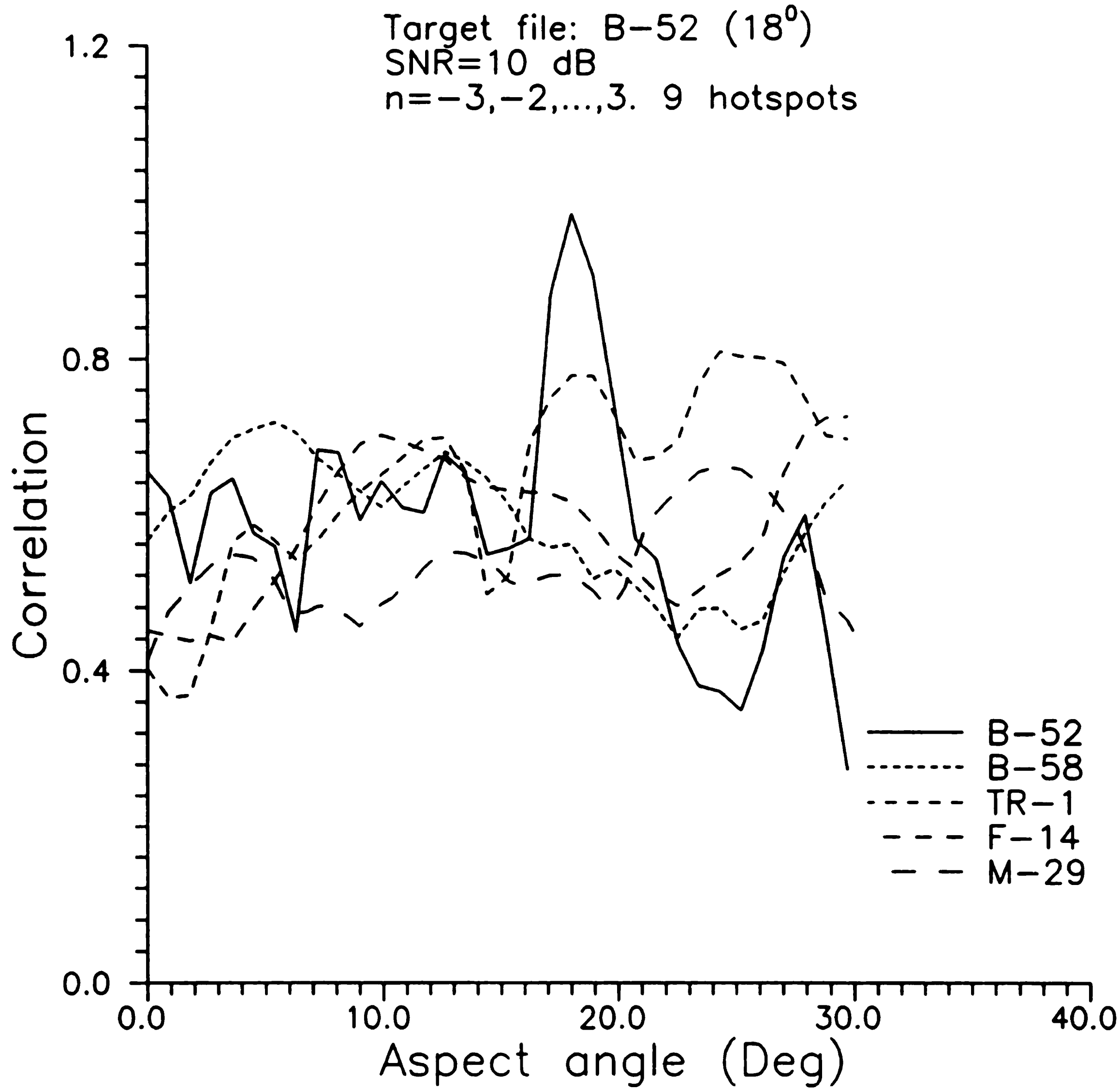

Figure 6.30 Maximum correlation of 18^0 B-52 response with responses from various targets reconstructed from time-domain representation using 9 scattering centers and n=-3,-2,...3. SNR=10 dB.

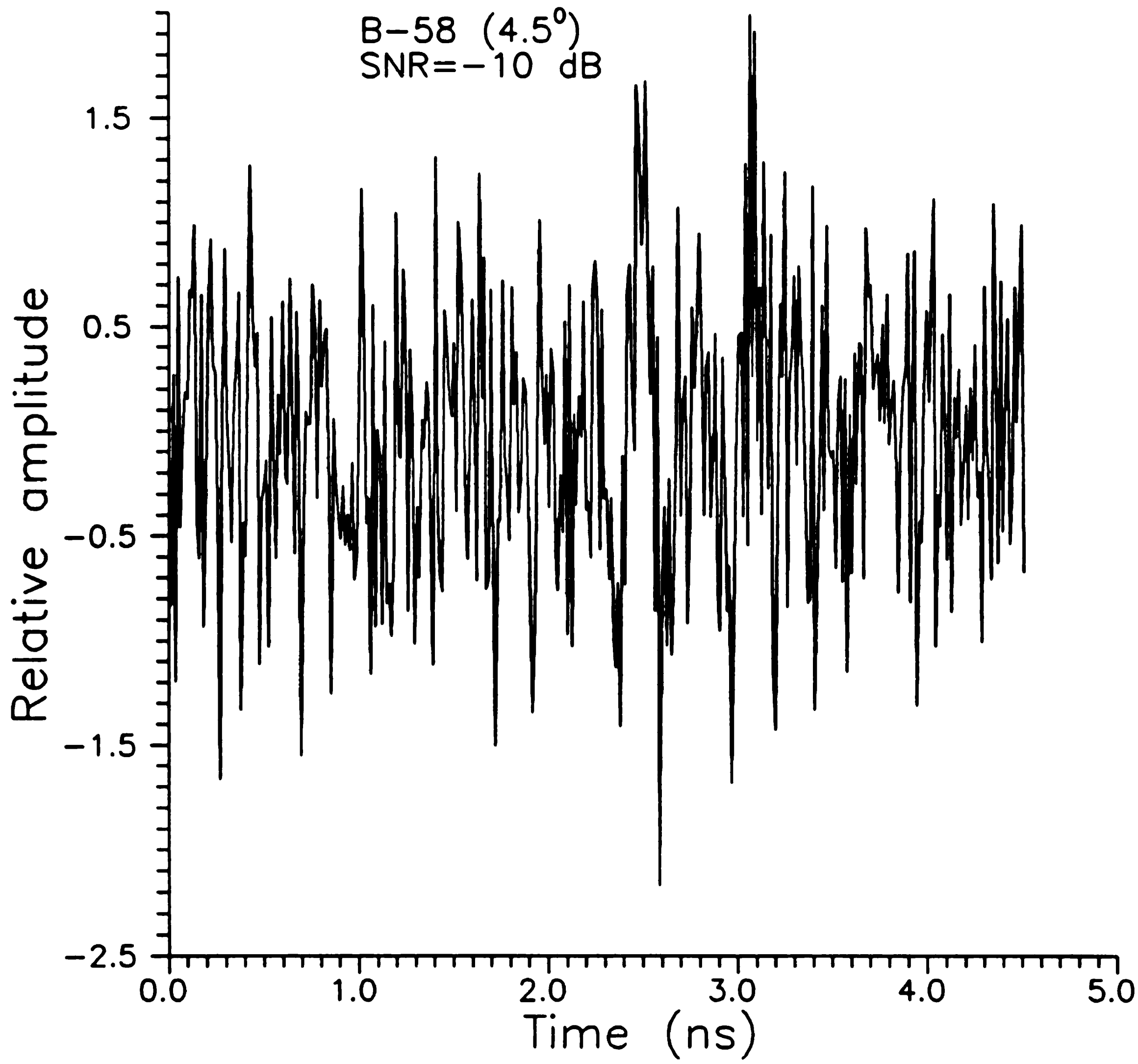

Figure 6.31 Response of 4.5° B-58 aircraft model with zero-mean white Gaussian noise added. SNR=-10 dB.

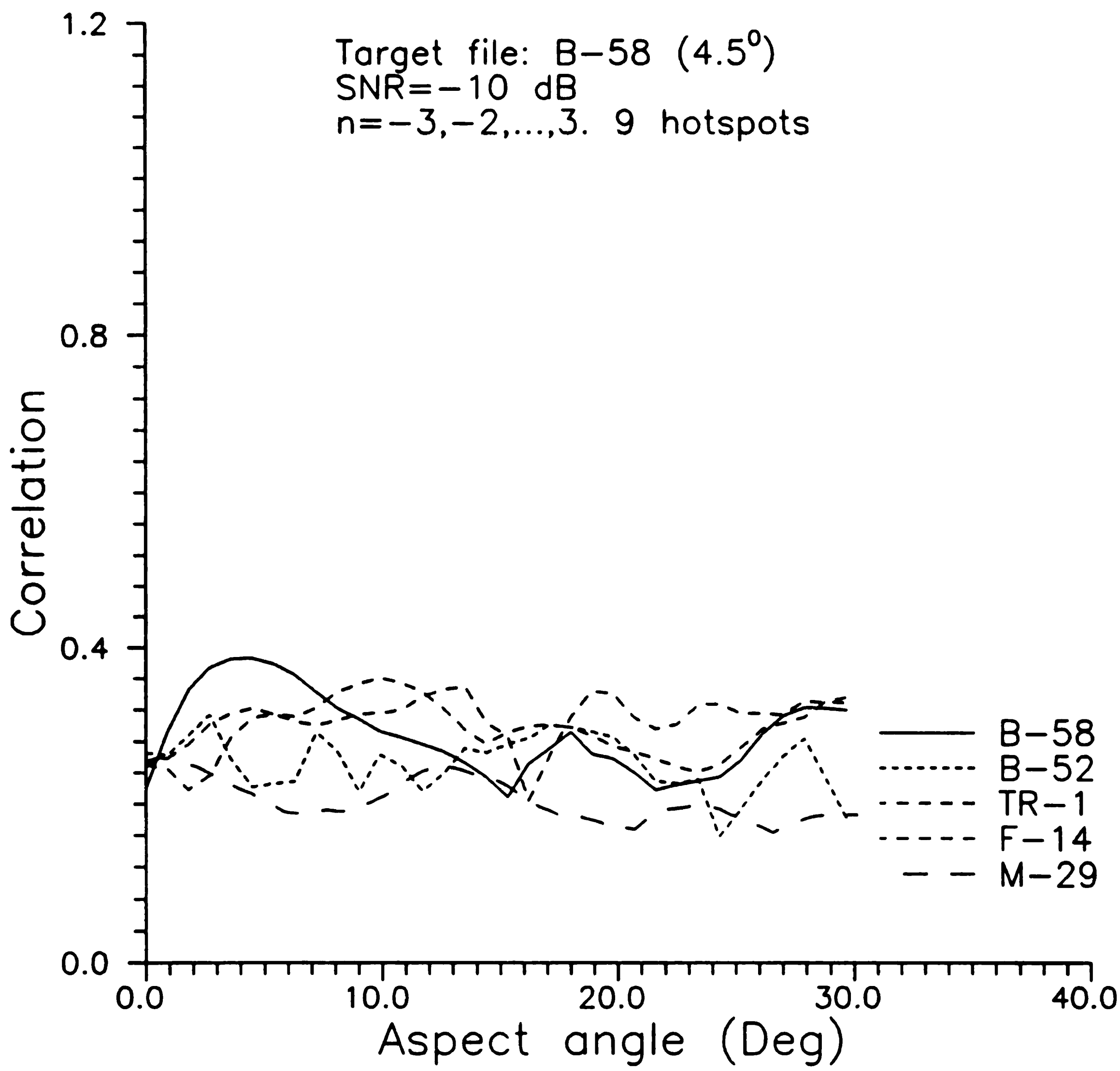

Figure 6.32 Maximum correlation of 4.5^0 B-58 response with responses from various targets reconstructed from time-domain representation using 9 scattering centers and n=-3,-2,...3. SNR=-10 dB.

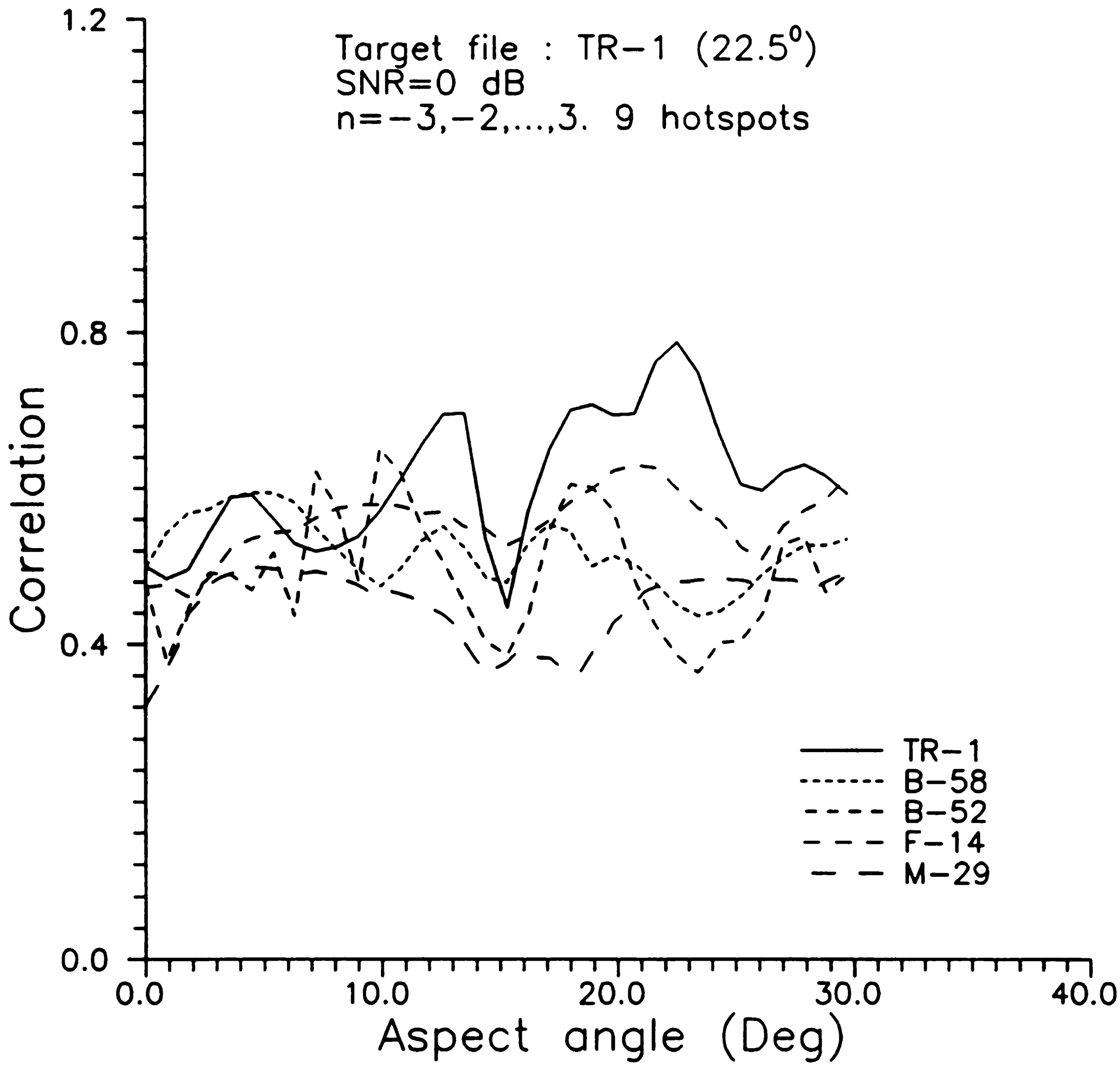

Figure 6.33 Maximum correlation of 22.5^0 TR-1 response with responses from various targets reconstructed from time-domain representation using 9 scattering centers and n=-3,-2,...3. SNR=0 dB.

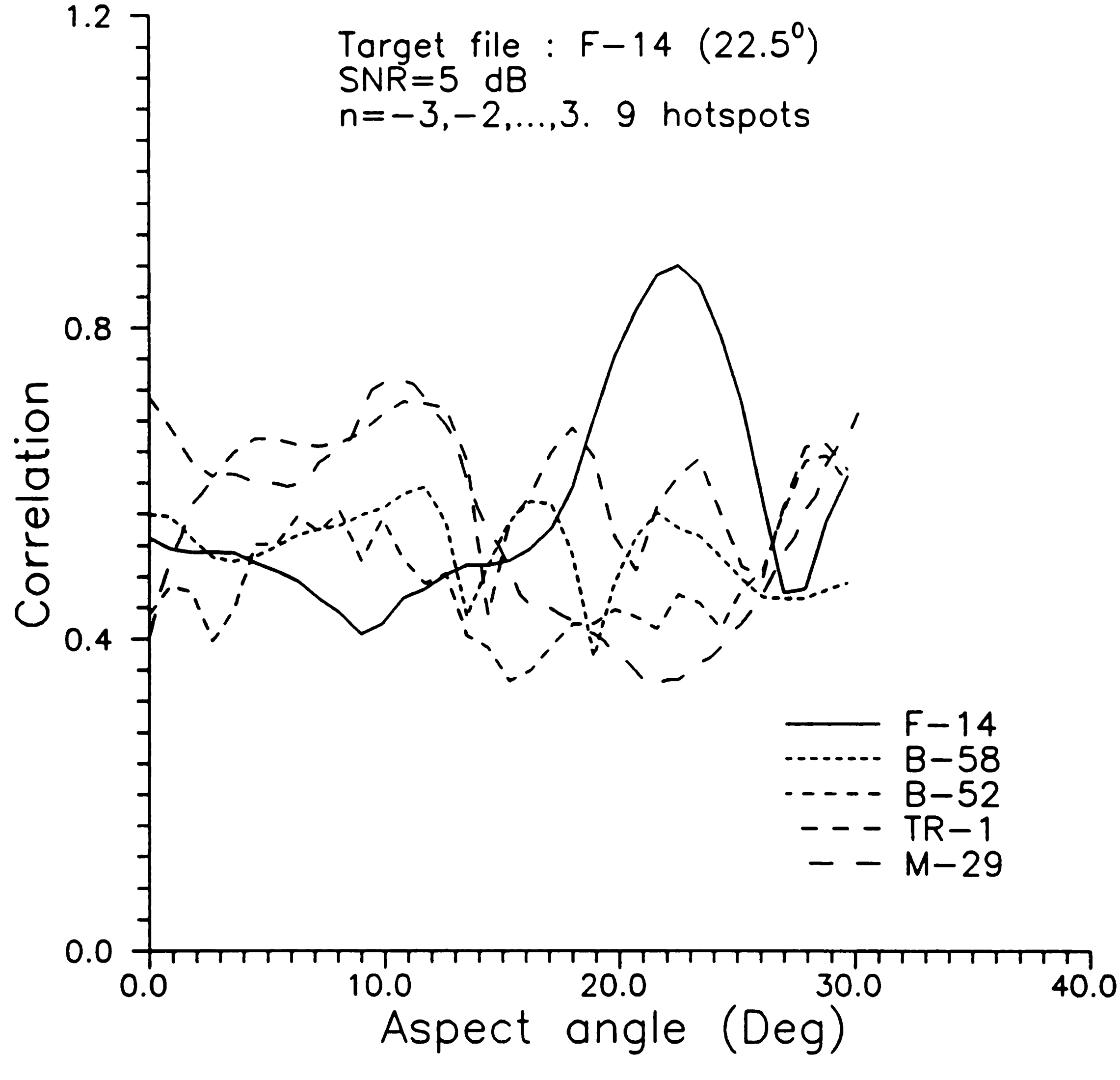

Figure 6.34 Maximum correlation of 22.5° F-14 response with responses from various targets reconstructed from time-domain representation using 9 scattering centers and n=-3,-2,...3. SNR=5 dB.

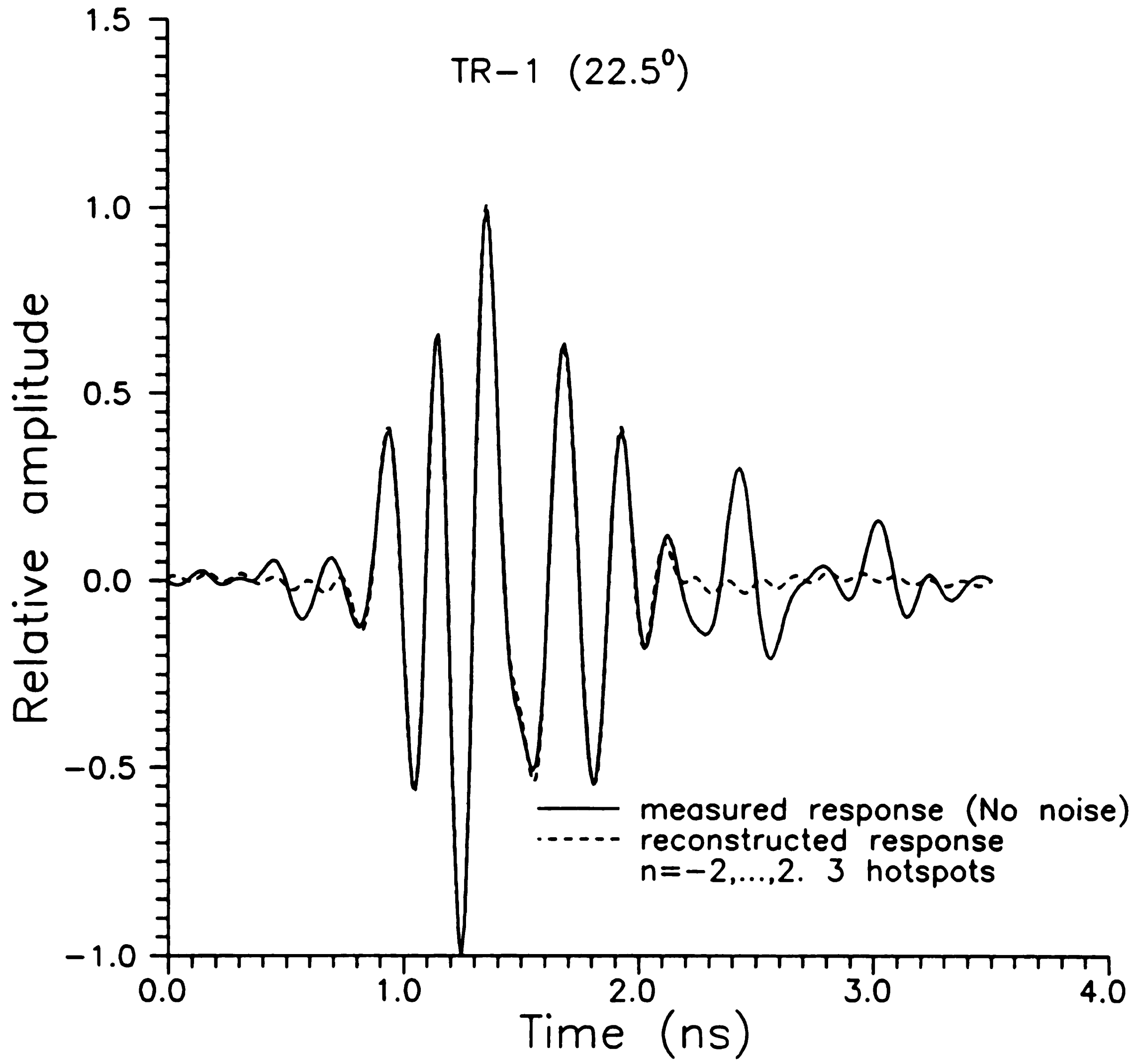

Figure 6.35 Measured early-time response of 22.5^0 TR-1, and reconstructed response using 3 scattering centers and n=-2,...2.

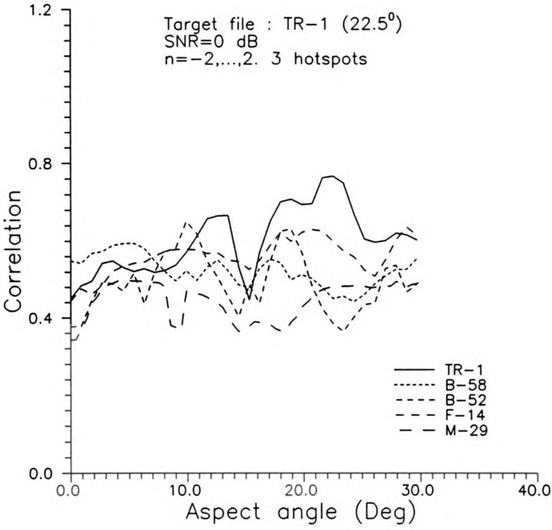

Figure 6.36 Maximum correlation of 22.5^0 TR-1 response with responses from various targets reconstructed from time domain representation using 3 scattering centers and n=-2,...2. SNR=0 dB.

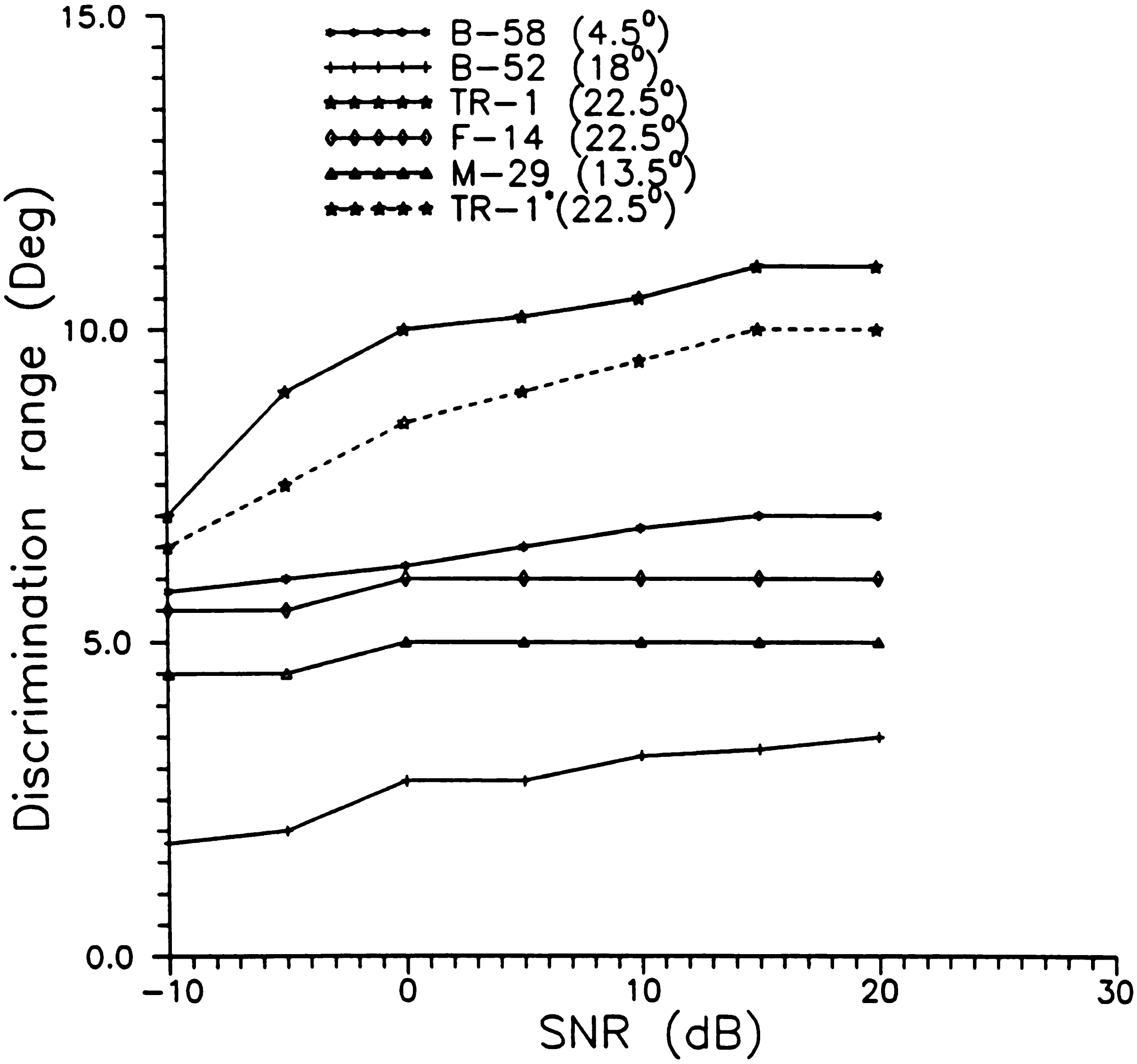

Figure 6.37 Discrimination range of aircraft targets as a function of noise level. Time domain technique used. TR-1* uses 3 scattering centers and n=-2,...,2.

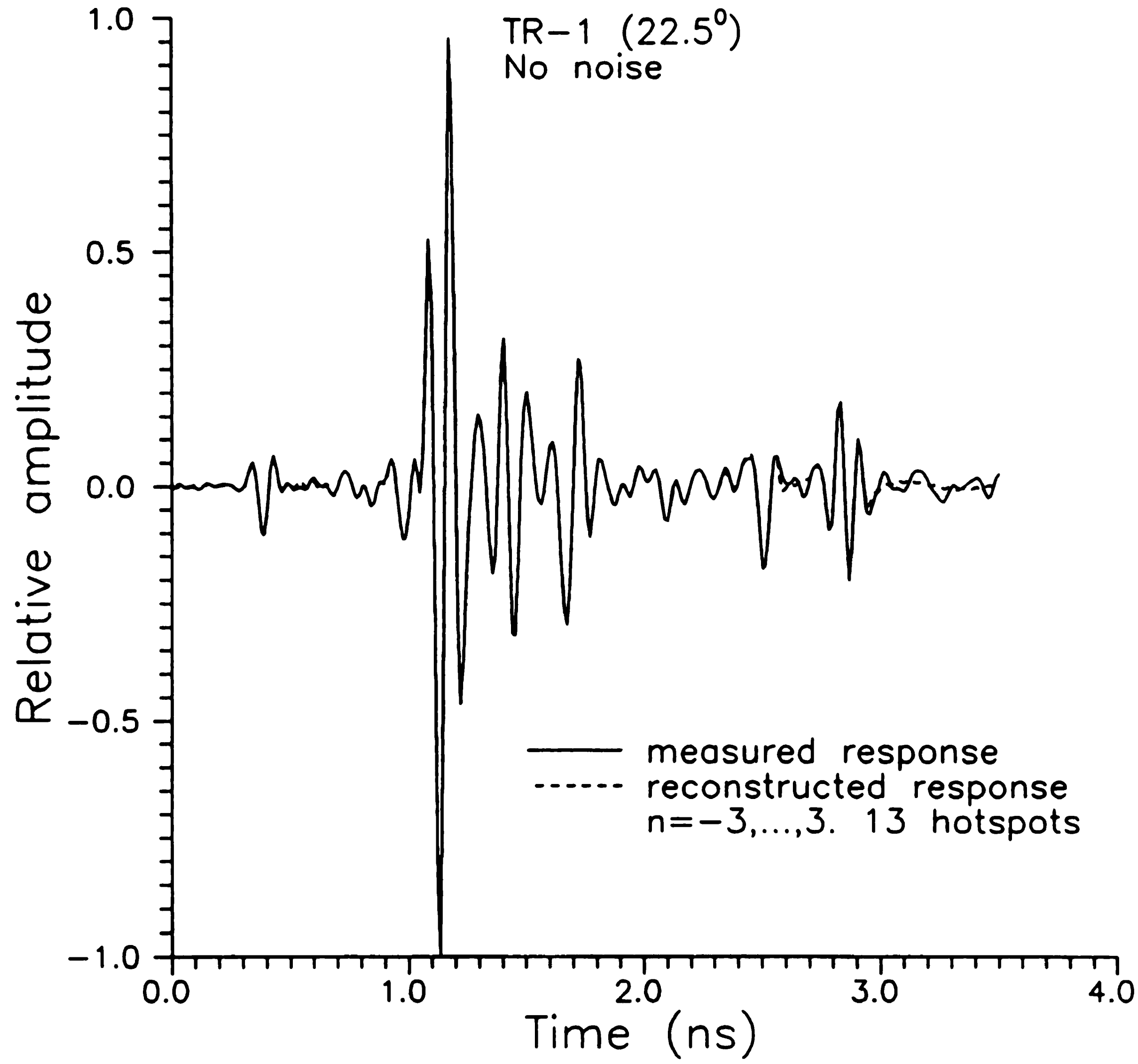

Figure 6.38 Measured early time response of 22.5^0 TR-1, and reconstructed response using 13 scattering centers and n=-3,...,3.

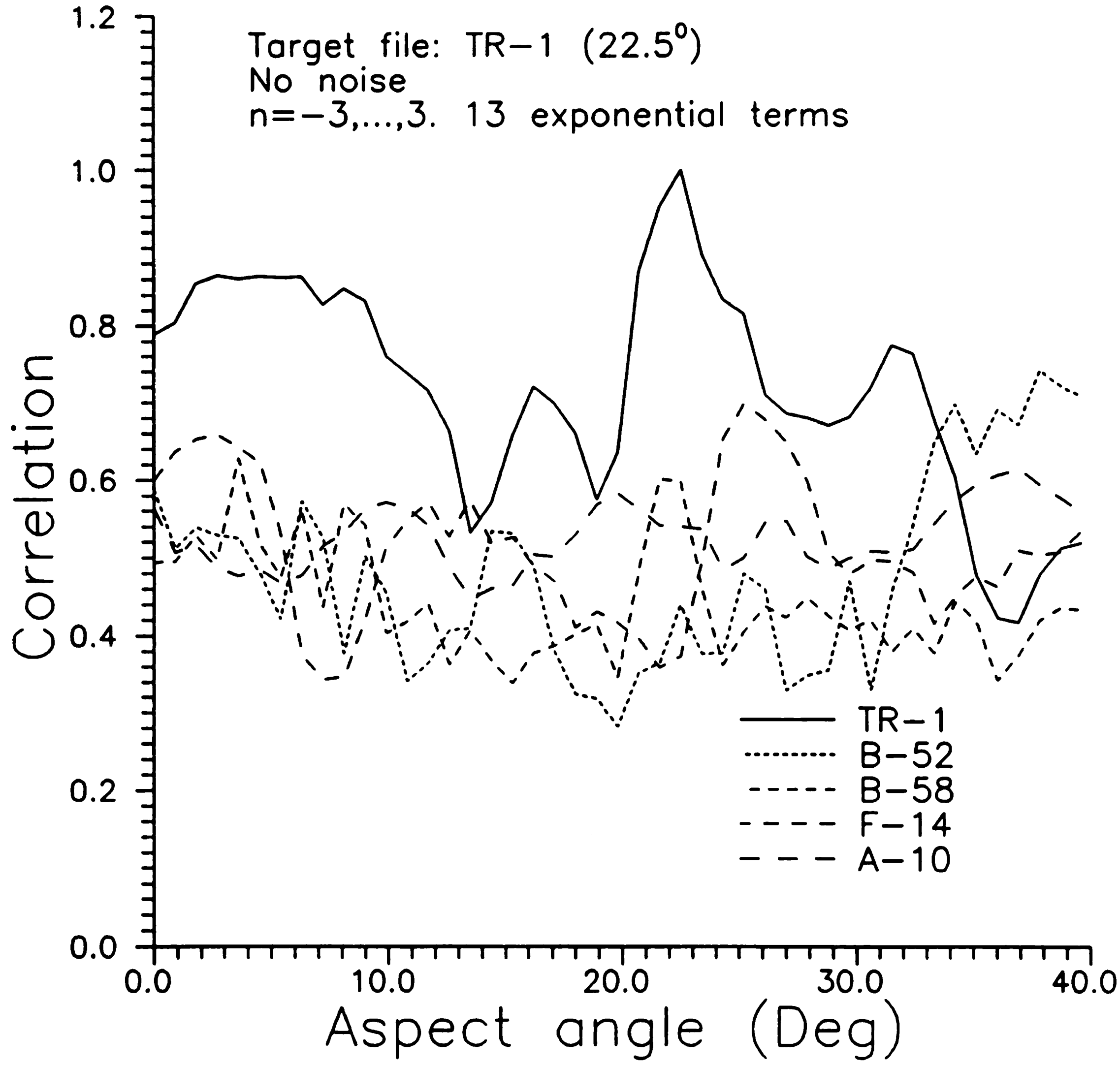

Figure 6.39 Maximum correlation of 22.5° TR-1 response with responses from various targets reconstructed from time domain representation using 13 scattering centers and n=-3,...,3.

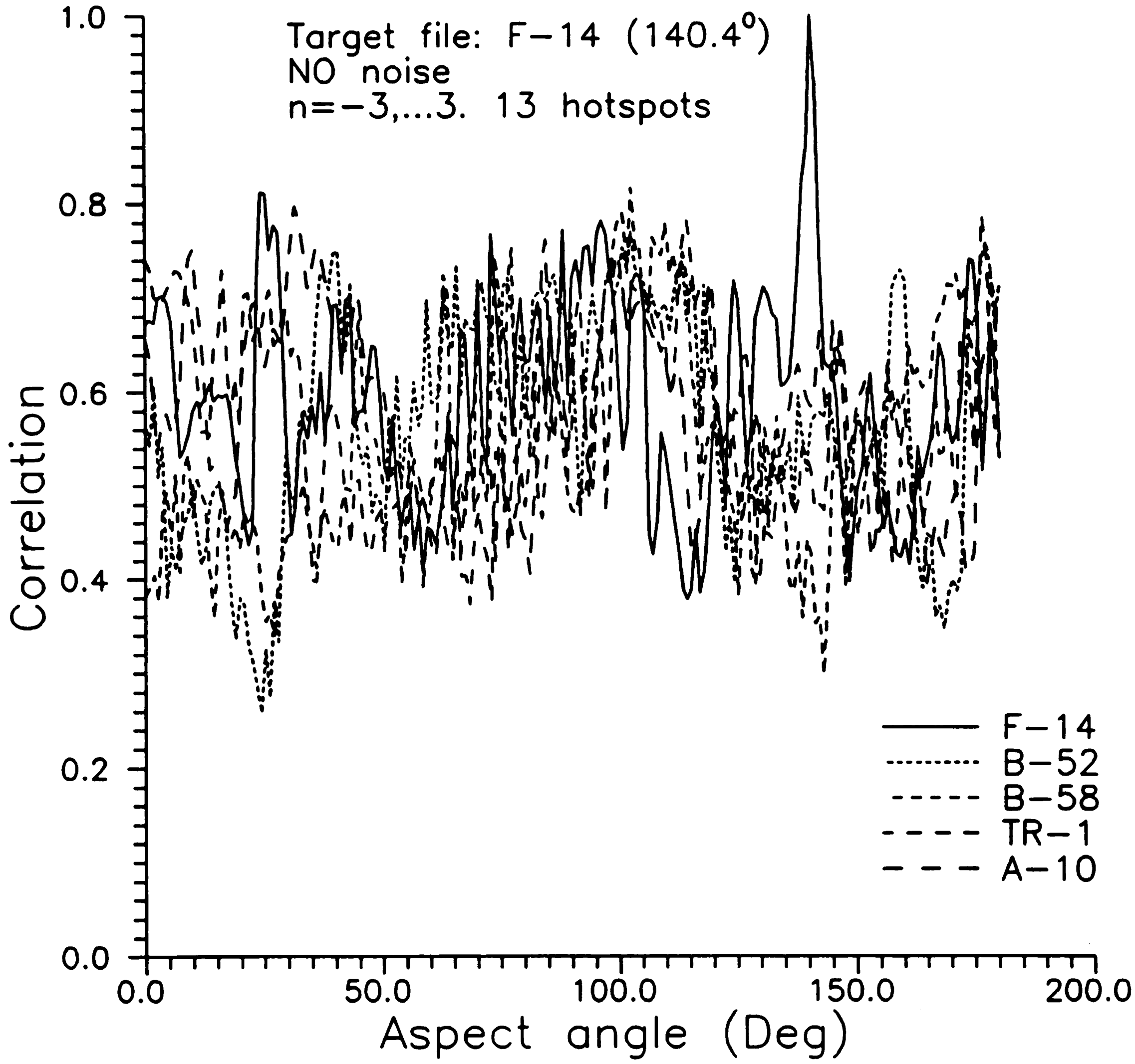

Figure 6.40 Maximum correlation of 140.4^0 F-14 response with responses from various targets reconstructed from time domain representation using 13 scattering centers and n=-3,...,3.

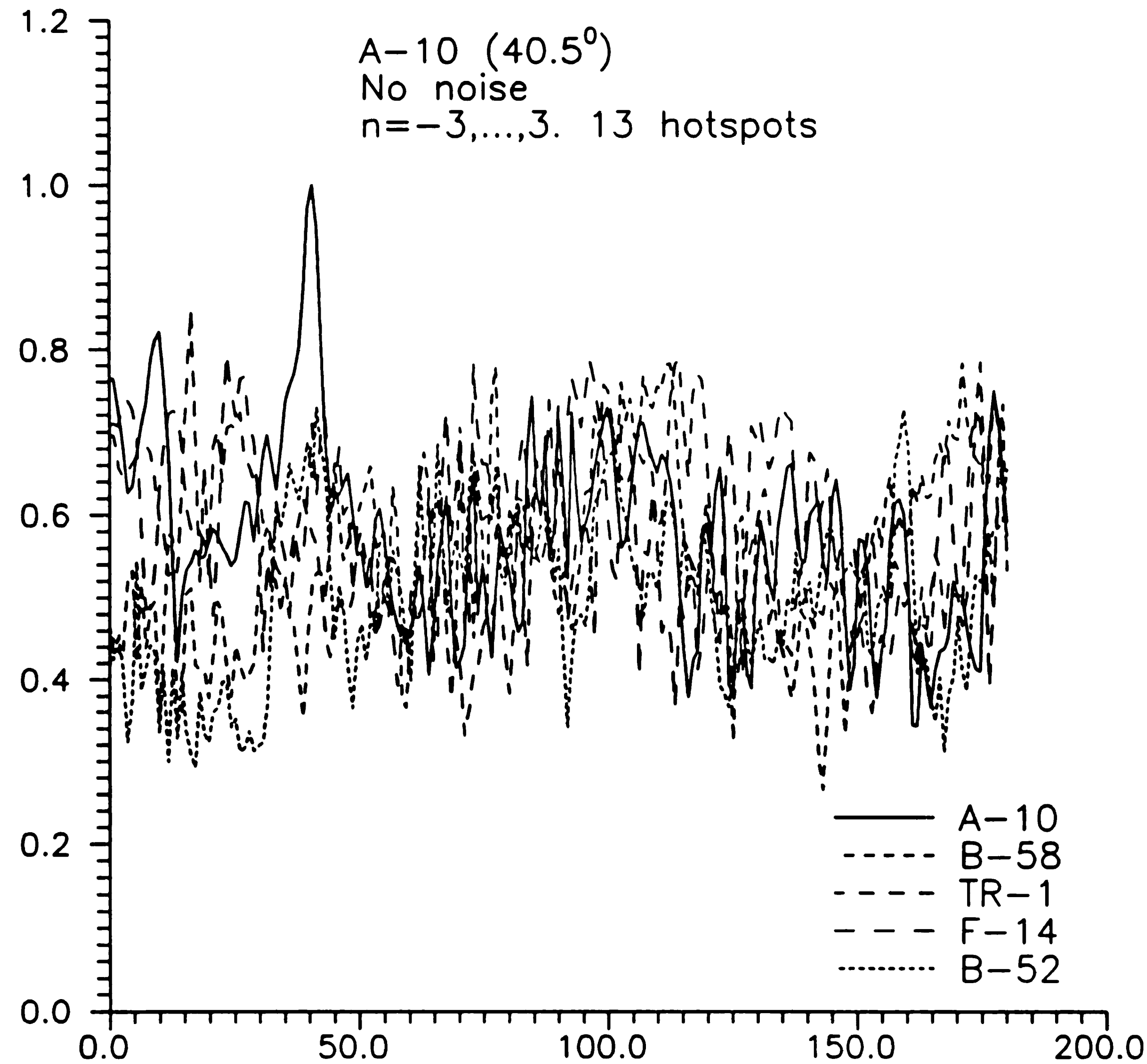

Figure 6.41 Maximum correlation of 40.5^0 A-10 response with responses from various targets reconstructed from time domain representation using 13 scattering centers and n=-3,...,3.

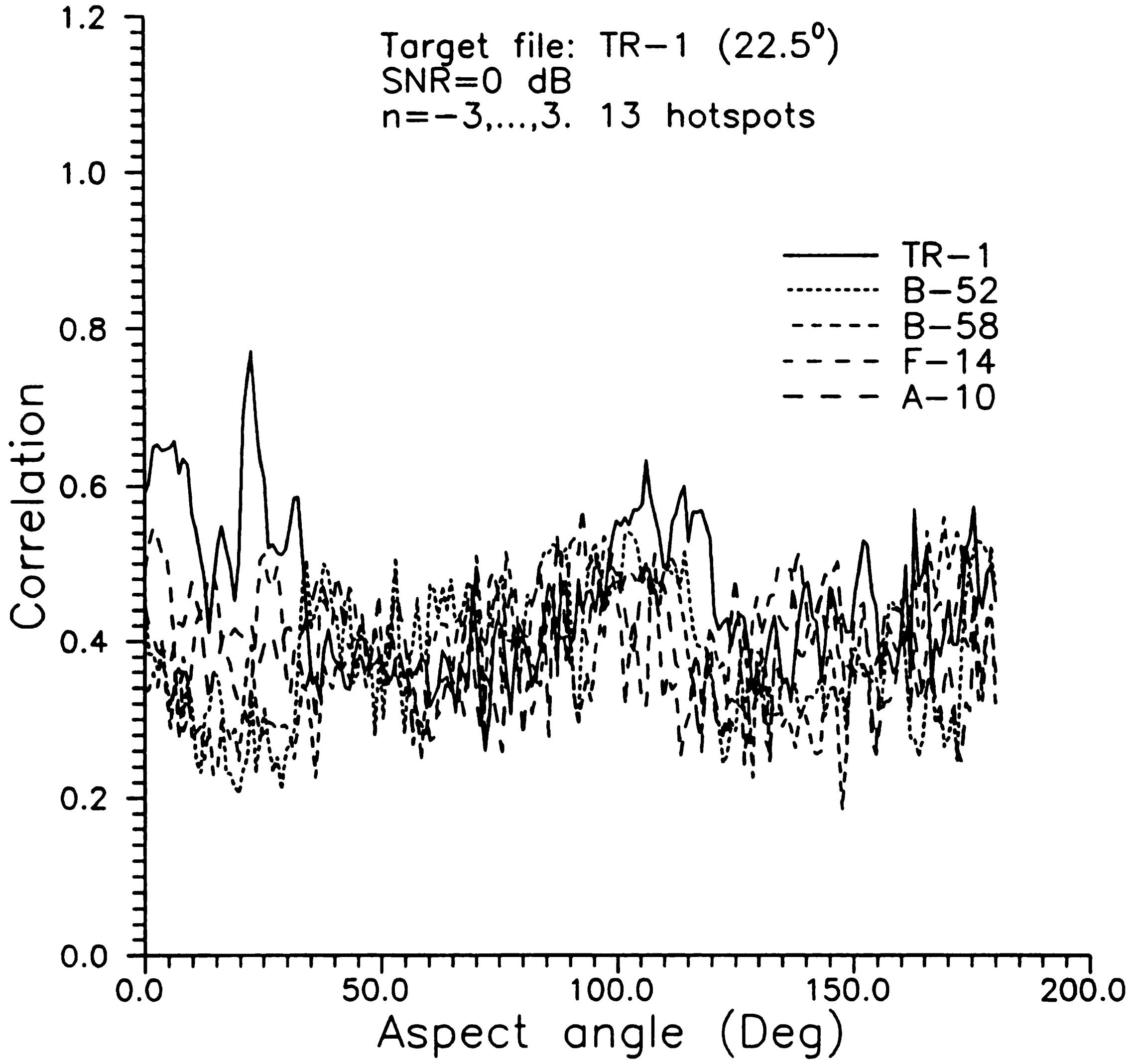

Figure 6.42 Maximum correlation of noisy 22.5^0 TR-1 response with responses from various targets reconstructed from time domain representation using 13 scattering centers and n=-3,...,3. SNR=0 dB.

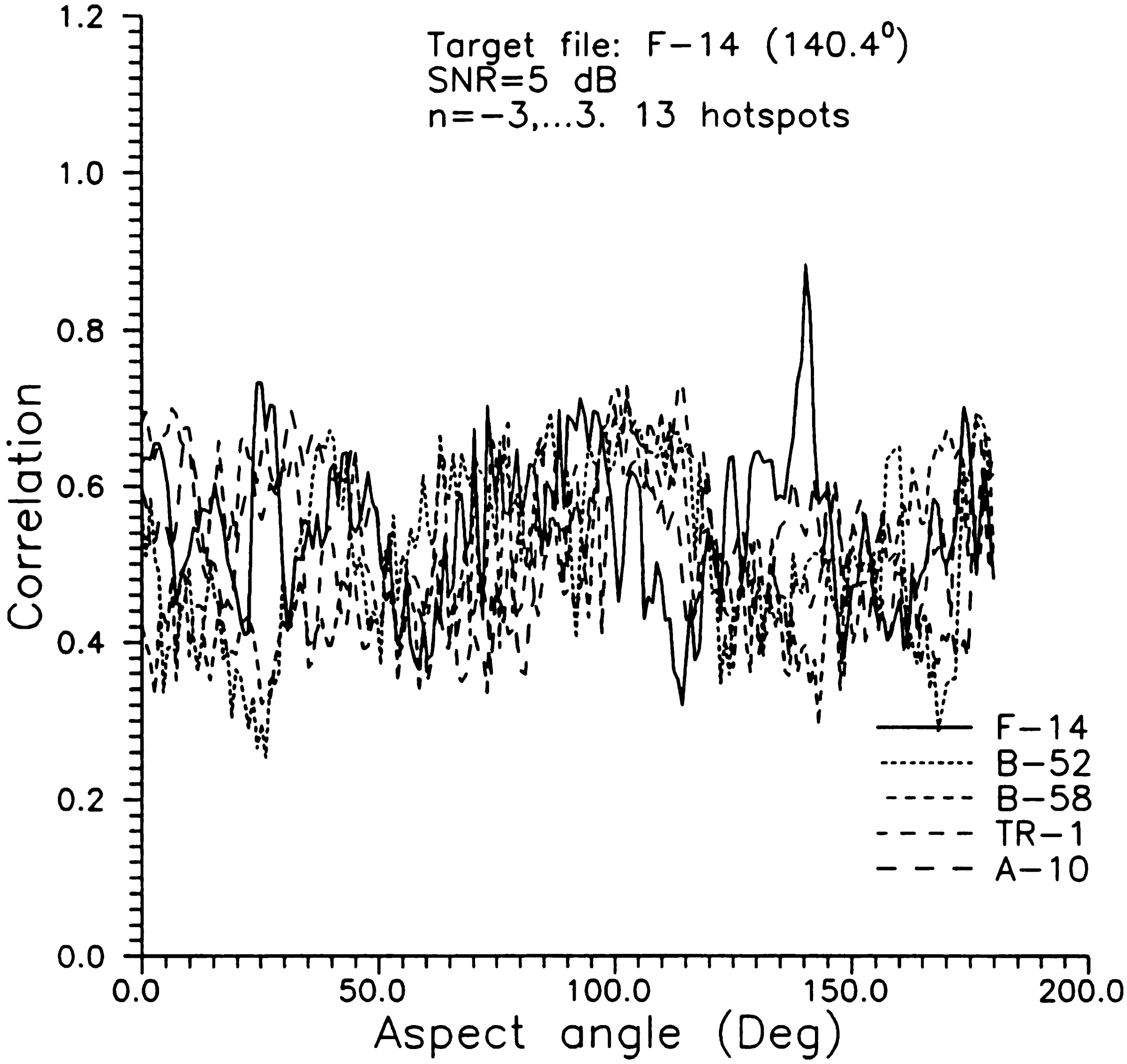

Figure 6.43 Maximum correlation of noisy 140.4^0 F-14 response with responses from various targets reconstructed from time domain representation using 13 scattering centers and n=-3,...,3. SNR=5 dB.

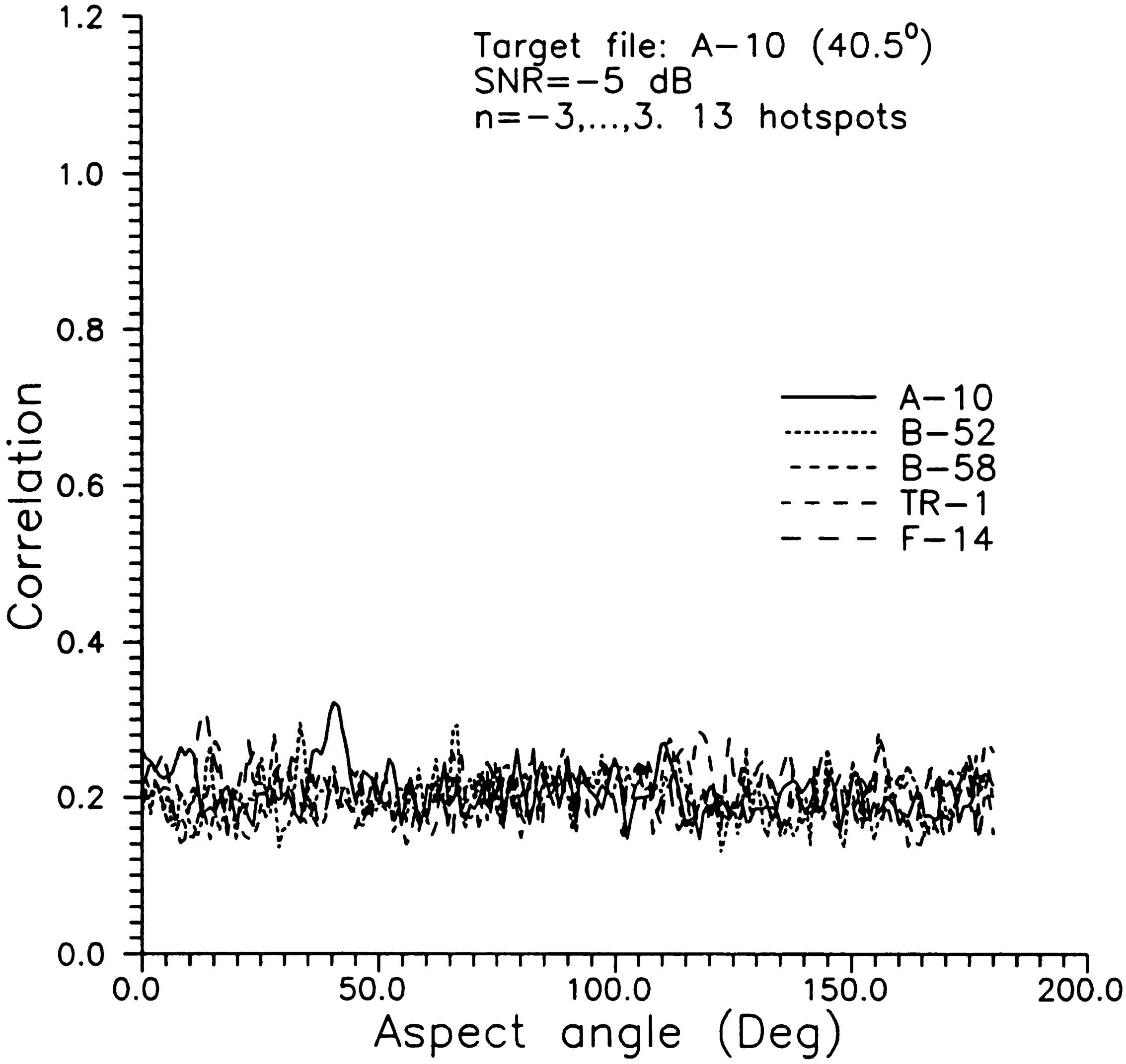

Figure 6.44 Maximum correlation of noisy 40.5^0 A-10 response with responses from various targets reconstructed from time domain representation using 13 scattering centers and n=-3,...,3. SNR=-5 dB.

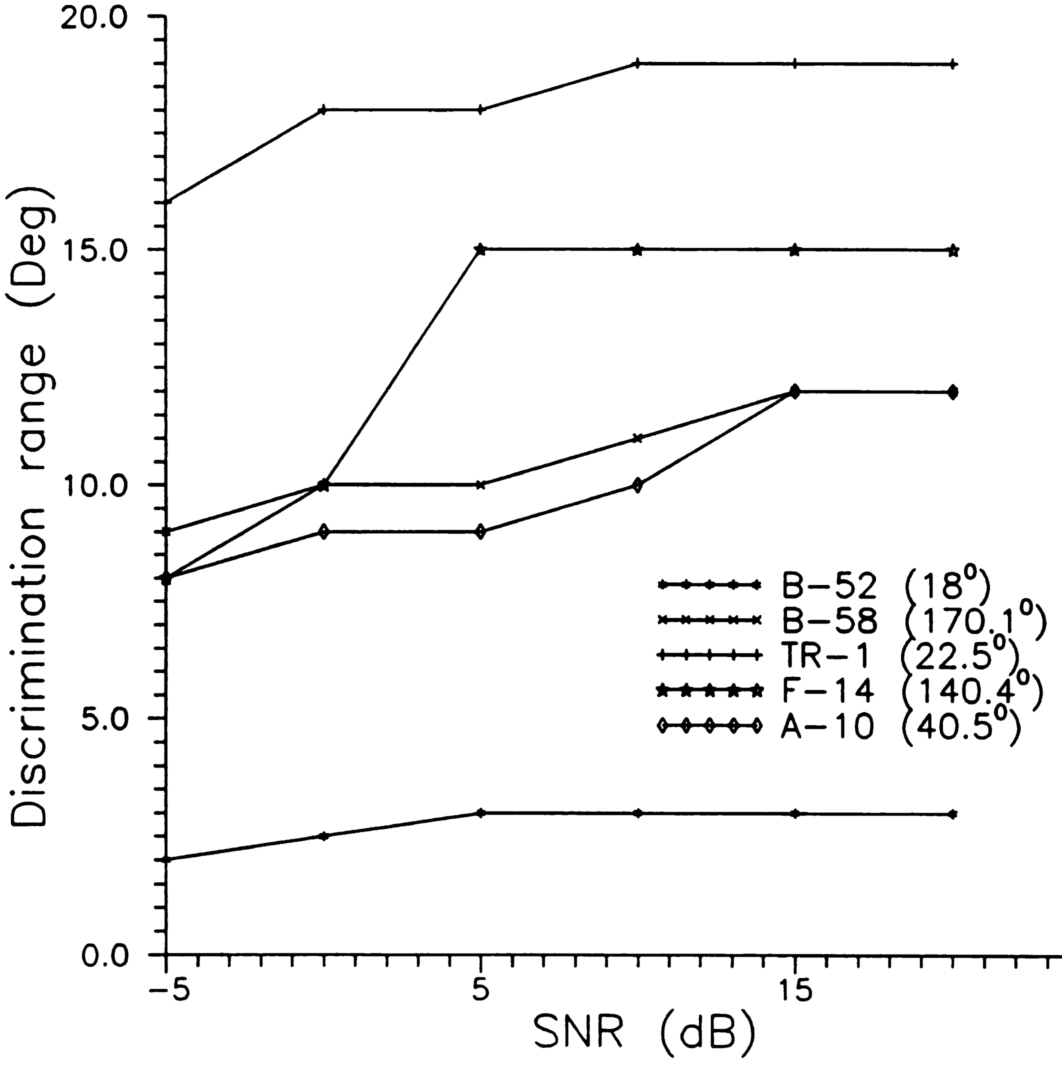

Figure 6.45 Discrimination range of aircraft targets as a function of noise level. Time domain technique used. The measured frequency band is 2-18 GHz.

CHAPTER 7

ANECHOIC CHAMBER MEASUREMENTS

7.1 Introduction

The early-time portion of the transient response is receiving more and more attention for use in radar target identification and detection. Analysis of the early-time response of complex targets using current theoretical and numerical models is difficult and time consuming. Thus, the accurate measurement of the early-time response of complex targets (i.e. aircrafts and missiles, etc.) is important and also necessary in the verification of current and future theoretical or numerical models.

There are two different schemes for performing transient measurement. The first method uses the traditional time domain reflectometry methods [44], [45], [46], [47] while the second one utilizes a Fourier synthesis approach [48], [49], [50]. The time domain reflectometry method has the important advantages of time-gating and rapid speed of measurement, but suffers the disadvantage of limited dynamic range and equipment instability which leads to timing jitter. In this dissertation, we do not exploit this method.

A vector network analyzer is capable of measuring both the magnitude and phase of the S-parameters of two port network over a very wide frequency domain. This capability gives the vector network analyzer the ability to synthesize the transient response of a target via the inverse discrete Fourier transform. Measurements using this configuration take longer than with time domain systems. Note that the sampling interval constraint limits the use of network analyzer system when the antennas are used on a ground plane since the reflections from the edges of the ground screen and the laboratory ceiling cause alaising.

A typical free-field dual antenna frequency domain measurement system is shown in Figure 7.1. A measurement of S_{21} produces a measure of scattering from port 1 to port 2 from both the scatterer and the environment. Amplifiers are added to the transmit channel to help boost the dynamic range of the measurements. Recently, the addition of wide-band horn antennas has allowed the frequency range of the system to be extended from the band 1-7 GHz to the band 2-18 GHz. Also a computer-controlled rotator allows measurements to be made automatically at a 0.15^0 aspect angle increment.

This chapter reviews the calibration and deconvolution method of the measurement system developed by Ross [50]. Examples of measured spectral responses of calibration targets (i.e. sphere) are presented and compared with theory. Various methods which improve the measurements of aircraft models are described briefly and summarized.

7.2 Calibration Procedure

Ross made a significant contribution to automatic measurements in the anechoic chamber at the MSU EM lab. The size of chamber is 24 ft in length, 12 ft in width, and 12 ft in height. Here we will review the calibration procedure. To make full advantage of the wide frequency sweep available with a network analyzer, the clutter and system transfer function must be removed from the measurement. That is, all repeatable systematic errors associated with anechoic chamber clutter, antennas, and transmission

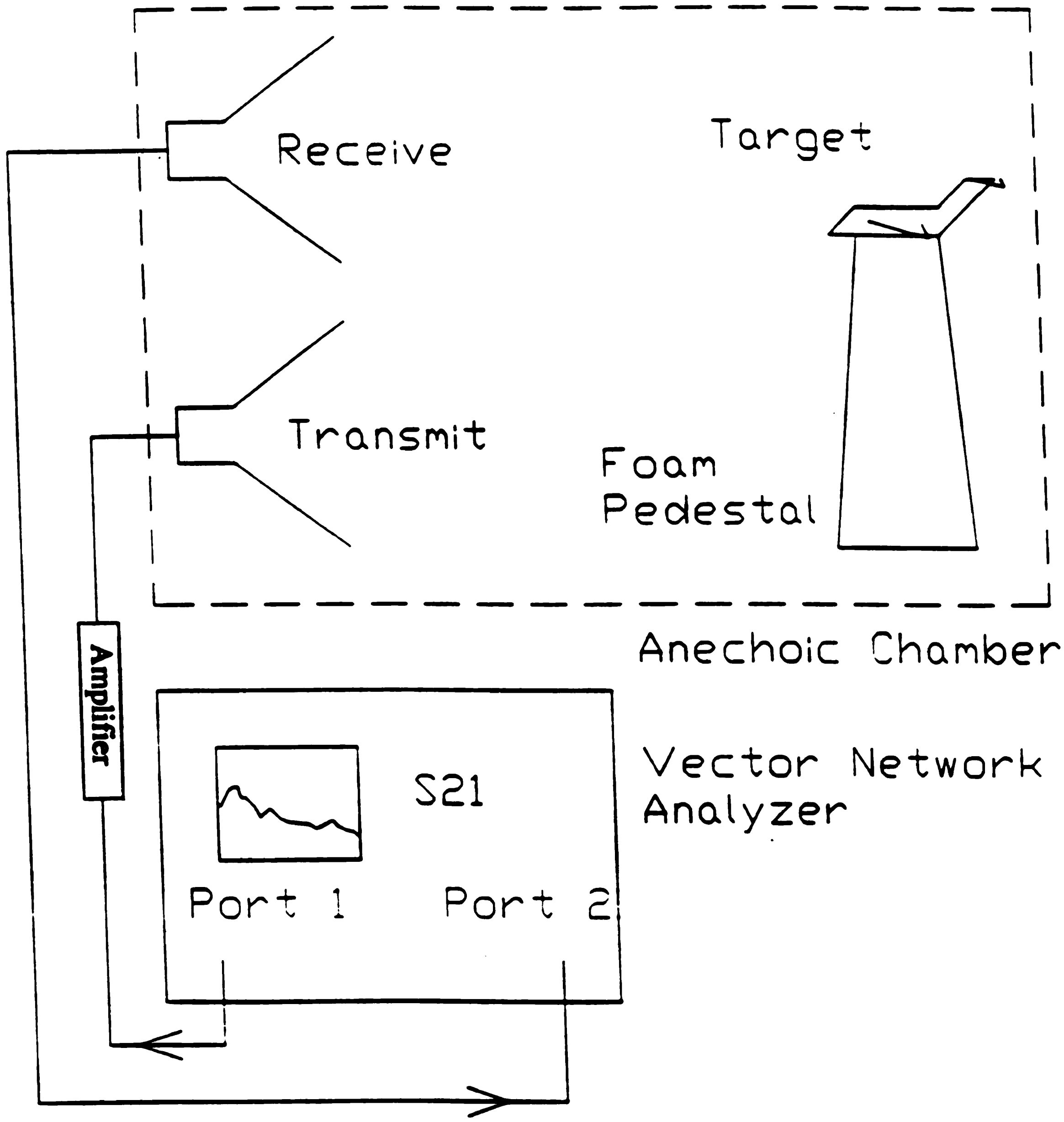

Figure 7.1 **Dual antenna free-field frequency domain transient measurement system.**

lines should be removed from the raw measurement.

First, the background response measured when the chamber is empty is subtracted from the raw target measurement. Figure 7.2 shows the spectral response of a 14 inch metal calibration sphere measured at 2-18 GHz. Other possible calibration targets include a thin wire. One of the difficulties with the wire is that the wire response is strongly aspect-dependent. It is very hard to determine the incident angle exactly. After the spectral response is zero-padding and transformed to the time domain, any interaction terms and noise that are sufficiently delayed beyond the end of the calibration target response can be eliminated. The spectral response obtained by transforming the time domain response using the FFT becomes much smoother than before as shown in Figure 7.3. Next the system function can be found by dividing this response by the theoretical value.

The theoretical scattered field response of a sphere was first solved by Mie in 1908 [51]. It has also appeared in many books [52], [53]. The notation used in the course notes by Chen [54] is used here.

Consider a plane wave incident on a perfectly conducting sphere as illustrated in Figure 7.4. The incident electric field is given by

$$\vec{E}^{inc}(\vec{r}) = \hat{x}E_0\exp(-jkz) \tag{7.1}$$

The far zone scattered electric field is obtained by approximating the spherical vector wave functions in Mie series [54]

$$E^s_\theta = -jE_0\frac{\exp(-jkR)}{kR}\sum_{n=1}^{\infty}\frac{2n+1}{n(n+1)}\left\{a_n\frac{P_n^{\,1}(\cos\theta)}{\sin\theta}+b_n\left[\frac{\partial}{\partial\theta}P_n^{\,1}(\cos\theta)\right]\right\}\cos\phi \tag{7.2}$$

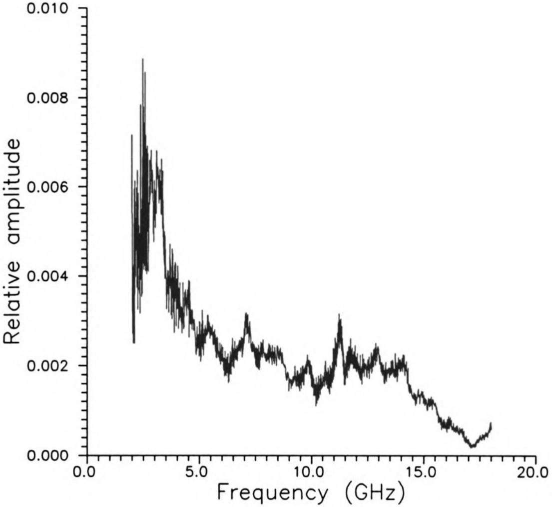

Figure 7.2 Spectral response of 14 inch metal calibration sphere. Measured using frequency domain system in MSU anechoic chamber.

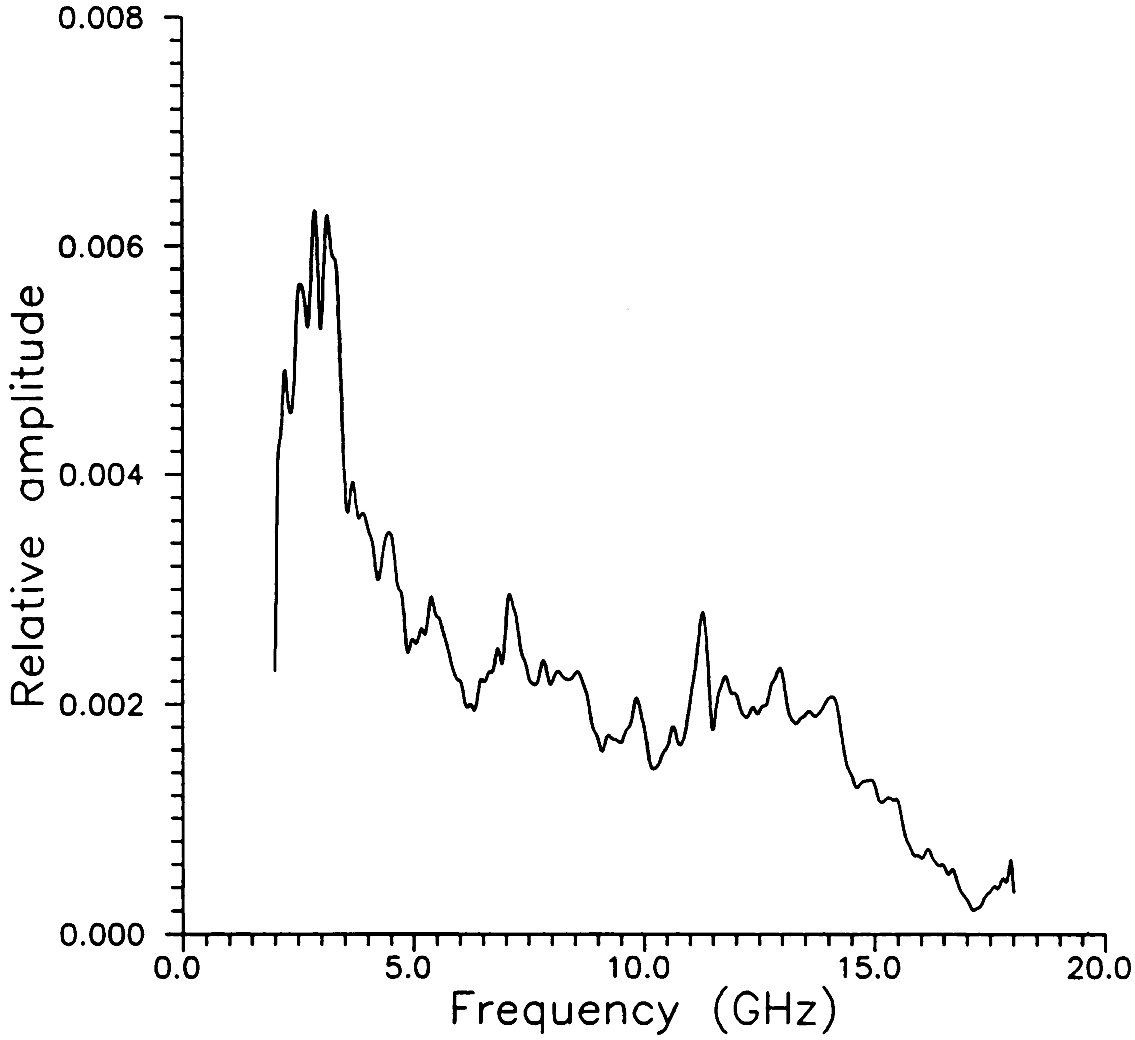

Figure 7.3 Spectral response of 14 inch metal calibration sphere after time domain filtering. Measured using frequency domain system in MSU anechoic chamber.

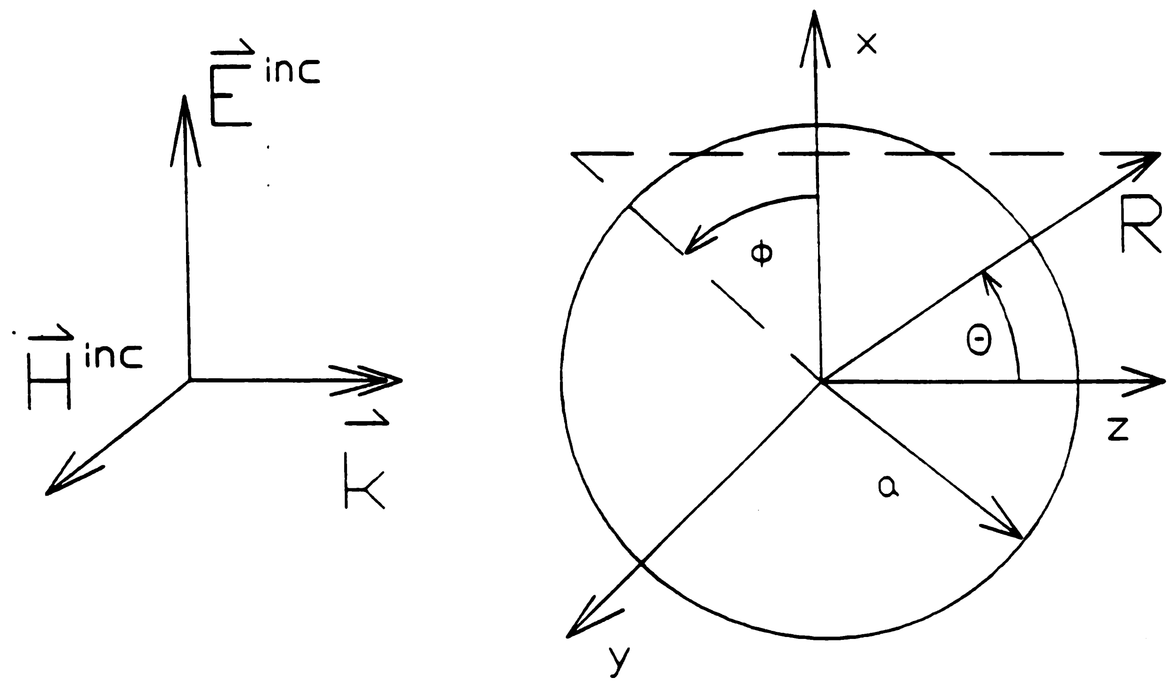

Figure 7.4 Geometry for sphere scattering problem.

$$E^s_\phi = jE_0 \frac{\exp(-jkR)}{kR} \sum_{n=1}^{\infty} \frac{2n+1}{n(n+1)} \left\{ b_n \frac{P_n^{\,1}(\cos\theta)}{\sin\theta} + a_n \left[\frac{\partial}{\partial\theta} P_n^{\,1}(\cos\theta) \right] \right\} \sin\phi \tag{7.3}$$

where a_n and b_n are found using the boundary conditions and are given by

$$a_n = \frac{j_n(ka)}{h_n^{(2)}(ka)} \qquad b_n = \frac{\frac{\partial}{\partial R}(Rj_n(kR))|R=a}{\frac{\partial}{\partial R}(Rh_n^{(2)}(kR))|R=a} \tag{7.4}$$

For the back-scatter case, the following relations are used to the evaluation of the Mie series in equation (7.2) and (7.3)

$$P_n^{\,1}(\cos\theta)\,|_{\theta=\pi} = -\frac{(-1)^n}{2}\,n(n+1) \tag{7.5}$$

$$\frac{\partial}{\partial\theta} P_n^{\,1}(\cos\theta)\,|_{\theta=\pi} = -\frac{(-1)^n}{2}\,n(n+1) \tag{7.6}$$

The expressions shown in (7.2) and (7.3) are programmed with the use of widely available generalized Bessel function subroutines. These subroutines are very accurate and efficient.

Figure 7.5 shows the theoretical waveform obtained using the above Mie series. The system transfer function obtained using this theoretical response is shown in Figure 7.6. To provide verification of the calibration process, a second sphere 3 inches in diameter is used. Figure 7.7 shows a comparison of the measured and theoretical spectral responses of the smaller sphere. The agreement is very good except in the high frequency region. This is probably due to the hole in the sphere and effects of windowing of extraneous system noise from the measured response.

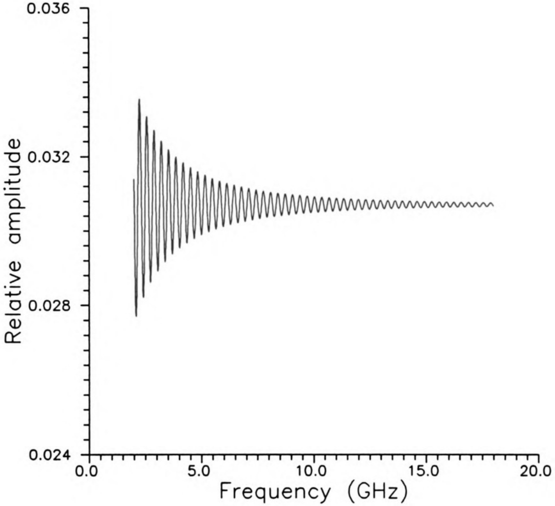

Figure 7.5 Theoretical response of 14 inch metal calibration sphere calculated using Mie series for MSU anechoic chamber configuration.

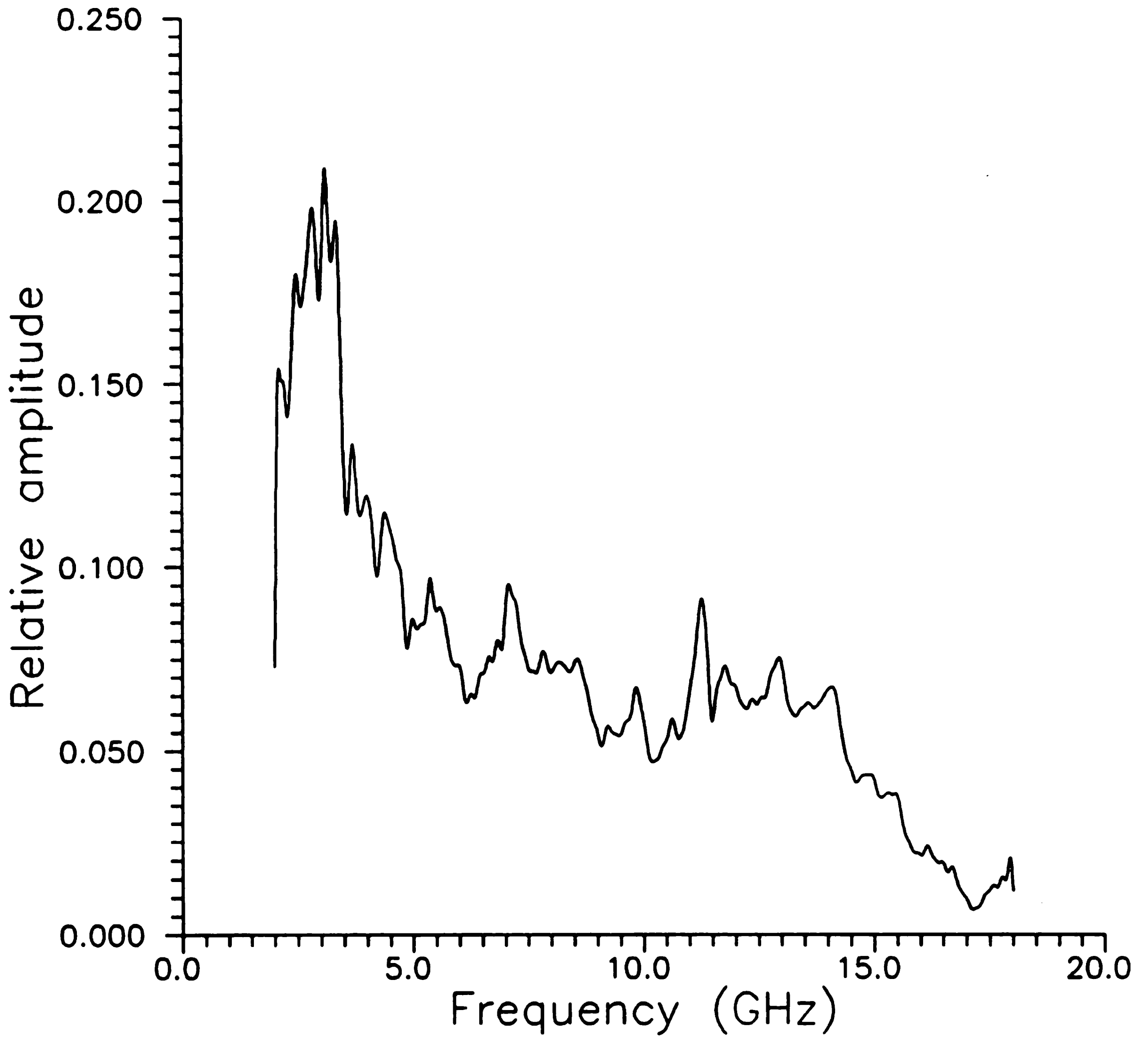

Figure 7.6 Transfer function of frequency domain system obtained using 14 inch diameter sphere as calibration standard.

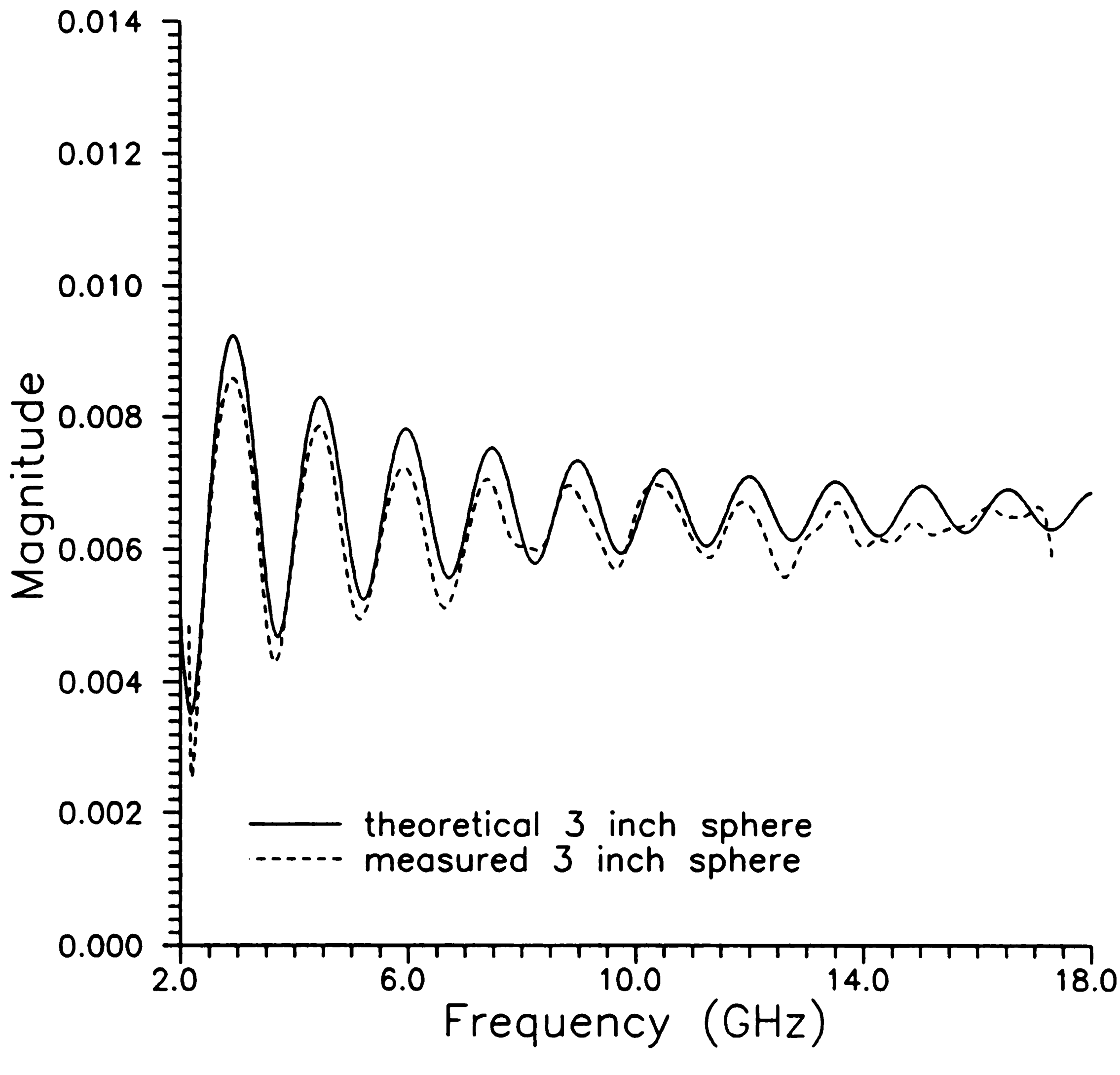

Figure 7.7 Comparison of theoretical and experimental frequency responses of a 3 inch diameter sphere. Measurements performed using frequency domain system in MSU anechoic chamber.

7.3 The Improvements In the Measurements of Aircrafts

The state of measurement ability at the EM lab at MSU has gone through several phases. At first, the scattered fields of scale aircraft models were measured in the frequency band of 1-7 GHz at a 5^0 aspect angle increment. The measurements were intervened by operators at each aspect angle by placing targets and removing targets to measure background response. This 5^0 interval was not fine enough to adequately describe the strong aspect-dependent nature of early-time response. Later on, we obtained a computer controlled rotator which allows the measurements of target scattered field response at aspect angle increments as fine as 0.15^0. The measurement software is modified so that the measurements can be made automatically without operator intervention. After about six hours a new background measurement must be taken to be subsequently subtracted from the measurements made during that time period to ensure measurement accuracy. The number of aspect angles that can be accommodated within that period depends upon the number of averages chosen and the IF bandwidth used. These data are saved to disk and later deconvolved automatically using a single calibration measurement.

The original wideband TEM horns (model H-1734) used in the experiment have a rated operational band of 0.5-6 GHz. To perform slightly bistatic measurements outside this rated frequency range, new antennas AEL H-1498 TEM horns and a HP-8349B amplifier (20 dB gain) were acquired to extend the frequency band limit to 2-18 GHz. A pair of low loss flexible cables 12 ft in length are also utilized to improve the measurement performance. Tests of the new cables have shown no more than 3.5 dB loss at 20 GHz compared to 25 dB at 18 GHz for the original RG-9B cable. Some properties of equipment used in the measurement are shown in Appendix A.

To extend the lower limit of the effective measurement bandwidth, we utilize two or more identical aircraft models with different scales. The larger model is measured in the frequency range 1-7 GHz or 2-18 GHz (lower limit is set by HP-8349B amplifier, upper limit set by antennas). The smaller model is measured in the range 0.4-4.4 GHz (lower limit is set by anechoic chamber and upper limit set by PPL- 5812 amplifier). The smaller model frequency axis is scaled by multiplying by a scaled factor *1/c* to account for the natural resonance of the target. The intensity axis is then scaled by multiplying by a factor of c to account for the size of smaller aircraft. We assume that all targets used in this thesis are linear and time-invariant. Since discontinuous phase will influence the accuracy of the measurement, a genetic algorithm was written that minimizes the squared phase error due to time shifts between two spectra over some range. After minimizing the phase errors, the spectra are spliced at a point over this range. This technique is called the splicing technique. The response will has a significant late-time component due to the presence of the extended low frequency band.

In addition to decreasing the low frequency limit via the scaling technique we are also pursuing an extrapolation scheme to estimate the low frequency response of the target. This scheme would provide information on target scattering from 0 GHz to the low frequency limit of the measurement system. By extrapolating the response to DC, low-pass weighting functions instead of the usual band-pass weighting functions can be used. These low-pass functions preserve the low-frequency resonance contributions and provide a clearer picture of the transient response occurring on the aircraft. In general, the magnitude of spectral response is quatratically extrapolated from the lowest measured frequency to 0 GHz since the quadratic model is relatively smooth and accurate for scattering at low frequencies. The response at 0 GHz is known to be zero. The phase is linearly extrapolated based on the value of the phase and its derivative at the lowest measured frequency.

Finally, some typical weighting functions used in this dissertation are shown in Figure 7.8, Figure 7.9, Figure 7.10, Figure 7.11, Figure 7.12, and Figure 7.13.

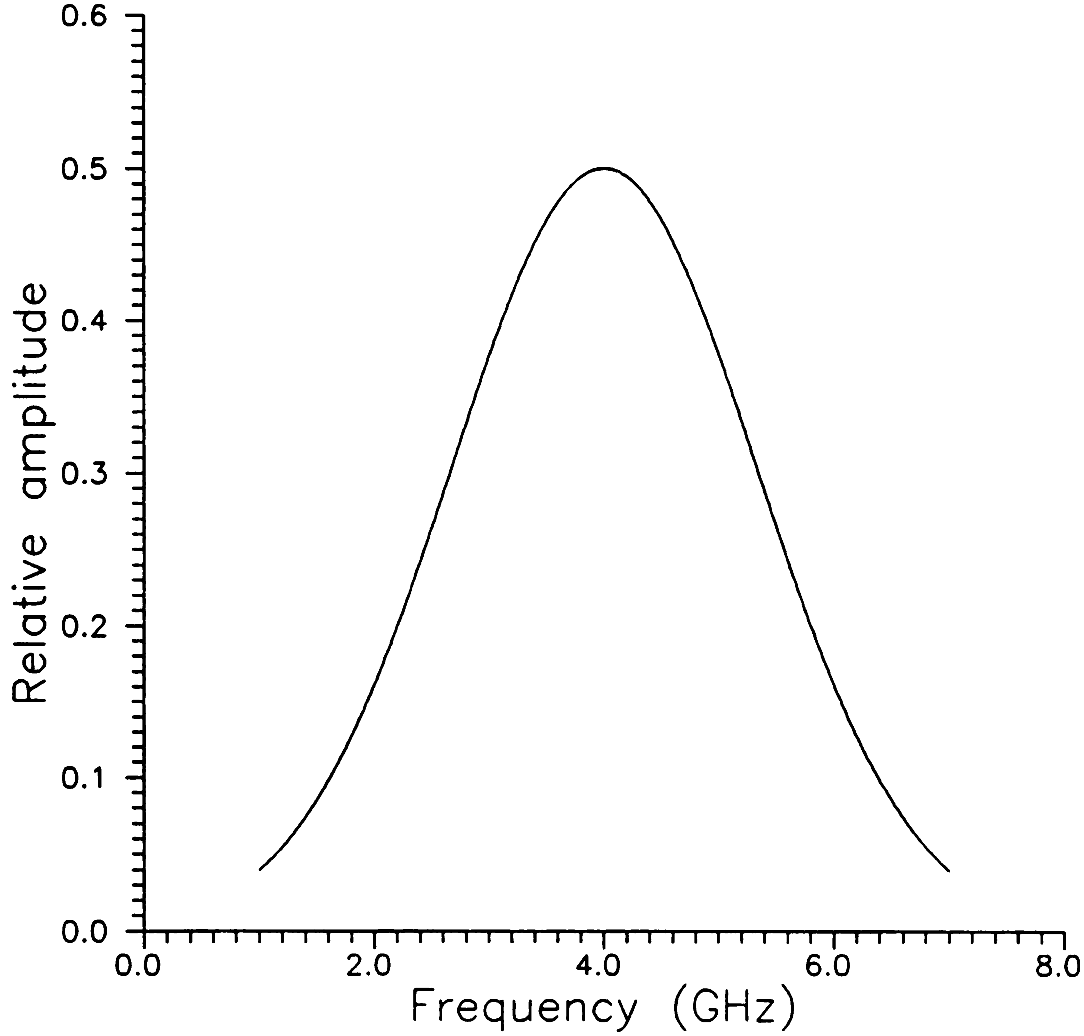

Figure 7.8 Gaussian modulated cosine pulse spectrum. τ=0.3 ns, f_c=4 GHz.

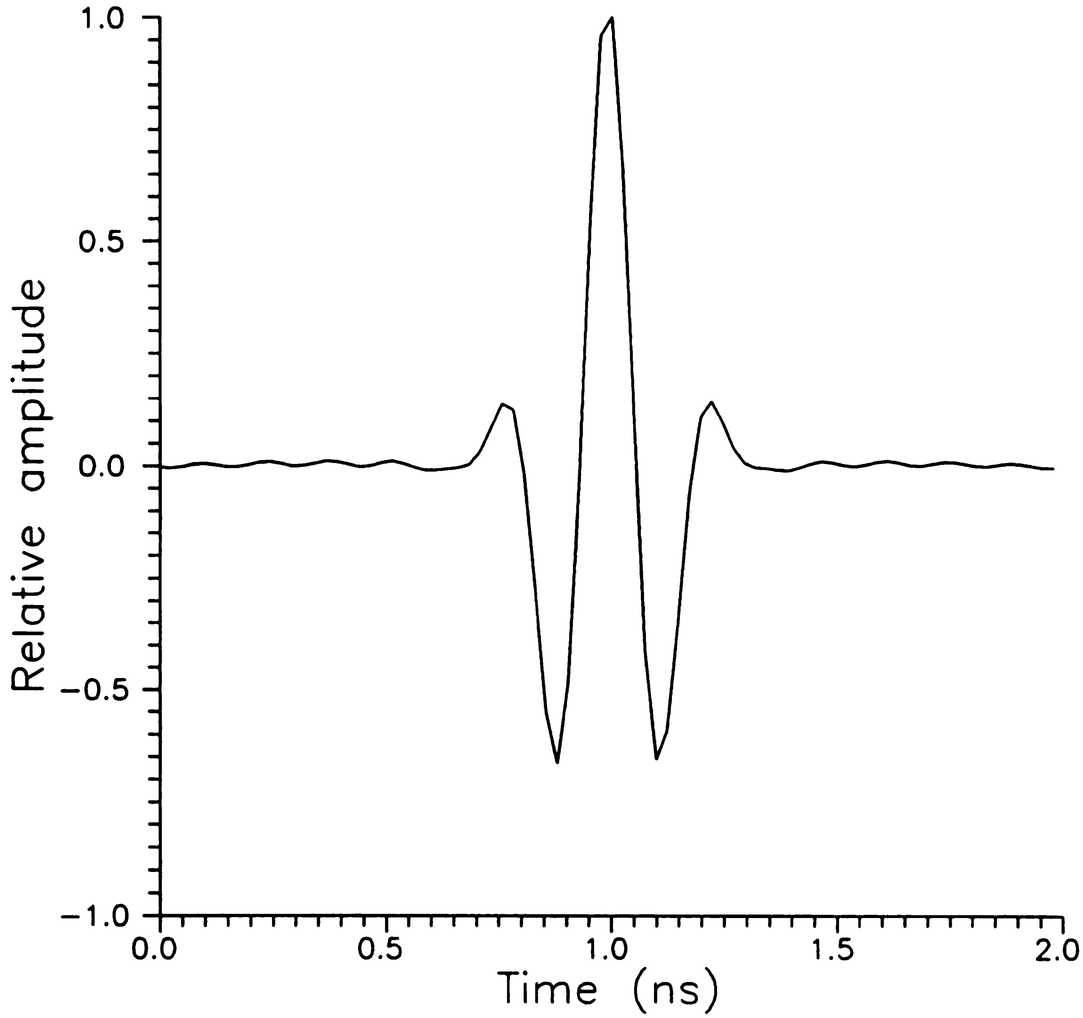

Figure 7.9 Gaussian modulated cosine pulse. τ=0.3 ns, f_c=4 GHz.

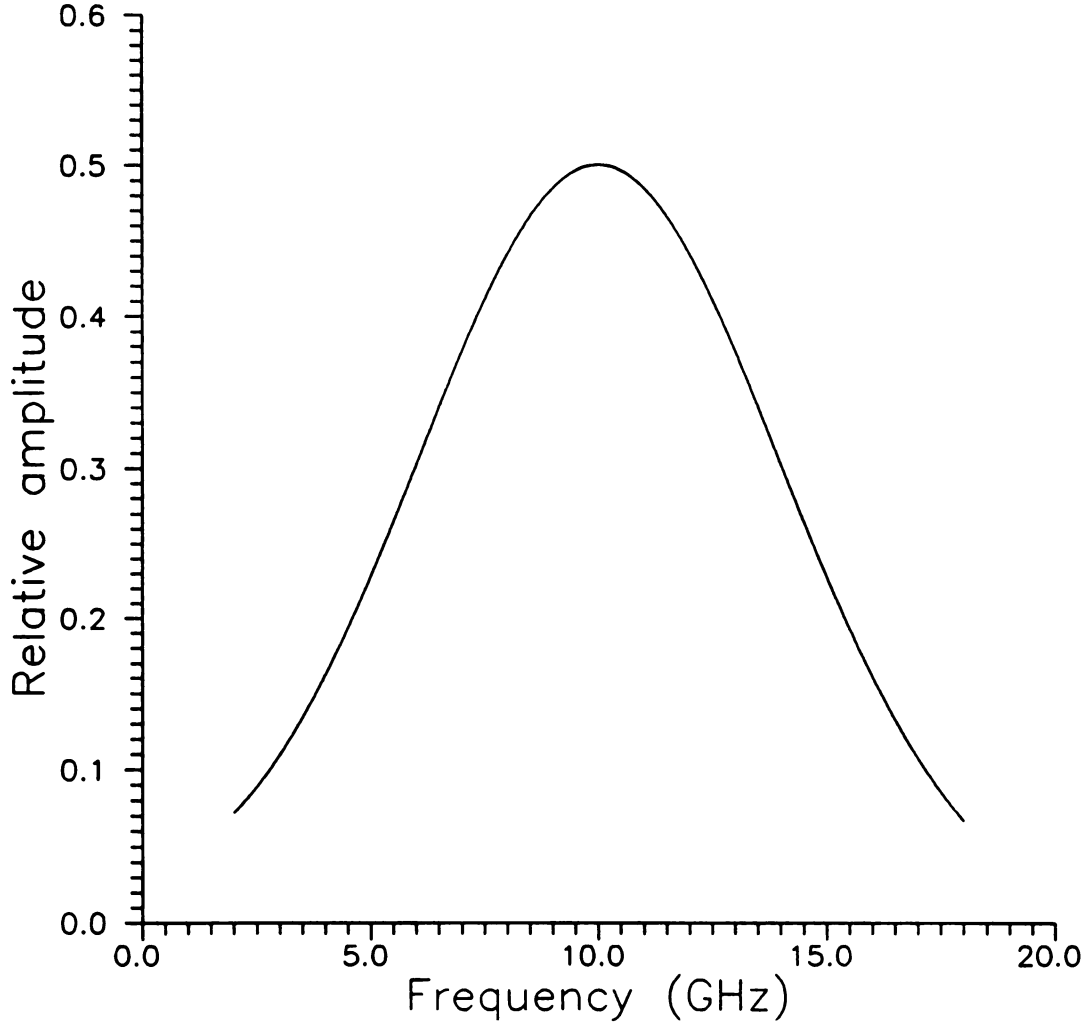

Figure 7.10 Gaussian modulated cosine pulse spectrum. τ=0.1 ns, f_c=10 GHz.

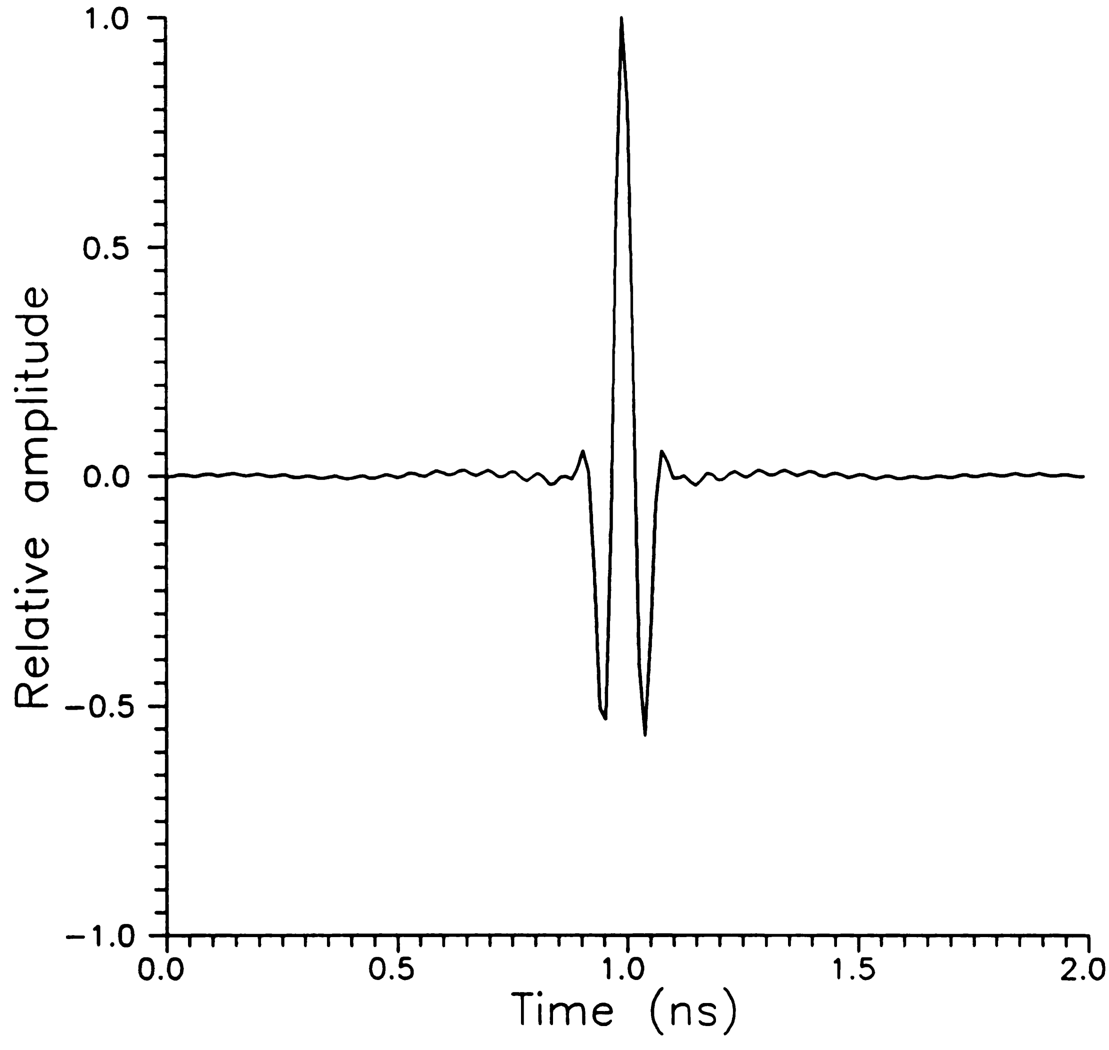

Figure 7.11 Gaussian modulated cosine pulse. τ=0.1 ns, f_c=10 GHz.

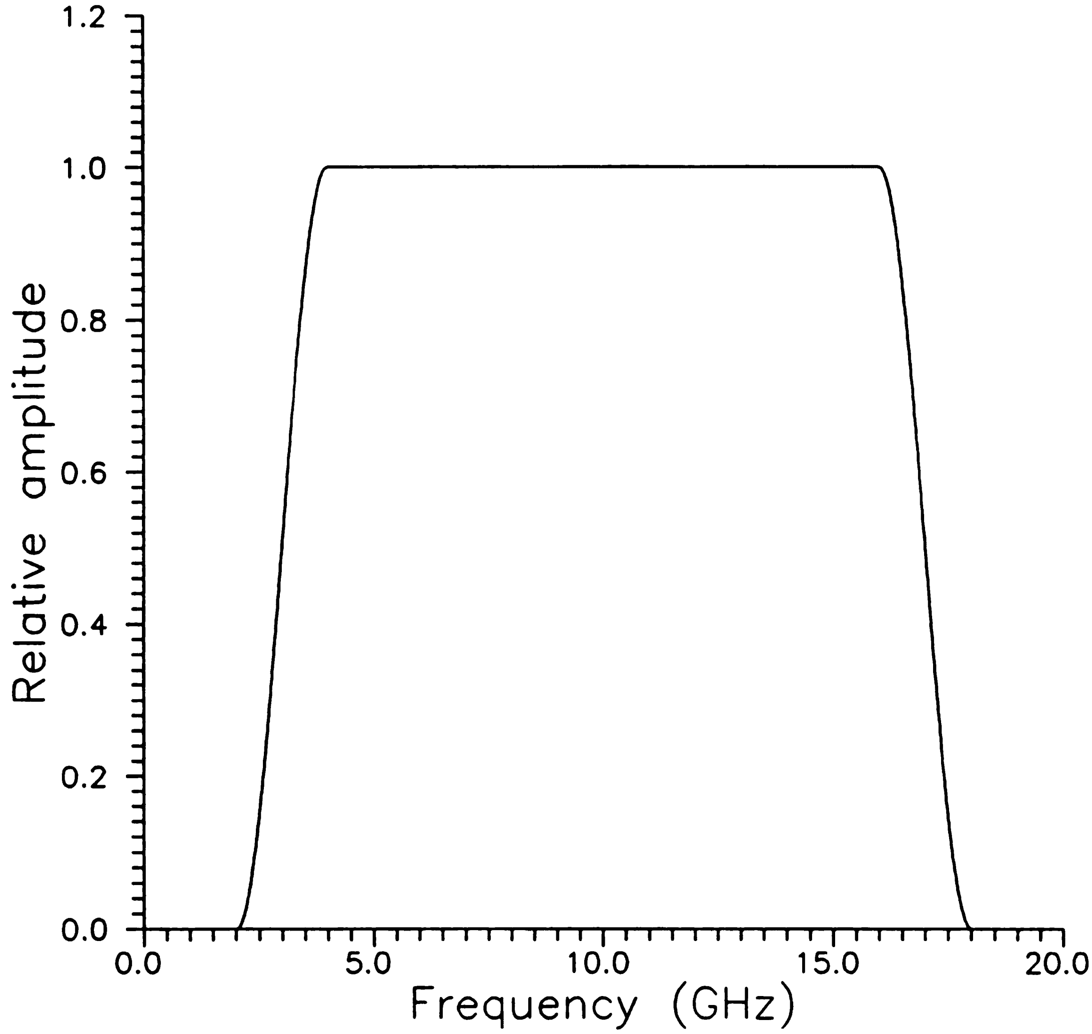

Figure 7.12 Pulse spectrum synthesized from 1/8 cosine taper over bandwidth 2-18 GHz.

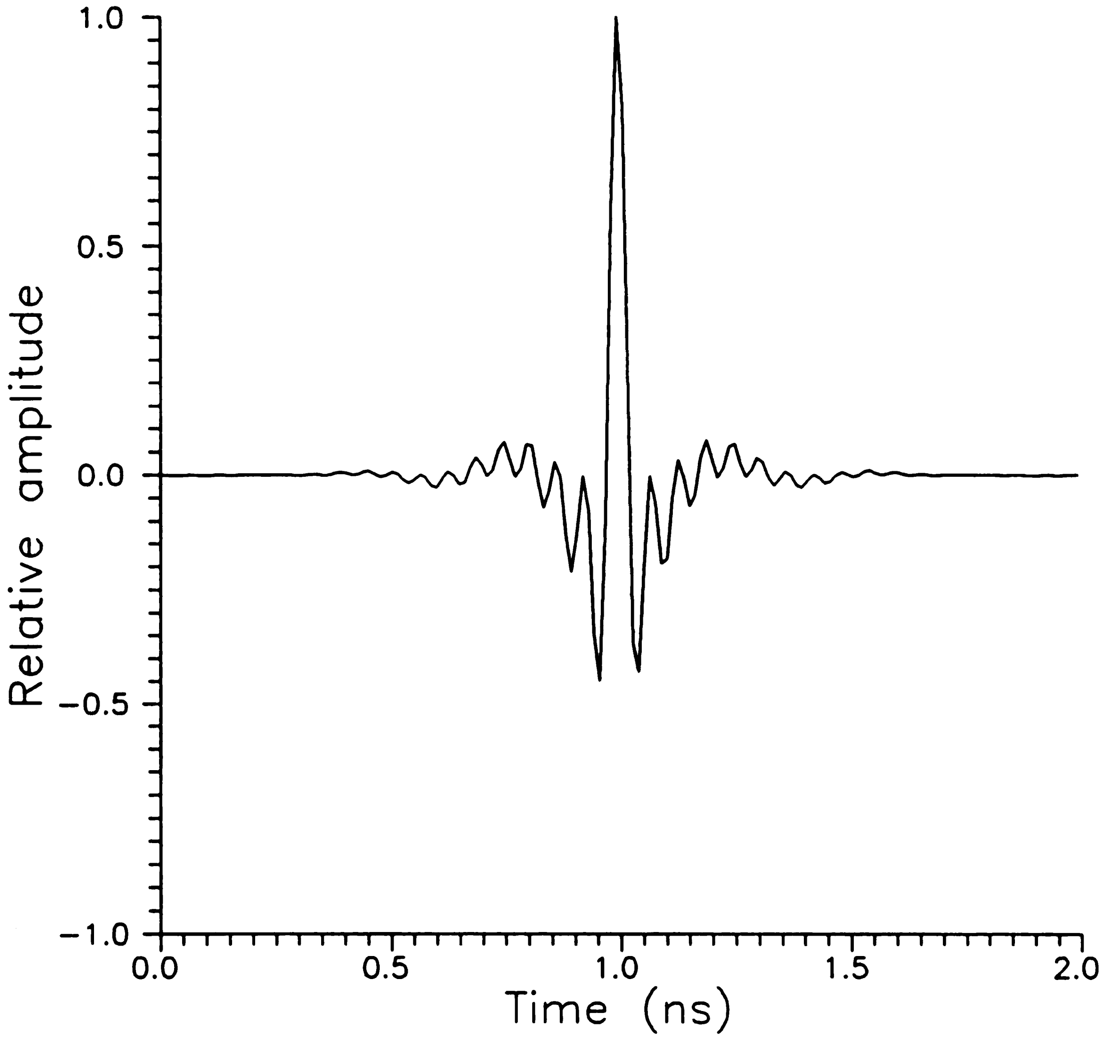

Figure 7.13 Pulse synthesized from 1/8 cosine taper over bandwidth 2-18 GHz.

CHAPTER 8

CONCLUSIONS

This dissertation has presented a number of topics and ideas related to the application of ultra-wideband radar target discrimination and identification. In chapter 2, Altes's model describing the transient early-time response behavior is evaluated using artificial and measured data in the presence of varying amounts of random Gaussian noise. The fitting scheme is good in the determination of scattering center temporal positions, pulse responses, and transfer functions with respect to the changes in the model parameters and to the changes in the frequency band employed if the overlapping of scattering center pulse responses is not severe. When the signals are contaminated with noise the performance of the scheme is degraded, but the largest dominant scattering centers can be reproduced quite well with noise level as high as SNR=10 dB, while the temporal positions of these scattering centers can still be extracted well with a noise level as high as SNR=-5 dB. We also show that varying the incident aspect angle by 10^0 for the B-58 leads to smooth and predictable changes in the reproduction of scattering centers. To reduce overlapping and obtain reasonable accuracy we should use a larger target or a larger bandwidth or a smoother window function or a better scheme such as a genetic algorithm (G.A.).

Chapter 3 attempts to provide a better understanding of the behavior of the scattering centers using a G.A. scheme. The performance of the G.A. is better than the method used in Chapter 2 when the overlapping phenomenon is severe. The drawback is that the G.A. consumes far more computer time. It is better to use the fitting scheme when scattering centers on the target are separated widely. We also note that the accuracy of the G.A. results is highly dependent on the population size and the bit string length. Overguessing or underestimating the number of scattering centers does not affect the reproduction of the brightest scattering centers very much. This gives us a method to choose the number of scattering centers by using a smaller number first, then increasing the number until better results are observed. The determination of scattering center transfer functions using the G.A. is also sensitive to noise. At least SNR=10 dB is required to obtain reasonable results.

Chapter 4 verifies the accuracy of the fitting scheme by comparing the measured transfer functions of three simple canonical targets: a flat plate, a 90^0 dihedral corner reflector, and a circular cylinder with the theoretical transfer functions determined by physical optics (PO). Both the magnitude and the phase of transfer functions are compared. To improve the results, the geometrical theory of diffraction (GTD) or physical theory of diffraction (PTD) is introduced to determine the contributions due to edge diffraction. We show that the transfer function of a particular scattering center is highly dependent on both the aspect angle of the excitation and on the physical properties of the surface at the specular point. The fitting scheme gives an adequate model to describe the behavior of the specular reflection.

It is concluded in Chapter 5 that there exists a duality between the transient late-time response and spectral early-time response of a target. The early-time E-pulse technique uses resonance cancellation in the frequency domain to eliminate the sinusoidal functions arising from the aspect-dependent temporal positions of specular reflections. Target discrimination using early-time information is then possible using an algorithm identical to that used with late-time data. The performance of early-time E-pulse discrimination is demonstrated using specular early-time scattering data for several scale aircraft models in the presence of various levels of noise. The results of this analysis serve as a baseline for comparison with other discrimination methods. When early-time and late-time target information is available, both portions of the response can be used to improve discrimination capabilities. The late-time E-pulse technique is used to identify a possible selection of targets. The possible aspect angles are estimated using stored late-time information. Squared error ratio (SER) is used as a measure of the quality of the smallest error and also a measure of radar target discrimination. Finally, the early-time E-pulse scheme is applied over a limited range of aspect angles for all the possible targets. The target can be identified with noise levels as low as SNR=0 dB in some cases. Note that the incident aspect angle of the unknown target may not be determined accurately in the presence of large amount of noise.

To perform correlation-based target discrimination, "frequency-domain" and "time-domain" techniques are used to reduce the amount of storage needed to hold the responses in Chapter 6. The frequency domain method is computationly quicker in extracting scattering center information. Both techniques require roughly the same amount of storage space in terms of scattering center temporal positions and amplitudes or complex times. Target discrimination based on the discrimination ratio and discrimination range has been investigated. The schemes are not sensitive to the determination of the beginning time of the transient response since they are based on maximum correlation. Both methods give quite similar results. The criteria for determing aspect angle increment to construct the data are based on discrimination range. In our cases, the identification is possible with noise level as low as SNR=-5 dB. It reveals that the two target discrimination methods are not sensitive to the noise in terms of discrimination range. Conservatively, a 2^0 discrimination range was observed. Higher resolution can enhance the ability to discriminate targets, but it requires more storage space and more computer parameter-extracting time.

Chapter 7 reviews the calibration procedure for making accurate transient scattering measurements using a frequency stepping vector network analyzer. Chapter 7 also mentions the improvements in the measurements of aircraft models by extending both the lower frequency and upper frequency limits via scaling, extrapolation, and wideband antennas.

In summary, this dissertation has addressed a number of topics pertinent to the application of UWB radar to the understanding of the scattering center behavior of radar targets and target discrimination. Though a number of problems associated with early-time target discrimination have been addressed in this dissertation, many interesting and useful problems associated with UWB radar remain. Specifically, ways to reduce ill-conditioning and determine scattering center transfer functions accurately when overlapping of scattering center pulse responses is severe should be investigated further. Effective implementation of the E-pulse and correlation schemes will also require more exhaustive studies of aircraft responses. The early-time E-pulse scheme based on the real part or imaginary part of spectral early-time responses is very sensitive to the determination of the beginning time. It is also useful to develop a scheme to reduce this sensitivity. There are several methods such as E-pulse, correlation, and neural network techniques to perform radar target discrimination. It would be useful to translate all these into a single measure of confidence in radar target discrimination.

APPENDIX A

APPENDIX A

EXPERIMENTAL EQUIPMENT

This appendix summarizes the apparatus used for the experimental portion of the research. The equipment used in the frequency domain scattering measurements is listed in Table A.1. There were three different configurations used at EM lab in MSU so far. The "low-band" configuration used the PPL-5812 amplifier to amplify the signal from port 1 of the network analyzer. The parameters used in this configuration are shown in Table A.2. The "high-band" configuration used the HP-8349B amplifier to amplify the signal from port 1 of the network analyzer. The parameters used in this configuration are described in Table A.3. The enhanced "high-band" configuration used the HP-8349B amplifier too. The parameters used in this configuration are demonstrated in Table A.4.

To accurately characterize the measurement system, the network analyzer was used to measure the gain of the amplifiers and attenuations of the cables over a wide range of frequencies. The results of these measurements are provided here to indicate the limitation of measurement system, the improvements, and baseline measurements to assess future equipment changes. The signal gain of the HP-8349B amplifier is shown in Figure A.1. Note that the gain is about 20 dB over 2 GHz. The gain of the PPL-5812 amplifier is shown in Figure A.2. The gain decreases a lot over 4 GHz. This attenuation

Table A.1 Equipment used for frequency domain scattering measurements.

Hewlett-packard HP-8720B vector network analyzer
Hewlett-packard HP-8349B microwave amplifier
Picosecond pulse labs PPL-5812 10 dB broadband amplifier
American electronics laboratory AEL H-1734 wideband TEM horn antennas
23.5 foot RG-9B cable with N-type connector
22.5 foot RG-9B cable with N-type connector
B&K precision D.C. power supply 1610 (for PPL amplifier)
Insulated wire inc. AEL H-1498 wideband TEM horn antennas
12 foot low loss cable with SMA connector

Table A.2 Low band measurement parameters.

Measurement parameter:	S21
Frequency sweep:	0.4 - 4.4 GHz
number of points:	401
IF bandwidth:	100 Hz
number of averages:	10
Sweep time:	30 seconds

limits usage of amplifier in higher frequency range. Cables losses for the system are shown in Figure A.3. Note that this cable is very lossy at high frequencies. Now a pair of low loss flexible cables 12 foot in length are available to help improve range performance. Tests of new cables are 3.5 dB loss at 20 GHz.

Table A.3 High band measurement parameters.

Measurement parameter:	S21
Frequency sweep:	1.0 - 7.0 GHz
number of points:	601
IF bandwidth:	100 Hz
number of averages:	10
Sweep time:	60 seconds

Table A.4 Enhanced high band measurement parameters.

Measurement parameter:	S21
Frequency sweep:	2.0 - 18.0 GHz
number of points:	1601
IF bandwidth:	100 Hz
number of averages:	2
Sweep time:	60 seconds

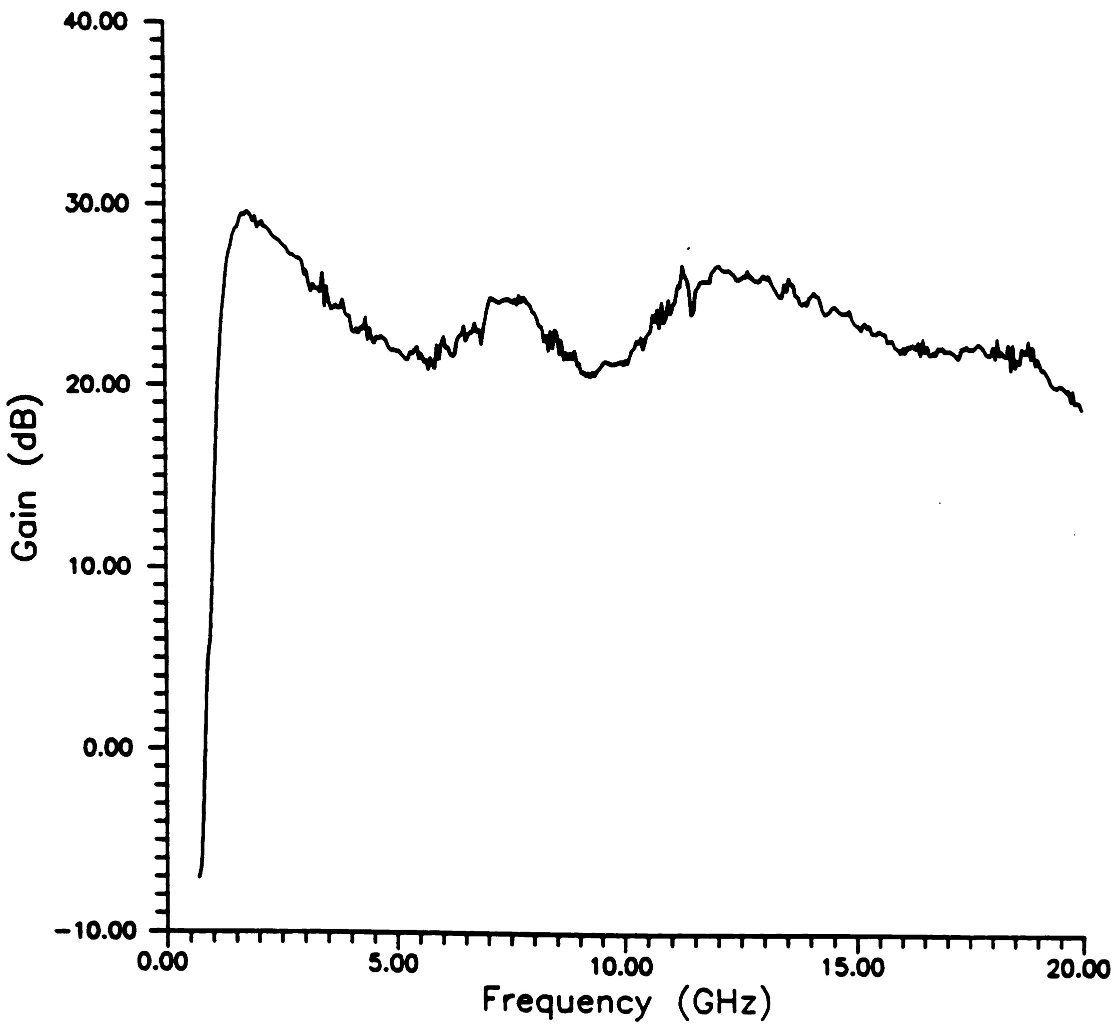

Figure A.1 Gain of HP8349B Microwave Amplifier measured using HP-8720B network analyzer. Amplifier input power = -30 dBm

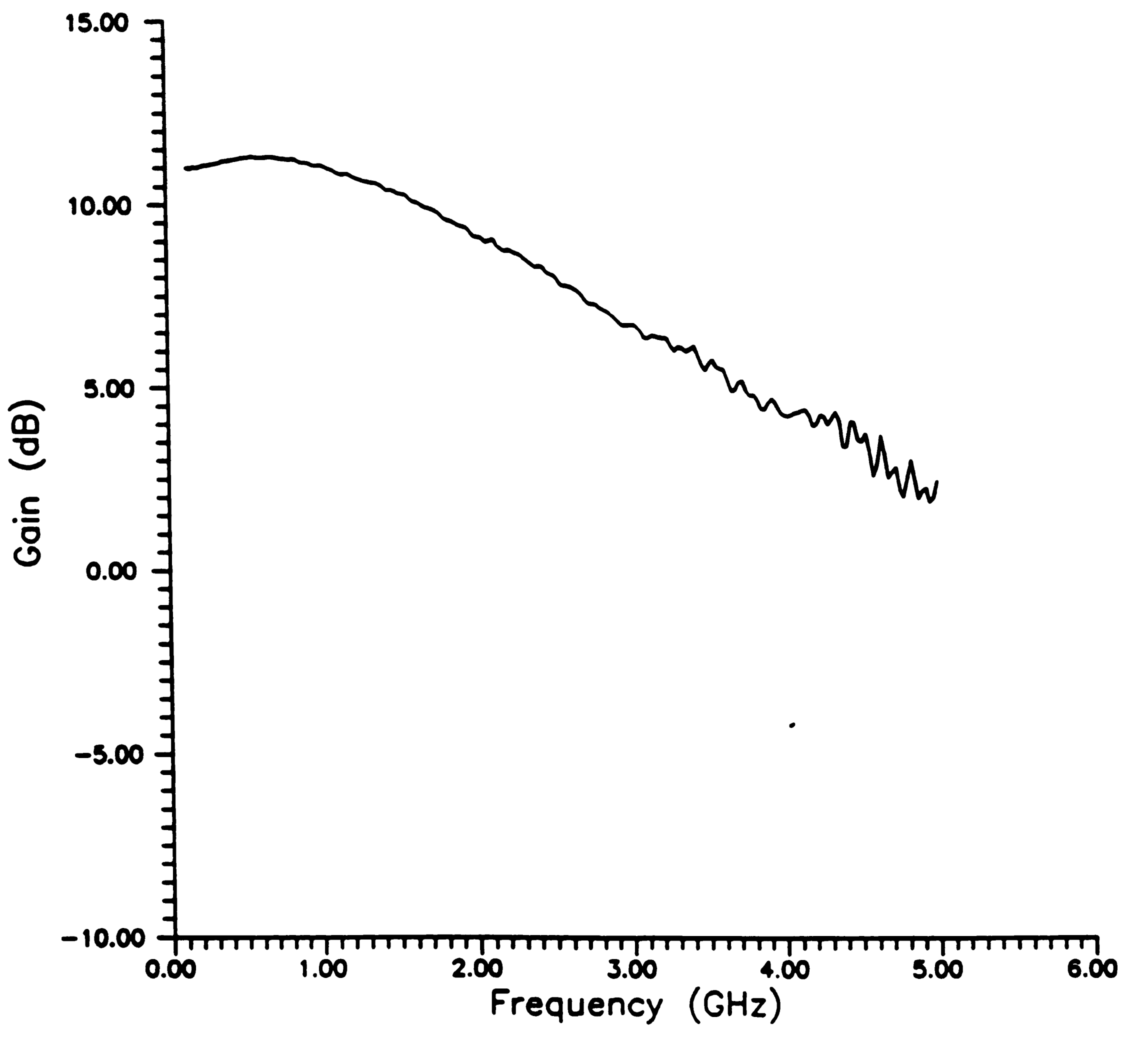

Figure A.2 Gain of PPL 5812 wide band amplifier measured using HP-8720B network analyzer. Amplifier input power = -10 dBm.

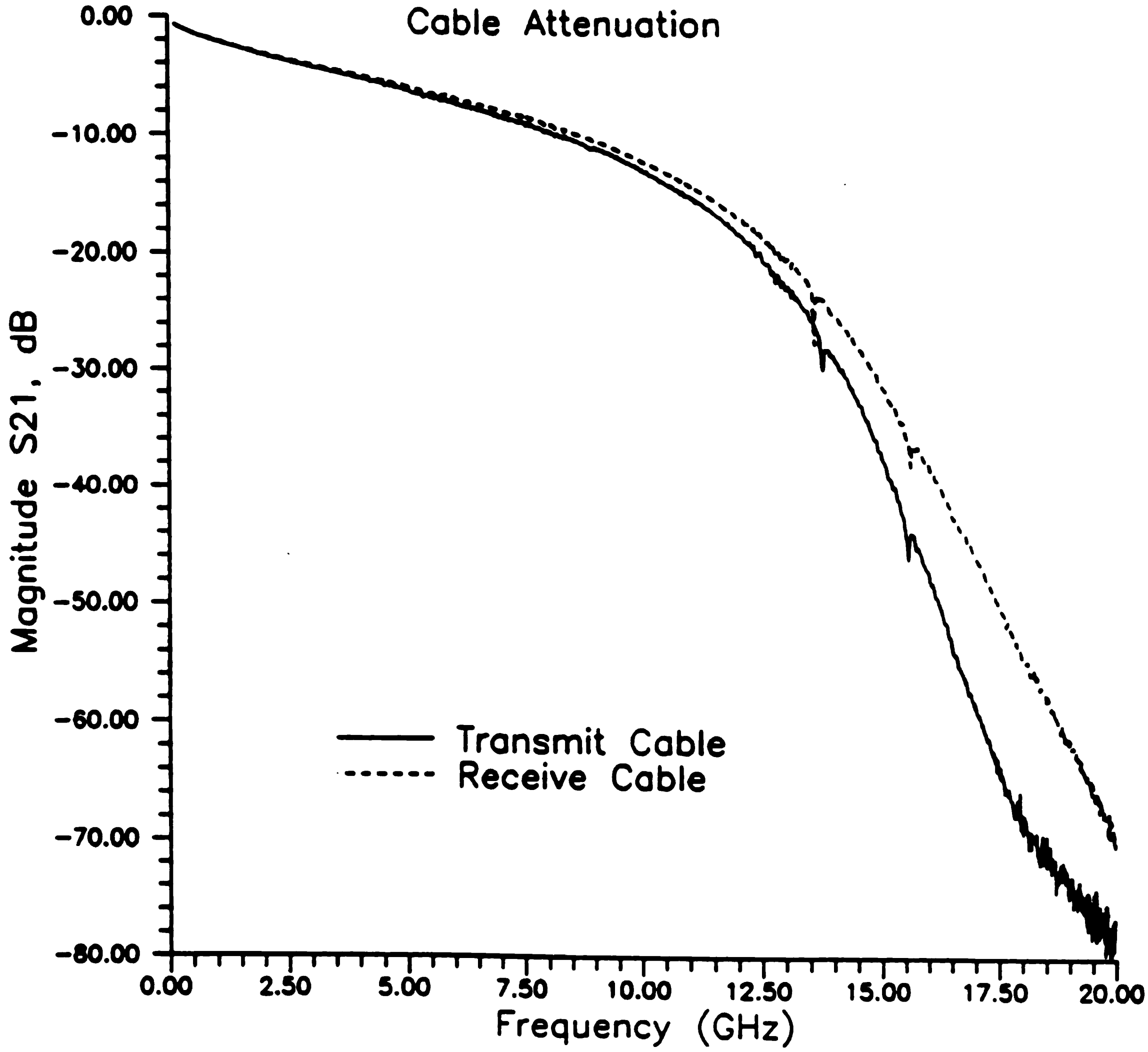

Figure A.3 Measured cable attenuation.

BIBLIOGRAPHY

BIBLIOGRAPHY

1. E. Kennaugh, "The K-pulse concept," *IEEE Trans. Antennas and Propogat.*, vol. AP-29, pp. 327-331, March 1981.

2. F. Y. S. Fok, D. L. Moffatt and N. Wang, "K-pulse estimation from the response of a target," *IEEE Trans. Antennas and Propogat.*, vol. AP-35, pp. 926-934, August 1987.

3. E. J. Rothwell, D. P. Nyquist, K. M. Chen and B. Drachman, "Radar target discrimination using the extinction-pulse technique," *IEEE Trans. Antennas and Propogat.*, vol. AP-33, no. 9, pp. 926-936, Sept. 1985.

4. E. J. Rothwell, K. M. Chen, D. P. Nyquist and W. Sun, " Frequency domain E-pulse synthesis and target discrimination," *IEEE Trans. Antennas and Propogat.*, vol. AP-35, no.4, pp. 426-434, April 1987.

5. K. M. Chen, D. P. Nyquist, E. J. Rothwell, L. L. Webb and B. Drachman, "Radar target discrimination by convolution of radar returns with extinction pulse and single-mode extraction signals," *IEEE Trans. Antennas and Propogat.*, vol. AP-34, no.7, pp. 896-904, July 1986.

6. K. M. Chen, D. P. Nyquist, E. J. Rothwell and W. Sun, "New progress on E/S pulse techniques for noncooperative target recognition," *IEEE Trans. Antennas and Propogat.*, vol. AP-40, pp. 829-834, July 1992.

7. P. Ilavarasan, E. J. Rothwell, K. M. Chen, D. P. Nyquist, "Extraction of natural frequencies from measured data set using genetic algorithm," submitted to *IEEE Trans. Ant. Propagat.*.

8. M. P. Hurst and R. Mittra, "Scattering center analysis via Prony's method," *IEEE Trans. Ant. Propagat.*, vol. AP-35, pp. 986-988, August 1987.

9. R. Carriere and R. L. Moses, "High resolution radar target modeling using a modified Prony estimator," *IEEE Trans. Ant. Propagat.*, vol. AP-40, pp. 13-18, January 1992.

10. E. J. Rothwell, K. M. Chen, D. P. Nyquist, P. Ilavarasan, J. E. Ross, R.

Bebermeyer, and Q. Li, "A general E-pulse scheme arising from the dual early-time/late-time behavior of radar scatterers," *IEEE Trans. Ant. Propagat.*, vol. 42, no.9, pp. 1336-1341, September 1994.

11. R. A. Altes, "Sonar for generalized target description and its similarity to animal echolocation systems," *J. Acoust. Soc. Amer.*, vol. 59, pp. 97-105, January 1976.

12. P. Ilavarasan, J. E. Ross, E. J. Rothwell, K. M. Chen, D. P. Nyquist, "Performance of an automated radar target discrimination scheme using E pulses and S pulses," *IEEE Trans. Ant. Propagat.*, vol. AP-41, no. 5, pp. 582-588, May 1993.

13. J. H. Holland, "Universal computer capable of executing an arbitrary number of subprogrames simultaneously," *Proc. of the eastern joint computer conference*, pp. 108-112, 1959.

14. H. J. Antonisse and K. S. Keller, "Genetic operators for high-level knowledge representations," *Genetic algorithms and their applications: Proc. of the Second International Conference on Genetic Algorithms*, pp. 69-76, 1987.

15. A. D. Bethke, "Genetic algorithms as function optimizers (technique report No. 212)," University of Michigan, Ann arbor, 1978.

16. A. Brindle, "Genetic algorithms for function optimization," Doctoral dissertation, University of Alberta, Edmonton, 1981.

17. T. H. Westerdale, "A reward scheme for production systems with overlapping conflict sets," *IEEE Trans. on Systems, Man, and Cybernetics, SMC-16 (3)*, pp. 369-383, 1986.

18. D. E. Goldberg, *Genetic Algorithms*, New York: Addison-Wesley, 1989, Ch. 1-4.

19. Asokek and S. K. Tanclon, "Radar cross-section of a finite planar structure coated with a lossy dielectric," *IEEE Trans. Ant. Propagat.*, vol. AP-32, pp. 1003-1006, May 1984.

20. D. S. Wang,"Limit and validity of the impedance boundary condition on penetrable surface," *IEEE Trans. Ant. Propagat.*, vol. AP-35, pp. 453-457, April 1987.

21. J. H. Richard, "Scattering by a ferrite-coated conducting sphere," *IEEE Trans. Ant. Propagat.*, vol. AP-35, pp. 73-79, Jan. 1987.

22. R. H. Clarke and J. Brown, "Diffraction theory and antenna," *John wiley & sons*, 1980.

23. Q. Li, "High frequency scattering and reduced scale computation of targets coated with a lossy dielectric," M.S. thesis, University of Science and Technology of China, Chengdu, P.R.China.

24. R. A. Ross, "RCS of rectangular flat plates as a function of aspect angle," *IEEE Trans. Antennas Propagat.*, vol. AP-14, pp.329-335, May 1966.

25. K. M. Siegel, *Appl. Sci. Res.*, Sec.B, vol. 7, pp.293-328, 1958.

26. T. Griesser and C. A. Balanis, "Backscatter analysis of Dihedral corner reflector using physical optics and the physical theory of diffraction," *IEEE Trans. Antennas Propagat.*, vol. AP-35, pp. 1137-1147, Oct 1987.

27. P. Ilavarasan, E. J. Rothwell, K. M. Chen, D. P. Nyquist, "Natural resonance extraction from multiple data sets using physical constraints," *Radio Science*, vol. 29, no.1, pp. 1-7, Jan. 1994.

28. C. E. Baum, E. J. Rothwell, K. M. Chen, D. P. Nyquist, "The singularity expansion method and its application to target identification," *Proc. IEEE.*, vol. 79, pp. 1481-1492, October 1991.

29. E. J. Rothwell, K. M. Chen, D. P. Nyquist, "Extraction of the natural frequencies of a radar target from a measured response using E-pulse techniques," *IEEE Trans. Ant. Propagat.*, vol. AP-35, pp. 715-720, June 1987.

30. E. J. Rothwell, K. M. Chen, "A hybrid E-pulse/least squares technique for natural resonance extraction," *Proc. IEEE.*, vol. 76, pp. 296-298, March 1988.

31. C. E. Baum, "On the singularity expansion method for the solution of electromagnetic interaction problems," *Interaction notes*, note 88, December 1971.

32. P. Ilavarasan, E. J. Rothwell, J. E. Ross, D. P. Nyquist and K. M. Chen, "Time domain radar target discrimination using S-pulse waveforms," presented at the 1991 north American Radio Science meeting, london, Ontario, Canada, June 22-25,1991.

33. M. L. Skolnik, Introduction to Radar Systems, new York: McGraw-Hill, 1980.

34. P. Ilavarasan, Q. Li, J. E. Ross, E. J. Rothwell, K. M. Chen, and D. P. Nyquist, "Combination of early-time and late-time based E-pulses to improve target identification," " submitted to *IEEE Trans. Ant. Propagat.*.

35. E. J. Rothwell, K. M. Chen, D. P. Nyquist, J. E. Ross and R. Bebermeyer, "A radar target discrimination scheme using the discrete wavelet transform for reduced data storage," *IEEE Trans. Ant. Propagat.*, vol. AP-42, pp. 1033-1037,

July 1994.

36. O. Rioul and M. Vetterli, "Wavelets and signal processing," *IEEE Signal processing*, vol. 8, no. 4, pp. 14-38, Oct. 1991.

37. S. G. Mallat,"A theory for multiresolution signal decomposition: the wavelet transform," *IEEE Trans. Pattern Anal. Machine Intell.*, vol. 11, no. 7, pp. 674-693, July 1989.

38. H. J. Li and S. H. Yang, "Using range profiles as feature vectors to identify aerospace objects," *IEEE Trans. Antennas Propagat.*, vol. AP-41, pp. 261-268, March 1993.

39. H. J. Li and V. Chiou, "Aerospace target identification - comparison between the matching score approach and the neural network approach," *J. Electromag. Waves Appl.*, vol. 7, No. 6, pp. 873-893, 1993.

40. R. G. Atkins, R. T. Shin and J. A. Kong, "A neural network method for high range resolution target classification," in *Progress in Electromag. Research 4*, J. A. Kong, Ed., Elsevier, N. Y., pp. 255-292, 1991.

41. H. J. Li, N. H. Farhat, Y. shen and C. L. Werner, "Image understanding and prediction in microwave diversity imaging," *IEEE Trans. Antennas Propagat.*, vol. 37, pp. 1048-1057, August 1989.

42. H. J. Li, F. L. Lin, Y. shen and N. H. Farhat, Y. shen, "A generalized interpretation and prediction in microwave imaging involving frequency and angular diversity," *J. Electromag. Waves and Appl.*, vol. 4, No. 5, pp. 415-430, 1990.

43. P. R. Younger, "Scattering center identification in three dimensions," MS thesis, Ohio State University, Department of Electrical Engineering, Columbus, Ohio, 1990.

44. M. A. Morgan, "Time-domain scattering measurements," *IEEE Trans. Antennas Propagat. Newsletter*, vol. 6, pp. 5-9, August 1984.

45. M. A. Morgan and B. W. McDaniel, "Transient electromagnetic scattering: Data acquisition & signal processing," *IEEE Trans. on Instrumentation and Measurement*, vol. 37, pp. 263-267, June 1988.

46. M. A. Morgan and N. J. Walsh, "Ultra-wide-band transient electromagnetic scattering laboratory," *IEEE Trans. Antennas Propagat.*, vol. 39, pp. 1230-1234, August 1991.

47. M. A. Morgan, "Ultra-wideband impulse scattering measurements," *IEEE Trans.*

Antennas Propagat., vol. 42, pp. 840-846, June 1994.

48. F. T. Ulaby, T. F. Haddock, J. East and M. Whitt, "A millimeter-wave network analyzer based scatterometer," *IEEE Trans. on Geoscience and Remote Sensing*, Vol. GE-26, pp. 75-81, Jan. 1988.

49. B. Drachman, "Two methods to deconvolve: L^1-method using simple algorithm and L_2-method using least squares and a parameter," *IEEE Trans. Antennas Propagat.*, vol. 32, pp. 219-225, March 1984.

50. J. E. Ross, "Application of Transient Electromagnetic Fields to Radar Target Discrimination," Ph. D. dissertation, Michigan State University, 1992.

51. Mie, *Ann. Physik*, 25, 377, 1908.

52. J. A. Stratton, *Electromagnetic theory*, New York and London: McGraw-Hill, 1941, pp. 563-573.

53. R. F. Harrington, *Time harmonic electromagnetic fields*, New York: McGraw-Hill, 1941.

54. K. M. Chen, *EE 836-electromagnetic waves I: course notes*, Michigan State University, 1992.